

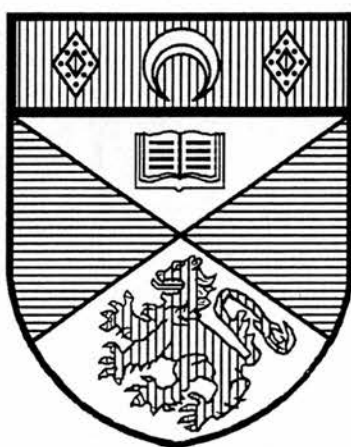
University of St Andrews



Full metadata for this thesis is available in
St Andrews Research Repository
at:

<http://research-repository.st-andrews.ac.uk/>

This thesis is protected by original copyright



The Surface Raman Spectroscopy of Polymer-Modified Electrodes

A thesis presented by Andrew Peter Taylor, B. Sc., to the University of St.
Andrews in application for the degree of Doctor of Philosophy.

February 1996.



TL
B 974

Declarations

I, Andrew Peter Taylor, hereby certify that this thesis has been composed by myself, that it is a record of my work and that it has not been accepted in partial or complete fulfilment of any other degree or professional qualification.

Signed _____

Date 12/2/96

I was admitted to the Faculty of Science of the University of St. Andrews under Ordinance General No. 12 on the 1st of October 1992 and as a candidate for the degree of Ph. D. on the 1st of October 1993.

Signed _____

Date 12/2/96

I hereby certify that the candidate has fulfilled the conditions of the Resolution and Regulations appropriate to the degree of Ph. D.

Signature of supervisor _____

Date 2nd Feb. 1996

Declaration

In submitting this thesis to the University of St. Andrews, I understand that I am giving permission for it to be made available for its use in accordance with the regulations of the University library for the time being in force, subject to any copyright vested in the work not being affected thereby. I also understand that the title and abstract will be published, and that a copy of the work may also be made and supplied to any *bona fide* library or research worker.

Courses Attended

The School of Chemistry requires that a number of courses be attended. These courses were: "Organic Reaction Mechanism" (Dr. A. R. Butler), "Advanced Spectroscopy" (Dr. J. A. Crayston), "Organic Synthesis" (Prof. D. Gani), "Solid State NMR" (Dr. K. D. M. Harris), "Bioinorganic Chemistry" (Dr. D. T. Richens), and "Advanced Electrochemistry" (Prof. C. A. Vincent)

Contents

Declarations	i
Courses Attended	iii
Contents	iv
List of Abbreviations	vi
Acknowledgements	ix
Abstract	xi

Chapter 1

Introduction

1.1	Modified Electrodes	1
1.2	Characterization of Modified Electrodes	12
1.3	Raman Spectroscopic Techniques	24
1.4	The Quartz Crystal Microbalance	35
1.5	Thesis Summary	37
1.6	References	38

Chapter 2

Studies on Aqueous Pyridine Solutions

2.1	Introduction	46
2.2	Experimental	51
2.3	Results	57
2.4	Discussion	68
2.5	Conclusions	83
2.6	References	84

Chapter 3

SE(R)R Spectra and Assignments for PMEs

3.1	Introduction	87
3.2	Experimental	90
3.3	Results	95
3.4	Discussion	105
3.5	Conclusions	112
3.6	References	113

Chapter 4

Quantitative Studies of the SE(R)RS Intensities at PMEs

4.1	Introduction	115
4.2	Experimental and Theory	122
4.3	Results	130
4.4	Discussion	141
4.5	Conclusions and Suggestions for Further Study	149
4.6	References	150

Chapter 5

Electrochemistry and SERS of Chromium Bipyridyl Complexes

5.1	Introduction	153
5.2	Experimental	154
5.3	Results	158
5.4	Discussion	170
5.5	Conclusions	182
5.6	References	183

List of Abbreviations

δ	Relative to tetramethylsilane.
4VP	4-vinyl pyridine.
AC, ac	Alternating current.
AES	Auger electron spectroscopy.
AFM	Atomic force microscope.
Ag / AgCl	Silver / silver chloride electrode.
AIBN	Azo(iso)butyronitrile.
AMU	Atomic mass units.
ATR	Attenuated total reflection.
bpy	2,2'-bipyridine.
CCD	Charge coupled device.
CME	Chemically modified electrode.
CT	Charge transfer.
CV	Cyclic voltammetry, Cyclic voltammogram.
DCM	4-(Dicyanomethylene)-2-methyl-6-(4-dimethylaminostyryl)-4 <i>H</i> -pyran.
DMF	Dimethylformamide.
DMSO	Dimethylsulphoxide.
EC	Electrochemical-chemical.
ECL	Electrochemiluminescence.
EL	Electroluminescence.
EM	Electromagnetic.
en	1,2-ethylene diamine.
EQCM	Electrochemical quartz crystal microbalance.
ESCA	Electron spectroscopy for chemical analysis.
ESR	Electron spin resonance.
FWHM	Full-width at half-maximum.
FT	Fourier-transform.

GC/MS	Gas chromatographic mass spectrometry.
HMDE	Hanging mercury drop electrode.
'iR'	Current multiplied by resistance.
IR	Infra-red.
ITO	Indium tin oxide.
LEED	Low energy electron diffraction.
MLCT	Metal-to-ligand charge transfer.
MV	Methyl viologen (1,1'-dimethyl-4,4'-bipyridinium).
NADH	Nicotinamide adenine dinucleotide, reduced form.
NCA	Normal coordinate analysis.
NMR	Nuclear magnetic resonance.
OMA	Optical multichannel analyzer.
ORC	Oxidation-reduction cycle.
ox	Oxalate.
PAA	Poly(acrylic acid).
phen	1,10-Phenanthralene
PME	Polymer modified electrode.
PPV	Poly(p-phenylenevinylene)
PVP	Poly(4-vinyl)pyridine.
py	Pyridine.
pzc	Potential of zero charge.
QCM	Quartz crystal microbalance.
RDE	Rotating disc electrode.
RR	Resonance Raman.
RRDE	Rotating ring disc electrode.
S/N	Signal to noise.
SAM	Self-assembled monolayer.
SCE	Saturated calomel electrode.
SECM	Scanning electrochemical microscope.

SEF	Surface-enhancement factor.
SEM	Scanning electron microscope.
SERS	Surface-enhanced Raman spectroscopy.
SERRS	Surface-enhanced resonance Raman spectroscopy.
SE(R)RS	Used in contexts where both SERS and SERRS experiments are referred to.
SEXAFS	Surface extended x-ray absorption fine structure.
SFG	Sum frequency generation.
SHG	Second harmonic generation.
STM	Scanning tunneling microscope.
SU(R)RS	Surface unenhanced (resonance) Raman spectroscopy.
SXRD	Surface x-ray diffraction.
TRRR, TR ³	Time-resolved resonance Raman.
UHV	Ultra-high vacuum.
UME	Ultramicroelectrode.
UV-vis	Ultra-violet visible spectroscopy.
VIEWS	Variable angle of incidence evanescent wave spectroscopy.
w/v	Weight per volume.
w/w	Weight per weight.
XPS	X-ray photoelectron spectroscopy.

Acknowledgements

I would like to express gratitude to Dr. Joe A. Crayston, my academic supervisor, for the enthusiasm and guidance without which I would not be able to present this work. I especially thank him for the prompt and tireless assistance he has given during the writing of this thesis, despite his being on sabbatical in California. I would also like to thank Dr. T. J. Dines of Dundee University for giving a substantial amount of help and guidance with Raman spectroscopic experiments.

Thanks are also due to Dr. Andrew Glidle and Dr. Robert Peacock of Glasgow University, who collaborated on the QCM work. The technical department of School of Chemistry in St. Andrews gave great assistance, most notably Jim Bews (computing support), Sylvia Smith (microanalysis), Melania Smith (NMR), Colin Smith (glassblowing), and Jim Rennie (mechanical works, including design and construction of the SERS cell).

Thanks also to various occupants of lab 248 in St. Andrews and of the Raman lab in Dundee who have done their best to help and to make the three (or so) years rather odd. Alan MacGregor, Caroline Smith, John Morrison, Julian Osman, Graeme Hunt and Paola Avogadro in St. Andrews and Saira Ellahi, Louise MacGregor and Mo Akhter in Dundee all deserve mentions by name. I would also like to thank, for assorted material help given over the years: Ali Christie, Stefan Clarke, Thomas Clifford, Andrew Danby, Prof. Bob Hay, Charles Lindall, John Smith, and Dr. Dave Richens

I am indebted to first the SERC and subsequently the EPSRC for financial support and also to both the EPSRC and the School of Chemistry for funding travel to the 30th ICCM meeting in Kyoto, Japan.

Two final thank-yous are necessary, to my family for their continued support and to my girlfriend Julie Cornish who went through the agony of thesis writing at the same time as me.

“Perseverance is not a long race; it is many short races one after another.”

Walter Elliott

Abstract

Applications of surface-enhanced Raman spectroscopies and the quartz crystal microbalance to electrode interfaces, especially polymer-modified electrodes, are investigated. The quartz crystal microbalance is used to investigate the adsorption of pyridine at electrochemically roughened silver electrodes from aqueous chloride electrolyte, using conditions comparable to those used in SERS studies. During roughening in aqueous chloride solution, delays seen between the onset of oxidation and reduction at the Ag surface and the commencement of frequency decrease and increase, respectively, are explained by release of trapped species upon initial formation of the AgCl layer and then re-trapping upon reduction. At anodic limits of +0.25 V and above, the reduction proceeds in two steps representing the reduction of two separate silver chloride phases. Below the silver oxidation potential corrosion inhibition of the silver surface by pyridine leads to a lower hysteresis between cathodic and anodic sweeps in the frequency vs potential plots when the heterocycle is present in solution. The most intense pyridine SERS spectra occur at potentials where the frequency of the quartz crystal is highest, suggesting that adsorption of the organic species leads to break-down of long-range viscous coupling of solvent to the surface *via* hydrogen-bonding interactions. Full assignments of the SERS spectrum of pyridine-*d*₅ are reported.

SERS spectra of 4-vinyl pyridine and poly(4-vinyl)pyridine at the silver electrode are reported and assigned. At negative potentials free-radical polymerization of the monomer and short-chain polymers can be initiated by H[•]. When dissolved oxygen is present, surface bound and organic peroxides may also be formed and bands due to these are assigned. SERRS spectra of [PVP-M(bpy)₂Cl]Cl (M = Ru or Os) adsorbed layers show typical 2,2'-bipyridine dominated spectra at Ag. Small changes in band positions due the oxidation of Os(II) to Os(III) were observed at a gold electrode for the 1400 -1700 cm⁻¹ region.

The metallopolymers are used as model systems for the quantification of the SERRS signal in polymer-modified electrodes, plots for intensity vs surface coverage of metal centres being obtained as a function of loading (py:M ratio) at a constant deposition mass and as a function of deposition mass at a constant loading. At very low surface coverages the

attenuation adjusted intensity can be modelled as a Freundlich isotherm with $I = 1.41c^{0.37}$ (c = the concentration, in mol dm^{-3} , of Ru centres in the film). At higher coverages surface plasmon damping and the increasing importance of resonance Raman scattering lead to substantial deviation from this equation. The potential of SERS for obtaining partition coefficients and diffusion coefficients of ions into polymer films is considered.

A series of $\text{Cr}^{\text{III}}(\text{bpy})_2(\text{L})(\text{L}')$ {L = OH, L' = OH₂ monomer and dimer; L = L' = Cl; and L = poly(acrylic acid), no L'} complexes are studied at glassy carbon by cyclic voltammetry and at silver by SERRS. Slow electron transfer in the reduction of Cr(III) to Cr(II) means that reduction waves are only observed for adsorbed species. The reduced species undergo ligand substitution reactions, and at a PVP modified electrode the dichloride can be reductively electrolyzed to form $[(\text{PVP})_2\text{-Cr}(\text{bpy})_2]^{3+}$ ($E^0_{1/2} = -0.32$ V vs SCE). Surface Raman spectra of the reduced complexes are thought to be in resonance with a broad ligand $\pi_7 \rightarrow \pi_{10}^*$ transition of the bipyridine radical anion, resulting in spectra which indicate that the electron is localized on one bipyridine. The aquahydroxo complexes, which have an initial 2+ charge per Cr centre, adsorb strongly at the Ag surface, as evidenced by a broad Cr-O vibration at around 550 cm^{-1} and by the fact that they stabilize the surface against chloride desorption and therefore show intense SERRS spectra at -1.1 V vs Ag / AgCl. The dichloro and poly(acrylic acid) complexes, which have an initial 1+ charge, do not show similar stabilization of SERRS sites.

Chapter 1

Introduction

1.1 Modified Electrodes

1.1.1 Historical Perspective

The term 'chemically modified electrode' (CME) was first used by Murray and co-workers in 1975 to describe their derivatization of tin oxide electrodes with substituted silanes.¹ Similar work using a platinum electrode derivatized with alkenes had been described two years previously by Lane and Hubbard.² The research area expanded rapidly after this with electrodes being modified not only by chemical derivatization, but also by physical adsorption of molecules and polymers at the surface. The terms 'surface modified electrode' and simply 'modified electrode' have also been used extensively to describe these films and can be used interchangeably with the term CME. The field of research covers any electrode that has had foreign molecules deliberately immobilized at its surface.³

In this chapter modified electrodes, and in particular polymer modified electrodes (PMEs), will be considered in more depth. Firstly, the various methods of preparation of modified electrodes will be considered along with the types of surfaces which result. The uses to which these can be put will be discussed next, as much of the work in the field is of an applied nature. Central to many of these applications is electrocatalysis, which is introduced first. Parallel with the reports of modified electrode devices, has developed a need for understanding of the underlying processes responsible. Characterization of electrodes by electrochemical and, increasingly importantly, spectroscopic techniques, has provided a great deal of this understanding, and in turn has suggested possible improvements in device technology. All the commonly used techniques are described in the text, with some emphasis on their application to PMEs, and the type of information each can be used to obtain. Particular emphasis is given to surface Raman spectroscopy and the quartz crystal microbalance (QCM), as these techniques are used in later chapters to characterize a number of modified electrode

systems. A summary of the other chapters in the thesis appears at the end of this chapter.

1.1.2 Types of Modified Electrode

No universal system has been adopted for the classification of modified electrodes. Divisions into thin layers, inorganic layers, and polymer-modified electrodes have been employed in a number of influential reviews³⁻⁵ and are discussed below.

Thin layers

The thin layer approach is the one involved in the early experiments detailed above, and both chemisorbed and physisorbed small molecules produce such thin layers. Thin layers may be considered to be either monolayer or sub-monolayer films of adsorbate and various strategies have been employed in their preparation.

Covalent attachment is used specifically to mean the attachment of electroactive groups to an electrode surface via the functionalization of this surface, silanization being a popular method. Thus the term is not analogous to chemisorption in this context – a molecule could be adsorbed directly onto a surface and form a covalent bond, and yet not strictly be covalently modified.

The simplest adsorption method is droplet evaporation, where a solution of adsorbate is introduced to the surface via a micropipette and the solvent is then allowed to evaporate.⁶ On many occasions it is better to electrosorb a modifier by altering the potential at the working electrode in an electrolytic solution that contains the modifier such that a layer is then deposited on the electrode.⁷

In a relatively recent development, self-assembled monolayers (SAMs) of surfactant molecules may be deposited onto electrodes. These layers organize themselves using a chemical functionality to chemisorb each molecule onto the electrode surface and hydrophobic regions through which neighbouring molecules interact. An important example of such a film is the alkanethiols at gold (111) crystal surfaces.⁸ The related Langmuir-Blodgett technique,⁹ in which layers of specifically designed molecules are deposited one by one onto an electrode,

aligning themselves according to what functional groups they contain, can be used to build up multilayers of molecules on an electrode. This is still regarded as a thin film technique as only a single monolayer of adsorbate is added for each pass of the electrode surface through a film of the adsorbate. Suitably derivatized alkane phosphonate layers can self-assemble on gold and silicon surfaces, and if the modified surface is then exposed to metals (e.g. zirconium), robust multilayers can be built up more simply than if the Langmuir-Blodgett technique were used.¹⁰

Inorganic Layers

There are many materials which, when deposited by, for example, electrosorption, do not form simple monolayer films, but complex films with heterogeneous morphological features such as pores. The types of molecules with which such surfaces can be obtained are usually very insoluble and will therefore form quite stable films.¹¹ Examples of such systems are polynuclear metal cyanides,¹² clays,¹³ zeolites,¹¹ metal oxides and layered double hydroxides.¹⁴

The cyanides are generally electroactive and can be deposited by electrochemical methods. However, clays and zeolites are non-conductive and need to be prepared by other means – these have included deposition within polymeric layers¹⁵ and the preparation of composite electrodes containing the modifier, for example carbon paste electrodes.¹⁶

Porous metal oxides and layered hydroxides have long been used as heterogeneous catalytic systems and have now been used to modify electrodes via a variety of methods. For example, several oxides have been attached to titanium surfaces using acetylacetonate complexes.¹⁴ Transition metal alkoxides may be used as precursors to thin oxide films *via* sol-gel processing routes, which give highly homogeneous films.¹⁷ For instance, WO_3 can be prepared by this method.¹⁸

Polymer-Modified Electrodes (PMEs)

A vast number of polymer systems have been studied as electrode modifiers as reviewed by Hillman¹⁹ and more recently by Labuda in his general review.⁵ The polymers may be electroactive themselves or may be used to bind electroactive molecules that may otherwise not

adsorb onto the electrode surface.

A polymer may be introduced to the electrode in a number of ways. Preformed polymers may be introduced by simple dip coating or droplet evaporation. Spin-coating, in which an electrode is rotated whilst the droplet evaporates may lead to more even and reproducible films. A second approach is to generate the polymer layer *in situ* by electrochemically polymerizing a solution containing the appropriate monomer units: for instance, pyrrole²⁰ or thiophene²¹ units are electropolymerized to create conducting polymers. The polymer, once deposited, may be further altered on the electrode by the introduction of electroactive groups or by cross-linking to increase its stability.

A more detailed introduction to some of the properties of various types of polymer modified electrode is given in section 1.1.4.

1.1.3 Applications of Modified Electrodes

The rapid growth in the area of modified electrodes has been driven by the promise of a substantial number of applications, detailed below. A majority of these arise from the mediated charge transfer to solution species through a modified layer and as a result there is substantial overlap between the various areas.²²

Electrocatalysis

In several studies, the immobilization of molecules at electrode surfaces has resulted in observations of catalytic properties, whether or not the species is active in a homogeneous system. Such electrocatalysis is similar to other forms of catalysis in that the presence of catalyst allows the reaction to proceed along a route with lower activation energy. The effectiveness of the catalyst may be gauged by either the overpotential for the reaction (the difference between the experimentally observed reaction potential and the theoretical value obtained by thermodynamics) or the catalytic current (the rate of reaction at a given potential). Electrocatalysis can be utilized in a number of ways and the purely synthetic applications are probably less important than those where energy conversion or analysis are the primary goal.

A large amount of work has concentrated on the reduction of small gaseous molecules, for example O_2 ²³ and CO_2 .²⁴ Both can be reduced to a number of different products depending on the number of electrons involved in the reaction. Macrocyclic complexes, especially porphyrins and phthalocyanines, have been used in both cases.

Oxygen undergoes either a two electron reduction to H_2O_2 or a four electron reduction to water; however, without mediation this can only be done at expensive electrodes such as Pt. Bimetallic systems have been widely investigated²⁵ and more recent studies have shown promising results for porphyrins coordinated by pendant pentammineruthenium moieties.^{26,27}

Electrocatalytic CO_2 reduction to CO has been reported²⁸ for $[Ni(cyclam)]^{2+}$ and for several related Ni and Co complexes.²⁴ The primary motivation is the conversion of a greenhouse gas into a useful chemical feedstock such as CH_3OH under conditions where a minimum amount of energy (in the form of electricity) is used.²⁹

Other examples of reactions of interest are the oxidation of chloride to chlorine³⁰ and the oxidation of alcohols,³¹ both mediated by surface-bound ruthenium-oxo complexes. The reduction of nitrates³² and N_2 ³³ to NH_3 are of interest in studies aimed at mimicking nitrogen fixation in plants. Many other examples are listed in various reviews.^{19,34,35}

A particularly exciting area of interest in electrocatalysis is that of biological reactions, which are of use for developing biosensor technologies. The immobilization of enzymes onto electrodes for sensors is a difficult area, and thus far a vast majority of work on the subject has concentrated on the rather robust enzyme, glucose oxidase. A sensor device in which an osmium bipyridyl polymer is used to mediate the transfer of electrons to glucose oxidase, which in turn catalyses the reduction of glucose to gluconolactone has reached clinical trials for real-time *in vivo* diabetes monitoring.³⁶ Mediation of the oxidation of the biological co-factor NADH could have wide applicability as further stable enzyme electrodes are developed.³⁷ Other sensors based on electrocatalysis are considered in the following sub-section.

Numerous chiral electrosyntheses have been reported, often utilizing poly(L-valine) modified electrodes.³⁸ The other role of an electrode modifier may be inhibitory: the purpose of the film being to prevent corrosion of the electrode, whilst still allowing beneficial reactions to proceed.³⁹

Analytical Applications

The sensitivity of electrochemical techniques to small amounts of analyte coupled with the selectivity conferred by a modified layer means that modified electrodes are a major area of research in sensor technologies.⁵ The requirements for sensor applications are a predictable and quantifiable response of some measured parameter with change in analyte concentration and the stability and reversibility of the response.

Electrochemical sensors can probe the redox properties of the analyte in one of two ways, by measuring the current passed at a particular electrode potential (amperometric sensor) or by measuring the variation in electrode potential as a function of concentration (potentiometric sensor), as in a pH sensor.

The modifying layer can aid the analytical function in a number of ways, which include binding of the analyte prior to a redox reaction (preconcentration), electrocatalysis of the redox processes of the analyte, and exclusion of interferent species (permselectivity). The use of conducting films such as polypyrrole and polyaniline has also led to electrochemical detection of ions that do not have redox couples at the electrode potential used: small ions such as halides may dope the conducting film and thus modify its electrochemical properties.⁴⁰

In a number of sensor applications, for example, *in vivo* sensing³⁷ and analysis of pollutants in streams,⁴¹ the analyte is flowing. The ability to detect a flowing analyte also enables certain CMEs to be coupled to various other analytical techniques such as liquid chromatography.⁴²

A number of practical applications for CME based sensors have been found, based on the criteria above. Recent examples include variations on the glucose oxidase based biosensor,^{43,44} a urea detector which works by polymer dissolution when the action of urease changes the solution pH, the dissolution being monitored by a.c. impedance,⁴⁵ an O₂ reduction sensor in which cobalt metalloporphyrins are immobilized within a clay electrode by poly(2-vinyl)pyridine,⁴⁶ and a CN⁻ sensor that works by measuring inhibition of a cytochrome oxidase enzyme modified electrode.⁴⁷ Chemical modification of electrodes is not an absolute prerequisite for sensors: for instance glassy carbon ultramicroelectrodes have been used for dopamine detection;^{48,49} however, careful pre-treatment of the electrode surface is required.

Photoelectrochemical Applications

A number of disparate applications arise from the photoelectrochemical and optical properties of modified electrodes, including solar energy conversion and display technologies (i.e. memory storage, electrochromic and electroluminescent devices), all of which will be considered briefly in this section. One common feature to all these applications is the requirement for a transparent electrode to allow free passage of photons to or from the photoactive layer. The most commonly utilized material for this is indium tin oxide coated glass (the ITO electrode).

Commercially viable systems in any of the areas listed above are of potentially huge value. For instance, it is estimated that the display technology market was worth 11.6 billion \$U.S. in 1994,⁵⁰ this being dominated still by the cathode ray tube.

Electroluminescent (EL) and electrochemiluminescent (ECL) devices are closely related. In an EL device, a thin polymeric film separates the anode and cathode, from which are injected electrons and holes respectively. The charges are conveyed through the film to a point where they meet and annihilate, producing light. A number of conducting polymers have shown this behaviour, notably poly(p-phenylenevinylene) (PPV).⁵¹ A large amount of research has been devoted to improving the processability of the polymer and altering the band gap (and therefore the λ_{\max} of luminescence) by the introduction of side chains onto the PPV.⁵²

ECL is a slightly different mechanism in which it is not the direct annihilation of electrons and holes that creates the photon, but the reaction of two components to form an excited state which then relaxes with the emission of light. An example of this is given by $\text{Ru}(\text{bpy})_3^{2+}$ under electrochemical conditions as has been investigated by Bard *et al* (Figure 1.1).⁵³

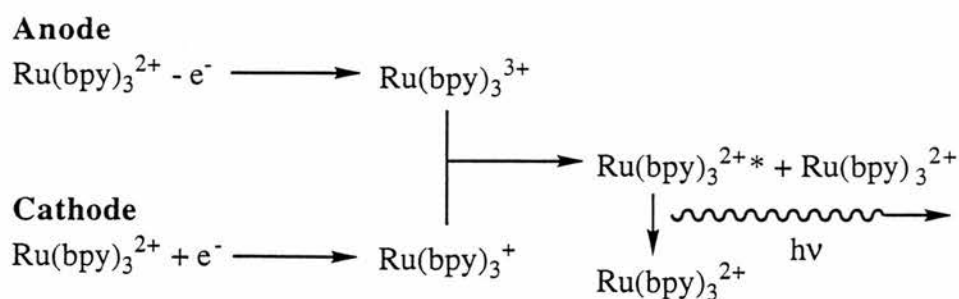


Figure 1.1: Mechanism of electrochemiluminescence for $\text{Ru}(\text{bpy})_3^{2+}$

In electrochromic devices, the electrode material changes colour in response to a change in potential, but does not spontaneously emit photons, and therefore an external light source is required to view the information. Common materials for use in these systems are inorganics oxides, for instance, systems based on V_2O_5 .⁵⁴ Certain conducting polymer materials also show potential dependent colour changes, dependent on the band gap energy, on becoming conducting.⁵⁵ Langmuir-Blodgett films of rare earth phthalocyanines are amongst a range of macrocycles also used.⁵⁶

The problem with both these and the EL and ECL displays is that it is difficult to achieve a range of colours. A potential system for overcoming this in electrochromic displays, using potential-induced electrostatic binding in polymer films, has been investigated in St. Andrews, and the principles are shown in Figure 1.2.⁵⁷

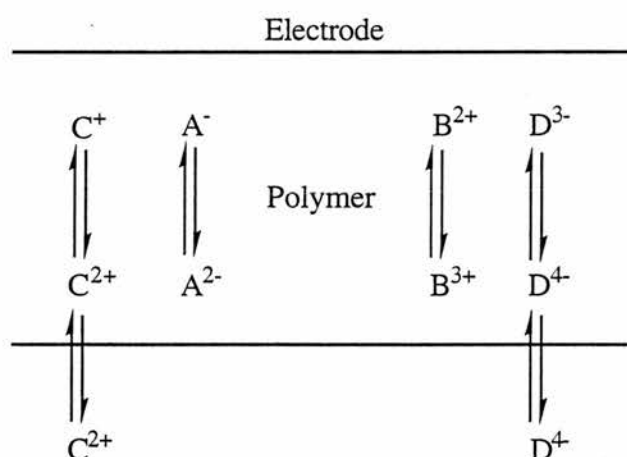


Figure 1.2: Possible schematic of a multicoloured electrochromic device. The actual species involved are $A^{2-} = [PVP-Ru(edta)]^{2-}$, $B^{2+} = [PVP-Ru(NH_3)_5]^{2+}$, $C^{2+} =$ methylviologen dication and $D^{4-} = [Mo(CN)_8]^{4-}$.

The system contains four redox species A - D of which A and B are bound covalently to the polymer, and C and D are able to migrate into and out of the film. If the redox couples of the species are such that D is most positive, followed by B, A and then C, then a reductive sweep will proceed as follows. Firstly D^{3-} will be reduced to D^{4-} in the film with some anion being expelled to maintain electroneutrality. The reduction of B^{3+} to B^{2+} will also require such

maintainance and so the remaining D^{4-} will be excluded. Then the reduction of A^- will occur, and the positive species, C^{2+} will be taken into the polymer layer, which is then itself reduced. In the reverse process the opposite reactions will occur, leading to the potential for up to 5 colour polyelectrochromism in ideal cases.

Information and image storage is one potential use for the electrochromic systems mentioned above. Yoneyama *et al*⁵⁸ demonstrated this application convincingly for polyacrylonitrile containing TiO_2 particles, on which a high resolution photographic image can be obtained. This can be erased by stepping the potential from open-circuit to +0.5 V vs SCE and other images can be subsequently developed. The film is stable for over 100 such "write-erase" cycles.

To a certain extent the processes that are required for a modified electrode solar energy conversion device are the opposite of those given in Figure 1.1. A large amount of research was done in the late 1970s and early 1980s on systems in which $Ru(bpy)_3^{2+}$ was used as a photosensitizer to harvest light.^{59,60} A photon will convert the ruthenium bipyridyl into its excited state, which is then susceptible to oxidation to Ru(III) by methylviologen (MV^{2+}). It was hoped that a combination of the reduced viologen and an appropriate catalyst would lead to an efficient water photolysis system. However, major problems came from the fact that the precursor processes to the water photolysis involve only one electron in this case and that back electron transfer (i.e. reduction of Ru(III) by MV^{+*}) was significant.⁶¹

Despite the problems with coupling water photolysis to the process, systems based on metal bipyridyl sensitizers and viologen excited state quenchers do generate significant photocurrents as reported by Grätzel⁶² and by Kaneko and co-workers.⁶³⁻⁶⁵ One of Kaneko's designs is schematically represented in Figure 1.3.⁶³ Cells utilizing conducting polymers or porphyrins have also been developed.⁶⁶

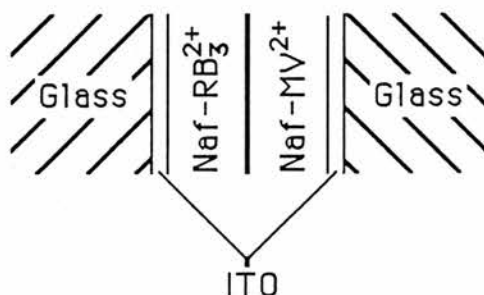
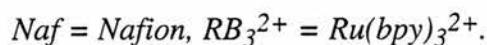


Figure 1.3: Schematic of a film used in one of Kaneko's photoresponsive electrode system.⁶³



1.1.4 Polymer-Modified Electrodes

Depending on the application there are a number of possible advantages to using a polymer film over the other methods described in section 1.1.2. The primary reason for this is that a polymer layer is a thick film, and so a larger number of redox centres can be immobilized when compared to thin film methods. Provided that charge transport and diffusion of solution species are facile, then for any electrocatalytic application this larger catalyst surface concentration means that a smaller catalyst turnover is required before a process becomes feasible. Another effect of the greater surface concentration is better contrast in optical devices. Polymers are also effective for preconcentration of analytes, and are simple to deposit. Some applications can only be achieved at PME's, in particular ion-exchange. The section will take the form of a brief review of some of the common types of polymers used in electrochemical applications. A much more comprehensive listing is given in Hillman's review.¹⁹

The common conducting polymers, polyacetylene (1), polythiophene (2), polypyrrole (3), polyaniline (4) and poly(phenylenevinylene) (5) are shown in Figure 1.4. The polymers all have conjugated backbones and function as large band-gap semiconductors unless they are exposed to oxidizing dopants such as iodine. Considerable quantities of dopants are required before their conductance maximises.⁶⁷ The polymer becomes positively charged and its electronic structure changes, with low lying conduction bands (called polarons or bipolarons

depending on the nature of the polymer species) leading to conduction. Of course, similar switching can be achieved by holding the polymers at an appropriate electrode potential. The main method for adjusting the electronic properties of the polymers in their conducting state has been by substitution onto the aromatic ring.^{52,55}

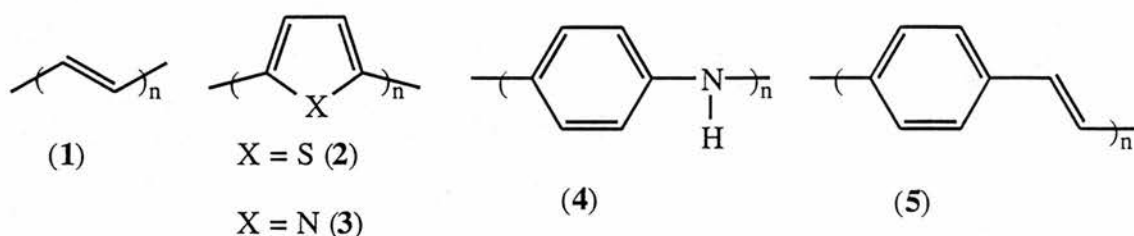


Figure 1.4: Structures of some conducting polymers.

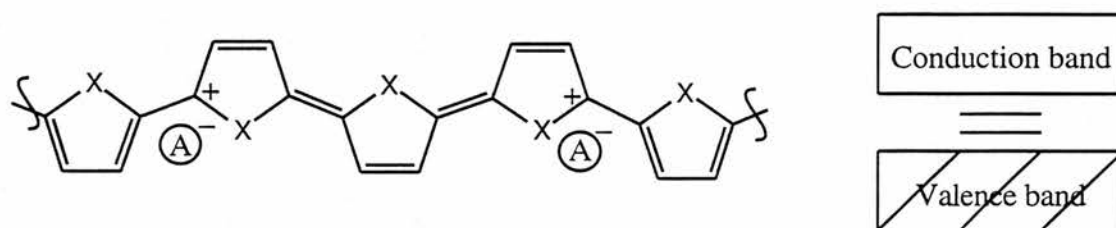


Figure 1.5: Molecular and band structures of polythiophene in a bipolaron conducting state.

Other types of polymers are generally vehicles for immobilization of redox active species. For charged species ion-exchange polymers, such as Nafion[®] (Du Pont's trade name for various polymeric fluorocarbon sulphonates) and poly(styrene sulphonate) (6) for cations, are used. For anions poly(4-vinyl pyridine) (PVP) is used, this being protonated at pHs below 5.5, or quaternised to create an anion exchange polymer which is not dependent upon pH (7).



Figure 1.6: Common ion-exchange polymers

PVP can also coordinatively bind redox species providing they have easily substituted ligands. This can be achieved by co-polymerization of uncoordinated and coordinated 4-vinylpyridine ligands, or by reacting pre-polymerized PVP with the complex either in a normal chemical synthesis or *in situ* on the electrode surface. All three approaches have been used in the preparation of [PVP-Ru(bpy)₂Cl]Cl,^{68,69} a system which has been extensively studied in this work. Figure 1.2 shows a PVP film being used simultaneously in both its coordinative and ion-exchange roles.

Polymers have also been especially designed for coordinative immobilization in electrochemical systems, usually by incorporation of chelating ligands. Two examples based on bipyridine are shown in Figure 1.7: poly(4-vinyl 4'-methyl bipyridine) (**8**)⁷⁰ and a polybutadiene containing pendant bipyridines (**9**).⁷¹ The polyacrylate system detailed in chapter 5 of this thesis is another such example.

Another class of polymers may be defined where the redox species is an integral part of the monomer unit. The commonest example of this is poly(vinylferrocene) (**10**), which has been used in a number of applications.⁷²

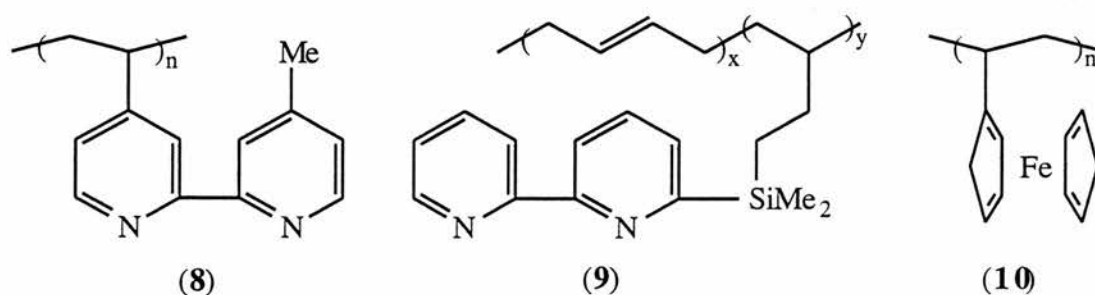


Figure 1.7: Other polymers for modified electrodes. For (**9**) $x = 0.17$, $y = 0.83$.

1.2 Characterization of Modified Electrodes

1.2.1 Introduction

Up until the early 1980s the most important techniques available to researchers in the field of modified electrodes were the electrochemical techniques: cyclic and linear sweep voltammetry,

chronocoulometry, chronoamperometry, rotating disk voltammetry, and so forth. These may be used to assess many of the kinetic and thermodynamic parameters of modified electrode films where electron and ion motion is involved. However, electrochemistry cannot be used directly to obtain structural information, and for this reason a large number of other techniques have been applied *in-situ* (on the electrode, immersed in electrolytic solution and under potential control) to probe modified electrodes. Many of these are adaptations of bulk spectroscopic techniques (e.g. UV-visible and IR-spectroscopies), although the amount of adjustment that needs to be made to allow surface specificity and *in situ* measurement varies from method to method.

1.2.2 Electrochemical Methods

Cyclic Voltammetry

Cyclic voltammetry is usually the method of choice for the initial characterization of a redox polymer (or indeed any other electrochemical system) before, if required, kinetic data are determined by other electrochemical methods, or structural characterization is achieved by spectroscopy. The technique measures the current that flows as the potential is varied linearly with time between two potential limits, with sweep rates generally being set between a few mV s^{-1} to a few hundred mV s^{-1} . From such an experiment the half-wave redox potentials of the electroactive species present can be determined.

The simplest use of cyclic voltammetry is for the identification of redox couples due to surface confined species which differ from those of solution species in two ways. The theoretical peak separation for a reversible couple of a species in solution (reversibility in the electrochemical sense implies not only that the re-oxidized or -reduced species is fully regenerated, but also that the electron transfer step involved is kinetically fast) is $59 \text{ mV electron}^{-1}$, whereas for a surface confined species there should be no separation. Secondly the dependence of peak height on sweep rate is different, scaling linearly with scan rate for a surface confined species, but scaling as $(\text{scan rate})^{1/2}$ for solution species. Theoretical curves for both circumstances are shown in Figure 1.8.

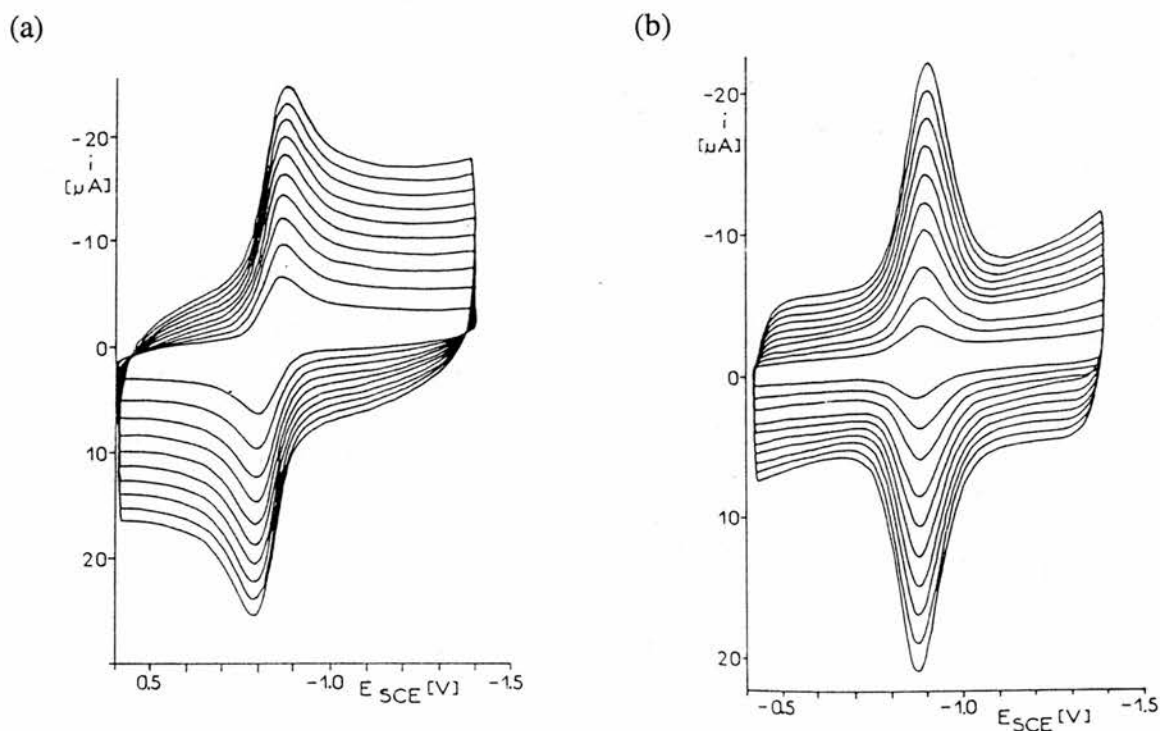


Figure 1.8: Theoretical CVs as a function of scan rate for the fully reversible process, $O + e^- \rightarrow R$, for (a) a species in solution, and (b) a surface confined species. Adapted from ref. 73.

Both the peak separation and peak height phenomena originate from the same fundamental difference between the electrochemistry of surface confined and solution species, which is that in the latter case the rate limiting step is mass transport of the species to the electrode. For the reaction in Figure 1.8 (a), as the reduction proceeds the concentration of oxidized species at the electrode surface is lowered, the peak maximum occurring at a point where both the thermodynamic driving force for the reduction and the concentration of oxidized species at the surface facilitate a rapid reaction.

On the other hand, for an ideal surface confined species diffusion is not a factor at typical scan rates, and if fast electron transfer is achieved then the CV shape is entirely dependent upon the equilibrium concentrations of the two species at any potential, as given by the Nernst equation (Equation 1.1). However, in conditions where thick polymer films are involved the actual CVs obtained may deviate from this ideal case.

$$E = E_{1/2} + \frac{2.3RT}{nF} \log_{10} \frac{[O]}{[R]}$$

(Equation 1.1)

For solution species irreversibility occurs when the rate of electron transfer is not sufficiently fast and so becomes the rate determining step. As a consequence of this the shape of the cyclic voltammogram changes, the peak separation increases and the peak height shows no simple dependence on scan rate, but increases more slowly than the (scan rate)^{1/2} dependence of the reversible case.

Practically, cyclic voltammetry can be used in a variety of ways to describe a redox polymer. In cases where the whole film is able to react it may be used to quantify the amount of redox species in the film, for instance in the ion-exchange of Ru(bpy)₃²⁺ into poly(styrene sulphonate) films⁷⁴ or indeed the loss of electroactive species from films.⁷⁵ If the redox species is incorporated into the film from solution, one can assess the nature of the incorporation by the position of the redox couple. In general, if a redox species is taken into the surface by ion-exchange its redox potential changes very little, but if there is coordination, as is the case with [Fe(CN)₅(H₂O)]^{2-/3-} in PVP for instance,⁷⁶ significant changes are seen (a 110 mV shift in the example given).

A common phenomenon in polymer films is that of 'break-in', where the first sweeps in a CV experiment cause irreversible changes in the electrochemical behaviour of the film. This can occur for a number of reasons, notably the initial incorporation into the films by solvent and electrolyte causing changes in the orientation and swelling of polymer chains.⁷⁷

Potential Step Methods

The techniques included under this heading are chronocoulometry and chronoamperometry, in which the charge and current, respectively, are plotted as a function of time immediately after a potential step across some redox couple. The advantage of this over cyclic voltammetry for collecting kinetic parameters is that appropriate control of the potentials can be used to negate the effect of 'iR' drop.

The main parameters which are measured by such techniques are the diffusion coefficients. There are three factors in the transfer of charge to a redox site in a finitely thick film; hopping of electrons through the film, movement of the redox active species and the maintenance of electroneutrality by movement of ions (redox or electroinactive) into the film. In an electrocatalytic application the movement of substrate in the film also needs to be considered. All these processes contribute to the measured diffusion coefficient from a potential step technique, termed D_{app} (where app = apparent). The relationship between the decay of the current in chronoamperometry and this coefficient is given by the Cottrell equation:

$$i(t) = (\Delta q/L) (D/\pi t)^{0.5} \quad \text{(Equation 1.2)}$$

In the above equation L is the thickness of the modified layer.

A plot of i versus $t^{1/2}$ gives a linear graph whose gradient is related to D_{app} . However, obtaining an absolute value for D_{app} is complicated by the need to estimate the *in situ* film thickness, which may be affected by solvent swelling, and indeed may even be different for the oxidized and reduced films. The diffusion coefficients that have been obtained tend to be around $10^{-10} \text{ cm}^2 \text{ s}^{-1}$ as opposed to $10^{-5} \text{ cm}^2 \text{ s}^{-1}$ for solution species.¹⁹

After determination of D_{app} , the next problem is to interpret this in terms of the nature of the diffusional process, in other words, which of the possibilities mentioned above is the predominant step. Electrons move through the film by hopping between redox sites, and so a theoretical equation may be developed that relates the electron transfer rate to the distance between redox centres. The Dahms-Ruff equation (1.3) is such a treatment.

$$D_{\text{electron}} = 1/6 d^2 k_{et} C \quad \text{(Equation 1.3)}$$

In the above d is the distance between redox sites, k_{et} is the electron transfer rate, and C is the concentration of redox sites in the film.

The effect of redox concentration on D_{app} is therefore an important diagnostic tool in determining the nature of the redox process. If D_{app} is proportional to C then electron hopping is the predominant step. Often, however, this is not the case and then a variety of behaviours are seen. For instance, electrostatically bound redox species may cross-link the polymer at high concentration and thus cause a decrease in D by restricting polymer motion,⁷⁸ as can counterions such as ClO_4^- .⁷⁹ For $Co(bpy)_3^{n+}$ in Nafion a different rate determining process occurs depending on the redox couple: the (II/I) couple is limited by electron hopping, but in the (II/III) couple physical motion of the redox centres occurs.⁸⁰

A pyridine-based polymer to which various mole percentages of Ru and Os bis(bipyridyls) were added was prepared by Facci *et al.*⁸¹ The potential step is chosen such that the Ru centres are electroinactive, they are present only to maintain the structure of the polymer at varying Os concentrations. The overall trend was for D_{app} to increase with Os concentration, but between $2 - 6 \times 10^{-4} \text{ mol cm}^{-3}$ D_{app} was independent of concentration. This behaviour was modelled with some success by Andrieux and Saveant for the case where mobility of counterions was rate limiting.⁸²

Rotating Disc Electrodes

The rotating disc electrode (RDE) and rotating ring disc electrode (RRDE) have been extensively used in solution electrochemistry to determine mechanism. The rotation rate allows a means of controlling the rate of mass transport to the electrode and so the behaviour of the peak current as a function of rotation rate can be used to determine the rate limiting step. In addition the ring in a RRDE can be set at a different potential to detect species generated in chemical steps. Mass transport is not important in PME's, however, the ejection of ions from polymer films have been studied at the RRDE.⁸³

AC Impedance

Over the last few years theories have been devised to enable the application of ac impedance to determining kinetic parameters in modified electrodes.⁸⁴ In this technique the working electrode is subjected to a small sinusoidal perturbation ($< \pm 5 \text{ mV}$) about a potential of interest,

often a half-wave redox potential. Over such a small range the current-potential relationship should be linear, although depending upon the capacitance of the system, the current response lags behind the potentiostatic perturbation. The frequency of the ac perturbation may be varied and the response monitored. The equations governing the ac impedance response have both real and complex components, and it is a complex plane response which is usually plotted. The shape of this impedance diagram may be modelled by an equivalence circuit containing various resistors and capacitors, and from such analysis components such as the uncompensated resistance of the electrolyte, resistance caused by charge transfer in the electrochemical reaction, the capacitance of the electrode double layer, or any other component contributing to the complex plane response may be quantified.

Double Layer Capacitance

The double layer capacitance of the electrode can be measured in a technique which is imaginatively called differential double layer capacitance measurement. A small amplitude ac signal is superimposed upon the potential sweep and the measurement circuitry is designed such that the equivalence cell can be reduced to the double layer capacitance in series with solution resistance and so the desired parameter is easy to determine. High capacitances suggest the adsorption of ions or polar solvents whilst lower values are obtained if organic species are adsorbed, as in the example of pyridine adsorption at silver electrodes in chapter 2. The value for a polymer electrode therefore depends on the adsorption characteristics of the polymer itself, and of incorporated solvent and ions. This value is generally obtained for polymer electrodes by ac impedance, an example of which has been demonstrated by McNiel *et al.*⁴⁵

Uses of Microelectrodes

One final point that is worth mentioning is the use of microelectrodes in this field. A microelectrode or (even smaller) ultramicroelectrode (UME) possesses several advantages over a large electrode including different diffusional characteristics, smaller double layer charging currents and 'iR' drop (since the current, i , is small), and the ability to run electrochemical

experiments in the absence of supporting electrolyte. The smaller charging effects allow cyclic voltammetry at UMEs to be undertaken at much faster scan rates.

In the field of modified electrodes, arrays of UMEs have also proved useful, for example in the profiling of the redox concentration of a quaternized PVP film containing hexacyanoferrate. The interdigitated array of microelectrodes is produced using photoresist technology, and each electrode records a current for its own particular zone of the film.⁸⁵

1.2.3 Spectroscopic Methods

UV-visible Spectroscopic Techniques

Because of its simplicity and the comparability of the results obtained to normal UV-visible spectra of solution chromophores, UV-visible spectroelectrochemistry (often simply referred to as spectroelectrochemistry) has become the most utilized spectroelectrochemical technique. Although reflectance measurements from common electrode materials have been made, it is usual to measure transmission through ITO electrodes.

UV-visible studies may be used to quantify extinction coefficient or the surface coverage of chromophore in the film, providing the other is known. It can also be used to look at redox changes or the generation of transient species. The information obtained may be of particular use in potential photoelectrochemical and electrochromic systems, where the absorbance spectrum is a critical parameter in the development of the application. The technique has also been used widely for monitoring the coloration that appears in conducting polymer films when electron delocalization occurs.⁸⁶

As well as absorption, one can also obtain information from emission in the visible region, whether this be fluorescence or luminescence. One example is the study of excited state $\text{Ru}(\text{bpy})_3^{2+}$ centres produced by comproportionation of Ru(I) and Ru(III).⁸⁷

*Vibrational Spectroscopic Techniques*⁸⁸

The information given by electrochemical and UV-visible techniques may allow identification of molecules within the modified layer if the chemical processes taking place are already well

characterized, but they lack the molecular specificity to facilitate identification of unknowns, and overlap of peaks may make multicomponent systems difficult to analyse. Vibrational spectroscopy, on the other hand, is highly specific and therefore does not suffer from the aforementioned problems.

As with UV-visible spectroelectrochemistry, a standard instrument can be adapted fairly readily to acquire *in situ* spectra, which always rely on reflectance of the beam from the working electrode. The main complications in IR-spectroelectrochemistry are those of sensitivity. This is due to the fact that the layer being probed is rather thin and that all common electrochemical solvents absorb strongly in the infra-red region. This places two main requirements on the technique: (i) a Fourier-Transform instrument used with a reflectance accessory is highly advantageous so that the multiple scans needed to achieve a satisfactory signal to noise ratio can be done over a reasonable timescale, and (ii) the working electrode surface must be as close as possible, typically a few micrometres, to the window through which the incident beam passes. This can be achieved either by external (or specular) reflectance, where the beam passes through a thin layer of solvent to sample the electrode, or by internal reflection (also called attenuated total reflection or ATR), where a thin layer metal electrode is deposited upon an IR transparent crystal and the modified layer is sampled by an IR beam reflecting inside the crystal. In the former diffusion to and from a macroscopic electrode surface can be severely hindered, and flow cells which prevent this problem have been reported.⁸⁹ A requirement for external reflection is that s-polarized light, i.e. light with its electrical vector parallel to the surface, is used, as p-polarized light (electrical vector perpendicular) does not interact with the surface.⁹⁰

The normal method for displaying an *in situ* IR spectra is by taking a background under some reference state (e.g. at a certain potential) and plotting changes in reflectance such that positive peaks denote creation of a species and negative peaks consumption. Although a majority of studies have concentrated on the adsorption of fairly simple species at electrodes, there are a few examples in which polymer electrodes are probed *in situ*, for instance, in the study of electropolymerized polypyrrole films.⁹¹

Surface-enhanced IR, discovered by Hartstein *et al.*,⁹² can be obtained on roughened

silver surfaces in either internal or external reflection modes,⁹³ and is just coming into use for *in situ* studies.^{94,95} It is analogous to surface-enhanced Raman spectroscopy (SERS), which is discussed in detail along with other Raman spectroelectrochemical methods in section 1.3.

Electron Spin Resonance Spectroscopy

As in solution, ESR is used in the electrochemical environment to detect radical species. The main modification needed to run *in situ* experiments is the design of an electrochemical cell to fit into the sample chamber. Predictably, one of the main applications of this technique has been in conducting polymer research, in an attempt to unveil the structure of the doped states. Polarons, which are radical cation species, increase the ESR signal. On going to more extreme potentials in polypyrrole ESR inactive metal-like species are formed.⁹⁶

Surface NMR Spectroscopy

Although surface specific NMR techniques are theoretically possible, no experimental details of a working system have yet been reported. However, there has been a report in which a specially designed electrochemical cell was used to study the magnetic susceptibility of oxidized and reduced forms of $\text{Fe}(\text{CN})_6^{3-/4-}$.⁹⁷ The volume of solution meant that the oxidation state of all Fe centres could be controlled.

1.2.4 Other Surface Techniques

The quartz crystal microbalance falls into this category and is considered in depth in section 1.4.

Ellipsometry

In this technique a visible or near IR / UV source with equal intensities of p- and s-polarized light (represented in vector notation as a circle, Figure 1.9) is reflected off the modified layer at an angle. The two types of polarized light interact differently with the surface layer and so each component of the reflected beam has a different intensity (represented as an ellipse).

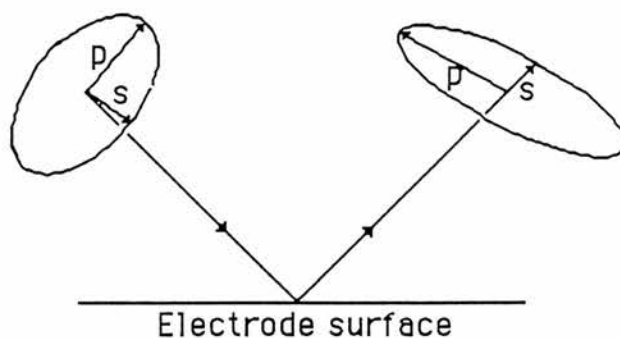


Figure 1.9: Vector representation of the interaction between *s*- and *p*-polarized light and an electrode surface.

Three real plane parameters can be defined, the angle between the plane of reflection and the major axis of the ellipse (α), the ratio of the major to minor axes ($\tan \epsilon$) and the magnitude of the major axis (I). The results are quoted as two further angles, Δ and Ψ , which are related to α and ϵ , but take into account complex components of the reflection equations.

The values of the measured parameters are dependent on film thickness, and so can be used to determine orientation in monolayer films, for example 1,2 bis(4-pyridyl)ethene, or to monitor film growth, for example in the electropolymerization of polythiophene and polypyrrole.⁹⁸

Microscopy Techniques

Imaging of the electrode surface with a spatial resolution of around 50 Å has, until recently, only been available *ex situ* under ultra-high vacuum (UHV) conditions, the most common technique being the scanning electron microscope (SEM). This is still important for imaging modified electrodes;⁹⁹ however, a number of *in situ* microscopy techniques have also come into use. These interrogate some interaction between an ultrafine microscope tip and the surface and can work either by using a feedback loop to adjust the height of the tip to keep the measured parameter constant, or can maintain a constant height and detect changes in the measured parameter.

In scanning tunneling microscopy (STM), the measured parameter is the electron tunneling current between the microscope tip and the surface, in atomic force microscopy it is

van der Waal's forces.¹⁰⁰ Both methods can achieve atomic resolution on clean, smooth surfaces, with AFM being a more general technique whilst STM is restricted to conducting surfaces. Attempts have been made to probe conducting PME's by both methods, with varying degrees of success.^{101,102}

For scanning electrochemical microscopy (SECM) the probe tip is a UME, which scans over the surface monitoring the concentration of redox species as a function of position (and therefore is probably more properly considered as an electrochemical technique). This has been used very successfully to probe polymer films, for instance, to monitor the ejection of $\text{Fe}(\text{CN})_6^{3-/4-}$ from PVP films.¹⁰³

The microscopy techniques, therefore, can provide information on both large and small scale relief features of an electrode surface. This can be useful when an application requires some degree of electrode surface roughness (such as SERS), or in monitoring how even deposition is, for instance, in a polymer-modified electrode. Knowledge of such properties can aid in interpretation of electrochemical data. At the atomic level, accurate profiling of where adsorbates are found is now available *in-situ*, and phenomena such as clustering of adsorbates can be seen.

*Non Linear Optical Methods*¹⁰⁴

Three methods are of interest for electrochemical studies. Second harmonic generation (SHG), a surface specific technique where the electrode is irradiated with a pulsed laser and reflected light at twice the frequency is measured, has been used at single crystal electrodes. In hyper Raman spectroscopy a similar frequency doubling occurs but from that is lost the frequency of surface vibrational transitions. However, this effect is 5 orders of magnitude weaker than normal Raman scattering.

Sum frequency generation (SFG) is a potential alternative to IR techniques in which two lasers, one visible and one a scanning infra-red laser are combined at the electrode, and some visible light is produced at the frequency $\omega_{\text{VIS}} + \omega_{\text{IR}}$, the amount increasing when the IR laser comes into resonance with a vibrational transition.

*Electron, Neutron and X-Ray Spectroscopies*¹⁰⁴

A large number of *ex situ* UHV techniques have been applied to electrochemical systems, amongst them the electron spectroscopies (AES, LEED etc.). Electrons interact strongly with matter, and so there is no prospect of any such technique being used *in situ*. However, with understanding and control of the changes that may take place on emersion and transfer into the UHV environment useful information can be gained, and potential control of the electrode can be achieved. Research has concentrated on phenomena at bare electrodes, because at poorly conducting surfaces, such as CMEs, excessive charging of the surface takes place.

X-ray spectroscopies (XPS or ESCA) have been successfully applied as *ex-situ* methods to probe the atomic composition of organic layers such as CMES. In contrast to electrons, X-rays and neutrons are much more penetrative and so can also be used *in situ*. The disadvantage is that the interaction of the beams with the interfacial region is also weak and so high energy synchrotron sources are required and for the *in situ* case only simple systems such as well ordered single-crystal surface electrodes give interpretable information on the surface atomic structure. Techniques that have been used are surface EXAFS (SEXAFS) and surface x-ray diffraction (SXRD). The use of neutron scattering to depth profile solvent population in conducting polymers has been pioneered by Hillman and co-workers.¹⁰⁵

1.3 Raman Spectroscopic Techniques

1.3.1 Introduction

Raman spectroscopy is a technique for recording the vibrational spectra of molecules and in many cases can be viewed as a complementary technique to infra-red spectroscopy, since often, especially for molecules of high symmetry, different vibrational modes are allowed in Raman and IR: Raman modes are allowed if there is a change in polarizability of the molecule during the vibration, whereas IR allowed modes involve a change in dipole moment. In molecules with a centre of symmetry the mutual exclusion principle holds, i.e. there are no coincident IR and Raman bands due to fundamental vibrations.

The Raman technique was discovered by C. V. Raman in 1928 using a mercury arc lamp.¹⁰⁶ Raman scattering occurs when an electron in the sample molecule is excited, usually by a monochromatic visible source, into a virtual state. The molecule may then relax in a number of ways. In the case where it relaxes back to the same vibrational level ($\Delta v = 0$) then light of the same wavelength as the source is emitted. This is called Rayleigh scattering or elastic scattering and is by far the most common occurrence. However, a small number of scattering events are inelastic (typically around 1 in 10^6), in other words, they involve a change in the vibrational level of the molecule ($\Delta v = \pm 1$). Where $\Delta v = -1$ the emitted photon is of higher energy than the source and is called anti-Stokes scattering and where $\Delta v = +1$ the emitted photon is of lower energy, giving Stokes scattering. Raman scattering is the collective name given to both of these types of events. All these possibilities are shown in Figure 1.10.

The technique required dark-room photographic techniques until the 1960s, when lasers became commercially available as high power, monochromatic light sources. In a traditional instrument, the laser is focussed onto the sample of interest by a series of optical components, and the scattered light is then passed through a series of monochromators to remove stray light, in particular the very strong Rayleigh line, before a photomultiplier detector is used to measure the light that has been admitted. By adjusting the monochromators, which are typically two or three diffraction gratings, a desired wavelength range can be swept and a typical vibrational spectrum can be obtained.

The "normal" Raman technique, as described above, has a number of disadvantages. Firstly, the high power laser source is advantageous for the simple reason that the Raman scattering phenomenon is very weak. Even with the use of a laser several scans of the wavelength region of interest are required in order to obtain a sufficient signal to noise ratio to resolve bands, and such an acquisition can take of the order of several hours. This compares unfavourably with, for instance FT-IR, where a similar spectrum could be acquired after only a few minutes.

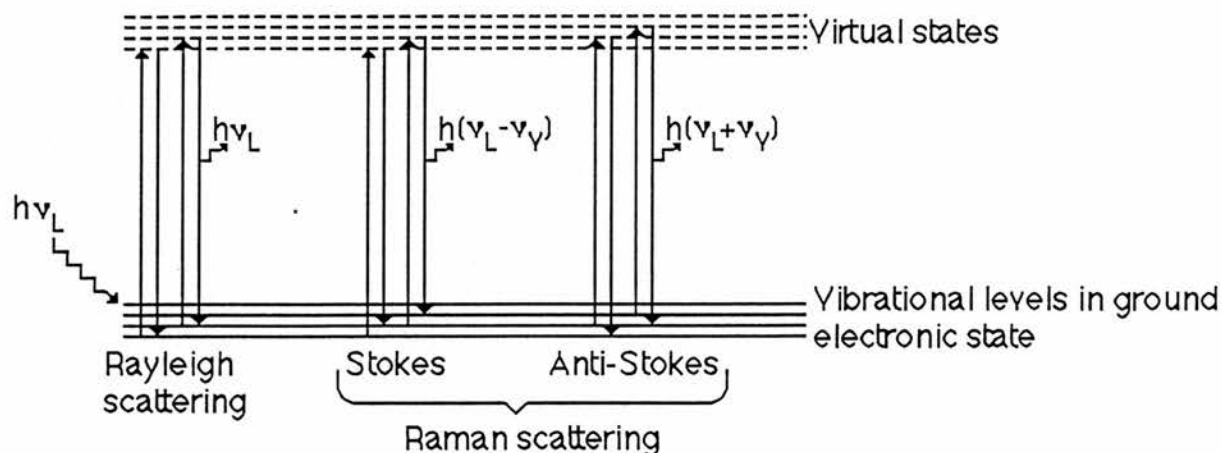


Figure 1.10: Scattering processes from laser irradiation.

A second problem is that of fluorescence, which occurs on visible excitation of a large percentage of samples. This produces a sloping background which may dominate the spectrum and make Raman bands more difficult to resolve. This problem can often be solved by using lasers of a longer wavelength; however, as the Raman scattering intensity drops off to the fourth power of incident wavelength, more scans are then required to obtain an acceptable spectrum.

If the description of Raman spectroscopy ended here, then it is clear that it would be regarded as a rather esoteric technique. Fortunately, advances in instrument design since the mid 1980s have improved the ease of acquisition for “normal” Raman spectra, and these will be considered briefly a little later. In addition to this there are various methods by which the total amount of Raman scattering may be increased, and these will be considered next.

1.3.2 Resonance Raman Spectroscopy

When the wavelength of the laser excitation matches a UV-visible absorption band of the sample, then instead of exciting electrons into a virtual state, the laser excites electrons into a region where there are real energy levels, and the probability of the excitation, followed by a scattering event is greatly increased.

In mathematical terms, resonance can be interpreted as the polarizability of the molecule becoming very large. Polarizability is given by the following equation:

$$[\alpha]_{\rho\sigma} = \frac{1}{hc} \sum_r \frac{[\mu_\rho]_{fr} [\mu_\sigma]_{ri}}{\bar{\nu}_{ri} - \bar{\nu}_0 + i\Gamma_{ri}} + \frac{[\mu_\sigma]_{fr} [\mu_\rho]_{ri}}{\bar{\nu}_{fr} + \bar{\nu}_0 + i\Gamma_{fr}}$$

(Equation 1.4)¹⁰⁷

In Equation 1.4, $[\alpha]_{\rho\sigma}$ is the $\rho\sigma^{\text{th}}$ component of the transition polarizability; $[\mu_\rho]_{fr}$ the ρ^{th} component of a transition dipole moment associated with the transition between energy levels f and r (ri representing a transition into an excited electronic state and fr a scattering event from this state); and ν are the wavenumbers associated with these transitions with ν_0 representing the laser line.

In the resonance case ν_{ri} approaches ν_0 and so the denominator in the first term of the summation becomes very small and dominates the summation. In the case where $\nu_{ri} \approx \nu_0$, the complex damping term, $i\Gamma$, in the denominator becomes significant and prevents the summation tending to infinity. Nevertheless, the transition polarizability, and therefore the Raman intensity, become very large.

The dependence on matching the laser wavelength with an electronic absorbance means that the technique is especially useful with visible lasers for inorganic complexes¹⁰⁸ and dye molecules.

A few experimental factors need consideration in the resonance Raman experiment. The concentration of the sample is important. For a normal Raman experiment, the best signal will be obtained by maximizing the concentration; however, since significant UV-visible absorbance takes place in the resonance case, the same is not true. Thus a balance needs to be struck between the sample being concentrated enough that sufficient Raman photons are produced, but not too concentrated that the incident and Raman scattered photons are self-absorbed by the sample.

The UV-visible absorbance needs also to be considered for other reasons. Because the photon flux from a laser is high, and electronically excited states may deactivate thermally,

sample heating and degradation may be a problem. This can be solved either by turning the laser down or, where this is not possible because an adequate signal cannot be obtained and the sample is a KBr disc, by rotating the sample so that no area is exposed to the sample for any length of time.

1.3.3 Surface Enhanced Raman Spectroscopy (SERS)¹⁰⁹⁻¹¹³

Surface-enhancement is a process that is supported by roughened surfaces of a number of metals, most notably the coinage metals copper, silver, and gold. The systems that support such enhancement include colloids, vacuum evaporated films and appropriately prepared electrode surfaces. Two mechanisms contribute to the overall enhancement, electromagnetic enhancement (EM mechanism) and charge-transfer enhancement (CT mechanism), and these will be considered in turn.

Electromagnetic Enhancement

This enhancement is dependent on surface roughness and has its origin in the electronic properties of the small clusters of metal atoms that make up such roughness features. The electrons within these clusters can be brought into resonance by excitation of the appropriate wavelength, this condition being known as surface plasmon resonance. The resonant particle generates a large internal electrical field which is given by the equation:

$$E_{in} = \left[\frac{1}{1 + [(\epsilon(\omega) / \epsilon_0) - 1] A} \right] E_0$$

(Equation 1.5)

In the above equation, E_{in} is the internal electrical field generated, $\epsilon(\omega)$ and ϵ_0 are dielectric constants for the bulk metal and surrounding medium, A is the depolarization factor of the rough metal particle (dependent on the particle shape if the particle is small (\ll the incident wavelength) and on size if the particle is larger), and E_0 is the electrical field of the laser

electromagnetic radiation.

Again the resonance condition is met as the real part of the denominator tends towards zero, and again it is an imaginary component (in this case of $\epsilon(\omega)$) that limits the size of the internal field. As the value of this is dependent on the metal used it is those metals with low imaginary components that allow large fields to develop. The real part of $\epsilon(\omega)$ is dependent on wavelength and thus Ag particles reach resonance with green and longer wavelength lasers, Cu and Au with red and near-IR lasers.¹¹⁴ The enhanced electrical field then interacts with the electrons of adsorbate molecules, increasing both the total amount of scattering, and the proportion of Raman scattering.

Charge-Transfer Enhancement

The CT enhancement arises from a close interaction between metal and adsorbate energy levels and as such only occurs for adsorbate molecules directly bonded to the metal surface. To describe this interaction it is first necessary to explain something of the band structure of the metal, and that for silver is shown in Figure 1.11. In this Figure energy is plotted on the vertical axis and a quantity known as the k -vector is plotted on the horizontal axis. For the bulk electrode the selection rule is that $\Delta k = 0$, meaning that the interband transition of a d-band electron to above the Fermi level of the nearly-free s,p-electrons is allowed, but intraband transitions within the s,p-band are not.

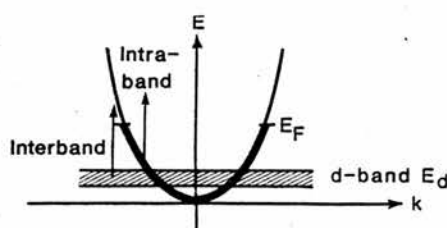


Figure 1.11: Band properties of a bulk silver electrode (from ref. 109).

The same diagram may be used to explain the behaviour of small clusters. As the cluster size becomes smaller and smaller, an uncertainty (Δk) arises in the k -value. For atomic scale roughness, this uncertainty is large enough that intraband transition become allowed, and it is the excited electrons from such processes that interact with the surface adsorbate to allow CT

enhancement. The processes that may occur once the intraband transition becomes allowed can be shown diagrammatically:

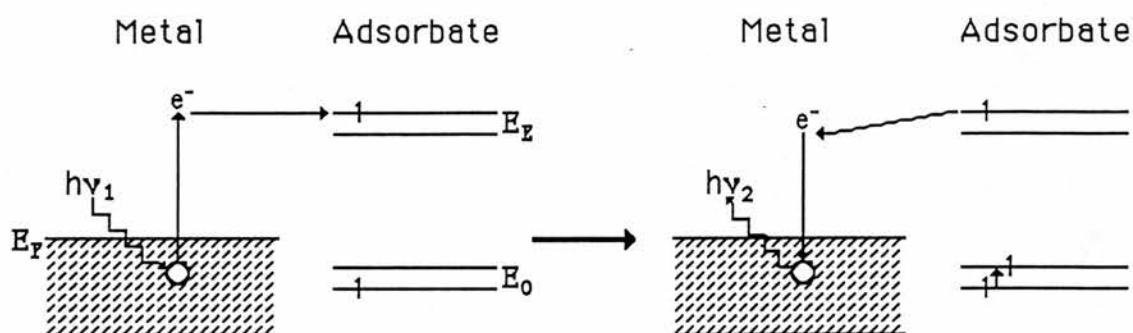


Figure 1.12: One of the processes involved in CT-SERS Enhancement. E_F represents the Fermi level of the metal, and E_0 and E_E ground and excited electronic states, respectively, of the adsorbate.

The first stage of the excitation in Figure 1.12 is photoexcitation of the intraband transition to create an electron-hole pair in the metal. The excited electron may then undergo charge-transfer into the adsorbate excited electronic state either by tunneling (for physisorbed species) or rehybridization (for chemisorbed species). On transfer of the electron back into the metal, the adsorbate is left in a higher vibrational level in E_0 , and the electron-hole recombination therefore is a Raman scattering event. A number of other schemes can be envisioned for such scattering, for instance movement of the adsorbate ground state electron into a lower vibrational state to give anti-Stokes scattering, or charge-transfer between the ground electronic state electrons and the hole.

A resonance condition may be set up between the metal Fermi level and the ground or excited electronic states if either $(E_F - E_0) = h\nu_1$ or $(E_E - E_F) = h\nu_1$, respectively. This energy difference is easily tunable in an electrochemical SERS experiment since the Fermi level is dependent on electrode potential.

Another consequence predicted by the CT model is the presence of scattering due to the silver itself, giving rise to a number of low Raman shift features between 2 - 200 cm^{-1} . For scans starting at 100 cm^{-1} , this is observed as a sloping background with the Raman intensity

decreasing towards higher shift.

Surface Selection Rules

The fundamental Raman selection rule that an allowed transition is one that gives rise to a change in polarizability still retains some relevance to SER spectroscopy: however, bands that are apparently Raman inactive do appear in SE(R)R spectra. For this reason surface selection rules have been developed by several workers.^{111,115} The most basic expression of these rules is given by “vibrations with a contribution normal to the surface are enhanced”. An explanation for such behaviour may be given by the adsorbate inducing an image dipole in the metal. The adsorbate dipoles and their images screen each other for a flat orientation and enhance one another for a perpendicular orientation as shown for pyridine in Figure 1.13.

The real situation, however, is more complicated. Firstly, the polarizability rather than the image dipole is the important parameter to consider, and consideration of this does not give a strict selection rule in favour of the enhancement of perpendicular modes. Secondly, the surface roughness features have quite a small radius of curvature, so that even a molecule adsorbed tangentially to its point of nearest contact with the surface will have a component perpendicular to another nearby point on the surface. Another factor that may lead to the appearance of bands that are Raman forbidden when considering the adsorbate alone is the lower symmetry the molecule will have when it is in the proximity of the surface.

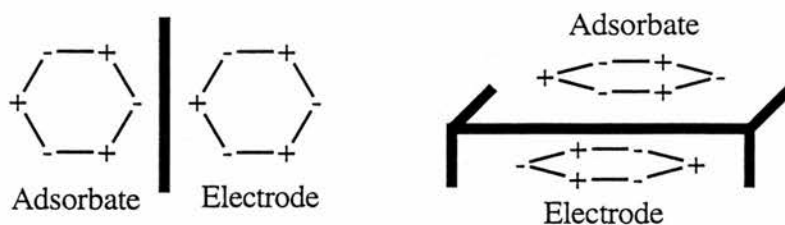


Figure 1.13: Image dipoles for pyridine adsorbed parallel and perpendicular to a metal surface.

Experimental Aspects

The two different SERS enhancement mechanisms detailed above may lead to enhancement of the Raman signal of up to 10^6 times compared to the signal if the surface adsorbed analyte had

its solution spectrum taken. The combination of surface and resonance enhancement in surface enhanced resonance Raman spectroscopy (SERRS), may lead to an enhancement of up to 10^{10} over normal Raman spectroscopy, making this the most sensitive vibrational spectroscopy technique available for surface analysis. Some intensity may be lost through self-absorption, but this effect is easily estimated using UV-visible spectroelectrochemistry,^{116,117} and can in any case be made negligible, since very low concentrations of analyte can be used. Detection limits can be as low as femtomoles, for example the analysis of proteins within intact zebrafish embryo cells has been reported.¹¹⁸

One consequence of this sensitivity is the need for cleanliness to avoid impurity bands appearing from previous samples. Hildebrandt and Stockburger when quantifying the SERRS response of Rhodamine 6G had to use fluorescence spectroscopy to correct for the effects of adsorption of the complex to cuvette walls,¹¹⁹ and Dines and Peacock, when studying SERRS enhanced metal bipyridyls used *aqua regia* washing between sample change.¹²⁰

A great advantage of SE(R)RS over the infra-red methods above is the fact that bulk water is Raman invisible, and that as a consequence the practicable pathlength of the beam through the solvent is long enough such that a standard electrochemical cell may be used. There are some benefits, however, to using a specifically designed cell such as that described in chapter 2, notably the ease of positioning the cell in the spectrometer to maximize the SE(R)RS signal. SERS has been achieved in non-aqueous systems such as methanol and acetonitrile, but solvent absorption does have to be countered by cell design in these cases.¹¹¹

The roughening in a SE(R)RS experiment can be achieved in a number of ways. Colloids and vacuum deposited layers (e.g. silver island films) of enhancing metals have particle sizes that will support enhancement. An electrochemical surface is usually prepared by anodization in an appropriate electrolyte. For a silver electrode alkali metal halides are the usual electrolyte, especially chloride. The electrode is taken to a potential positive of where the silver to silver chloride reaction occurs, and is then re-reduced. Because AgCl is sparingly soluble, Ag atoms are able to migrate and can then be redeposited to form roughness features. The potential may be controlled either by setting up a cyclic voltammetric scan or by potential step methods, the latter giving more control over the current density passed in the oxidative portion,

which in turn controls the surface morphology. This aspect is discussed further in chapter 2.

The need for roughening in electrochemical SERS places limitations on the useful potential window for the technique. For silver, therefore, good quality SERS spectra can only be obtained between 0 V and about -1 V vs Ag / AgCl. The negative limit is placed upon the electrode because atomic scale roughness features which contribute towards the CT enhancement are destroyed below about -0.6 V, causing a gradual decay in SERS intensity. More positive limits of around +0.6 V can be achieved at a gold electrode.¹¹⁴

Deposition techniques may be used to extend the generality of electrochemical SERS. Enhancement of spectra is seen on SERS inactive electrode materials if either an overlayer or underlayer of an enhancing metal is used, which can be achieved, for instance, by underpotential deposition of the thin layer. Examples of electrodes that have been studied in this manner are Au on Ag, a range of metals (Pb, Tl, Cd, Cu, Hg) on both Ag and Au, and Ag on Pt and semiconductor electrodes.¹¹¹ Advantage has been found in using two SERS active materials: thin layers of Cu and Ag deposited on gold, have both the excitation properties of the overlayers combined with the stability to negative potential excursions of gold.¹²¹

1.3.4 Applications of SE(R)RS

Studies that use surface Raman spectroscopies in the electrochemical environment have tended to concentrate on a small number of systems, such as N-heterocycles (especially pyridine, see chapter 2) at silver, interfacial solvent and ion molecules¹¹¹ and alkanethiol SAMs at gold.¹²² Many of the systems that have been widely studied by RRS, such as conjugated macrocycles^{123,124} and metal bipyridyls (see chapters 3-5), have also been studied by SERS.

Examples of the application of SERS to polymer modified electrodes are few, although several reports of polymer characterization on colloids and evaporated films have been made.¹²⁵ Amongst the polymers that have been studied at electrodes are PVP and a complex of PVP with Ru(bpy)Cl₄ (see chapter 3). The use of poly(amino acid) films to immobilize iron porphyrins for SERRS experiments has also been reported.¹²⁶

1.3.5 Instrumental Advances¹²⁷

The single most important advance in Raman technology over the last decade or so has been the widespread use of the optical multichannel analyser (OMA) as a detector system for spectrometers. The OMA consists of more than 1000 photosensitive elements, each monitoring a different wavelength, and so the full wavelength range can be recorded simultaneously rather than needing to be scanned. One of the most sensitive detectors available is the charge coupled device (CCD), which is also used in modern camcorders. The net result is that a Raman spectrum can be taken more quickly, therefore enabling the study of rapid events, and also increasing the S / N ratio of a spectrum taken over a given time when compared to a normal dispersive instrument.

A technique that has developed as a result of the OMA is time-resolved resonance Raman spectroscopy (TRRR or TR³). This is used to look at short lived excited-states of molecules by the use of two lasers, one a pulsed laser which is used to populate the excited state, and another the laser from which the scattering is achieved. TR³ studies have played a central role in the controversy over whether the electron in metal-to-ligand charge transfer (MLCT) excited-states of metal tris(bipyridyls) is localized on a single bipyridyl ligand or delocalized amongst all three. Mainstream opinion favours the localized model,¹²⁸ although the results of matrix isolation studies can be argued to favour the delocalized model.¹²⁹

Another advantage of the short time required to obtain a spectrum with an OMA is that it removes much of the uncertainty regarding possible changes in the structure of the sample during the scan. This is of particular use in a SERS experiment where the electrode may not be stable with time, and the sample may be introduced to the solution after a roughening cycle, in which case an OMA allows the adsorption of the sample at the electrode to be monitored.¹³⁰

The use of the OMA with CCD detection may also open the way for surface unenhanced Raman spectroscopy (abbreviated SURS by Pettinger).¹¹³ Most of the studies done so far have been *ex-situ* under UHV conditions, although *in-situ* spectra have been reported for 4-cyanopyridine at Rh¹³¹ and for Pt in aqueous sulphuric acid.¹³²

Two other advances in Raman technology are worthy of brief mention. The first is the

advent of FT-Raman spectroscopy using a 1064 nm laser.¹³³ The Fourier-Transform is another method by which the whole Raman spectrum can be taken at once: however, FT technology is only possible in the IR (and longer wavelength) regions, and the dependence of Raman scattering on the inverse fourth power of wavelength means that scattering in this region is weak. A second advance that may find use for SERS spectroscopy is the use of fibre optic sampling, which has been demonstrated for Ru(bpy)₃²⁺ and an Ag sol immobilized in a poly(vinyl alcohol) matrix.¹³⁴

1.4 The Quartz Crystal Microbalance

1.4.1 Introduction and Theory

For many years the quartz crystal microbalance (QCM) has been used to determine the mass of films deposited by vacuum evaporations.¹³⁵ It was thought that the technique would not be applicable to electrochemical systems as the contribution from viscous loading would be too great. This was proved wrong in the late 1960s by Jones and Mieure,¹³⁶ but it was over a decade later that the subject was developed into an active field by Nomura and co-workers.¹³⁷

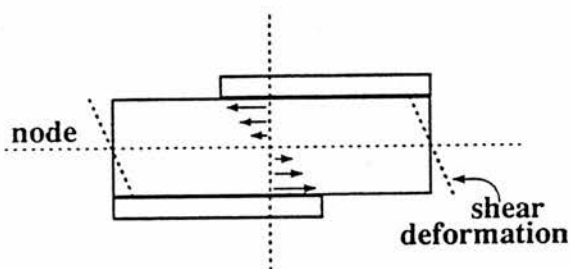


Figure 1.14: Response of a quartz crystal to a resonant alternating current. (from ref. 138)

The principle that the electrochemical QCM (EQCM) is based on is piezoelectric in origin. The application of an electrical field, for example an alternating current, across a piezoelectric material causes a deformation of the material (Figure 1.14). This oscillation can be brought into resonance by altering the frequency of the electric field.

In the electrochemical case, a quartz crystal (very similar to that found in a watch), upon which a thin layer of gold has been vapour deposited, acts as the working electrode. Typically, the fundamental mode of the crystal used comes into resonance at a frequency of around 10 MHz. The exact frequency depends upon the “mass” of the crystal, including any material that is attached to it. A reference crystal, the mass and therefore resonant frequency of which are constant, is used to calibrate the change in frequency of the working crystal: this can be determined with a resolution of 1 Hz (i.e. 1 mass unit in 10 million) and decreases linearly with mass as determined by the Sauerbrey equation:¹³⁹

$$\Delta f = -C_f m$$

(Equation. 1.6)

In the above equation Δf is frequency change, C_f is a measured constant incorporating all the material properties of the particular quartz crystal, and m is the mass per unit area of deposit.

Ideally, the bulk electrolyte does not cause a frequency change, which is therefore caused entirely by adsorbed (e.g. pyridine, Cl^- , or polymer layers) or trapped (e.g. H_2O at roughened Ag, counterions and solvent in polymer layers) species.

However, the frequency change registered at an EQCM may also be due to non-mass dependent changes, for example the viscoelastic properties of the adsorbed materials may also cause frequency changes. In particular, thick polymer films or roughened electrode surfaces may invalidate the Sauerbray equation. Even when these problems are absent, long-timescale experiments need to be thermostatted to prevent changes in the temperature, and therefore the viscosity, of bulk solvent affecting the results.

One way of determining whether non-mass dependent effects are significant is admittance spectroscopy.¹⁴⁰ In this the response of the crystal at near-resonant frequencies is

determined, and broadening of range over which the crystal responds to AC current indicates a viscoelastic effect.

1.4.2 Applications of the QCM to Modified Electrodes

The QCM provides an ideal means to measure the flux of solvent and ions between solution and a polymer layer, and by correlating the changes in frequency with charge passed one can attempt to separate the effects of charged and uncharged species. A parameter that is often used for this purpose is Φ which is the mass change unaccounted for once the contribution of ionic species is subtracted out, and is therefore attributed to solvent. The mass change due to ionic species can be gauged by measuring the charge flux and then multiplying this by m/Fz where m is the atomic mass of the ion present, z is its charge and F is Faraday's constant.

Studies such as these have been used to measure solvent and ion fluxes during the break-in of films such as poly(vinylferrocene)^{141,142} and polythiophene¹⁴³ and the lower swelling that occurs in PVP films when perchlorate is used as an electrolyte.¹⁴⁰ The microbalance has also found a use in biosensor technology, especially in sensors based on antibody-antigen interactions.¹⁴⁴

1.5 Thesis Summary

The techniques described in sections 1.3 and 1.4 assume prime importance during the remainder of this thesis. Chapter 2 concerns the system which has been most studied by SERS, pyridine, with the QCM being utilized in an attempt to unravel the importance of adsorption of each of the various component species that make up the SERS active film in this case.

Chapters 3 and 4 deal with the polymer-modified electrode which has been used as the primary model system in this study, i.e. [PVP-M(bpy)₂Cl]⁺ (M = Ru or Os). Chapter 3 describes and discusses the basic feature of the SE(R)RS spectra of these layers and of their component parts, including a probe of the Os (II / III) couple at a gold working electrode.

Chapter 4 deals with attempts to quantify the Raman signal of the Ru system as a function of various parameters, and compares the results with similar studies for simple monomeric species. The main parameters considered are the effect of polymer loading (pyridine : Ru ratio), polymer coverage (amount of polymer deposited) and the possible contributions of several factors are considered. Possible extensions of this work, for instance, the use of SERS to monitor ion permeation into a polymer-modified electrode layer are considered.

Finally, chapter 5 deals with the electrochemistry and SER spectroscopy of some solution chromium bipyridyl systems. An electrochemical method for incorporation of the chromium bis(bipyridyl) species into PVP films is reported, thus creating a route which parallels the well known PVP chemistry of Ru and Os. The potential of using this as a non-resonant system for comparative studies with the Ru and Os polymers is assessed.

1.6 References

- 1 P. R. Moses, L. Wier and R. W. Murray, *Anal. Chem.*, 1975, **47**, 1882.
- 2 R. F. Lane and A. T. Hubbard, *J. Phys. Chem.*, 1973, **77**, 1401 and 1411.
- 3 K. D. Snell and A. G. Keenan, *Chem. Soc. Rev.*, 1979, **8**, 259.
- 4 L. R. Faulkner, *Electrochim. Acta*, 1989, **34**, 1699.
- 5 J. Labuda, *Ion Selective Electrode Rev.*, 1992, **14**, 33.
- 6 K. H. Lubert, M. Schnurrbusch and A. Thomas, *Anal. Chim. Acta*, 1982, **114**, 123.
- 7 J. Labuda and V. Plaskon, *Anal. Chim. Acta*, 1990, **228**, 259.
- 8 C. D. Bain and G. M. Whitesides, *Angew. Chem., Int. Ed. Engl.*, 1989, **101**, 506.
- 9 H. Tachibana and M. Matsumoto, *Adv. Mater.*, 1993, **5**, 796.
- 10 H. Lee, L. J. Kepley, H.-G. Hong, S. Akhter and T. E. Mallouk, *J. Phys. Chem.*, 1988, **92**, 2597.
- 11 D. R. Rolinson, *Chem. Rev.*, 1990, **90**, 867.
- 12 K. Itayi, H. Okahoshi and S. Toshima, *J. Electrochem. Soc.*, 1982, **129**, 1498.

- 13 A. Fitch, A. Lavy-Felder, S. A. Lee and M. T. Kirsch, *J. Phys. Chem.*, 1988, **92**, 6665.
- 14 F. Beck and W. Gabriel, *J. Electroanal. Chem.*, 1985, **182**, 355.
- 15 B. deVismes, F. Bedioui, J. Devynck and C. D. Bied-Carrington, *J. Electroanal. Chem.*, 1985, **187**, 197.
- 16 B. R. Shaw, K. E. Creasy, C. J. Lanczycki, J. A. Sargeant and M. J. Tirhado, *J. Electrochem. Soc.*, 1988, **135**, 869.
- 17 G. R. Lee and J. A. Crayston, *Adv. Mater.*, 1993, **5**, 434.
- 18 P. Judenstein and J. Livage, *J. Mater. Chem.*, 1991, **1**, 621.
- 19 A. R. Hillman, in *Electrochemical Science and Technology of Polymers*, ed. R. G. Linford, Elsevier, 1987, p. 103.
- 20 D. Curran, J. Grimshaw and S. D. Perrera, *Chem. Soc. Rev.*, 1991, **20**, 391.
- 21 J. Roncali, *Chem. Rev.*, 1992, **92**, 711.
- 22 A. R. Hillman, in *Electrochemical Science and Technology of Polymers*, ed. R. G. Linford, Elsevier, 1987, p. 241.
- 23 A. J. Appleby, *J. Electroanal. Chem.*, 1993, **357**, 117.
- 24 J. P. Collin and J. P. Sauvage, *Coord. Chem Rev.*, 1989, **93**, 245.
- 25 J. P. Collman, C. S. Benscome, R. R. Durand Jr., R. P. Kreh and F. C. Anson, *J. Am. Chem. Soc.*, 1983, **105**, 2699.
- 26 C. Shi and F. C. Anson, *Inorg. Chem.*, 1992, **31**, 5078.
- 27 B. Steiger, C. Shi and F. C. Anson, *Inorg. Chem.*, 1993, **32**, 2107.
- 28 C. I. Smith, J. A. Crayston and R. W. Hay, *J. Chem. Soc., Dalton Trans.*, 1993, 3267.
- 29 P. Christensen, A. Hamnett, A. V. G. Muir and J. A. Timney, *J. Chem. Soc., Dalton Trans.*, 1992, 1455.
- 30 C. D. Ellis, J. A. Gilbert, W. R. Murphy, and T. J. Meyer, *J. Am. Chem. Soc.*, 1983, **105**, 4842.
- 31 K.-Y. Wong, V. W.-W. Yam and W. W.-S. Lee, *Electrochim. Acta*, 1992, **37**, 2645.
- 32 A. P. Doherty and J. G. Vos, *J. Chem. Soc., Faraday Trans.*, 1992, **88**, 2903.

- 33 D. L. DuBois, *Inorg. Chem.*, 1984, **23**, 2047.
- 34 N. L. Pocard, D. C. Alsmeyer, R. L. McCreery, T. X. Neenan and M. R. Callstrom, *J. Mater. Chem.*, 1992, **2**, 771.
- 35 M. D. Ryan, E. F. Bowden and J. Q. Chalmers, *Anal. Chem.*, 1994, **66**, 360R.
- 36 T. J. Ohara, *Platinum Metals Rev.*, 1995, **39**, 54.
- 37 T. Ohsaka, K. Tanaka and K. Tokuda, *J. Chem. Soc., Chem. Commun.*, 1993, 222.
- 38 N. Tanako, *Denki Kagaku*, 1992, **60**, 93.
- 39 A. B. Bocarsly, S. A. Galvin and S. Sinha, *J. Electrochem. Soc.*, 1983, **130**, 1319.
- 40 J. Ye and R. P. Baldwin, *Anal. Chem.*, 1988, **60**, 1979.
- 41 J.-M. Zen and M.-J. Chung, *Anal. Chem.*, 1995, **67**, 3571.
- 42 K. Stulik and V. Pacàková, *Electrochemanalytical Measurements in Flowing Liquids*, Ellis Horwood, Chichester, 1987.
- 43 A. Ricklin and I. Willner, *Anal. Chem.*, 1995, **67**, 4118.
- 44 H.-Z. Blu, S. R. Mikkelsen and A. M. English, *Anal. Chem.*, 1995, **67**, 4071.
- 45 C. J. McNiel, D. Athey, M. Ball, W. O. Ho, S. Krause, R. D. Armstrong, J. D. Wright and K. Rawson, *Anal. Chem.*, 1995, **67**, 3928.
- 46 M. Yuasa, N. Nagaiwa, M. Kato, I. Sekine and S. Hayashi, *J. Electrochem. Soc.*, 1995, **142**, 2612.
- 47 A. Amine, M. Alafarny, J. M. Kaufmann and M. N. Pekli, *Anal. Chem.*, 1995, **67**, 2822.
- 48 D. K. Y. Wong and L. Y. F. Yu, *Anal. Chem.*, 1995, **67**, 3583.
- 49 J. H. T. Luong and R. S. Brown, *Anal. Chim. Acta*, 1995, **310**, 419.
- 50 B. Bowonder, S. L. Sarnot, M. S. Rao and D. P. Rao, *Electronics Information and Planning*, 1994, **21**, 683.
- 51 J. H. Burroughes, D. D. C. Bradley, A. R. Brown, R. N. Marks, K. Mackay, R. H. Friend, P. L. Burns and A. B. Holmes, *Nature*, 1990, **347**, 539.
- 52 G. Gustafsson, Y. Cao, G. M. Treacy, F. Klavetter, N. Colaneri and A. J. Heeger, *Nature*, 1992, **357**, 477.
- 53 I. Rubinstein and A. J. Bard, *J. Am. Chem. Soc.*, 1981, **103**, 5007.

- 54 A. Talledo and C. G. Granqvist, *J. Appl. Phys.*, 1995, **77**, 4655.
- 55 A. Iraqi, J. A. Crayston and J. C. Walton, *J. Mater. Chem.*, 1995, **5**, 1831.
- 56 M. L. Rodriguez-Mendez, R. Aroca and J. A. DeSaja, *Chem. Mater.*, 1992, **4**, 1017.
- 57 C. M. Lindall, J. A. Crayston and D. J. Cole-Hamilton, *J. Mater. Chem.*, 1995, **5**, 955.
- 58 H. Yoneyama, N. Takahashi and S. J. Kubawata, *J. Chem. Soc., Chem. Comm.*, 1992, 716.
- 59 K. Kalyanasundaram, J. Kiwi and M. Grätzel, *Helv. Chim. Acta*, 1978, **61**, 2720.
- 60 P. K. Ghosh and T. G. Spiro, *J. Am. Chem. Soc.*, 1980, **102**, 5543.
- 61 L. A. Worl, G. F. Strouse, J. N. Younathan, S. M. Baxter and T. J. Meyer, *J. Am. Chem. Soc.*, 1990, **112**, 7571.
- 62 M. Grätzel, *Coord. Chem. Rev.*, 1991, **111**, 167.
- 63 G.-J. Yao, T. Onikubo and M. Kaneko, *Electrochim. Acta*, 1993, **38**, 1093.
- 64 Y. Ueno, K. Yamada, T. Yokota, K. Ikeda, N. Takamiya and M. Kaneko, *Electrochim. Acta*, 1993, **38**, 129.
- 65 T. Onikubo, R.-J. Lin and M. Kaneko, *J. Electroanal. Chem.*, 1993, **361**, 143.
- 66 D. Wöhrle and D. Meissner, *Adv. Mater.*, 1991, **3**, 129.
- 67 M. F. Rubner, in *Molecular Electronics*, ed. G. J. Ashwell, Research Studies Press, Taunton, 1992, p. 80.
- 68 J. A. Clear, J. M. Kelly, C. M. O'Connell and J. G. Vos., *J. Chem. Res. (M)*, 1981, 3039.
- 69 C. M. Lindall, J. A. Crayston, D. J. Cole-Hamilton, A. Glidle and R. D. Peacock, in preparation.
- 70 S. L. Bommarito, S. P. Lowery-Bretz and H. D. Abruña, *Inorg. Chem.*, 1992, **31**, 502.
- 71 A. Iraqi, M. Watkinson, J. A. Crayston and D. J. Cole-Hamilton, *J. Chem. Soc., Chem. Comm.*, 1991, 1767.
- 72 F.-R. F. Fan, M. V. Mirkin and A. J. Bard, *J. Phys. Chem.*, 1994, **98**, 1475.
- 73 J. Schreurs and E. Barendrecht, *Recl. Trav. Chim. Pays-Bas*, 1984, **103**, 205.

- 74 M. Matja and L. R. Faulkner, *J. Electroanal. Chem.*, 1984, **169**, 77.
- 75 K. Shigehara, E. Tsuchida and F. C. Anson, *J. Electroanal. Chem.*, 1984, **175**, 291.
- 76 K. Shigehara, N. Oyama and F. C. Anson, *J. Am. Chem. Soc.*, 1981, **103**, 2552.
- 77 N. Oyama and F. C. Anson, *J. Electrochem. Soc.*, 1980, **127**, 640.
- 78 J. Facci and R. W. Murray, *J. Electroanal. Chem.*, 1981, **124**, 339.
- 79 R. J. Mortimer and F. C. Anson, *J. Electroanal. Chem.*, 1982, **138**, 325.
- 80 D. A. Buttry and F. C. Anson, *J. Am. Chem. Soc.*, 1983, **105**, 685.
- 81 J. S. Facci, R. H. Schmehl and R. W. Murray, *J. Am. Chem. Soc.*, 1982, **104**, 4959.
- 82 C. P. Andrieux and J.-M. Savéant, *J. Phys. Chem.*, 1988, **92**, 6761.
- 83 H. Braun, F. Decker, K. Doblhofer and H. Sotobayashi, *Ber. Bunsenges. Phys. Chem.*, 1984, **88**, 345.
- 84 M. F. Mathias and O. Haas, *J. Phys. Chem.*, 1993, **97**, 9217.
- 85 I. Fritsch-Faules and L. R. Faulkner, *Anal. Chem.*, 1992, **64**, 1118.
- 86 G. Tourillon and F. Garnier, *J. Phys. Chem.*, 1983, **87**, 2289.
- 87 D. A. Buttry and F. C. Anson, *J. Am. Chem. Soc.*, 1982, **104**, 4824.
- 88 B. Bedin and C. Lamy, in *Spectroelectrochemistry: Theory and Practice*, ed. R. J. Gale, Plenum, 1988.
- 89 J. O'M. Bockris and B. Yang, *J. Electroanal. Chem.*, 1988, **252**, 209.
- 90 N. J. Harrick, *Reflexions*, Harrick Scientific Corporation, Ossining, NY, Summer 1986.
- 91 J. Y. Yin, T. Ando, N. Teremae and H. Haragichi, *Bunseki Kagaku*, 1991, **40**, 799.
- 92 A. Hartstein, J. R. Kirkley and T. C. Tsang, *Phys. Rev. Lett.*, 1980, **45**, 201.
- 93 Y. Nishikawa, K. Fujiwara, K. Ataka and M. Osawa, *Anal. Chem.*, 1993, **65**, 556.
- 94 K. P. Ishida and P. R. Griffiths, *Anal. Chem.*, 1994, **66**, 522.
- 95 E. Johnson and R. Aroca, *J. Phys. Chem.*, 1995, **99**, 9325.
- 96 H. L. Bandey, P. Cremins, S. E. Garner, A. R. Hillman, J. B. Raynor and A. D. Workman, *J. Electrochem. Soc.*, 1995, **142**, 2111, and references therein.
- 97 M. E. Sandifer, M. Zhao, S. Kim and D. A. Scherson, *Anal. Chem.*, 1993, **65**, 2093.

- 98 A. Hamnett, *J. Chem. Soc., Faraday Trans.*, 1993, **89**, 1593.
- 99 E. F. Sullenberger and A. C. Michael, *Anal. Chem.*, 1993, **89**, 1593.
- 100 P. A. Christensen, *Chem. Soc. Rev.*, 1992, **21**, 197.
- 101 J. C. Brumfield, C. A. Goss, E. A. Irene and R. W. Murray, *Langmuir*, 1992, **8**, 2810.
- 102 H. Yang, F.-R. F. Fan, S.-L. Yau and A. J. Bard, *J. Electrochem. Soc.*, 1992, **139**, 2182.
- 103 J. Kwak and F. C. Anson, *Anal. Chem.*, 1992, **64**, 250.
- 104 A. J. Bard, H. D. Abruña, C. E. Chidsey, L. R. Faulkner, S. W. Feldberg, K. Itaya, M. Majda, O. Melroy, R. W. Murray, M. D. Porter, M. P. Soriaga, H. S. White, *J. Phys. Chem.*, 1993, **97**, 7147.
- 105 R. M. Richardson, M. J. Swann, A. R. Hillman and S. J. Roser, *Faraday Discuss.*, 1992, **94**, 295.
- 106 F. A. Miller and G. B. Kaufman, *J. Chem. Ed.*, 1989, **66**, 795.
- 107 M. Diem, *Introduction to Modern Vibrational Spectroscopy*, John Wiley & Sons, New York, 1993.
- 108 R. J. H. Clarke and T. J. Dines, *Angew. Chem. Int. Ed. Engl.*, 1986, **25**, 131.
- 109 R. K. Chang, *Ber. Bunsenges. Phys. Chem.*, 1987, **91**, 296.
- 110 R. L. Birke and J. R. Lombardi, in *Spectroelectrochemistry: Theory and Practice*, R. J. Gale ed., Plenum, 1988.
- 111 J. E. Pemberton, in *Electrochemical Interfaces: Modern Techniques for in-situ Characterization*, H. D. Abruña ed., VCH, 1991, p. 193.
- 112 A. Otto, I. Mrozek, H. Grabhorn and W. Akemann, *J. Phys.: Condens. Matter*, 1992, **4**, 1143.
- 113 B. Pettinger, in *Adsorption of Molecules at Metal Electrodes*, J. Lipkowski and P. N. Ross eds., VCH, 1992, p. 285.
- 114 B. Chase and B. Parkinson, *J. Phys. Chem.*, 1991, **95**, 7810.
- 115 M. Moskovits, D. P. DiLella and K. J. Maynard, *Langmuir*, 1988, **4**, 67.
- 116 K. A. Macor and T. G. Spiro, *J. Am. Chem. Soc.*, 1983, **105**, 5601.

- 117 W. J. Albery, A. R. Hillman, R. E. Hester and K. Hutchinson, *J. Chem. Soc., Faraday Trans. I*, 1984, **80**, 2053.
- 118 E. A. Todd and M. D. Morris, *Appl. Spectrosc.*, 1994, **49**, 545.
- 119 P. Hildebrandt and M. Stockburger, *J. Phys. Chem.*, 1984, **88**, 5935.
- 120 T. J. Dines and R. D. Peacock, *J. Chem. Soc., Faraday Trans. I*, 1988, **84**, 3445.
- 121 L.-W. H. Leung, D. Gosztola, and M. J. Weaver, *Langmuir*, 1987, **3**, 45.
- 122 J. E. Pemberton, M. A. Bryant, R. L. Sobcinski and S. L. Joa, *J. Phys. Chem.*, 1992, **96**, 3776.
- 123 B. Vlckova, P. Matejda, J. Simonova, K. Cermakova, P. Pancoska and V. Baumruk, *J. Phys. Chem.*, 1993, **97**, 9719.
- 124 S. E. Roark and K. L. Rowden, *Anal. Chem.*, 1994, **66**, 261.
- 125 G. Xue, *Prog. Polym. Sci.*, 1994, **19**, 317.
- 126 S. E. J. Bell, M. Devenney, J. Grimshaw, J. Trocha-Grimshaw and J. J. McGarvey, *J. Chem. Soc., Chem. Commun.*, 1992, 221.
- 127 J. Andrews, *Spectroscopy Europe*, 1995, **7**, 8.
- 128 D. P. Strommen, P. K. Mallick, G. D. Danzer, R. S. Lumpkin and J. R. Kincaid, *J. Phys. Chem.*, 1990, **94**, 1357.
- 129 P. Huber and H. Yersin, *J. Phys. Chem.*, 1993, **97**, 12705.
- 130 Q. Feng, W. Yue and T. M. Cotton, *J. Phys. Chem.*, 1990, **94**, 2082.
- 131 C. Shannon and A. Champion, *J. Phys. Chem.*, 1988, **92**, 1385.
- 132 T. Maeda, Y. Sasaki, C. Horie and M. Osawa, *J. Electron Spectrosc. Rel. Phenom.*, 1993, **64-5**, 381.
- 133 J. C. Rubim, M. L. A. Temperini, P. Corio, O. Sala, A. H. Jubert, M.E. Chanconvillalaba and P. J. Aymonino, *J. Phys. Chem.*, 1995, **99**, 345.
- 134 S. B. Ellahi and R. E. Hester, *Anal. Chem.*, 1995, **34**, 108.
- 135 C. Lu and A. Czanderna eds., *Applications of the Piezoelectric Quartz Crystal Microbalance. Methods and Phenomena*, Elsevier, New York, 1984.
- 136 J. L. Jones and J. P. Miure, *Anal. Chem.*, 1969, **41**, 484.
- 137 T. Nomura and M. Sakai, *Anal. Chim. Acta*, 1986, **182**, 161 and references therein.

- 138 D. A. Buttry, in *Electrochemical Interfaces: Modern Techniques for In-Situ Interface Characterization*, H. D. Abruña ed., VCH, 1991, p. 529.
- 139 G. Z. Sauerbrey, *Z. Phys.*, 1955, **159**, 206.
- 140 A. P. Clarke, J. G. Vos, A. Glidle and A. R. Hillman, *J. Chem. Soc., Faraday Trans.*, 1993, **89**, 1695.
- 141 M. D. Ward, *J. Electrochem. Soc.*, 1988, **135**, 2747.
- 142 A. R. Hillman, N. A. Hughes and S. Bruckenstein, *J. Electrochem. Soc.*, 1992, **139**, 74.
- 143 A. Rudge, I. Raistrick, S. Gottesfeld and J. P. Ferraris, *Electrochim. Acta*, 1994, **39**, 273.
- 144 D. Leech, *Chem. Soc. Rev.*, 1994, **23**, 205.

Chapter 2

Studies on Aqueous Pyridine Solutions

2.1 Introduction

2.1.1 Preamble

The first report of what is now referred to as surface-enhanced Raman spectroscopy (SERS) was made in 1974 by Fleischmann *et al.*,¹ who were studying the adsorption of pyridine onto silver from an aqueous potassium chloride electrolyte, and attributed the high intensity to an increase in surface area due to roughening. It was 1977 before two groups noted that the spectra were far too intense to be explained in this manner and were due to a previously unknown mechanism.^{2,3} The excellent SERS signal given by pyridine containing systems has led to wide investigation of such systems, and these studies have been of great use in understanding the mechanisms through which the surface-effect operates. Explanations for the behaviour of the surface vibrational spectrum of pyridine have often been in terms of the surface-enhancement mechanisms,^{4,5} and although the orientation of pyridine at the surface has been the subject of much discussion,^{1,6-10} there are relatively few detailed studies on the extent of adsorption of pyridine at the SERS active silver surface.^{11,12} In this chapter the relevant literature will be reviewed, after which new results using the quartz crystal microbalance (QCM) will be reported and compared with those obtained by SERS. Full assignments for the SERS spectrum of pyridine-*d*₅ are also reported for the first time.

2.1.2 The Pyridine SERS Spectrum

A comparison of the bands and assignments found in this study and in the literature¹³ for the full-range (100 - 1700 cm⁻¹) SERS spectrum of pyridine is given in Table 2.2 in the results section. Attempts to obtain mechanistic and orientational information have concentrated on a few small areas of this spectrum, particularly the low frequency region (100 - 300 cm⁻¹),

where metal-atom bond stretches are seen, and in the region of pyridine ring breathing modes ($900 - 1100 \text{ cm}^{-1}$). Some of the possible orientations of pyridine on silver are shown in Figure 2.1.

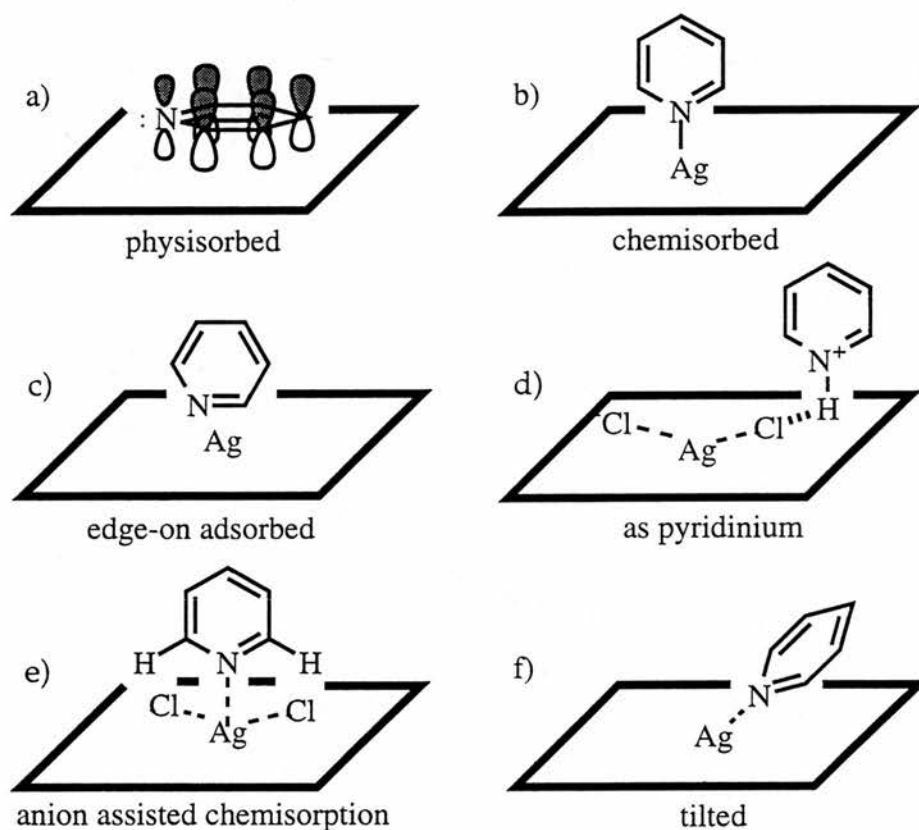


Figure 2.1: Some possible orientations of pyridine at a silver electrode.

In the low frequency region evidence has been sought for Ag-N and Ag-Cl stretches, which would arise from pyridine chemisorption onto the surface and chloride adsorption during the roughening cycle, respectively. Pettinger and Wetzel,¹⁴ in assessing the importance of adatoms to surface enhancement, took Raman spectra at -0.9 V , where they assigned Ag-N modes at 170 cm^{-1} and 252 cm^{-1} using prior adsorption isotherms to show that Cl^- is desorbed at this potential. An Ag-Cl mode at 243 cm^{-1} is assigned at higher potentials. In another study they suggest that much of the inelastic continuum, a broad region of inelastic scattering at low frequency, is due to numerous silver, chloride, and pyridine modes other than the symmetrical

stretches. Regis *et al.*,¹⁵ in a SERS study of pyridine adsorption at ultra-high vacuum (UHV) suggest X_2^- and $Ag^0-X_2^-$ as candidates.

Dornhaus and Chang⁶ look in particular at the nature of the 210-243 cm^{-1} band (peak values at -1 V and -0.05 V respectively) and show a similar intensity dependence throughout the voltage range as for the 1008 cm^{-1} ring breathing mode. They conclude that the band is not simply an Ag-N or an Ag-Cl stretch, but some combination of Ag, Cl^- and pyridine, all co-adsorbed.

It seems, therefore, that the evidence from this region alone is not as conclusive as might have been hoped, and it is in fact the behaviour of the ring breathing modes (900 - 1100 cm^{-1}) under a variety of conditions that has yielded the most information on the orientation of pyridine at the surface. The 1008 and 1035 cm^{-1} bands, which have maximum intensity at -0.6 V have been widely attributed to pyridine physisorption as the potential of zero charge (pzc) is approached (see Table 2.1).^{1,7,8,15,16} This demonstrates the limitations of the SERS surface selection rule that only modes with a component normal to the surface are enhanced (see chapter 1).¹⁷

The main controversy has been over the assignment of the 1025 cm^{-1} band. At low pH this is assigned to the ν_{12} trigonal ring breathing mode of pyridinium, the ν_1 totally symmetric mode contributing to the intensity of the 1008 cm^{-1} band (for a depiction of normal modes see Figure 2.3).⁴ Towards neutral and weakly basic pHs the 1025 cm^{-1} band only appears immediately after an ORC and is irreversibly lost after a cathodic potential excursion beyond only -0.2 V.¹ Here, it has been assigned to either chemisorbed pyridine^{1,9,11} or, once again, pyridinium.^{15,16} (however, pyridine's $pK_a = 5.2$). It has been suggested that $Ag^0-Cl_2^-$ may react with adsorbed water and so facilitate pyridinium formation,¹⁵ though no reaction scheme for this is given.

Crystal face	PZC / V vsSCE	Crystal face	PZC / V vs SCE
(111)	-0.70	(110)	-0.98
(100)	-0.85	polycrystalline	-0.94 to -0.98

Table 2.1: Potentials of zero charge for various crystal faces of silver in mixed perchlorate / chloride electrolyte.⁸

2.1.3 Adsorption Studies

Although numerous studies have been made on the adsorption of halides and pyridines on silver, only a very few have been attempts to understand the nature of the SERS active surface. The most concerted attempt was by Fleischmann and co-workers, who used differential double layer capacitance measurements to characterise the adsorption of chloride and pyridine separately and together as a function of potential on several single-crystal face electrodes of silver and on smooth and rough polycrystalline electrodes.¹¹ Similar measurements were carried out simultaneously with SERS to correlate the two sets of results.¹² An electrode of 125 μm diameter was used so that the incident laser light could be focussed over the whole silver surface, enabling the effect of illumination on adsorption to be assessed. It was found that many of the changes in the pyridine SERS spectrum could be correlated with the capacitance peaks, which are associated with adsorption / desorption processes, except that the capacitance data were reversible on potential excursions as far negative as -1.5 V, whereas SERS intensity is lost below -0.8 V. The loss of a capacitance peak at -0.15 V, however, was found to correlate with the loss of the 1025 cm^{-1} band.

Another Fleischmann paper¹⁸ deals with SERS evidence for adsorption of solvated metal ions onto the chloride layer, looking in particular at $\nu(\text{O-H})$ bands in the 3000- 3800 cm^{-1} region. This concludes that the solvation spheres of the alkali metals are interrupted to different degrees by this adsorption: adsorbed Li^+ maintains secondary and tertiary solvation spheres throughout the potential range, but for K^+ the secondary solvation sphere is held progressively

less strongly the more positive the potential is of pzc.

A substantial series of electrochemical adsorption studies has been made for pyridine on gold and silver single-crystal surfaces.^{19,20} On polycrystalline gold electrodes the results of the adsorption studies, using both chronocoulometric and radiochemical techniques, have been correlated with SERS,^{21,22} but are discussed mainly in terms of the limited usefulness of SERS as an analytical tool.

The studies on silver single-crystal faces are less well advanced, and have been limited to potentials negative of the pzc due to problems of accuracy and precision.²³ The limiting surface concentration for vertically adsorbed pyridine molecules is $6.5 \times 10^{-10} \text{ mol cm}^{-2}$. This value is attained between about -0.8 V and -1.1 V (the exact values are dependent on solution concentration) for the (210) and (311) faces of silver, but the value for the (110) face is $4.5 \times 10^{-10} \text{ mol cm}^{-2}$,²⁴ corresponding to a tilted orientation. From the results that can be obtained positive of pzc it seems that the surface coverage of pyridine decreases for all faces, indicating flatter conformations. The region where accurate chronocoulometric results can be obtained is a different potential range from that of interest in SERS, due to interference from anion adsorption positive of pzc, and therefore attempts to correlate the two sets of data have not been reported and appear unlikely.

Korwer *et al*²⁵ used the resistance change of thin film silver electrodes to probe the ORC cycle. Large increases in film resistance accompanied the formation of the AgCl layer and these were not fully recovered on re-reduction due to the surface roughness. The relaxation of these roughness features, caused by re-incorporation of Ag into the lattice, could be monitored over several hours and increased substantially in rate when the electrode potential was pulsed to -1.5 V. The group also witnessed the inhibition by pyridine of surface corrosion caused by Cl⁻.

Only one previous study used the quartz-crystal microbalance to look at the Ag → AgCl reaction commonly used to create a roughened, SERS active surface.²⁶ Frequency changes are reported for a number of different galvanostatic ORCs, and the values compared with the expected mass response if the chloride reaction takes place in isolation from other processes (Φ). Confirmation of the relationship between frequency and mass is sought via a.c. impedance measurements and also by bringing overtones of the quartz oscillator into

resonance, both methods for separating the contributions from rigidly and viscously coupled mass. They also suggest from theoretical calculations that the elastic properties of the surface will not affect the resonant frequency because the surface is an antinode of the resonance. The conclusions drawn from the study, summarized by the schematic in Figure 2.11, however, remain qualitative in nature.

2.2 Experimental

2.2.1 Materials

Reagent grade pyridine was distilled according to the method recommended by Loewenthal,²⁷ first being dried over KOH, decanted and then distilled onto 5 Å molecular sieves, discarding the heads. Pyridine-*d*₅ (99.4%, Fluorochem) was used as received.

Potassium chloride, sodium chloride, and lithium chloride were all Analar grade and were dried at 200°C and stored in a dessicator.

Solutions were made up with distilled water.

2.2.2 Raman Spectroscopy

Spectrometer

Raman spectra used various lines of a Coherent Radiation Innova 90-6 argon-ion laser as the source. Spectra were recorded on a Spex 1403 spectrometer fitted with a photomultiplier detector. Typical operating conditions were: laser power, *ca.* 100 mW at sample; scan speed = 1 cm⁻¹ s⁻¹; integration time = 1 s, and spectral slit width = 2 cm.

Potentiostat

Potential control during Raman experiments was achieved using either a home-built potentiostat attached to a JJ Instruments PL3 X-Y recorder or a EcoChimie µAutolab with PC control.

Electrochemical Cell

Surface-enhanced Raman spectra initially used a standard 3-necked glass electrochemical cell containing a silver working electrode, a saturated calomel reference electrode (SCE) and a platinum wire counter electrode. A vast majority of experiments used a purpose-built teflon SE(R)RS cell with optically-clear flat glass windows (Figure 2.2). The SCE was replaced by a luggin capillary Ag / AgCl reference electrode prepared by a literature method.²⁸ The working electrode had area = 0.125 cm², and was inclined at 30° to the incident laser beam. Scattered radiation was collected at 90°. The cell was designed so that it could be positioned reproducibly in the spectrometer with any adjustment required for focussing being achieved by X- and Y-micrometer screws.

Sample Preparation

Typical conditions for ORCs of the Ag electrode were: scan range = -0.6 to +0.3 V vs standard Ag / AgCl, scan rate = 100 mV s⁻¹, and no. of cycles = 10. These values were adjusted to take into account small potential drifts that the home-made reference electrodes were susceptible to. Under these conditions *ca.* 4 mC (*ie.* 32 mC cm⁻²) of charge would be passed on each cycle. Roughening was done either in the absence (*ex-situ* roughening) or presence (*in-situ* roughening) of pyridine and good spectra were obtainable by either method. The electrolytic solution used in roughening was in all cases 0.1 mol dm⁻³ KCl(aq).

Ordinary Raman spectra were taken either on the solid samples or on solutions.

Data Analysis

Spectral data were converted to a form readable by the Perkin-Elmer IRDM software package via a home-written BASIC program. Thus the data manipulation capabilities of the IRDM can be utilised when viewing Raman spectra. The conversion programme scales the Raman intensities from 0 to 1 and any scaling of the spectra needs to be done manually.

Vibrational bands have been assigned in the results and discussion section according to the Wilson numbering system for benzene (Figure 2.3).²⁹

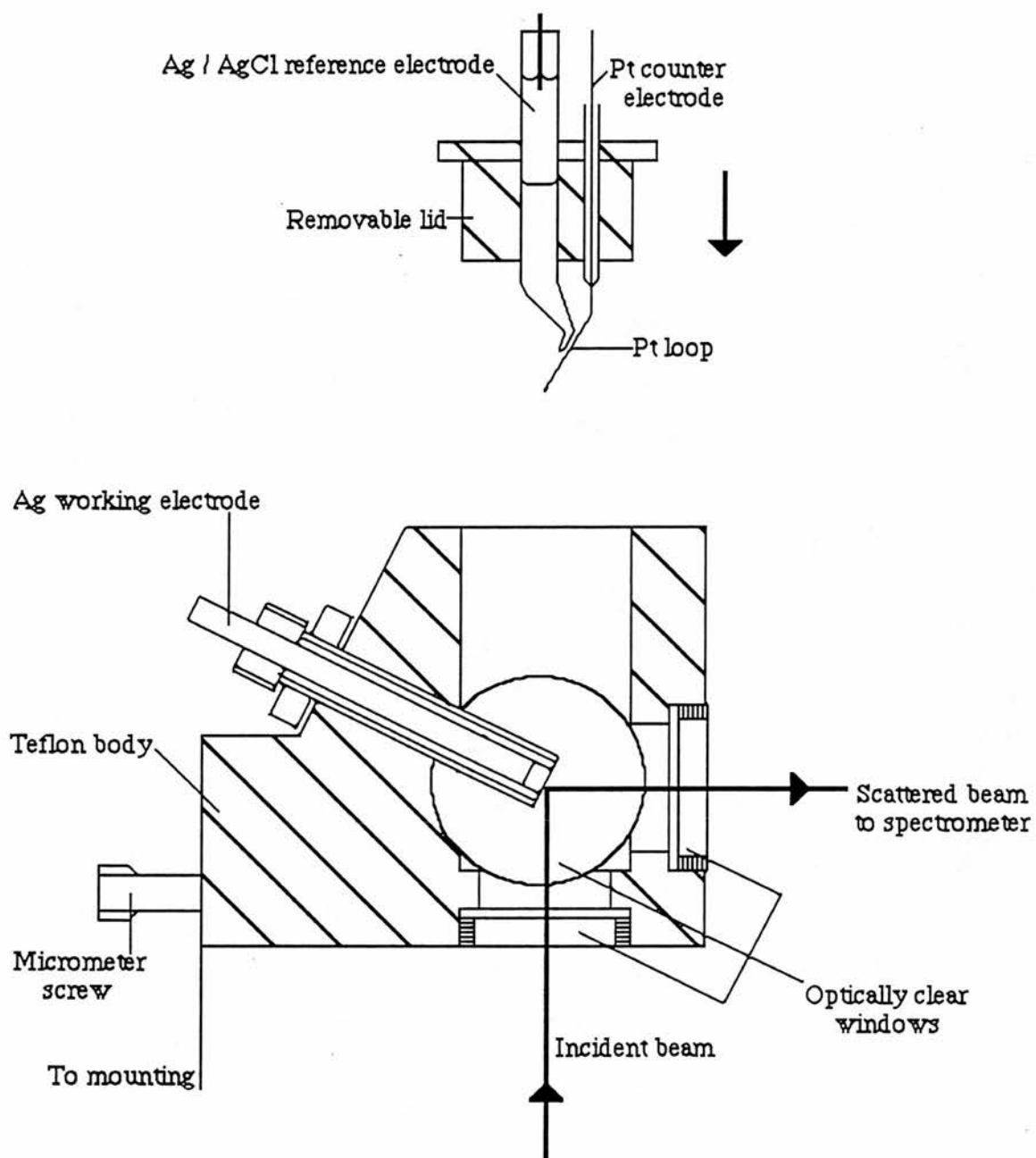


Figure 2.2: Diagram of the home-made cell used in SE(R)RS Experiments

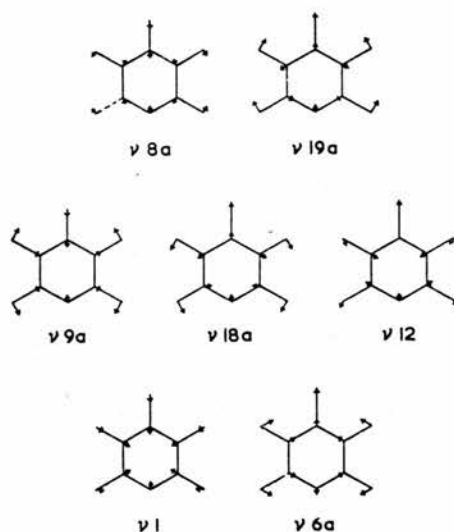


Figure 2.3: Totally symmetric ring vibrations of pyridine, numbered according to Wilson's system

2.2.3 Quartz-crystal microbalance

Quartz Crystals

The quartz crystals employed were 10 MHz AT-cut laboratory monitor crystals (ICM Lab Monitor Crystals, Oklahoma City), with vacuum-deposited overlayers of gold. The electrodes had a geometric area of *ca.* 0.22 cm² at this stage.

The mass sensitivity of the quartz crystals used, before silver deposition, has been previously determined as 0.232 Hz cm² ng⁻¹.^{30,31} This means that for an electrode area of 0.22cm² and under conditions where the Sauerbrey equation holds 1 Hz corresponds very closely to a mass change of 1 ng.

Silver Deposition

The gold electrode was cleaned by cycling in 1 mol dm⁻³ HClO₄(aq) between 0 V and +1.4 V vs SCE at 10 mV s⁻¹ until a satisfactory response was obtained.³² This was typically between 10 and 15 cycles.

Silver was deposited onto the working electrode face of the crystal from 1 mmol dm⁻³

aqueous AgNO_3 solution. The potential was scanned from +0.5 V to 0 V vs SCE at 5 mV s^{-1} at which potential it was held until the crystal frequency had changed by approximately 10 kHz, equivalent to a deposition of *ca.* 10 μg of silver.

Electrochemical Cell

The electrochemical cell consisted of the quartz crystal attached by two gold contacts, one of which acted as the working electrode, a platinum wire counter electrode and an SCE reference electrode. The cell was earthed.

The cell differed from previously reported designs,³¹ in that the quartz crystal was mounted vertically rather than horizontally and was held in place with epoxy resin. This modification significantly reduces noise caused by bulk movements of the electrolyte.

Instrumentation

The oscillator circuit used was, with minor modifications, that of Bruckenstein and Shay.³⁰ An Oxford Electrodes potentiostat was used to achieve electrochemical control. The oscillator circuit and its power supply were housed in a Faraday cage earthed to the potentiostat. All measurements were made at ambient temperature ($20 \pm 2 \text{ }^\circ\text{C}$). The timescales of each experiment were such that constant temperature could be assumed and thus temperature effects on frequency are considered negligible.

Frequency, potential, current and charge measurements were recorded via a Keighley Data Acquisition System 570 interfaced to an IBM ATX computer. The data were analysed either by a program written in the University of Glasgow, or were converted into ASCII format for import into a Lotus 1-2-3 worksheet.

Sample Preparation

All electrolytes were made up from the components as described in section 2.2.1. Adjustment of the pH was done using dilute aqueous solutions of KOH for all solutions, immediately before the electrolyte was used, and the quoted pH values are those measured at this point. The amount of KOH used to adjust the pH of NaCl or LiCl solutions is such that the concentration

of K^+ would be several orders of magnitude below that of the cation of interest. The solutions were then thoroughly degassed with N_2 before introduction to the electrochemical cell, and the cell was filled and emptied several times for each solution to ensure that no contamination from the previous experiment affected the results. The frequency after each rinse of solution could be monitored to ensure this, the solution being used once a consistent frequency value was obtained on consecutive rinses.

Electrochemical QCM Scans

Roughening scans on the silver coated quartz crystal electrodes were done, except where stated, under the following conditions. Potentials were swept from 0 V vs SCE to the appropriate anodic limit and then to -0.8 V, the cycle being completed by sweeping once more to about 0 V. The scan rate was 50 mV s^{-1} . The number of scans necessarily varied between each crystal because the ORCs themselves were subject to study, however, the final roughening cycles before studies on the adsorption at negative potentials vs SCE always had an anodic limit of +0.25 V.

Studies on the adsorption at negative potentials were done on sweeps between 0 V and -0.8 V vs SCE at a scan rate of 5 mV s^{-1} . This scan rate was used to try and ensure that equilibrium was maintained between the surface and the solution.

The study which compares the *in-situ* ORC cycle with SERS signal was done in a slightly different manner to those above. The scan was done in $0.1 \text{ mol dm}^{-3} \text{ KCl (aq)}$ containing 0.05 mol dm^{-3} pyridine, with a single ORC cycle between -0.6 V and +0.2 V vs SCE at 10 mV s^{-1} . The solution was held at the following potentials for the time necessary to take a SERS spectrum (3 minutes, except as noted for 0 V): -0.6 V before and immediately after the ORC, 0 V (held for 1 hour with spectra acquired at the beginning and end of this period), -0.1 V and then in increments of -0.1 V as far as -0.6 V. Simultaneous measurement of the SERS spectrum gave very poor signals because of difficulties in fulfilling the twin demands of optical alignment and preventing noise of the QCM traces from imperfect wiring connections. Thus, the SERS data used are those from the usual SERS cell (Figure 2.2) and the bulk silver electrode, replicating the conditions of the QCM experiment exactly. Scans were

taken between 950 - 1050 cm^{-1} at 2 $\text{cm}^{-1} \text{ s}^{-1}$.

2.3 Results

2.3.1 Raman Spectroscopy of Pyridine

Raman spectra of pyridine- h_5 and - d_5 solutions in 0.1 mol dm^{-3} aqueous KCl electrolyte are shown in Figures 2.4 and 2.5, respectively, and the assignments are given in Table 2.1.

Raman shift / cm^{-1}					Assignment
Pyridine- h_5			Pyridine- d_5		
Liquid ¹³	SERS ¹³	Fig. 2.4	Liquid ³²	Fig. 2.5	
3054	3063	3059	2293	2298	ν_2 (C-H stretch)
3036			2270		ν_{13} (C-H stretch)
			2254		
1583	1596	1596	1530	1552	ν_{8a} (aryl C=C stretch)
1572	1571	1570			ν_{8b} (aryl C=C stretch)
1482	1480	1480	1340	1338	ν_{19a} (aryl C=C stretch)
1218	1212	1215	886	889	ν_{9a} (C-H in-plane bend)
1068	1063	1065	823	829	ν_{18a} (C-H i-p bend)
1030	1037	1035	1006	1002	ν_{12} (ring breathing)
992	1010	1008	962	974	ν_1 (ring breathing)
652	650	650			ν_{6b}
605	636	635	582	601	ν_{6a}
		623			-
	231	213		201	skeletal (Ag-ads stretch)

Table 2.2: Band positions and assignments for SERS spectra of pyridine.

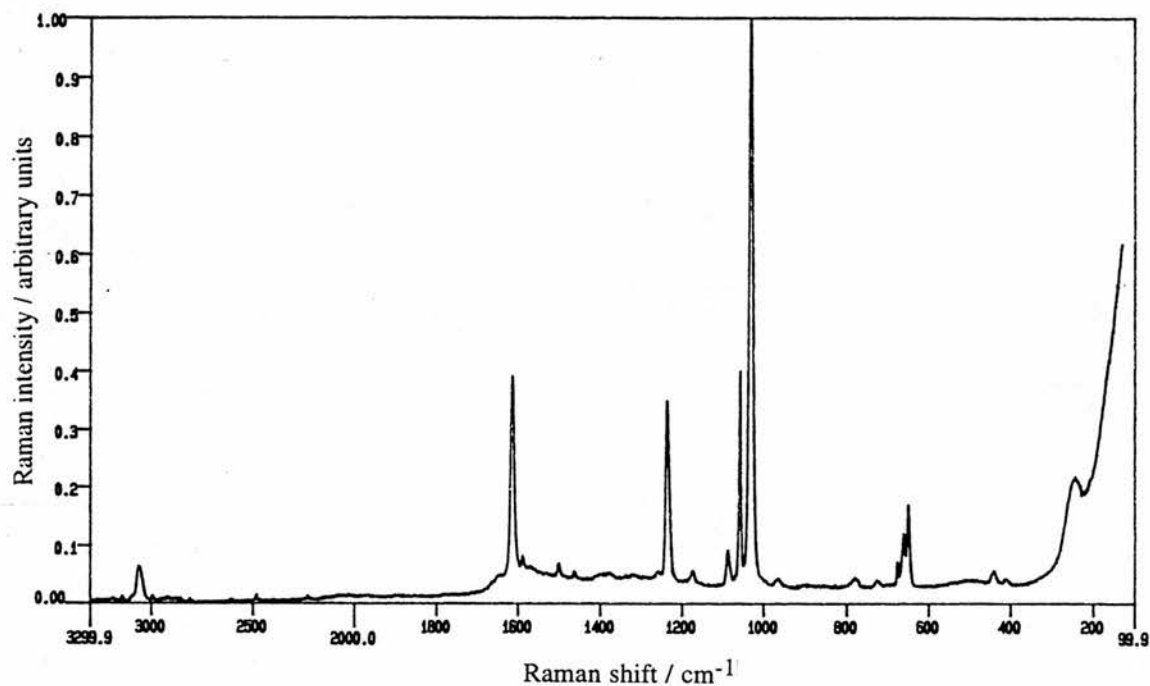


Figure 2.4: SERS spectrum of 0.05 mol dm^{-3} pyridine in 0.1 mol dm^{-3} KCl (aq), in-situ roughening, -0.6 V vs Ag / AgCl, laser = 514.5 nm , 1 scan, $100 - 3300 \text{ cm}^{-1}$ at $1 \text{ cm}^{-1} \text{ s}^{-1}$.

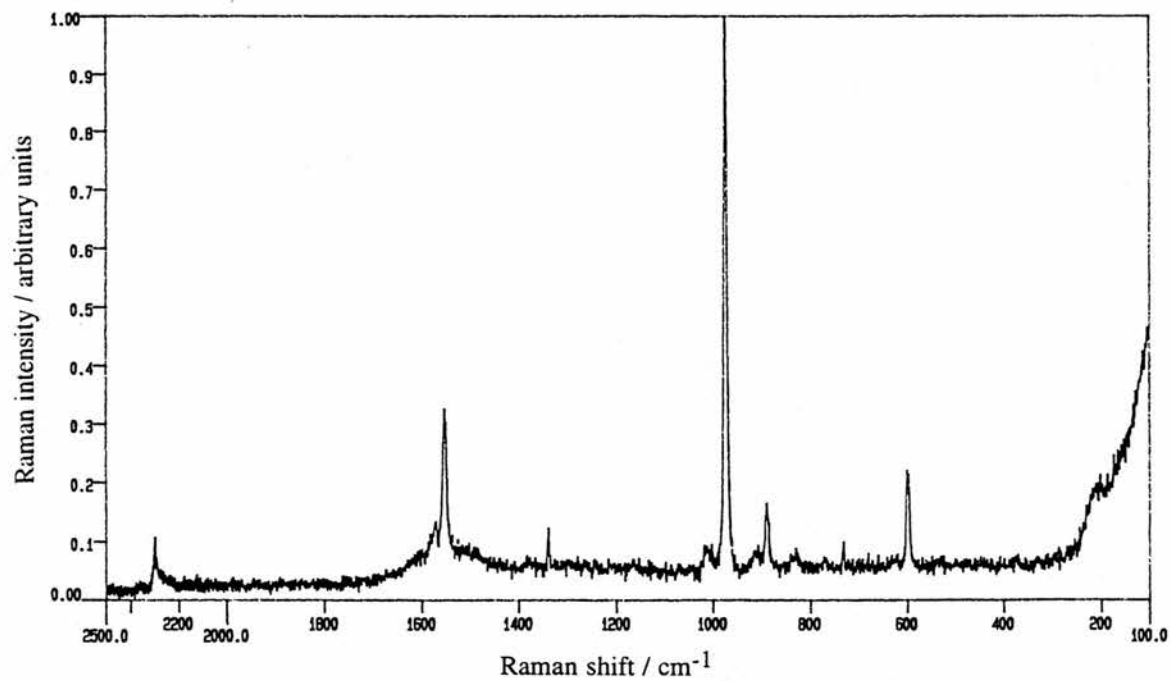


Figure 2.5: SERS spectrum of pyridine- d_5 . Conditions: $ca. 0.01 \text{ mol dm}^{-3}$ in 0.1 mol dm^{-3} KCl (aq), in-situ roughening, -0.6 V vs Ag / AgCl, laser = 528.7 nm , 1 scan, $100 - 2500 \text{ cm}^{-1}$ at $1 \text{ cm}^{-1} \text{ s}^{-1}$.

2.3.2 Quartz Crystal Microbalance Studies

Deposition of the Ag Overlayer

Three separate crystals (numbered 1, 2, and 3) were prepared during the course of this study, and the deposition parameters for each are given in Table 2.3.

Crystal	$\Delta f_{\text{deposition}} / \text{Hz}$ $\approx -\Delta m_{\text{deposition}} / \text{ng}$
1	-9400
2	-10200
3	-10100

Table 2.3: Frequency changes upon silver deposition for each crystal used.

The current and frequency vs potential responses before and after silver deposition in KCl electrolyte show little resemblance to one another, showing that only a negligible amount, if any, of the gold remains exposed after the deposition procedure.

Mass Response of the Underpotential Deposited Silver Films

The mass response of the quartz crystal was not calibrated to ensure that the mass sensitivity of the crystal remained the same after deposition of the silver in this case. It is clear from Figure 2.7 that the frequency changes during non-oxidative experiments on the 0.1 mol dm^{-3} KCl solutions differed widely, dependent on which of the crystals was used; however, the data from the ORCs show similar charge and frequency responses in all of the films throughout the experiments, showing that the mass sensitivity is similar for all experiments. The differences observed between films are, therefore, probably due to differences in surface roughness, which in turn are due to differences in the ORC procedures to which each film was exposed. This was unavoidable since the ORC conditions themselves were the subject of considerable study. Attempts were made to increase the frequency changes given by the films that were less

responsive in non-oxidative studies by carrying out further ORCs of varying anodic limits and scan rates; however, these had little further effect.

Oxidation-Reduction Cycles in Chloride Electrolyte

The CVs and frequency vs potential responses for numerous ORCs at 50 mV s^{-1} scan rates are shown in Figure 2.6. The behaviour of all of the ORC cycles displayed show a number of common features. On going to a potential more positive than the electrode has been exposed to previously, there is an irreversible frequency drop after the first ORC scan (Figs. 2.6 c,d). On subsequent scans to the same anodic limit the trace remains, to a first approximation, constant, scans tracking the route of the previous cycle.

A delay between the onset of oxidation and the frequency decrease is often seen, and in some cases there is in fact a frequency increase which occurs in the first few seconds of the oxidation current passing. This phenomenon is more marked for the the break-in scan than for subsequent scans, and is seen primarily for KCl solutions (Fig. 2.6b). Once the frequency starts to decrease, it continues to do so throughout the oxidation portion of the ORC.

Similarly, there is a delay between the onset of reduction and and the frequency starting once more to increase. Indeed, for KCl, in the first stage of reduction of the surface, the decrease of frequency as a function of potential (and therefore as a function of time) is at its greatest. The frequency decrease is less marked for LiCl and NaCl solutions, but its timescale is similar. If the scan rate of the ORC is lowered to 5 mV s^{-1} , then the frequency minimum is still around 50 mV negative of the charge maximum in KCl, suggesting that the phenomenon is not due to a slow kinetic process.

The frequency does then increase as the reduction continues, and the point at which the rate of frequency increase suddenly drops does coincide with the last potential at which the cathodic current becomes negligible. The portion of the curve where there is no ORC current is qualitatively similar to the non-oxidative scans for each electrolyte, as discussed below.

Solution	pH	Crystal	Scan type ^a	Limit / V vs SCE	$-\Delta f / \text{Hz} \approx \Delta m / \text{ng}^b$	Charge / μC^c	e^- / nmols	$\Delta m : e^- / \text{g mol}^{-1}$
KCl	7	1	BI	+0.08	353	980	10.17	34.7
			SQ		225	980	10.17	22.1
KCl*	7	1	BI	+0.13	608	1568	16.27	37.3
			SQ		353	1568	16.27	21.7
KCl*	7	1	BI	+0.25	3284	8039	83.39	31.3
			SQ		2108	7843	81.36	25.9
KCl	9	2	BI	+0.20	2706	8039	83.39	32.4
			SQ		1588	7647	79.32	20.0
KCl	9	2	BI	+0.20	2029	7058	73.21	27.7
			SQ		1176	7058	73.21	16.7
LiCl	8.95	3	BI	+0.20	3382	7843	81.36	41.6
			SQ		2411	7843	81.36	29.9
LiCl*	7	2	SQ	+0.20	1255	5294	54.91	22.9
LiCl	7	2	SQ	+0.20	2058	7353	76.28	27.0
NaCl	9.2	3	SQ	+0.20	1311	6176	64.07	20.5

Table 2.4: QCM and charge measurements on ORCs in 0.1 mol dm^{-3} alkali metal halide solutions. ^a BI = break-in scan and SQ = subsequent scan. ^b Assuming Sauerbrey's equation holds and measured from 0 V on the anodic sweep to the frequency minimum. ^c Anodic portion of sweep. * Data shown in Figure 2.7.

Table 2.4 correlates the charge passed in the ORC cycles with the frequency response. Note that the frequency and charge changes are measured from the maximum to the minimum points of a single cycle of the respective curves, and so, as discussed above, the potentials over which these two parameters are measured do not exactly coincide.

The values obtained are compared with those expected for the case where the only surface reaction is either the oxidation of Ag to AgCl or the subsequent reduction and where the Sauerbrey equation holds. The exact value for this case is $35.453 \text{ g mol}^{-1}$ (of electrons), which is equivalent to $-2.72 \mu\text{C Hz}^{-1}$. The break-in scans do give values of around 35, but in subsequent scans the $\Delta m : e^-$ ratio is substantially lower (on average $\approx 35\%$). One further estimate that can be made, assuming that oxidation and reduction between Ag and AgCl are the only reactions, is the extent of the reaction in terms of monolayers of AgCl. The formation of a monolayer of AgCl at an initially planar electrode has been calculated to require the passage of *ca.* $135 \mu\text{C cm}^{-2}$ of charge.³³ Therefore, in the experiments shown in Table 4.2 between 50 and 500 monolayers of AgCl are formed.

Cycles in 0.1 mol dm⁻³ Cl⁻ Below the Ag to AgCl Oxidation Potential

Frequency vs potential traces for 0.1 mol dm^{-3} aqueous solutions of KCl, NaCl and LiCl at neutral pHs and at $\text{pH} \approx 9$ (comparable to the pH of pyridine containing solutions) are shown in Figure 2.7 along with a representative trace of the cyclic voltammogram obtained under the conditions under which these scans were done.

Qualitatively, there is little difference either between scans for the different cations or between scans for the same cation on changing from pH7 to pH9, as evidenced by the positions of the frequency maxima and the amount of hysteresis relative to the total frequency change during the course of the scans. The sense of the hysteresis is towards higher frequency on the anodic sweep than on the cathodic sweep. When pyridine is present in the system such hysteresis is not observed, but can be restored if the solution replaced with pure 0.1 mol dm^{-3} MCl.

There are no major differences in the CVs of any of the solutions, and they all show a very weak, irreversible current for O_2 reduction at around -0.3 V vs SCE . This is despite the fact that solutions are degassed prior to and during transfer of solution in a pipette. The size of the cathodic current varies slightly between scans, but this value cannot be correlated to any other experimentally derived parameter.

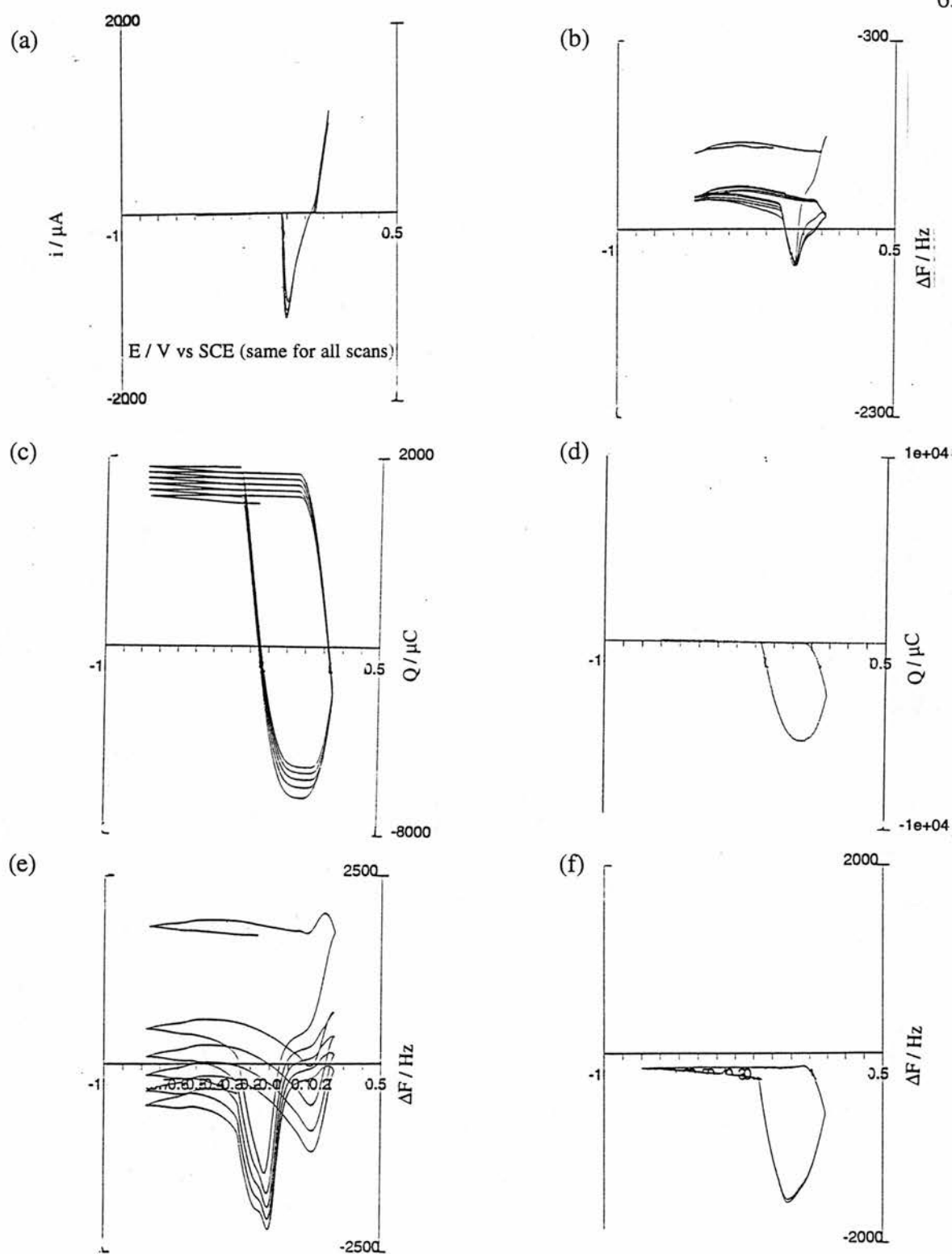


Figure 2.6: QCM responses for ORCs denoted by * in Table 2.4: (a) CV in $0.1 \text{ mol dm}^{-3} \text{ KCl(aq)}$ at pH7: anodic limit = $+0.13 \text{ V}$. (b) Frequency vs potential plot, conditions as in (a). (c) Charge vs potential plot; $0.1 \text{ mol dm}^{-3} \text{ KCl(aq)}$; pH7; anodic limit = $+0.25 \text{ V}$. (d) Charge vs potential plot; $0.1 \text{ mol dm}^{-3} \text{ LiCl(aq)}$; pH7; anodic limit = $+0.20 \text{ V}$. (e) Frequency vs potential plot, conditions as in (c). (f) Frequency vs potential plot, conditions as in (d).

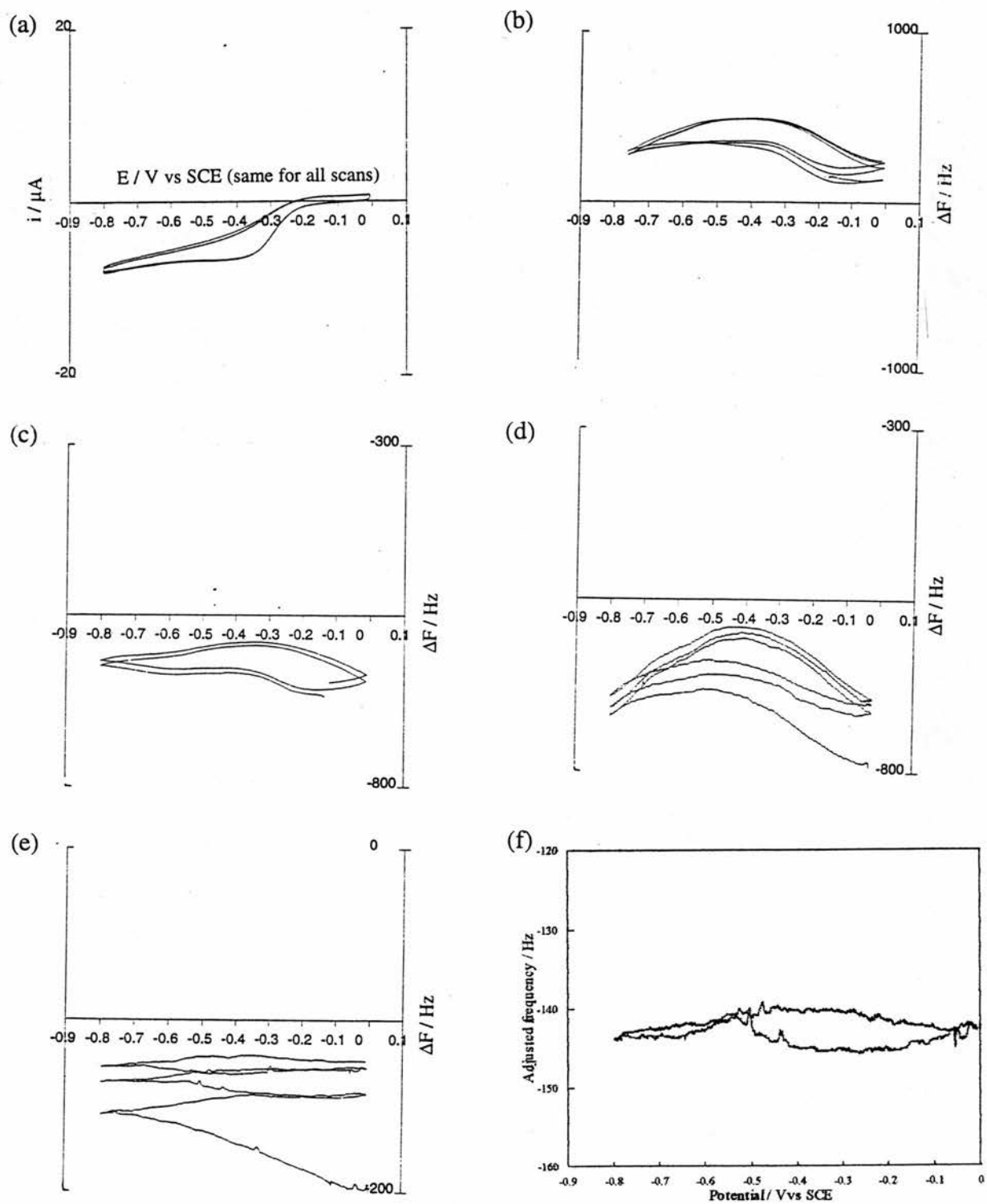


Figure 2.7: QCM responses from non-oxidative cycles in $0.1 \text{ mol dm}^{-3} \text{ Cl}^-$, scan rates = 5 mV s^{-1}
 (a) representative ORC trace. (b-f) frequency vs mass traces for (b) KCl, pH7; (c) KCl, pH9;
 (d) LiCl, pH8.95; (e) LiCl, pH8.95 affected by drift; (f) scan (e) after manipulation using
 Lotus 1-2-3 to make $\Delta f = 0$ between consecutive anodic limits by assuming constant drift.

The large differences in the size of frequency changes appear to be entirely due to differences between the responses of the three crystals used, and it is the quantitative irreproducibility between and, indeed, within films that is the limiting factor in the analysis of this data.

Figure 2.7 (e) and (f) demonstrate another problem encountered in some runs; that of a slow drift to higher frequency, attributed to corrosion, which means that consecutive scans do not coincide. Manipulation of the curves in the Lotus 1-2-3 worksheet program, using the assumption that drift is constant, leads to curves of similar shape to those where the problem is absent.

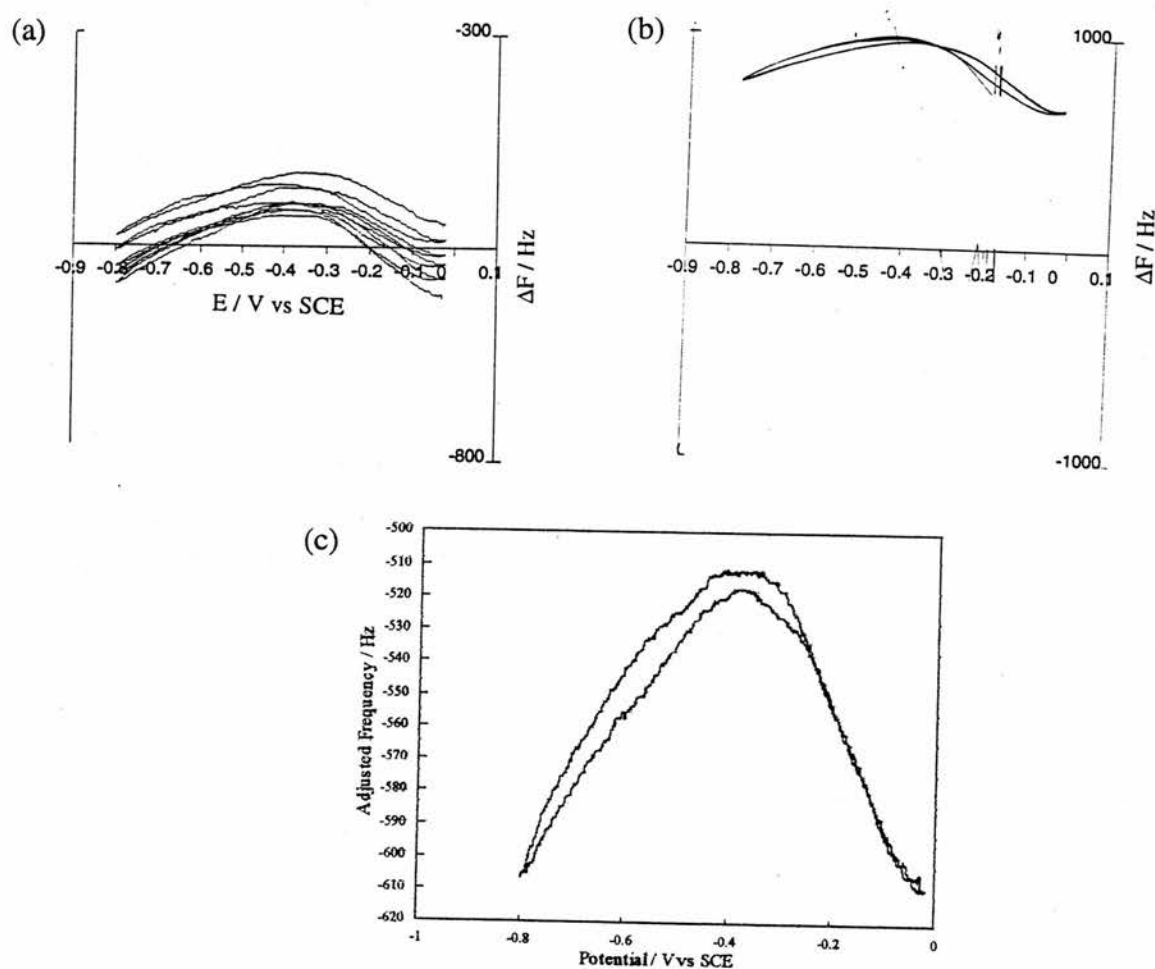


Figure 2.8: QCM frequency vs mass responses for $0.1 \text{ mol dm}^{-3} \text{ Cl}^-$ solutions containing 0.05 mol dm^{-3} pyridine. Scan rate = 5 mV s^{-1} . (a) KCl, pH 7 (b) LiCl, pH 9.2 (c) scan (b) after correction for drift.

Cycling in 0.1 mol dm⁻³ KCl Solutions Containing 0.05 mol dm⁻³ Pyridine Below The Ag to AgCl Oxidation Potential

The shape of the frequency vs potential curves for pyridine solutions are not dissimilar to those for halide alone, in that the frequency maximises at potentials of around -0.55 V, and there is no observable difference in the CVs. An important difference, however, is the lack of hysteresis in the frequency vs potential scans between 0 V and -0.8 V. The data are shown in more detail in Figure 2.8. The same dependence on the particular crystal used is seen as for the studies in chloride only. The effect of frequency drift can also be compensated in the same manner as for chloride.

2.3.3 Comparison of Raman Intensities with QCM Frequency Responses

A frequency vs potential trace covering the whole timescale of this experiment is given in Figure 2.9 and a comparison of the responses of both SERS intensities and frequency with potential is given in Figure 2.10. Although attempts were made to measure SERS spectra and QCM traces simultaneously, the cell set-up used led to poor SERS signals being recorded. Therefore, in the data used for Figure 2.10 the SERS and QCM results were acquired separately but under identical conditions. Table 2.5 shows that at -0.6 V the SERS signal does scale with the frequency decrease for the three points taken.

As a function of potential, the overall integrated intensity of the ring breathing region shows quite major changes whilst the frequency change observed in the QCM trace is very small relative to the changes observed during the ORCs. The changes in intensity of the 1008 cm⁻¹ band and of the whole ring breathing region (dominated by the 1008 cm⁻¹) tend to increase as mass decreases. The same is observed for the 1035 cm⁻¹ band, although the intensity changes for this band, both proportionately and in absolute terms, are much lower than for the other regions.

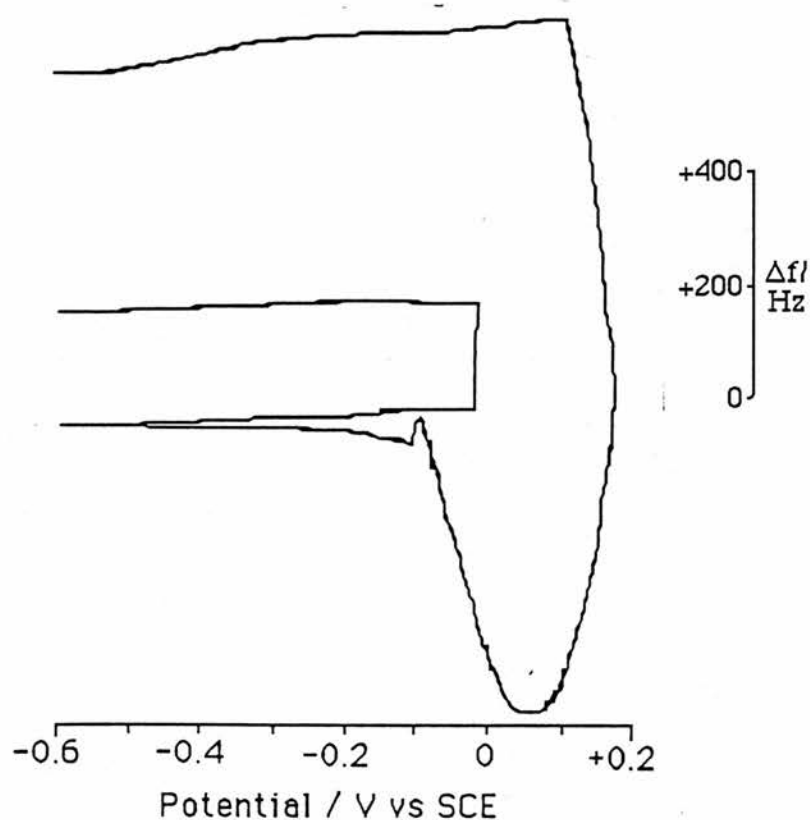


Figure 2.9: Frequency vs potential plot for an ORC cycle between -0.6 V and $+0.2$ V at 10 mV s^{-1} in 0.1 mol dm^{-3} KCl containing 0.05 mol dm^{-3} pyridine. Potentials were held for 3 minutes at -0.6 V before and immediately after the ORC, then at 0 V for 1 h, then for 3 minutes each at increments of -0.1 V.

Point at which spectrum was taken	Integrated intensity of ring breathing region / 10^3 cts	Frequency Change / Hz
Before ORC	6	0
Immediately after ORC	215	-833
After ORC and acquisitions	132	-561

Table 2.5: Raman intensities and frequency changes at -0.6 V vs Ag / AgCl before and after ORC cycles.

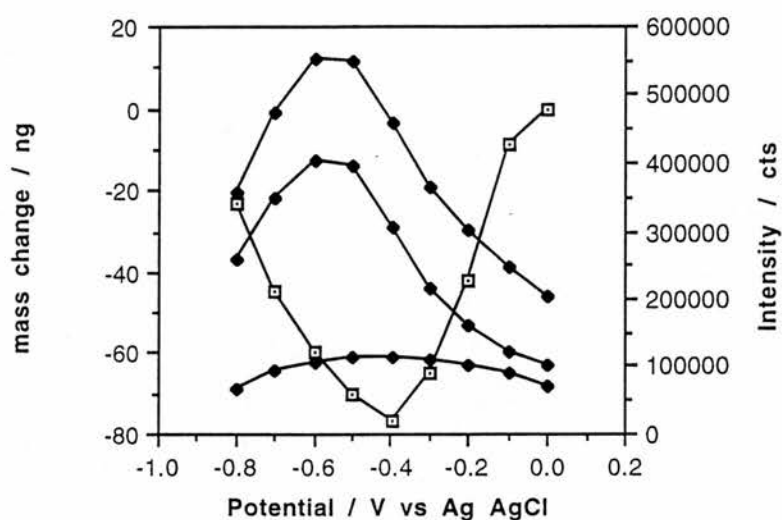


Figure 2.10: Plots of: (a) integrated SERS intensities (black diamonds) of, from top to bottom, the whole ring breathing region, the 1008 cm^{-1} band and the 1035 cm^{-1} band; and (b) frequency or mass change (white squares): versus potential.

2.4 Discussion

2.4.1 Pyridine SERS

The spectroscopic findings of this study correspond well with literature results, with the ring breathing bands for physisorbed pyridine at around 1010 cm^{-1} and 1035 cm^{-1} showing slight potential dependent shifts, and the 1025 cm^{-1} band, appearing for scans taken at a potential of 0 V where this potential is set immediately after an anodic scan.

In the absence of any strikingly different results for pyridine- h_5 , it remains only to comment briefly on the assignment of the 1025 cm^{-1} band used in this study, which will be that of anion-assisted chemisorption (Fig. 2.1e). The evidence for the other proposed structure, pyridinium (Fig 2.1d), is tenuous; Notholt and Ludwig¹⁶ make this assignment despite the absence of a critical band at 997 cm^{-1} , assigned to $\text{C}_5\text{D}_5\text{H}^+$, at neutral pH, claiming that this is merely due to the low intensity of the band. Regis *et al*¹⁵ suggest a mechanism by which pyridinium might be formed at neutral pH, but do not support this with any evidence.

Furthermore, the conditions under which a pyridine- d_5 band appears at 985 cm^{-1} in a study by Saito¹⁰ supports the assignment of this to the anion-assisted process.

A number of SERS studies on pyridines have included work on deuterated analogues^{10,15,16,34} but, remarkably, Table 2.2 is the first report of a full-range spectrum for pyridine- d_5 . The assignments are based on band shifts determined by normal coordinate analysis in normal Raman spectra,³² coupled with a comparison of relative band intensities between the SERS of deuterated and undeuterated pyridine. The wavenumber shifts between the liquid and SERS spectra are the same for both the deuterated and normal pyridine, as expected. The lower concentration of the pyridine- d_5 has led to worse signal to noise ratio than for the undeuterated compound, and a relatively small number of bands have been assigned. In particular, none of the weak b_1 bands, which are assigned at 1570 cm^{-1} and 650 cm^{-1} in the pyridine- h_5 surface spectrum and expected at around 1540 cm^{-1} and 623 cm^{-1} in pyridine- d_5 , are seen.

2.4.2 Interpretation of the QCM Response

It has been argued by Beck *et al*²⁶ that non-mass dependent frequency changes, due to microstructural changes in the solid film itself, are not significant in studies of this type. However, because of the possibility of viscoelastic coupling of electrolyte on a roughened surface (Figure 2.11), mass dependence does not necessarily follow the linear relationship of the Sauerbrey equation.

When the ratio of viscously to rigidly coupled mass remains approximately constant, for example, when the silver electrode microstructure does not change, then the following pairs of terms; “frequency decrease” with “mass increase”, and “frequency increase” with “mass decrease”; may be used interchangeably. Therefore, for each of the QCM experiments discussed below, surface microstructure is considered first, with QCM responses being described only in terms of frequency change. Mass changes are only discussed once a frequency change has been attributed to a mass dependent process.

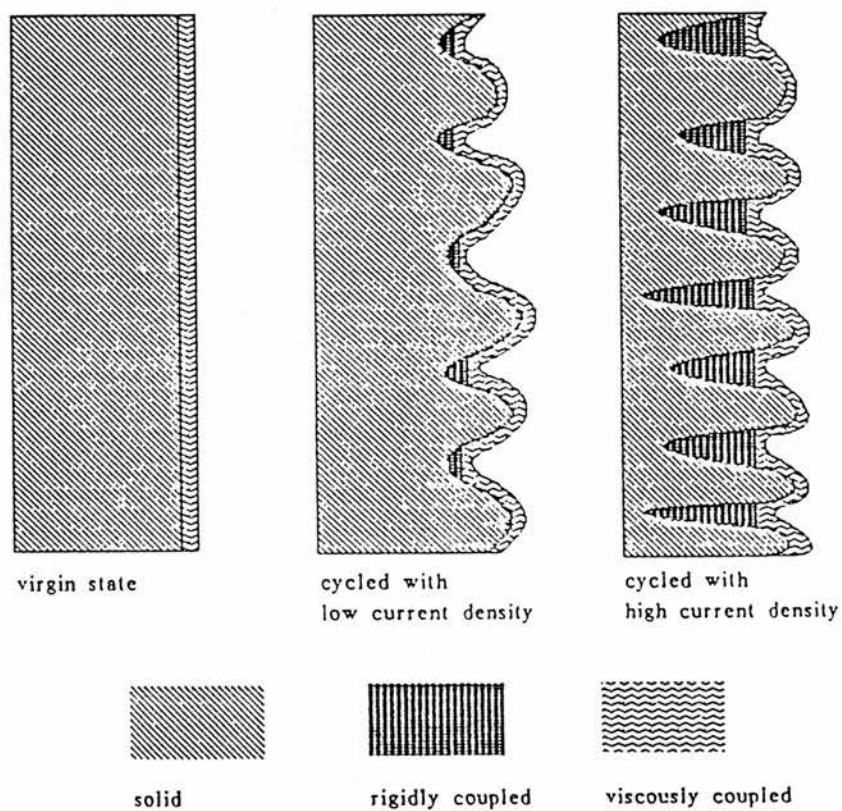


Figure 2.11: Schematic representation of rigidly and viscously coupled electrolyte.

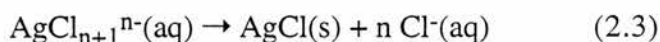
2.4.3 QCM Studies of Oxidation-Reduction Cycles

The typical oxidation-reduction QCM traces, as shown in Figure 2.6 can be separated into a number of regions where different processes are occurring. Five regions may be defined, and these will each be discussed in turn. The initial potential is 0 V vs SCE, and at +0.06 V the

oxidation of silver to silver chloride commences. This is the first region of interest.

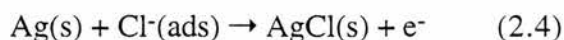
Break-in Oxidation of Silver Film

On a true break-in scan contributions to the frequency change may come from the following:



Reaction (2.1), silver oxidation, will be the main mass-dependent contribution to the frequency change as this stage. The reactions (2.2) and (2.3) are the forward and reverse reactions from which $\text{AgCl}_{n+1}^{\text{n-}}$ is produced. Equilibrium concentrations of these species are very low throughout the oxidative scan, and so their mass dependent contribution will be small. This also means that large scale loss of silver into solution *via* reaction (2.2) does not occur, as evidenced by frequencies returning to the same value after subsequent scans. However, the two reactions contribute to the roughening of the silver electrode, reaction (2.2) creating a dissolved species which may migrate before being reprecipitated at a different site, and this process may alter the number of coupled species.

The frequency (or mass) : charge ratio ($\Delta m / \Delta e$) is a diagnostic indicator of the processes occurring. For reaction (1), under ideal conditions, $\Delta m / \Delta e$ should be $\approx 35.5 \text{ g mol}^{-1}$. The value when taking the oxidative region in isolation is, however, rather less than this (N.B. the values given in Table 2.4 include mass increase on the reductive portion). One possibility is that some of the Cl^- involved in the oxidation is already adsorbed at the surface.



The $\Delta m / \Delta e$ ratio also leads to the suggestion that the mass of coupled species at this stage in the cycle is not increasing dramatically due to surface roughness.

So far the processes for a true break-in sweep have been considered. A true break-in

sweep is one in which the silver is newly deposited and has no history of oxidation before the sweep: such a film is termed a virgin film. No sweeps under typical conditions (see experimental) have been successfully recorded for a virgin film. For the purpose of subsequent discussion, then, a break-in sweep is defined as one where a previously roughened Ag film is excused to a more positive anodic potential. These may be termed break-in in the sense that the frequency responses of these scans are different to those of subsequent scans, whose frequency responses rapidly reach a steady-state from one scan to the next.

This now facilitates discussion of other features seen in the experimental break-in scans, most notably the delay often seen between the onset of oxidation and the decrease in frequency. Often, in fact, the onset of oxidation is accompanied by a marked frequency increase. The surface adsorbed chloride will be the most readily available for oxidation, and so reaction (2.4) is expected to be particularly important relative to reaction (2.1) in these early stages of oxidation, leading to a small rate of mass increase. This has also been suggested by Birss and Smith,³³ who in electrochemical studies of this potential region, observed a pre-wave just below the potential at which the main Ag to AgCl oxidation takes place and attributed this to partial electron transfer to adsorbed chloride. At the anodic limits used in this study, the pre-wave is dominated in CVs by the main oxidation and is not observed. However, the rate of oxidation (and current density) when the frequency is increasing is still relatively slow, because of the triangular waveform used.

From these considerations alone one would expect a very slow frequency decrease with $\Delta m / \Delta e$ substantially lower than 35 ng nmol^{-1} . A further process that may occur is that dissolution of AgCl_{n+1}^{n-} species may release previously trapped ions, in other words, the surface roughness changes may actually lead to a lowering of the mass of coupled electrolyte. It will be silver atoms at the extremities of surface features that will be most available for ligation by more than one chloride ion and so some roughness may actually be lost. Loss of roughness features in this manner will uncouple more electrolyte mass than if the silver were lost from the bulk. The observed behaviour may be compared with the fact that a single ORC may be as efficient in producing SERS spectra as multiple ORCs² – the surface microstructure reaches an equilibrium state fairly quickly, and does not continue *ad infinitum* to produce ever

more of the roughness features that support surface-enhancement.

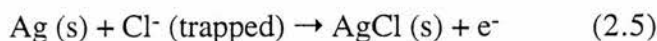
As the ORC cycle proceeds, a frequency decrease is soon seen. Here, the current density is higher, and more solution Cl^- is consumed. The increasing concentration of AgCl should continue to drive formation of further small amounts of AgCl_{n+1}^{n-} , but these will be from less extreme sites, and so the quantity of electrolyte being uncoupled or untrapped is expected to be less.

The triangular ORC waveforms used in these experiments are expected to produce a range of surface roughness features, and it is the anodic process that defines these. The critical parameter is current density, and a schematic of the results obtained is given in Figure 2.11, where a low current density is $\approx 0.2 \text{ mA cm}^{-2}$ and a high current density $\approx 2 \text{ mA cm}^{-2}$.²⁶ By this definition an excursion even to $+0.10 \text{ V}$ vs SCE produces a high current density. Schumacher *et al*³⁵ derived a very simple expression relating the mass change on the break-in oxidation of silver to silver oxide to the average corrugation size, assuming regular features such as those shown in Figure 2.11. The relationship, $\Delta m = \rho \varepsilon / 2$ (where ρ = the density of water and ε = the corrugation diameter), can be applied to the current system, although two points need to be made. Firstly, because several break-in cycles were done to increasingly positive anodic limits, the irreversible mass gain for any break-in scan is taken to be a summation of the value for that particular scan plus all break-in scans that have gone before it. Secondly, some morphological relaxation of the system is expected to have taken place between the various ORCs, but this is not allowed for in the equation above. On this basis, the average surface diameter for an excursion to $+0.08 \text{ V}$ is estimated as 20 nm and for the anodic limit of $+0.25 \text{ V}$ the value is at least 110 nm .

Excursion to a more positive anodic limit will increase the maximum current density and therefore change the surface microstructure; this is the phenomenon of break-in. On re-reduction after such a break-in cycle an irreversible mass increase is always seen, suggesting that there is more trapped electrolyte than before. Successively more positive anodic limits of $+0.08$, $+0.13$, $+0.20$, and $+0.25 \text{ V}$ vs SCE were scanned in 0.1 mol dm^{-3} KCl at pH 7. Thus in the case of the $+0.13 \text{ V}$ break-in scan (Fig. 2.6,b), which had previously been exposed to an anodic limit of only $+0.08 \text{ V}$, one would expect there to be less trapped electrolyte than in the

+0.25 V break-in scan (Fig. 2.6,e), which had previously been exposed to +0.20 V.

The consequence of this is that the reaction (2.5) is more important for the +0.25 V film than for the +0.13 V film:

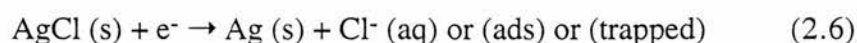


This reaction will cause similar behaviour to that discussed for reaction (4) and so one would expect a greater frequency decrease in the initial stages of oxidation for the +0.25 V anodic limit. This is indeed observed: the comparative values are +80 Hz and +270 Hz for the +0.13 V and +0.25 V limits, respectively.

The oxidative phase ends at +0.06 V on the cathodic sweep.

Reduction

The behaviour of the frequency vs potential trace during the reductive phase can be explained by processes analogous to those for the oxidative portion. The major redox process taking place is:



Reactions (2.2) and (2.3) continue, the reverse reaction, (2.3), to AgCl and then on to silver, dominating.

In the first stage of the reduction a rapid frequency decrease is seen. An analogous combination of factors may be used to explain this as to explain the frequency increase at the onset of oxidation; reduction to produce adsorbed and trapped Cl⁻ and the low rate of reduction at low reduction underpotential will both lower the contribution of AgCl reduction to a frequency increase, and re-trapping of electrolyte will actually cause a frequency decrease.

This feature is far more prominent in the reductive portion than in the oxidative portion. It appears that the re-establishment of roughness features is a rapid process, occurring in the first second of reduction, and that after this little further re-trapping occurs.

The consequence of this is that $\Delta m / \Delta e$ approaches 35 g mol^{-1} as the reductive sweep progresses, demonstrating that the roughness changes at this point are small. In contrast, for the oxidative process, $\Delta m / \Delta e$ never approaches 35 g mol^{-1} , showing that loss of roughness and untrapping of ions is important throughout this process. The rapid re-establishment of roughness features explains the lack of dependence of the SERS response on the reductive current density, which has been demonstrated by Tuschel *et al.*³⁶

The frequency vs potential plot for the +0.25 V anodic limit (Fig. 2.6, e) shows a shoulder on the reductive frequency minimum, even though no such feature is observed in the charge vs potential plot (Fig. 2.6, c). This is assigned a slightly different type of roughness feature than the one that gives the main frequency minimum. The nature of this has not been determined, although both features are expected to be three-dimensional AgCl phases. Although the main electrochemical reduction peak is equivalent to the “c₂” reduction of Birss and Smith,³³ which creates SERS active sites, the new feature is not the same as either reduction in that paper.

The roughening of the silver surface to an increasingly positive potential may have two effects, to reduce the number of atomic scale roughness sites by increasing dissolution of these (reaction 2.2)³⁷ and the formation of larger scale surface features, as observed by Byahut and Furtak³⁸ for over 40 monolayers at Ag(111), but substantially more for a polycrystalline surface. It is the latter oxidative effect that is the more likely candidate for the reductive shoulder on the frequency vs potential plots here, the behaviour becoming apparent in this case after the passing of about 400 monolayers worth of charge.

SERS intensity at a polycrystalline electrode starts to decrease if the average size of surface features exceeds around 100 nm,³⁶ close to the 110 nm average particle size estimated for the +0.25 V anodic limit. The formation of a distinct type of roughness feature that is surface inactive could provide a qualitative explanation of this phenomenon.

The rate of frequency change drops dramatically once reduction is complete and the portion of the QCM trace between this and the onset once more of oxidation is similar to the non-oxidative scans discussed in section 2.4.4.

Subsequent Oxidations

The same processes will occur for a subsequent oxidation as for a break-in oxidation. The difference, therefore, is in the relative contributions of each process to the QCM trace.

The similarity of the CVs and charge plots between break-in and subsequent scans shows that the silver to silver chloride reactions, (2.1), (2.4), and (2.5), sum to the same total for each. One would expect, however, that with more trapped Cl^- (and water) present, the subsequent oxidations would have a greater contribution from reaction (2.5) and a lesser contribution from reaction (2.1). This would lead to a lower frequency decrease overall in the oxidative sweep, and this, indeed, is seen for both Figures 2.6, (b) and (e).

One would also expect the frequency increase at the onset of oxidation to be affected. The greater number of trapped Cl^- anions contributing to the AgCl reaction along with the greater possibility for release of trapped species in a subsequent scan, would be expected to lead to a larger initial frequency increase upon the commencement of oxidation than for a break-in scan to the same anodic limit. This is a similar argument to that previously used for the comparison of the +0.13 V and +0.25 V break-in scans. The actual behaviour is more complicated than this.

For the +0.13 V anodic limit, no frequency increase is observed. Two possibilities are tentatively put forward. Firstly, there is the possible effect of film ageing affecting the break-in scan. Surface restructuring, to give flatter features, occurs on a timescale of several hours,³⁸ but it is possible that the initial stages of this process occurring in the time that passes between one experiment and the next (of the order of minutes), render the film more susceptible to the untrapping process on the break-in oxidation than on subsequent oxidations, which affect a freshly deposited silver layer.

The second possibility is that the adsorption of Cl^- is slightly different in the initial scan than in subsequent scans. The adsorbed Cl^- in the scans will be used primarily in the early stages of oxidation and lower the amount of frequency decrease. If, in subsequent scans, there were fewer Cl^- atoms adsorbed, maybe because the surface had not had time to equilibrate with electrolyte fully, then the frequency decrease will tend to be higher due to lesser influence of this component. Note that this is slightly different to the undoubtedly greater effect of trapped

Cl^- in the subsequent scans than in the break-in scans, because these ions are not specifically adsorbed at the surface, and they should contribute towards lowering the $\Delta m / \Delta e$ ratio throughout the oxidative scans.

The similarity between subsequent scans to the same anodic limit, for limits up to +0.20 V is explained by an observation of Beck *et al*²⁶, who showed that the same silver features are formed in subsequent oxidation cycles to the same anodic limit, and that new silver is only attacked on a break-in scan.

The behaviour of subsequent scans at the +0.25 V anodic limit is quite different. Here, the frequency increase is more marked for the subsequent scans than for break-in scans, however, the onset of this frequency increase is not until +0.13 V, well into the oxidative region. The magnitude of this frequency increase becomes larger scan by scan, and corresponds with the growth of the reductive shoulder mentioned previously. Another feature is that the QCM trace does not reach a true steady-state.

This is probably the effect of the larger scale roughness features that are produced at this potential. The smaller roughness features, present in the break-in scan, allow untrapping of ions immediately on oxidation. The larger scale features, which become more prevalent with each scan, require a larger quantity of AgCl and AgCl_{n+1}^{n-} formation before there is sufficient erosion to allow untrapping. The different oxidative properties are accompanied by the different reductive properties that result in the frequency shoulder.

One final point that needs to be made about the cycles in $0.1 \text{ mol dm}^{-3} \text{ KCl}$ concerns the $\Delta m / \Delta e$ values quoted in Table 2.4. These values are calculated from the maximum extent of both the charge and frequency changes, and as such cover both the untrapping and trapping stages of each ORC scan. Thus, for a break-in scan one would expect a $\Delta m / \Delta e \approx 35.5 \text{ g mol}^{-1}$ for the overall AgCl reaction (assuming uptake and release of adsorbed and trapped Cl^- match), plus a contribution from the fact that trapping exceeds untrapping, giving a total $\Delta m / \Delta e$ value that should exceed 35. For subsequent steady-state scans, where trapping and untrapping balance each other one would expect a $\Delta m / \Delta e$ value close to 35.

What, in fact, is observed, are values much lower than this; close to 35 g mol^{-1} for a break-in scan, and around $20 - 25 \text{ g mol}^{-1}$ for subsequent scans. The expected values are

obtained from a much more simplified model of the roughening than has been used in the previous discussion. It is clear that a large number of processes contribute to the overall frequency response, and this final assertion extends the boundary of how far the different processes can be unravelled, at least from the information obtained in this study.

pH Dependence

No major dependence on pH is seen in the pH 7 - 9 region studied. In sufficiently alkaline solution (pH 13, e.g. with OH⁻ electrolyte), silver oxide films are formed via the hydroxide species at around +0.24 V vs SCE.⁴⁰⁻⁴² These conditions can in no way be seen as relevant to this study. However, physical abrasion of the Ag surface in 1 mol dm⁻³ KOH leads to the potential of the Ag(OH) producing reaction becoming far more favourable at -0.44 V,⁴³ and the role of oxide in CN⁻ SERS has been suggested by Mahoney and Cooney at pHs as low as 10.5, on the evidence of Auger spectroscopy.⁴⁴ The lack of evidence in this study for similar processes does not discount their role in pyridine SERS completely as, in the Mahoney study, laser damage to the surface was an essential prerequisite for the silver oxide-cyanide phase.

Cation Dependence

Figure 2.6 (f) shows a mass vs frequency plot for 0.1 mol dm⁻³ LiCl at pH 7 under ORC conditions. This is entirely representative of the results given in both LiCl and NaCl electrolytes. The main difference between these and KCl traces are in the delays between onset of oxidation and frequency decrease and between onset of reduction and frequency increase.

These delays are still evident in both LiCl and NaCl electrolytes, but the frequency increase which often occurs with the onset of oxidation and the large frequency decrease on the onset of reduction (attributed in KCl to the dominant mass effects of untrapping and trapping, respectively) are seen to a much lesser extent.

All the alkali metal chloride electrolytes support SERS enhancement to a similar extent. As this enhancement is quite dependent on the average size of large scale surface roughness features³⁶ and the CVs of each electrolyte produce very similar current densities, it is a reasonable assumption that each electrolyte produces very similar Ag surface features. Another

piece of evidence for this is that, with multiple scans to the +0.20 V anodic limit, the growth of small frequency minima in the frequency vs potential plots of LiCl and NaCl are observed on reduction (*ca.* 0 V in Fig. 2.6, f). These can be attributed to the same process that produces the shoulder in the KCl frequency vs potential trace at anodic limits of +0.20 V and above.

That trapping and untrapping create a smaller frequency change in LiCl and NaCl could be attributed simply to the lower masses of the cations than in K⁺. Despite the low bulk mass contribution (<1%) of the salt to the electrolyte, above the pzc (-0.9 V) Cl⁻ adsorption is favoured by the electrode. This in turn creates a layer of adsorbed hydrated metal ions, as was found by the SERS study of Fleischmann and Hill on coordinated water modes.¹⁸ Thus the surface mass contribution of ionic species is expected to be higher.

The same study also describes another effect that may contribute to the observed mass traces. At around 0 V the solvation spheres of the three metals studied are quite different: Li⁺ has up to three strongly bound solvation spheres, Na⁺ two, and for K⁺ only the primary sphere is strongly bound. If any trapping and untrapping is from sites that limit the size of species that are able to pass, then one could imagine this presenting a higher activation barrier to Li⁺, with its strong coordination to water, than to K⁺. Electroneutrality would then also demand a slower ingress and egress of trapped, solvated Cl⁻ into and out of the pores of the roughened Ag surface, which may lower the overall density of the trapped layer quite considerably.

2.4.4 QCM Studies at Below 0 V in Solutions Containing Pyridine

The primary features that require explanation in the frequency vs mass traces shown in Figure 2.7 are the hysteresis shown in the steady-state scans and, by contrast, the marked lack of hysteresis when pyridine is present (Figure 2.8). Two processes are known to occur for roughened films within the potential window studied. Firstly, a reconstruction of the adsorbed chloride layer at around -0.5 V is evidenced by differential capacity peaks at this potential for single crystal, polycrystalline, and roughened Ag electrodes¹¹ and by resistance changes on stepping to -0.6 V.²⁵ Secondly, below -0.6 V an irreversible loss of SERS intensity occurs at a

point where there is no visible change in the film under a scanning electron microscope (SEM).^{36,45} This is attributed to a loss of atomic scale roughness.

The second process occurs equally with pyridine present⁴⁵ and absent.³⁶ However, the co-adsorption of pyridine onto the roughened surface does suppress the capacitance peak due to surface reconstruction of Cl^- . This, therefore, may contribute the hysteresis in solutions without pyridine present. Another process which almost certainly has an effect on the hysteresis is corrosion of the Ag surface in the presence of Cl^- , a process that is inhibited in the presence of pyridine. A similar closure of a hysteresis loop caused by the corrosion inhibition properties of pyridine is seen in the resistance measurements of Körwer *et al.*²⁵

The suppression of the capacitance peak by pyridine may also be viewed as a form of corrosion inhibition. Before Cl^- can be adsorbed at different surface sites¹¹ enough desorption of Cl^- must take place for these sites to become available. With a layer of pyridine present, the desorption process and, as a consequence, the reorientation are inhibited.

An overall lowering of capacitance across the potential range is observed when pyridine is present ($1250 - 2750 \mu\text{F cm}^{-2}$ in Cl^- alone, $750 - 1500 \mu\text{F cm}^{-2}$ in Cl^- containing pyridine).¹¹ The reduced capacitance when an organic layer is present is very closely related to a lower polarity of the adsorbed layer. The consequence of this for frequency vs potential plots is that a marked frequency increase, of about 100 ng cm^{-2} , is seen on replacing chloride solution with chloride / pyridine solution. This is shown by comparison of Fig. 2.7 (b) with Fig. 2.8 (a), consecutive experiments plotted on the same absolute frequency scale. The cause of this is the breakdown of an extended layer of adsorbed water, which contributes substantially to the mass in Cl^- alone but is lost in the presence of the organic layer.

The final feature of the frequency vs potential traces requiring consideration is the shape. For Cl^- alone there is a broad frequency maximum between about -0.5 and -0.3 V on the anodic sweep, the values being slightly more negative on the cathodic sweep. The frequency maximises at around -0.4 V with pyridine present, and this maximum is less broad. Both maxima coincide with capacitance peaks due to re-orientation.

However, one would expect Cl^- to desorb on average as pzc is approached, and so a mass increase towards -0.8 V is not expected. One feature that may cause an increase at

negative potentials is the loss of atomic scale roughness: small adatoms, once Cl^- has desorbed, are rapidly incorporated back into the silver lattice,¹¹ where they will constitute rigidly coupled rather than viscously coupled mass.

Several capacitance peaks in the pyridine containing system are attributed to unspecified reorientations at various crystal faces. From the SERS evidence these processes on a cathodic sweep will, on average, take pyridine into a flatter conformation, as Cl^- ceases to stabilise chemisorption. The maximum adsorption of a neutral is expected close to pzc, and so more pyridine will be adsorbed there. If this were monolayer adsorption, one would expect a continued frequency increase due to continued breakdown of the extended solvent layer. However, multilayer adsorption on any crystal face would lead to a frequency decrease, as is observed below -0.5 V. Although no multilayer adsorption is seen in the studies of Hamelin and co-workers at potentials negative of pzc,^{22,23} the 50 mmol dm^{-3} concentration of pyridine used in this study is much higher than in any of the adsorption studies.

2.4.5 Comparison of SERS Band Intensities and QCM Results

The preceding discussion provides a basis upon which to comment on how the adsorption processes of pyridine at silver might affect the resulting Raman spectrum, and what the relative effects of adsorption itself and enhancement mechanisms might be to the SERS response.

The fact that a different ORC procedure was used to create roughened films for the SERS study does not invalidate the qualitative discussion of the processes occurring below the silver oxidation potential – the same processes should still occur. One difference noted by several workers, including Saito,¹⁰ is that there is a delay of the order of 30 minutes before the maximum pyridine SERS intensity is obtained when *ex-situ* roughening is employed. With *in-situ* roughening, as done in this experiment, this factor need not be considered in the correlation of the data. Slow pyridine adsorption may be one contributory factor to the drift in frequency seen for some of the *ex-situ* studies above, although surface reconstruction is still likely to be major cause of this.

Between 0 V and -0.4 V it has been suggested above that reorientation of pyridine into flatter conformations and greater adsorption (as a percentage of monolayer coverage) cause a frequency increase. This is accompanied by an increase in SERS intensity, especially of the 1008 cm^{-1} band (Fig. 2.10). In this region then, SERS intensity is seen to scale with adsorption. The SERS intensity continues to increase to -0.6 V, the rate of increase slowing considerably between -0.5 and -0.6 V. This coincides with a frequency decrease attributed to multilayer adsorption. The slower increase in SERS signal may indicate that multilayer adsorption becomes increasingly significant: Zwemer *et al* show that several monolayers contribute to the SERS intensity, although the directly adsorbed monolayer contributes the most.⁴⁶

At potentials below -0.6 V the SERS signal decreases due to a loss of atomic scale roughness. However, this process is not the only contributory factor to the frequency trace, and so at this point SERS and QCM studies show sensitivity to different physical processes and comparison between them becomes unproductive. In other words, it is changes in the electronic properties of the surface that dominate SERS intensity changes, but these do not affect the electrode mass to such an extent. A similar limit to the correlation of SERS to electrochemical results below -0.6 V is seen for differential capacitance.^{11,12}

The relationship between quartz crystal frequency and SERS at a constant potential (Table 2.5) demonstrates the effect of ageing on the roughened silver surface. The gradual flattening of this surface over several hours³⁹ is observed here over its first hour, and causes both the apparent electrode mass and the SERS intensity to decrease. The main process here, where there has been no excursion to the region where atomic scale roughness is destroyed, is loss of large scale roughness features (i.e. 50 - 100 nm). These features have been shown to be important in producing SERS^{36,45} and their loss will lead to untrapping of electrolyte, explaining both the observed effects. For the two data points obtained an approximately linear relationship is seen between mass change and SERS intensity, suggesting that both scale similarly with the amount of surface roughness. Two provisos need to be made: the small number of data points means that a linear relationship cannot be firmly established and the statement implies nothing about the size of any surface features that might be present. The

majority of the frequency increase due to flattening occurred on holding the potential at 0 V vs Ag / AgCl for 1 h in this study, but the effect of changing this potential has not been considered.

2.5 Conclusions

The QCM responses of pyridine adsorption at a roughened silver electrode provide a useful contribution to the understanding of the adsorption processes that contribute to the SERS response of this system. When faradaic processes, such as surface oxidation, are occurring, the frequency vs potential trace reflects both these processes and associated non-faradaic processes such as trapping and untrapping of ions by the roughened electrode. At this stage the QCM is a promising indicator of the non-faradaic processes occurring.

Below the silver oxidation potential frequency changes can be attributed to adsorption and desorption processes in the extended layer. These can in turn be related to SERS intensity changes.

There are several ways in which this study could be extended in the future. Indeed, one original aim of this work was to calculate the contributions from each component (electrolyte cations and anions, pyridine, and water) by looking at the differences in the frequency response on undergoing a series of substitutions. Thus, lithium, sodium, and potassium chlorides were studied, and it was planned to substitute water by D₂O and pyridine by pyridine-*d*₅ and the substituted pyridines, 4-picoline (4-methyl pyridine) and 3,5-lutidine (3,5-dimethyl pyridine). The substituted pyridines were chosen as good models because both retain C_{2v} symmetry, are not substituted in the 2- position, and therefore would not have hindered chemisorption, and have similar electron density in the aromatic ring to the parent heterocycle. Unfortunately, although the QCM traces that were obtained were qualitatively reproducible, it was not considered that the quantitative reproducibility was sufficient at this stage to facilitate such a study.

2.6 References

- 1 M. Fleischmann, P. J. Hendra and A. J. McQuillan, *Chem. Phys. Letts.*, 1974, **26**, 163.
- 2 D. L. Jeanmaire and R. P. van Duyne, *J. Electroanal. Chem.*, 1977, **84**, 1.
- 3 M. G. Albrecht and J. A. Creighton, *J. Am. Chem. Soc.*, 1977, **99**, 5215.
- 4 H. Wetzal, H. Gerischer and B. Pettinger, *Chem. Phys. Letts.*, 1981, **78**, 392.
- 5 I. Pockrand, *Chem. Phys. Letts.*, 1982, **92**, 514.
- 6 R. Dornhaus and R. K Chang, *Solid State Comm.*, 1980, **34**, 811.
- 7 M. Fleischmann and I. R. Hill, *J. Electroanal. Chem.*, 1983, **146**, 353.
- 8 D. J. Rogers, S. D. Luck D. E. Irish, D. A. Guzonas and G. F. Atkinson, *J. Electroanal. Chem.*, 1984, **167**, 237.
- 9 V. V. Marinjuk, *Sov. Electrochem.*, 1986, **22**, 282.
- 10 H. Saito, *J. Raman Spec.*, 1993, **24**, 191.
- 11 M. Fleischmann, J. Robinson and R. Waser, *J. Electroanal. Chem.*, 1981, **117**, 257.
- 12 M. Fleischmann, P. R. Graves, I. R. Hill and J. Robinson, *Chem. Phys. Letts.*, 1983, **98**, 503.
- 13 B. Pettinger, *Chem. Phys. Letts.*, 1981, **78**, 404.
- 14 B. Pettinger and H. Wetzal, *Chem. Phys. Letts.*, 1981, **78**, 398.
- 15 A. Regis, P. Dumas and J. Corset, *Chem. Phys. Letts.*, 1984, **107**, 502.
- 16 J. Notholt and P. K. Ludwig, *Chem. Phys. Letts.*, 1989, **154**, 101.
- 17 V. M. Hallmark and A. Champion, *Chem. Phys. Letts.*, 1984, **110**, 561.
- 18 M. Fleischmann and I. R. Hill, *J. Electroanal. Chem.*, 1983, **146**, 367.
- 19 L. Stolberg, D. E. Irish and J. Lipkowski, *J. Electrochem. Soc.*, 1987, **134**, 187C.
- 20 J. Lipkowski, L. Stolberg, D. F. Yang, B. Pettinger, S. Mirwald, F. Henglin and D. F. Kolb, *Electrochim. Acta*, 1994, **39**, 1045, and references therein.
- 21 L. Stolberg, J. Lipkowski and D. E. Irish, *J. Electroanal. Chem.*, 1991, **300**, 563.
- 22 J. Lipkowski, L. Stolberg, S. Morin, D. E. Irish, P. Zelenay, M. Gamba and A. Wieckowski, *J. Electroanal. Chem.*, 1993, **355**, 147.

- 23 A. Hamelin, S. Morin, J. Richer and J. Lipkowski, *J. Electroanal. Chem.*, 1989, **272**, 241.
- 24 A. Hamelin, S. Morin, J. Richer and J. Lipkowski, *J. Electroanal. Chem.*, 1991, **304**, 195.
- 25 D. Körwer, D. Schumacher and A. Otto, *Ber. Bunsenges. Phys. Chem.*, 1991, **95**, 1484.
- 26 R. Beck, U. Pitterman and K. G. Weil, *J. Electrochem. Soc.*, 1992, **139**, 453.
- 27 H. J. E. Loewenthal, *A Guide for the Perplexed Organic Experimentalist*, John Wiley and Sons, Chichester, U.K., 1990.
- 28 D.T.Sawyer and J.L.Roberts,Jr., *Experimental Electrochemistry for Chemists*, John Wiley and Sons, Chichester, U.K., 1974.
- 29 R.J.H.Clarke and M.J.Stead, *J. Chem. Soc, Dalton Trans.*, 1981, 1760.
- 30 S. Bruckenstein and M. J. Shay, *Electrochim. Acta*, 1985, **30**, 1295.
- 31 A. P. Clarke, J. G. Vos, A. Glidle and A. R. Hillman, *J. Chem. Soc., Faraday Trans.*, 1993, **89**, 1695.
- 32 D. A. Long and W. O. George, *Spectrochim. Acta*, 1963, **19**, 1777.
- 33 V. I. Birss and C. K. Smith, *Electrochim. Acta*, 1987, **32**, 259.
- 34 H. D. Stidham and S. M. Harris, *J. Raman Spec.*, 1985, **16**, 193.
- 35 R. Schumacher, J. G. Gordon and O. Melroy, *J. Electroanal. Chem.*, 1987, **216**, 127.
- 36 D. D. Tuschel, J. E. Pemberton and J. E. Cook, *Langmuir*, 1986, **2**, 380.
- 37 G. Aloisi, A. M. Funtikov and R. Guidelli, *Surf. Sci.*, 1993, **296**, 291.
- 38 S. Byahut and T. E. Furtak, *Langmuir*, 1991, **7**, 508.
- 39 R. Waser, H. Wiese and K. G. Weil, *Ber. Bunsenges. Phys. Chem.*, 1984, **88**, 1177.
- 40 J. G. Becerra, R. C. Salvarezza and A. J. Arvia, *Electrochim. Acta*, 1988, **33**, 1431.
- 41 J. C. Hamilton, J. C. Farmer and R. J. Anderson, *J. Electrochem. Soc.*, 1986, **133**, 739.
- 42 B. V. Tilak, R. S. Perkins, H. A. Koslowska and B. E. Conway, *Electrochim. Acta*, 1972, **17**, 1447.

- 43 G. T. Burstein and R. C. Newman, *Electrochim. Acta*, 1980, **25**, 1009.
- 44 M. R. Mahoney and R. P. Cooney, *Chem. Phys. Letts.*, 1985, **117**, 71.
- 45 N. A. Cross and J. E. Pemberton, *J. Electroanal. Chem.*, 1987, **207**, 93.
- 46 D. A. Zwemer, C. V. Shank and J. E. Rowe, *Chem. Phys. Letts.*, 1980, **75**, 201.

Chapter 3

SE(R)R Spectra and Assignments for PMEs

3.1 Introduction

In this chapter are discussed the SE(R)RS spectra of the component parts that make up the model complex $[PVP-M(bpy)_2Cl]Cl$, namely poly(vinyl pyridine), the corresponding 4-vinyl pyridine monomer and the parent metal tris(bipyridyls). The basic SERR spectral features of the metallopolymers are also reported. The surface Raman spectra of most of these have been reported previously, and so results and experimental methodologies are compared and contrasted with the literature. Indeed, the electrochemical SERRS spectra of a polymer containing both ruthenium bipyridyl and PVP have been studied both at silver^{1,2} and copper³ by Chambers and Buck, although from the synthetic methodology given, it would seem that their metallopolymer is different from the well characterized polymer used in this study and its composition in terms of metal coordination cannot be predicted from the information given.

A large amount of interest in the chemistry of transition metal polypyridyls, particularly of Ru but also of several other metals, was generated by the efforts in the late 1970s to develop systems for solar energy conversion (see Chapter 1). The role played by the metal complex is that of photosensitizer, being converted into its excited-state by a visible photon of the appropriate wavelength. This excited-state can be used to trigger reactions that would not otherwise be photosensitive themselves, providing the excited-state lifetime is long enough to allow collision with other molecules. This has led, in turn, to major spectroscopic efforts into understanding the ground and excited-state photochemistry of photosensitizer complexes. The area has been reviewed extensively by Juris *et al*⁴ and by Krausz and Ferguson, who concentrate on the $[Ru(bpy)_3]^{2+}$ ion.⁵

The advantages of immobilizing the photoactive species in a polymer film are several. Firstly, it is a convenient way to attach the moiety to an electrode to enable generation of such processes as electrochemiluminescence (ECL) or to generate photocurrents by separating the photochemical and chemical reactions of, for instance, the $[Ru(bpy)_3]^{2+}$ / methylviologen

system. Secondly, as the photoexcitation of $[\text{Ru}(\text{bpy})_3]^{2+}$ is a one electron process and most potential chemical applications (e.g. water photolysis) involve multielectron transfers, the ability to group the photoactive molecules together in a predictable way could be highly advantageous.⁶

Resonance Raman spectroscopy has been a commonly used technique in excited-state characterization of metal polypyridyl complexes. For $[\text{Ru}(\text{bpy})_3]^{2+}$ itself, RR studies have been a particularly useful method of determining whether the metal-to-ligand charge transfer (MLCT) excited-states are localized upon one bipyridyl ligand or delocalized between all three. This is done by comparing the spectra with the ground state spectra (where bpy is neutral) and with alkali metal bipyridyls salts such as $\text{Li}^+(\text{bpy}^{\bullet-})$ and $\text{Na}^+(\text{bpy}^{\bullet-})$.⁷ If the structure is delocalized, one would expect to see bands at frequencies intermediate between the ground state and alkali metal bipyridyl frequencies, if localized, one would expect to see bands for both neutral and anionic bipyridyl, the intensities of which would be dependent on the number of negative charges the bipyridyl ligands carry between them. The structure of reduced forms of metal bipyridyls can be analysed in the same way, where one can use RR spectroscopy to determine whether reductions are metal or ligand based, and whether the electrons on any reduced ligands are localized or delocalized.⁸

Results from resonance Raman point to a localized model in the $^3\text{MLCT}$ excited-state of both Ru and Os tris(bipyridyls)⁷ and this has been supported by normal coordinate analysis (NCA) of isotopically unsubstituted, deuterated, and ^{15}N -substituted analogues.⁹ Excited-state studies have also been done on mixed ligand diimine complexes to study on which ligand the electron will localize. For instance, in $[\text{Ru}(\text{bpy})_2(\text{bpz})]^{2+}$ (bpz = 2,2'-bipyrazine), the MLCT excited state electron is found to be localized on the bipyrazine ligand.¹⁰

In contrast, the SERRS of electrochemically reduced $[\text{Ru}(\text{bpy})_3]^+$ in propylene carbonate suggests a delocalized ligand based reduction, though the surface is thought to play a role in this result, since it disagrees with the results obtained by ESR and UV-visible spectroscopy.⁸ RR studies have also been carried out with both chemical and electrochemical oxidation of Ru and Os tris(bipyridyls) in liquid SO_2 , with different results depending on the metal involved.¹¹ The reactions undergone in all these processes are highlighted in Figure 3.1.

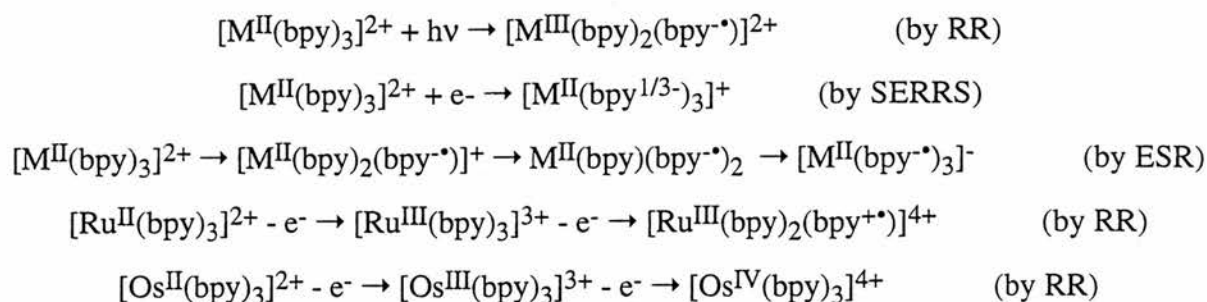


Figure 3.1: Some reactions of Group 8 transition metal bipyridyls, highlighting either the localized or delocalized nature of the reaction.

RR and SE(R)RS studies have also been done on the ground state spectra of $[M(\text{bpy})_3]^{2+}$ ¹² and on related complexes in which there are non-diimine ligands present.¹⁻³ The spectra obtained from RR and SERRS experiments are very similar to one another for these complexes. This similarity between surface and bulk spectra is also observed when the laser is not in resonance with the complex. When resonance enhancement is present, the spectra are dominated by bipyridyl bands, such that those due to other ligands are not observed.

The intense SERRS spectra given by transition metal bipyridyls and in particular those of ruthenium, plus the relative ease with which the metal centres can be coordinatively incorporated into PVP modified electrodes,¹³ make them ideal model compounds for the study of SE(R)RS in polymer modified electrodes. The phenomena which might be measured inside the film could include the distribution of redox centres and the charge transport of ions into the film. Note that SE(R)RS has specificity towards the polymer / electrode interface, and therefore for a thick polymer film the bulk polymer will give less intense scattering. SE(R)RS is one of the few techniques that is specific for this particular interface, and therefore information obtained from this technique could give different insights into the structure of PMEs.

3.2 Experimental

3.2.1 Materials

4-vinyl pyridine (4VP) was freshly redistilled under reduced pressure, discarding the heads. Purity was confirmed by GC/MS. Commercial poly(4-vinyl) pyridine (PVP) (Scientific Polymer Products inc., Ontario, NY) was reprecipitated twice from methanol by addition of diisopropyl ether and was then dried *in vacuo* at 80 °C. Another sample of PVP was synthesized by free radical polymerization of 4VP, as described below. For this azo(iso)butyronitrile (AIBN) was recrystallized from dry ether and absolute ethanol was dried by refluxing with magnesium turnings and iodine following the method recommended by Vogel,¹⁴ and was then distilled onto freshly activated 3 Å molecular sieves.

The syntheses of Ru(bpy)₂Cl₂¹⁵, Os(bpy)₂Cl₂¹⁶ and [PVP-Os(bpy)₂Cl]Cl¹⁷ were done according to literature methods and are not described any further here. The reaction stoichiometry used in the synthesis of the Os metallopolymer was 10:1 py:Os. The synthetic method for the osmium bipyridyl metallopolymer is analogous to that for the ruthenium polymer, described below.

All other compounds used were reagent grade and were used as received.

3.2.2 Characterization

N.M.R. Spectra were obtained on either a Bruker AM300 spectrometer (300 MHz) or a Gemini (200 MHz).

Infra-red spectra were run on a Perkin-Elmer 1710 Fourier-Transform instrument with a resolution of 4 cm⁻¹ or less. All I.R. spectra were obtained from KBr disks.

GC mass spectra were acquired on a Finnegan Mat INCOS instrument.

Microanalyses were carried out by the Departmental Microanalysis Service.

UV-visible spectra were obtained on one of the following spectrophotometers: a Philips PU8720, a Shimadzu UV-2101PC, or a Perkin-Elmer Lambda 14.

3.2.3 Syntheses

PVP

This followed a procedure first reported by Katchalsky *et al.*,¹⁸ and modified by Calvert and Meyer.¹⁹ In a Pyrex tube adapted for attachment to a high-vacuum line were added 4VP (21 cm³, 195 mmols), dry ethanol (50 cm³) and AIBN (0.11 g). The mixture was freeze-pump-thaw degassed three times, then the tube was sealed and heated to 65 °C for 4 days. The mixture was poured into *ca.* 1.5 dm³ of water and a pale pink solid precipitated. This was filtered and redissolved in EtOH, precipitated with diethylether, redissolved in EtOH and decolourized with activated charcoal. The charcoal was removed by filtration over diatomaceous earth and the EtOH removed yielding white product. Yield = 2.58 g, 12.6 %. ¹H NMR: (300 MHz) δ_{H} (DMSO-*d*₆) 1.58 (broad, 2.5H), 2.05 (s), 6.60 (broad, 2H), 8.25 (broad, 2H). These are in agreement with literature values.²⁰ The resonance at $\delta_{\text{H}} = 2.05$ is assigned to AIBN derived end-groups and so can be used to calculate molecular weight.¹⁹ From this the number average molecular weight (M_n) is determined as ≈ 3000 Dalton

[PVP-Ru(bpy)₂Cl]Cl

This followed a procedure reported by Clear *et al.*¹³. Appropriate amounts of commercial PVP and Ru(bpy)₂Cl₂ to give reaction stoichiometries of about 3:1 (PVP pyridine units:Ru centres), 10:1, 20:1 and 100:1 (exact values are given in Table 3.1) were dissolved in methanol and were refluxed for 2 days. A metallopolymer of *ca.* 10:1 composition was also made using the PVP sample described in the above synthesis. The progress of the reaction can be monitored by the disappearance of the UV-visible band of Ru(bpy)₂Cl₂ at around 550 nm. The solvent was removed by evaporation, and the products reprecipitated from dichloromethane / hexane solutions, except for the 3:1 reaction product, which was not sufficiently soluble in CH₂Cl₂, and so was rinsed this with solvent to remove starting material. The products were stored in the dark. Yields, estimates of the product stoichiometry, UV-visible data are given in Table 3.1. Infra-red (KBr disc) (cm⁻¹, intensity) (for "10:1" sample) : 2925 (m), 1600(s), 1418(m), 826(w), 766(m), 524(m).

The parameters in Table 3.1 are calculated as follows. Yield is calculated in the simplest way possible, given by equation 3.1:

$$\% \text{ Yield} = \frac{\text{Mass of product}}{\text{Mass of PVP in reaction} + \text{Mass of Ru complex in reaction}} \times 100$$

Equation 3.1

The calculation of product stoichiometry uses UV-visible spectroscopy to estimate the number and therefore the mass of ruthenium centres in a known mass of metallopolymer, and the remaining mass is assumed to be PVP. The extinction coefficient of the 496 nm UV-visible band is assumed to be 8500, the same as that of the monomer complex $[\text{Ru}(\text{bpy})_2(4\text{VP})\text{Cl}]\text{Cl}$.²¹ The calculation is similar to that of Calvert and Meyer for $[\text{PVP-Ru}(\text{bpy})(\text{terpy})]\text{Cl}_2$ polymers.¹⁹ The formula derived by this method is given in equation 3.2:

$$\text{py:Ru} = \frac{1}{\text{AM}_{4\text{VP}}} \left(\frac{\epsilon [\text{Pol}]}{A} - \text{AM}_{\text{Ru}} \right)$$

(Equation 3.2)

In equation 3.2 $\text{AM}_{4\text{VP}}$ and AM_{Ru} are the atomic masses of a 4-vinylpyridine monomer unit (= 105.14, this moiety is also referred to in the text as the pyridine unit, after the example of Calvert and Meyer¹⁹) and the $[-\text{Ru}(\text{bpy})_2\text{Cl}]\text{Cl}$ unit (= 484.35), respectively; ϵ is the extinction coefficient (= 8500, as indicated above); A is the measured absorbance, and $[\text{Pol}]$ is the concentration of metallopolymer in solution in g dm^{-3} .

Once all the numerical values are substituted, the above formula reduces to:

$$\text{py:Ru} = 80.8[\text{Pol}]/A - 4.61$$

(Equation 3.3)

Literature values¹³ for comparison with Table 3.1 are: UV-visible spectroscopy (MeOH)

(λ_{\max} , nm ($\epsilon_{356} / \epsilon_{496}$)): “2:1”; 354, 495 (1.38); “100:1”; 352, 493 (1.50).

Experimental Parameter	Desired PVP (as pyridine):Ruthenium Ratios			
	“3:1”	“10:1”	“20:1”	“100:1”
Mass PVP used / g	0.24	0.48	0.53	0.50
Mass Ru(bpy) ₂ Cl ₂ used / g	0.36	0.26	0.1284	0.0212
Reaction mixture stoichiometry (py:Ru)	3.07	8.50	19.01	108.52
Yield / %	97	80	91	42
Estimated loading of Ru (py:Ru) (from eqn. 3.1)	3.51	13.09	22.53	114.33
λ_{\max} / nm	357, 498	361, 497	356, 498	355(sh), 495
$\epsilon_{356} \div \epsilon_{496}$	1.34	1.35	1.32	1.86

Table 3.1: Yield and Spectroscopic data for [PVP-Ru(bpy)₂Cl]Cl metallopolymers.

The conventions used to describe these polymers in this text are: desired ratios (“3:1” etc.) are used to describe polymers in the text, estimated values are used in calculations, and x denotes the number of pyridines coordinated to Ru in [PVP_x-Ru(bpy)₂].

3.2.4 Electrochemistry

Cyclic voltammograms were obtained using one of the following set-ups: a Pine Instruments RDE4 potentiostat connected to a Graphtec WX3200 X-Y recorder, an E. G. & G. PARC 273A interfaced to a PC, or an EcoChimie μ Autolab with PC control.

Typically home-built glassy carbon (GC) or silver working electrodes, a saturated calomel (SCE) reference (Russell electrodes), and a Pt wire (99.99%, Aldrich) counter electrode were used.

3.2.5 Raman Spectroscopy

The spectrometer, potentiostats, instrumentation and data analysis method are as described in chapter 2, except for the additions noted below. The roughening cycles for polymeric samples were performed in 0.1 mol dm^{-3} KCl alone. The procedure for Ag electrodes is described in chapter 2. For surface-unenhanced resonance Raman experiments (SURRS) on copper the electrode surface was not roughened.

Studies at gold electrodes using a dye laser

A Coherent-Radiation CR-599 pumped dye laser containing DCM dye (Aldrich) was used to access laser lines in the 630 - 660 nm range, the dye being excited by 5 W of the 488.0 nm line of the Ar^+ ion laser. The red laser line was used in conjunction with a gold working electrode, which allowed study at potentials positive of 0 V vs Ag / AgCl. This electrode was roughened using an adaptation of the method of Chase and Parkinson²². Five oxidation-reduction cycles were done between -0.2 V and +1.2 V vs Ag / AgCl at 20 mV s^{-1} in 0.1 mol dm^{-3} KCl(aq).

Polymer deposition

Deposition of the polymers was done as follows after ORC cycles had been completed. Excess water was drawn from the edge of the working electrode with a piece of tissue and any remaining water was allowed to evaporate at room temperature for at least a further two minutes. The polymer was droplet evaporated onto the working electrode by application of a known volume and concentration of polymer solution from a micropipette. The solvent was then allowed to evaporate until the electrode surface appeared dry (typically 5 minutes for EtOH) and the electrode was then returned to the SERS cell. The polymer adsorbed poorly onto unroughened Cu, and so coating on this surface were allowed to dry for at least 3 days.

3.3 Results

3.3.1 4-vinyl pyridine

Figures 3.2 and 3.3 show the normal Raman spectra of liquid 4-vinyl pyridine with 514.5 nm and 457.9 nm excitation, respectively. The bands are consistently shifted 2 - 3 cm^{-1} to higher wavenumber when the 514.5 nm laser line is used, denoting that some charge-transfer interaction with the surface does take place. In addition to the bands which are also seen in the SER spectra (as detailed in Table 3.2), a number of bands that do not have a_1 symmetry are observed. Those at 1423 and 1408 cm^{-1} (at 514.5 nm) can be assigned to $\delta(=\text{CH}_2)$, but the origins of weak bands at 1335, 1302, and 1235 cm^{-1} are unclear. These unassigned vibrations are also seen by Tashiro *et al*, but they do not discuss this region in their study.²³

Figure 3.4 shows the SER spectra, after *in situ* roughening, of *ca.* 0.05 mol dm^{-3} 4-vinyl pyridine in 0.1 mol dm^{-3} aqueous KCl solution as a function of potential, and also shows that of pyridine itself for comparison. The bands common to normal and surface spectra are assigned in Table 3.2 and compared with those for pyridine (from chapter 2) for the ranges scanned: 100 cm^{-1} - 3300 cm^{-1} for normal Raman and 900 cm^{-1} - 1700 cm^{-1} for the SER spectra. Once more, weak bands are observed in the 1250 cm^{-1} - 1450 cm^{-1} region, including the $\delta(=\text{CH}_2)$ modes at around 1410 cm^{-1} and 1425 cm^{-1} . Other bands at around 1300 cm^{-1} are consistent with a build up of carbonaceous products.²³

The 4VP spectrum shows significant potential dependence, both in its overall intensity, which is much greater at negative potentials, and in the relative intensities and positions of the bands. The band at 1503 cm^{-1} is the most intense in the spectrum at -0.8 V and -0.6 V, but decreases in intensity even more rapidly than other bands at positive potentials and is barely detectable at 0 V. The intensity of a band at about 900 cm^{-1} (on the edge of the range scanned) varies considerably with potential. There is also significant potential-induced shifting of some bands; from 1604 cm^{-1} to 1592 cm^{-1} and from 1203 cm^{-1} to 1211 cm^{-1} ; on going from 0 V to -0.8 V.

3.3.2 PVP

Figure 3.5 shows and Table 3.2 assigns the full range SER spectrum of a droplet evaporated film of PVP after roughening in aqueous 0.1 mol dm^{-3} KCl. In addition to the expected lack of the monomer double bond modes at 1632 cm^{-1} and 1410 cm^{-1} , there are significant differences in the band positions between 4VP and PVP. Modes attributed to the vibration of the polymer itself are detailed in Table 3.2 but other bands are seen in similar positions to those in 4VP noted above.

3.3.3 [PVP-M(bpy)₂Cl]Cl (M = Ru or Os)

Basic Features of RR and SERR Spectra

SERRS spectra obtained with 514.5 nm excitation at -0.6 V vs Ag / AgCl are shown for "10:1" ruthenium and osmium metallopolymer at silver in Figure 3.6 and for the ruthenium polymer only at copper in Figure 3.7. The assignments are compared with those for $\text{Ru}(\text{bpy})_3^{2+}$ and $\text{Os}(\text{bpy})_3^{2+}$ in Table 3.3. The spectra of the polymers are very similar to one another, and to those of the parent bipyridyls, both in band positions and in relative intensities, as has already been shown by Chambers and Buck.^{1,2} Additional bands, not included in the table of assignments, are sometimes observed in the ruthenium complex with the short chain polymer at 903 cm^{-1} and 1211 cm^{-1} . These are similar to those seen in both 4-vinyl pyridine and PVP spectra.

The bands which can be unambiguously identified at the copper electrode (Fig. 3.7) are at Raman shifts of 384, 668, 732, 1168, 1320, 1484, 1556 and 1608 cm^{-1} .

Raman shift / cm ⁻¹					Assignment
Pyridine		4-vinyl pyridine		PVP	
Liquid ²⁴	SERS	Liquid	SERS	SERS	
3054	3059	3092*		3050	C-H stretch
3036		3053*			
		3013*	>1700		
-	-	1633	1631	-	vinyl C=C stretch
1583	1596	1597	1595	1597	ν_{8a} (aryl C=C stretch)
	1570	1550	1543	1554	ν_{8b} (aryl C=C stretch)
1482	1480	1496	1506	1519	ν_{19a} (aryl C=C stretch)
1218	1215	1201	1211	1210	ν_{9a} (C-H in-plane bend)
1068	1065	-	1055	1065	ν_{18a} (C-H in-plane bend)
1030	1035	787	<900	790	ν_{12} (ring breathing)
992	1008	991	1002	1008	ν_1 (ring breathing)
652	650	667	<900	660	ν_{6b}
	635				-
605	623				ν_{6a}
	213			213	Ag-Cl stretch

Table 3.2: Raman shifts and assignments normal Raman and SER spectra of pyridine-h₅, 4-vinyl pyridine and PVP at 514.5 nm (except * = 457.9 nm) and, in SERS experiment, -0.6 V vs Ag / AgCl.

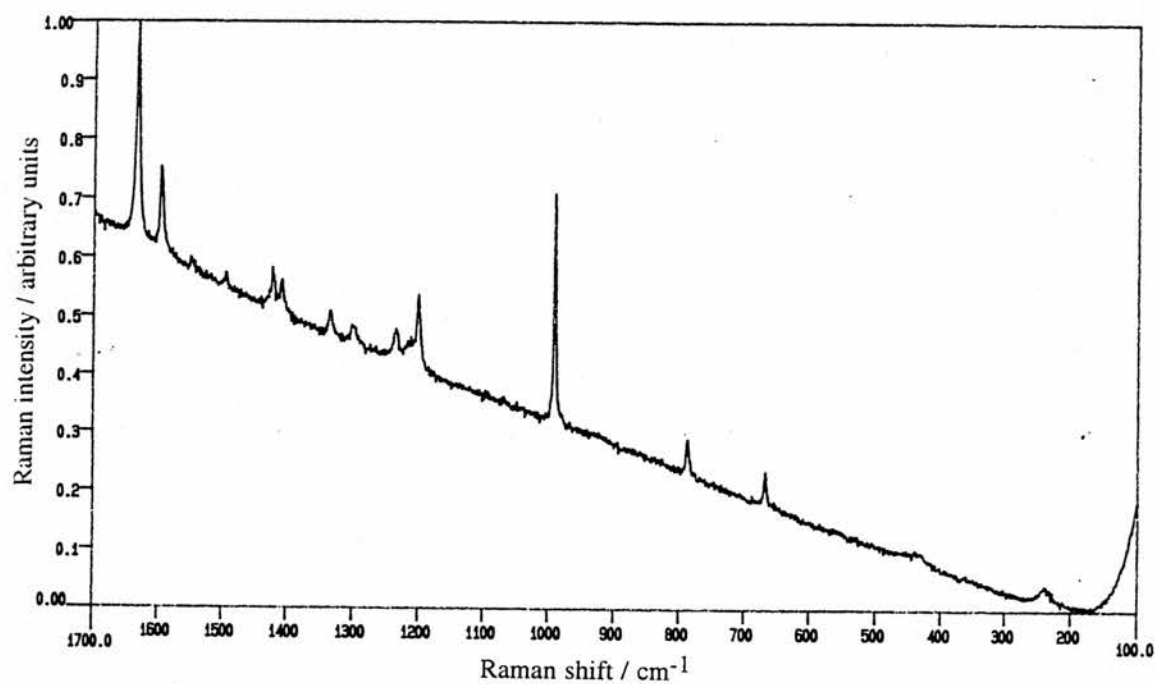


Figure 3.2: Normal Raman spectrum of liquid 4-vinyl pyridine, laser line = 514.5 nm.

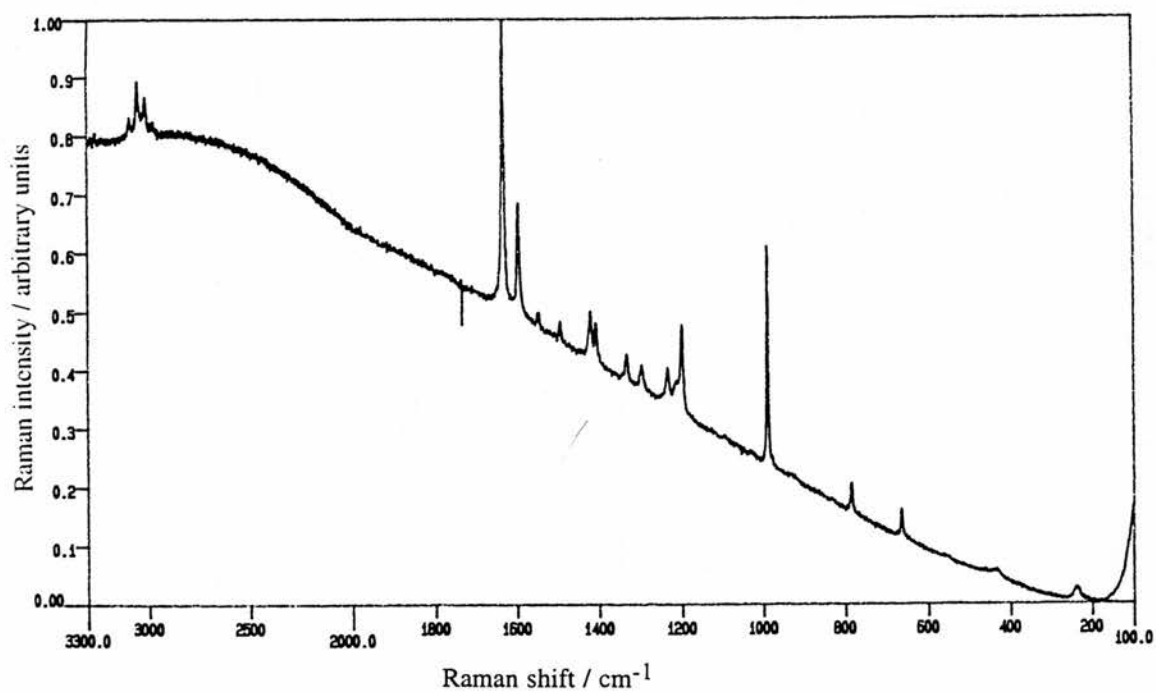


Figure 3.3: Normal Raman spectrum of 4-vinyl pyridine. Laser line = 457.9 nm.

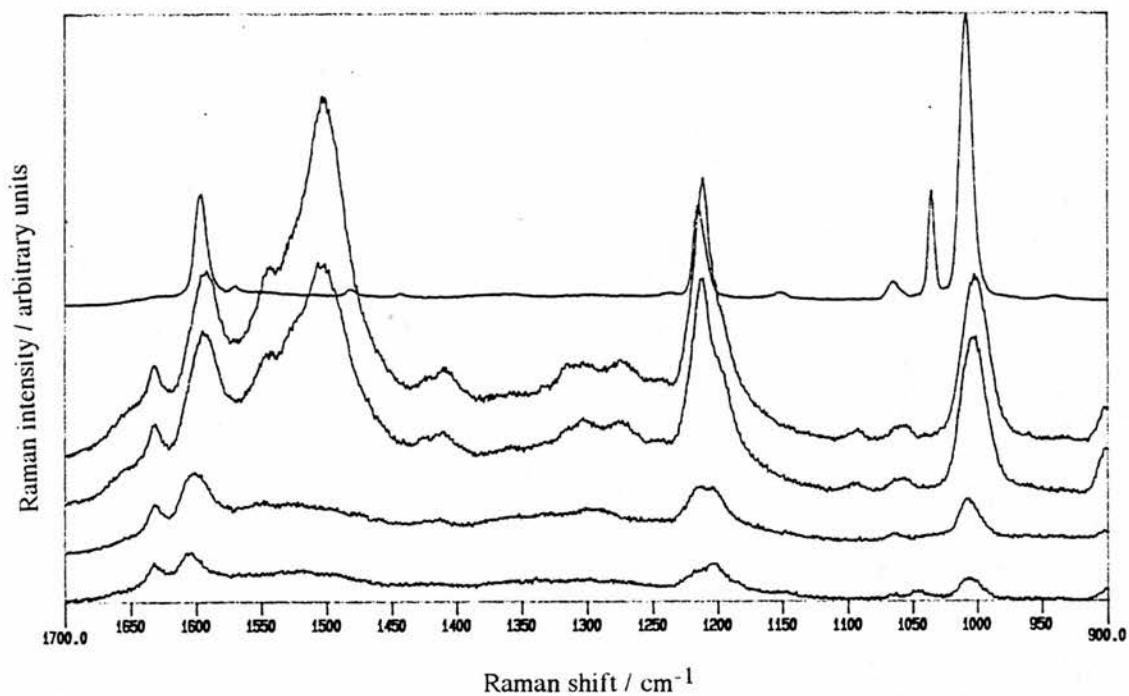


Figure 3.4: SERS spectra of 0.05 mol dm^{-3} 4-vinyl pyridine in 0.1 mol dm^{-3} KCl after in situ roughening. Laser line = 514.5 nm . Power = 150 mW . Potentials (from top to bottom) are: pyridine at -0.6 V , 4VP at -0.8 V , -0.6 V , -0.3 V and 0 V vs Ag / AgCl.

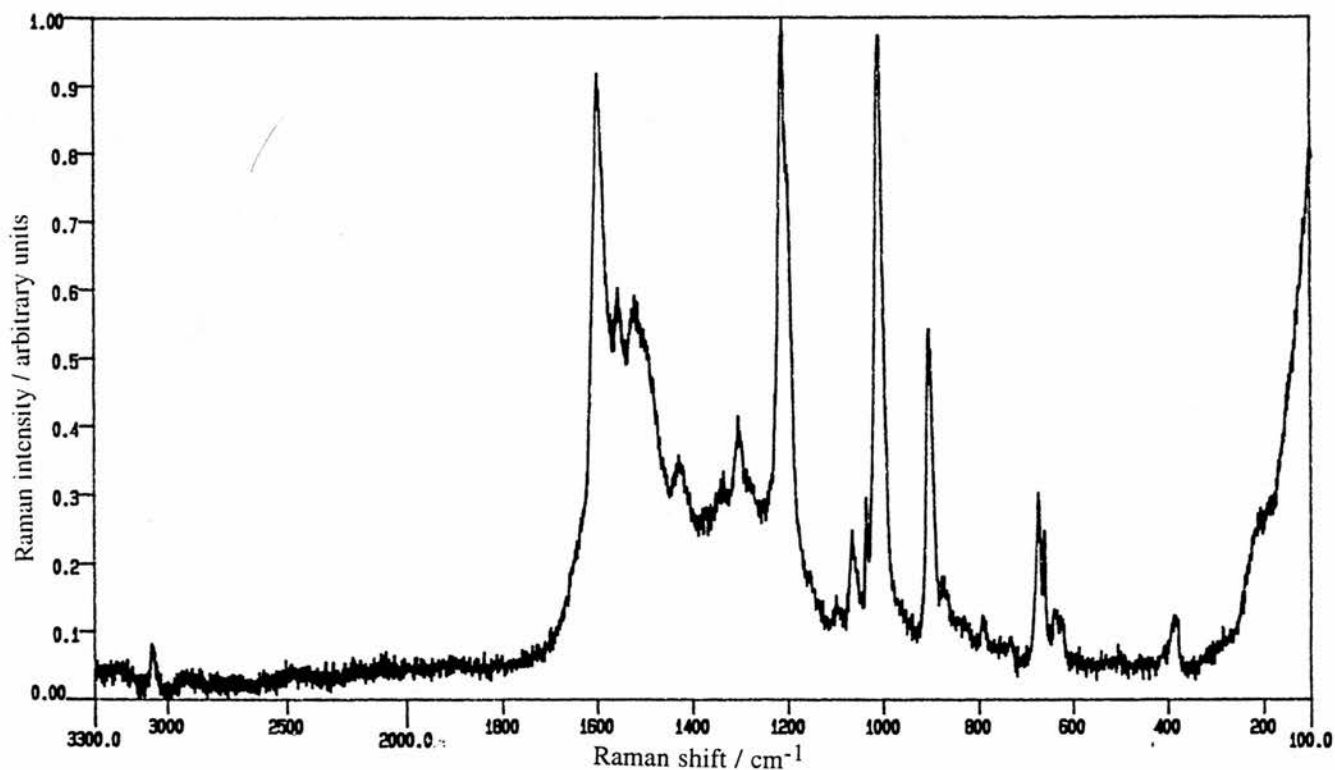


Figure 3.5: SERS of Ag electrode modified with PVP droplet evaporated from MeOH solution. Electrolyte = 0.1 mol dm^{-3} KCl, -0.6 V vs Ag / AgCl. Laser excitation = 514.5 nm .

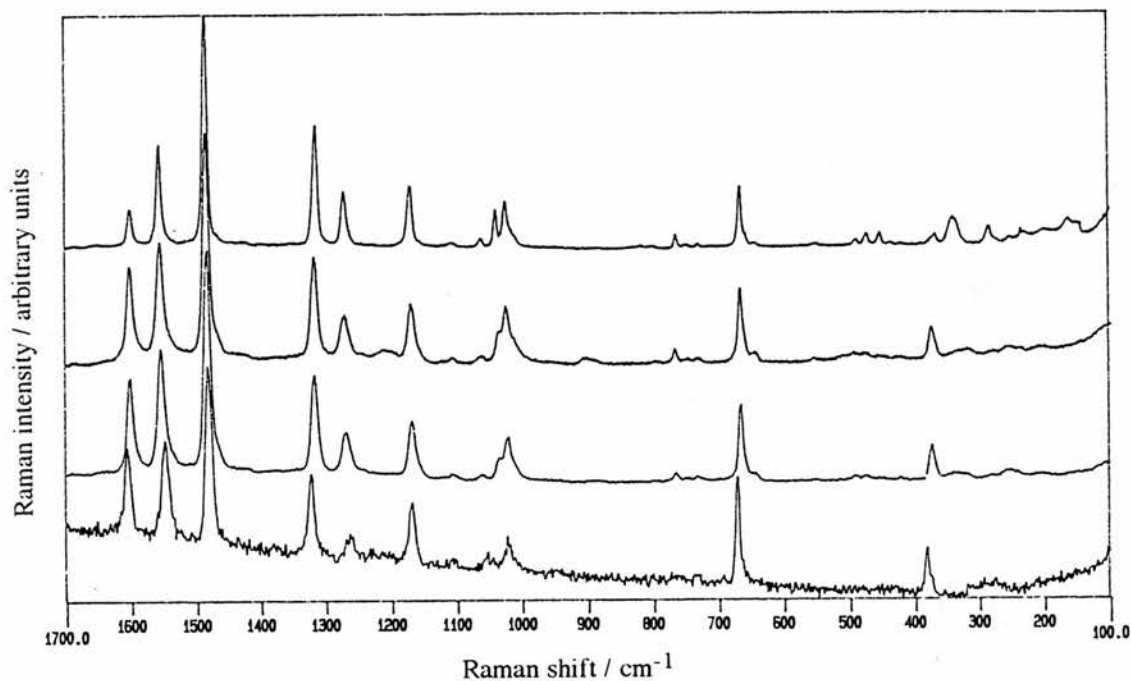


Figure 3.6 SERRS spectra at Ag of "10:1" polymers. Conditions: 514.5 nm excitation, potential = -0.6 V vs Ag / AgCl. Spectra (from top to bottom): (a) $\text{Ru}(\text{bpy})_3^{2+}$ at Ag colloid (from ref.12), (b) $[\text{PVP-Ru}(\text{bpy})_2\text{Cl}]\text{Cl}$ synthesized with short-chain polymer, (c) $[\text{PVP-Ru}(\text{bpy})_2\text{Cl}]\text{Cl}$ synthesized with commercial polymer (d) $[\text{PVP-Os}(\text{bpy})_2\text{Cl}]\text{Cl}$

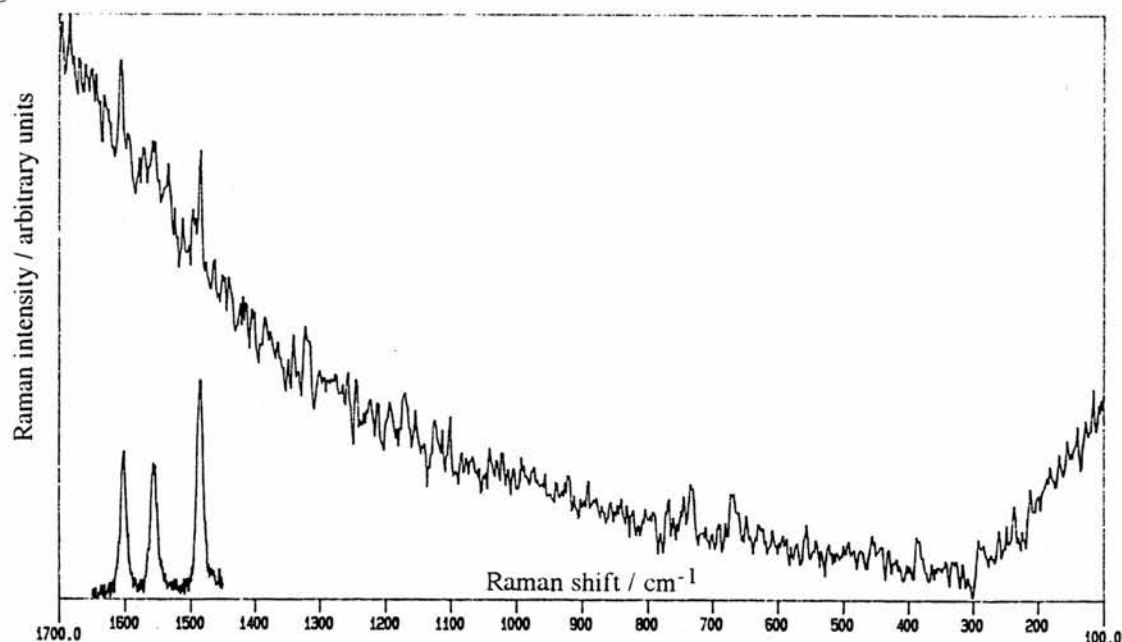


Figure 3.7: SURRS spectrum of $[\text{PVP-Ru}(\text{bpy})_2\text{Cl}]\text{Cl}$ at copper. Conditions: 514.5 nm excitation, Power = 40 mW, open-circuit potential, 12 scans. Insert is spectrum for one scan at Ag under identical conditions and reduced in intensity $\times 100$.

Raman shift / cm ⁻¹				Assignment
Ru(bpy) ₃ ²⁺ ref.12	PVP- Ru(bpy) ₂ Cl ⁺	Os(bpy) ₃ ²⁺ ref.25	PVP- Os(bpy) ₂ Cl ⁺	
201	208			M-N,M-Cl bends (Ru,Os,Ag)
254	250		274	out of plane ring bend
338	340			-
371	372		380	Ru-N, Os-N stretch
424	422			out of plane ring bends
438				
454				
-	474			
491	490			in-plane ring bends
554	556			
646				
667	664		670	
732	732		732	overtone: 2 x 371
749	746			-
766	764			in-plane ring bend
803		<900		C-H out of plane bend
1027	1020	1029	1022	v ₁ (ring breathing)
1042	1034 (sh)		1040	v ₁₂ (ring breathing)
1065	1062	1048	1052	v _{18a} (C-H in-plane bend)
1109	1108		1106	
1172	1168	1175	1168	v _{9a} (C-H in-plane bend)
1273	1268	1268	1262	
1317	1316	1322	1322	C ₂ -C ₂ ' stretch
1486	1482	1491	1482	v _{19a} (aryl C=C stretch)
1558	1554	1558	1548	v _{8a} (aryl C=C stretch)
1602	1600	1610	1606	
1653				combination: 1273 + 371
1691	1688			combination: 1317 + 371

Table 3.3 Bands and assignments for the spectra of [PVP-M(bpy)₂Cl]Cl (M = Ru or Os), at 514.5 nm on an Ag electrode at -0.6 V. Literature results are from SERRS at Ag colloid (Ru), and resonance Raman in aqueous solvent (Os)

Potential Dependence at Silver

Figure 3.8 shows the spectrum of [PVP-Ru(bpy)₂Cl]Cl as a function of potential for the short-chain polymer. Very little change is seen in band positions and in relative spectral intensities, except for the bands due to peroxide assigned bands, as discussed elsewhere in this chapter. It should be noted that absolute values of intensity are not used in Figure 3.8, as the focussing of the laser was not identical for each acquisition in this particular instance.

Exciting Wavelength Dependence

Figure 3.9 compares spectra acquired at a number of wavelengths of the Ar⁺-ion laser. Attempts were made to standardize these experiments as much as possible, the figure reflects the different relative SERRS intensities obtained for each wavelength. No adjustment has been at this stage to correct for the different powers used at each wavelength; however, chapter 4 details the manipulation of this data set to obtain SERRS excitation profiles. Qualitatively, there is very little difference between the spectra, which show the same bands as detailed in Table 3.3.

Studies on the Os(II/III) Couple at Gold

Figure 3.10 shows the spectrum of [PVP-Os(bpy)₂Cl]Cl as a function of potential at the gold electrode. The Os(II/III) couple is observed at +0.25 V vs SCE on glassy carbon²⁶ and at +0.20 V vs SCE on gold, as shown in Figure 3.11. Thus, the two potentials at which spectra were acquired represent Os in oxidation states +2 and +3, respectively. Table 3.4 compares these two spectra with literature results for Os(bpy)₃ⁿ⁺ (n = 2, 3).¹¹ The shift in positions of the metallopolymer bands for the Os(II/III) couple are in reasonable agreement with the values for the parent complex. The 1560 cm⁻¹ and 1612 cm⁻¹ bands for SERS of the metallopolymer are weak, however, and therefore there may be some error in the quoted band positions.

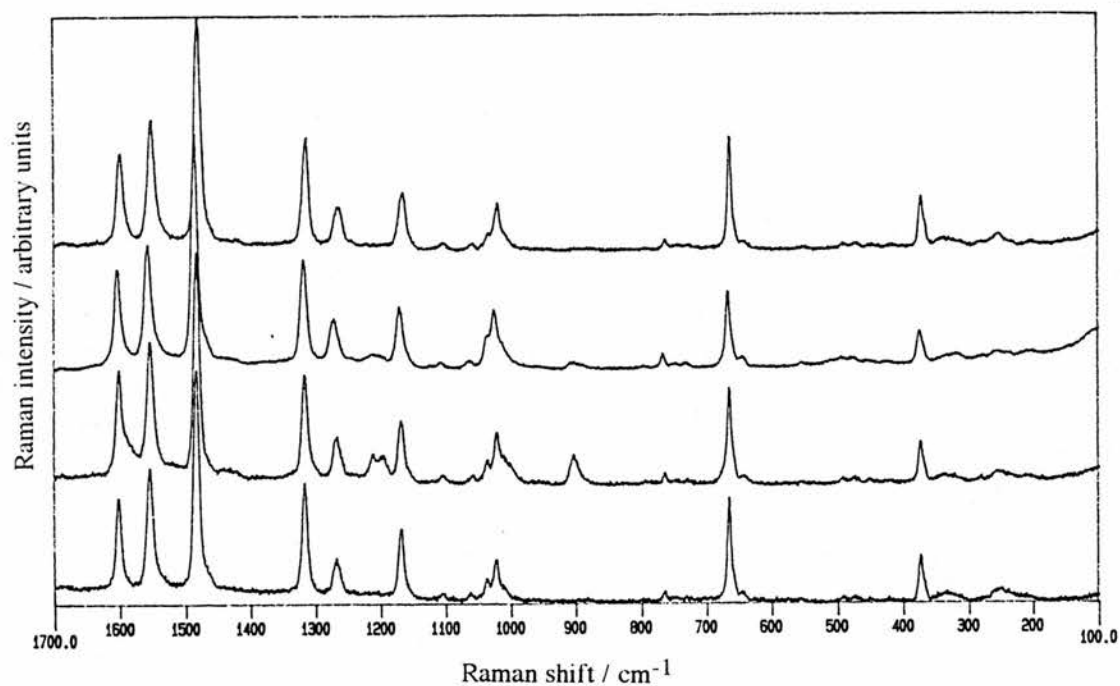


Figure 3.8: SERRS of short-chain, "10:1" [PVP-Ru(bpy)₂Cl]Cl, Ag electrode, 514.5 nm, 150 mW power. Potentials (vs Ag / AgCl) from top to bottom are; (a) -0.8 V, (b) -0.6 V, (c) -0.3 V, (d) 0 V.

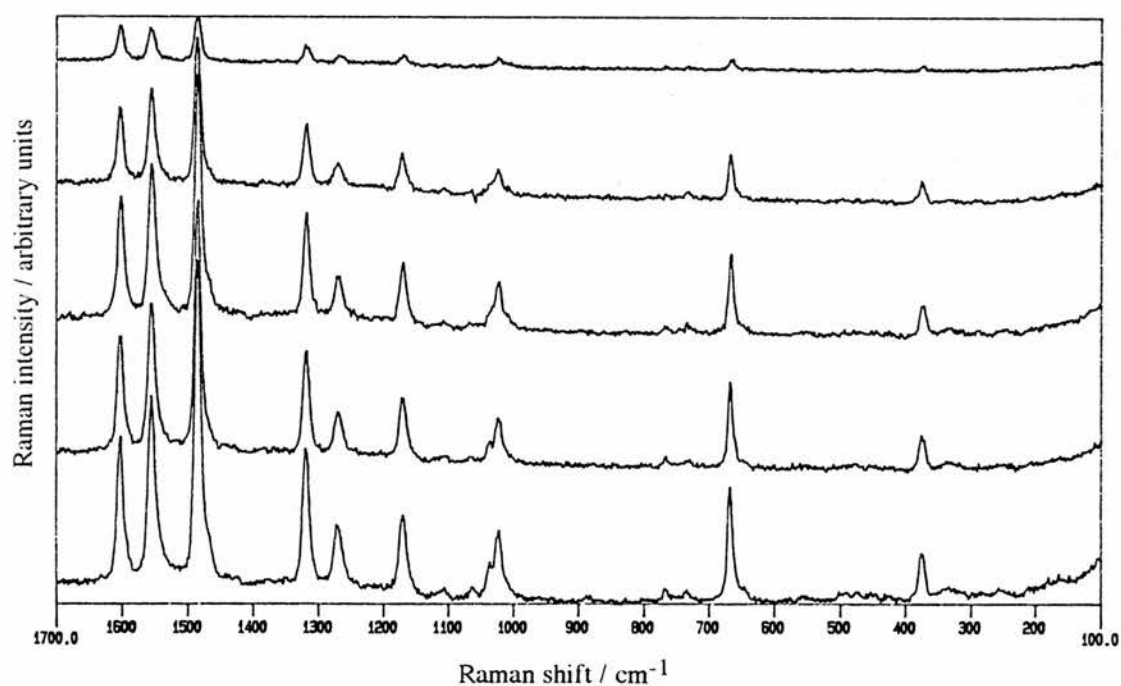


Figure 3.9: SERR spectra of "10:1" [PVP-Ru(bpy)₂Cl]Cl, Ag electrode, -0.6 V vs Ag / AgCl. From top to bottom: (a) 457.9 nm, 50 mW, (b) 488.0 nm, 80 mW, (c) 496.5 nm, 100 mW, (d) 501.7 nm, 100 mW and (e) 514.5 nm, 130 mW.

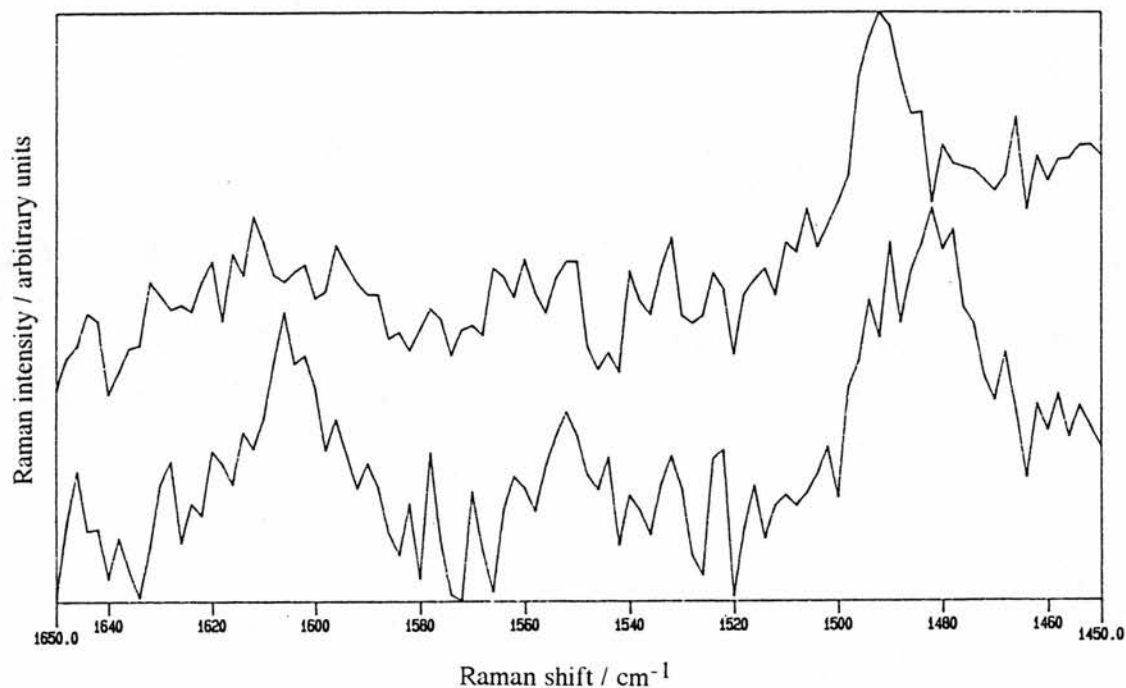


Figure 3.10: SERS of $[PVP-Os(bpy)_2Cl]^{n+}$ at a roughened Au electrode. Laser line = 647.0 nm. Power \approx 50 - 100 mW. ca. 30 scans for each spectrum. Top; potential = +0.6 V vs Ag / AgCl, Os^{III}, $n = 2$; bottom; 0 V vs Ag / AgCl, Os^{II}, $n = 1$.

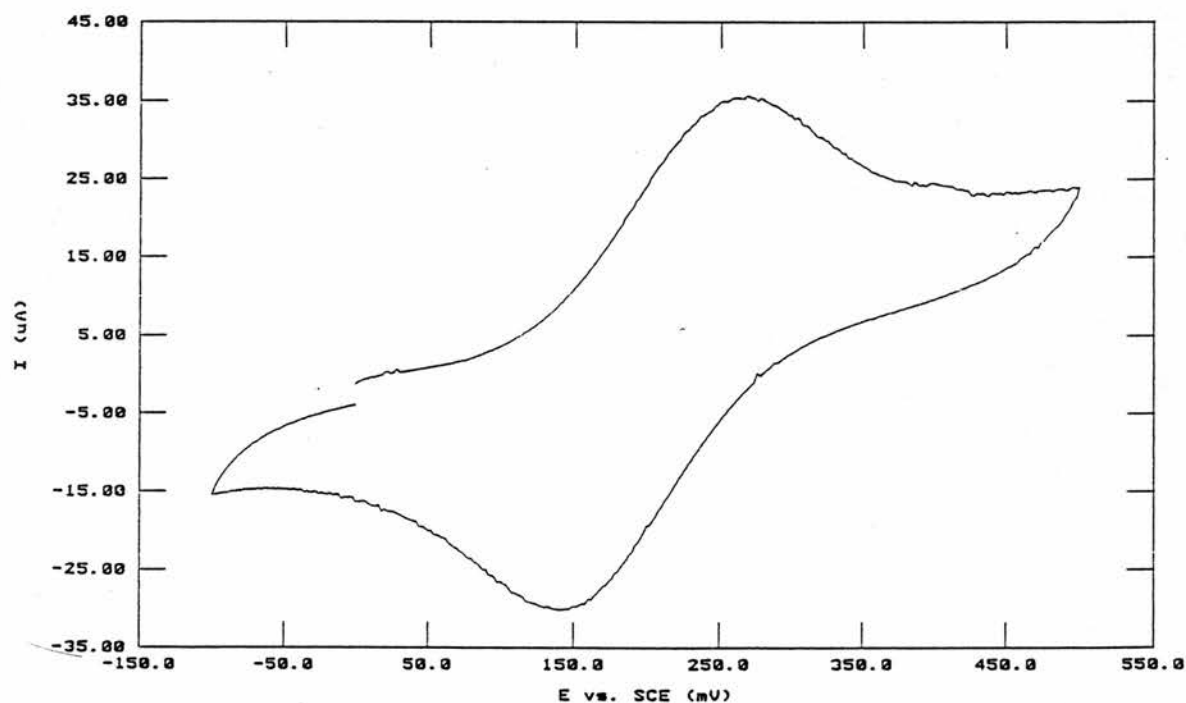


Figure 3.11: CV of the Os(II/III) oxidation of $[PVP-Os(bpy)_2Cl]^{n+}$ at gold. Conditions: Scan rate = 100 mV s⁻¹, SCE reference electrode, Pt wire counter electrode, electrolyte = 0.1 mol dm⁻³ LiClO₄ (aq). Surface concentration of Os = 180 nmol cm⁻² from 5 μ l deposition.

$\text{Os}(\text{bpy})_3^{2+}$	$[\text{PVP-Os}(\text{bpy})_2\text{Cl}]^+$	$\text{Os}(\text{bpy})_3^{3+}$	$[\text{PVP-Os}(\text{bpy})_2\text{Cl}]^{2+}$
1489	1482	1502	1492
1557	1552	1567	1560
1610	1606	1610	1612

Table 3.4: Position of aryl C=C stretching modes in RR and SERRS of Os(II/III) bipyridyl complexes. The values for $\text{Os}(\text{bpy})_3^{n+}$ are from Gaudiello et al.¹¹

3.4 Discussion

3.4.1 4-vinyl pyridine

The first issue to be considered for the SERS spectra of 4VP is whether one can determine the orientation of SERS active molecules at the surface. The evidence from the ring breathing region in Figures 3.4, where the ν_1 totally symmetric mode is still one of the strongest in the spectrum at all potentials (even though the intensity of the spectrum as a whole is much less at 0 V), suggests that the adsorption is similar to that of pyridine and that the major bands in this region can be assigned to physisorbed species (see Fig. 2.1). No experiments were done under the conditions where one might expect the 4VP equivalent of the 1025 cm^{-1} band of pyridine to appear (i.e. 0 V immediately after an ORC and with no cathodic excursion beyond -0.2 V).

Having invoked the similarity between the spectra of unsubstituted and 4-vinyl substituted pyridines as evidence of similar adsorption, it must also be noted that there are important differences. The strong 1002 cm^{-1} band in 4VP, is not actually the most intense in the SER spectra; instead the 1211 cm^{-1} band and, at below -0.6 V, the 1506 cm^{-1} band are more intense. Comparison of the relative intensities of the three bands between 1450 cm^{-1} - 1650 cm^{-1} with those of Tashiro *et al.*,²³ suggest that significant electropolymerization to PVP takes place at negative potentials. Any 4VP present as polymer, may be less rigidly orientated at the electrode surface, and so this may lead to the small changes in relative intensities

observed. Also, the relative intensity of the 1632 cm^{-1} vinyl C=C stretch might be expected to decrease as the concentration of these double bonds drops.

It was suggested that a free-radical mechanism was responsible for the electropolymerization of 4VP at silver, initiated by the electroreduction of H^+ to H^\bullet .²³ The propagation step involves reaction of this with 4VP to produce alkyl radicals, which in turn propagate along the chain to form PVP, as shown in Figure 3.12.

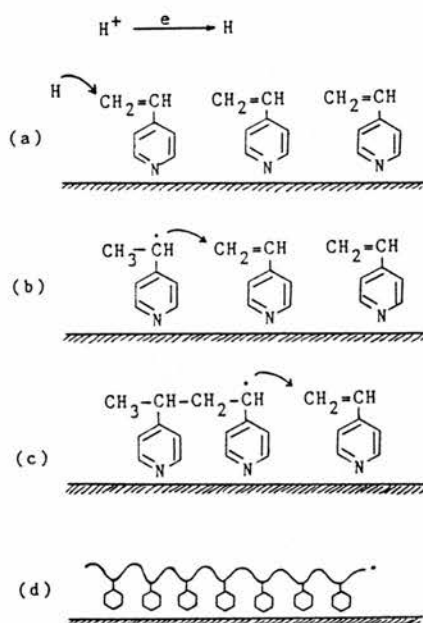


Figure 3.12: Scheme for the electropolymerization of 4-vinyl pyridine, as envisioned in ref. 23

The appearance of new bands at 1592 cm^{-1} and 905 cm^{-1} are also consistent with polymerization. The first mode is close to the ν_{8a} mode at 1604 cm^{-1} , and the evidence for a new band is a substantial shift in the peak maximum, to 1595 cm^{-1} , at -0.6 V and lower. Tashiro *et al*²³ attributed these new bands, as well as the 674 cm^{-1} band, to peroxide and superoxide species generated by termination steps involving O_2 , which is itself a diradical. The presence of O_2 , however, does not prevent the polymerization reaction from proceeding.²³

The behaviour of the 1211 cm^{-1} band, which shifts from 1203 cm^{-1} at 0 V , is also interesting, since at -0.3 V two bands are distinguishable at 1213 cm^{-1} and 1204 cm^{-1} , and the band which is less intense at any potential is always observed as a shoulder. Tashiro *et al*²³

attribute this change to PVP formation, suggesting that the ν_{9a} band of 4VP is gradually replaced by the equivalent PVP mode at 1218 cm^{-1} . This is supported by a similar assignment for a band at 1219 cm^{-1} by Roth and Boerio,²⁷ but in both this study and in one by Garrell and Beer²⁸ the band is observed at a wavenumber shift that is about 10 cm^{-1} lower. The similarity in behaviour and occurrence of this band to those at 905 cm^{-1} and 1592 cm^{-1} in 4VP, PVP and [PVP-Ru(bpy)₂Cl]Cl (Figure 3.13) in this study, however, leads to the conclusion that this band is also connected with the presence of O₂ radicals. In contrast, the 674 cm^{-1} band of Tashiro *et al*, seen here at 667 cm^{-1} , has been assigned to the ν_{6b} mode, in accordance with the two PVP studies.^{27,28}

There is a slight difference in the behaviour of the three peroxide / superoxide assigned bands as a function of potential: the 1592 cm^{-1} and 1213 cm^{-1} bands increase monotonically as the potential becomes more negative, whereas the 905 cm^{-1} band shows more complicated behaviour. The influence of electrode history is probably important in this case, as the spectra were acquired in the order -0.8 V , -0.6 V , 0 V , -0.3 V , with no further roughening cycles or cleaning between acquisitions. The radical reactions creating these bands proceed more rapidly at more negative potentials, and so all three bands are strong at -0.8 V . The loss of intensity of the 1592 cm^{-1} and 1213 cm^{-1} is quite rapid on going from -0.6 V to 0 V , suggesting that these species freely desorb; behaviour that would not be expected of a polymer of sufficient molecular weight. The 905 cm^{-1} band, however, disappears more slowly, and may be assigned to a more strongly adsorbed species.

On the basis of the above discussion the bands may be assigned to the following stretching modes: peroxide O-O (905 cm^{-1}), the C-O of a C-O-O species (1211 cm^{-1}), and an RCO₂⁻ species (1592 cm^{-1}). The intensities of the latter two would be dependent on the orientation of these species with respect to the Ag electrode, including any adsorption effects. The O-O stretch could come from either the C-O-O bonded species or from Ag bound peroxide. Direct binding of O₂²⁻ to Ag would explain the greater persistence of the 905 cm^{-1} band and the Raman shift is also more consistent with a metal bound peroxide species, which may occur anywhere between 750 cm^{-1} and 950 cm^{-1} .²⁹

Although the frequency of the 1592 cm^{-1} band is consistent with a carboxylate, such

bands are expected to be of only weak to medium intensity in the Raman spectrum. However, for SERS active species that adsorb at silver, such as benzoic acid and pyridine 4-carboxylic acid (isonicotinic acid), the bands are observed to be quite intense.³⁰ The species containing a C-O-O bond could be an intermediate in the formation of this final carboxylate. The formation of carboxylates under these circumstances arises from photochemical rather than free-radical processes.³¹ The exact nature of the species, however, will not be speculated on any further.

3.4.2 PVP

Given that there is evidence for PVP formation in the SER spectra of 4VP at negative potentials, comparison of 4VP and PVP spectra should be informative. Comparing the values for both in Table 3.2 and in Figures 3.4 and 3.5, it can be seen that there are significant differences between the two sets of results, both in band positions and intensities, although 4VP spectra at -0.6 V and -0.8 V resemble those of PVP more than spectra acquired at more positive potentials do. It is possible that mainly short chains are formed in the 4VP termination steps, some of which involve oxygen, and that these are able to desorb from the electrode and equilibrate with the solution when the electrode potential is taken more positive.

Bands that are observed in similar positions at -0.6 V for both 4VP and the $M_n = 3000$ polymer are those attributed to peroxide reactions at 905 cm^{-1} , 1210 cm^{-1} and 1597 cm^{-1} . It seems here that the PVP is susceptible to further electropolymerization at the Ag surface. Assuming H^\bullet radicals are formed, the initial reaction stage in this instance would probably be the reaction of this with the AIBN fragment $\text{C}(\text{CH}_3)_2\text{CN}$, present as an end-group in the polymer. In turn, the formation of radicals on one of the monomer units of PVP would occur leaving the polymer susceptible to the same termination reactions with O_2 that are observed in 4VP, and thus the same bands would be expected to appear.

On the other hand, the higher molecular weight commercial PVP sample (M_n estimated at 50000 Daltons³²), does not show the three intense bands assigned to O_2 . Because of the much longer chain length, there will be many fewer end-groups, and therefore there is much less scope for any propagation reaction to occur. Any free-radical reaction is therefore much

less vigorous and O₂ has less opportunity to become involved in termination steps.

The adsorption of the polymer at the surface, both for neutral and protonated states, has been found to be complicated by restrictions in the polymer geometry, for instance, the ability of the chains to penetrate into concave surface features²⁸ and the flexibility of the chains during solvent evaporation from the modified layer, which is dependent on the concentration of solution from which the layer is deposited.³³ The spectrum in Figure 3.5 was obtained after deposition from a semi-dilute solution ($\approx 1\%$ w/w) using the terminology of Xue.³³ This means that coil shrinking, and therefore strong adsorption of pyridine-rings to the surface, is not expected to occur and a relatively weak SERS spectrum should result. When considering that deposition was from MeOH in these experiments and from DMF in Xue's work, then one would expect faster evaporation from MeOH, giving even less opportunity for the polymer to re-orientate in these experiments. Despite all these factors, adequate SERS spectra are obtained; although, in cases where spectra are comparable, PVP gives a far weaker signal than does pyridine itself.

3.4.3 [PVP-M(bpy)₂Cl]Cl (M = Ru or Os)

Appearance of Bands Assigned to Oxidized Polymer

When the polymer with $M_n = 3000$ is used to synthesize ruthenium metallopolymer the bands attributed to peroxide species at 905 cm⁻¹ and 1215 cm⁻¹ are clearly visible, even though the metallopolymer bipyridyl bands are strongly resonance enhanced. The 1597 cm⁻¹ is hidden underneath the intense 1603 cm⁻¹ band of the metallopolymer, but can be observed as a slight asymmetry in this band in Fig. 3.8(c). The reactivity of the polymer backbone when the short chain polymer is used provides a possible source of complication if it is to be used as a model complex for the description of polymer SE(R)RS, and so subsequent studies used the metallopolymers synthesized with higher molecular-weight commercial PVP, except where noted otherwise.

Spectra at Ag Electrodes

Figure 3.6 and Table 3.3 give direct comparisons between the data obtained in this study and previously published results for $\text{Ru}(\text{bpy})_3^{2+}$ and $\text{Os}(\text{bpy})_3^{2+}$, both from SERRS and RRS experiments. All the spectra are very similar, being dominated by bands assigned to bipyridine vibrational modes. Certain of these bands shift by a few cm^{-1} on replacing Ru for Os, as indicated in Table 3.3, but these changes are relatively minor. There is also a marked similarity, both in band positions and relative intensities, between RR spectra and SERR spectra. This has been previously commented on by Dines and Peacock,¹² and is explained by weak adsorption of the tris(bipyridyls) on the surface. This means that little orientation of the metal complex takes place at the surface, and therefore no specific modes are enhanced because they have the correct symmetry at the electrode to interact effectively with surface plasmons.

For the PVP metallopolymers, the band wavelengths and relative intensities are also very similar and, therefore, the same basic conclusions can be drawn. A few minor differences can be observed between Figure 3.6(a) and (c), for instance, the slightly higher relative intensities of the 1554 cm^{-1} and 1600 cm^{-1} bands and the lesser intensity of the 1034 cm^{-1} (which becomes a shoulder of the 1020 cm^{-1} band) in the PVP complex. Little change in the spectrum is seen due to symmetry lowering in the complex.

Potential and wavelength variation also result in only small changes in the relative intensities and band positions. Potential dependent changes in Figure 3.8 can be attributed almost entirely to the presence of peroxide. Of the bipyridine assigned bands that at 1034 cm^{-1} shows the most variation, being stronger at potentials close to 0 V. The lack of potential dependence has also been observed by Chambers and Buck,² who tracked the SERRS intensity of several bands as a function of potential and found that their PVP metallopolymer gave a particularly invariant response, when compared to other ruthenium bipyridyls, including the monomer analogue, $[\text{Ru}(\text{bpy})(\text{py})_4]^{2+}$. This is explained by the insolubility of the polymer in water, which prevents total desorption of Ru centres from the silver surface. The argument is equally applicable here.

The spectra of the Ru metallopolymer at different wavelengths could be expected to change for two reasons, the difference in resonance enhancement between the wavelengths and

the difference in self-absorption (i.e. UV-visible absorption) of both incident and Raman scattered radiation. The quantitative aspects of both of these are considered in detail in chapter 4, but a few qualitative points are appropriate here. Firstly, the effect of both factors is expected to affect band intensities rather than positions, since neither affects the structure of the adsorbate (contrast this with surface-enhancement, where structural changes may occur on adsorption). At all the wavelengths studied resonance will be with the 497 nm metallopolymer band, assigned to the triplet MLCT band, and so enhancement will be of modes associated with this adsorption. Thus, once more, the relative intensities of bands are expected to change little, though the absolute intensities of the SERR spectra should vary according to how close the exciting wavelength is to the UV-visible maximum. The relative intensities are found to change little, and even the 457.9 nm spectrum is closer in features to non-resonant metal bipyridyl spectra such as those displayed by Cr(III) bipyridyls (chapter 6) or that of Ru(bpy)₃²⁺ at 647.1 nm.³⁴ Note that the resonance-enhancement of Os and Ru bipyridyls is expected to be quite similar ([PVP-Os(bpy)₂Cl]Cl has $\lambda_{\text{max}} = 486 \text{ nm}$, $\epsilon = 11000 \text{ dm}^3 \text{ mol}^{-1} \text{ cm}^{-1}$,¹⁷ compared to values of 497 nm and 8500 dm³ mol⁻¹ cm⁻¹ for Ru).

[PVP-Ru(bpy)₂Cl]Cl at the Cu Electrode

The spectrum in Figure 3.7 was taken at 514.5 nm excitation, under conditions where copper is not surface-enhancing,²² and the electrode was not roughened. However, the excitation wavelength is still fairly close to the absorption maximum of the adsorbate, and so under these conditions a SURRS spectrum (which is essentially just a resonance Raman spectrum of a surface adsorbed molecule) is recorded. The original aim of this study was to quantify the intensity vs surface concentration of Ru responses under conditions where there was no surface-enhancement, but this proved impossible as obtaining a signal from the system required several scans, adsorption of the polymer at the unroughened electrode was poor, and the use of powers higher than *ca.* 50 mW led to a blackening of the electrode surface, presumably because of graphitization. As a consequence the SURRS response was unreliable. Reasonable adsorption could be achieved, however, by allowing the polymer to dry on the electrode, at room temperature, for at least 3 days. The spectrum displayed in Figure 3.7

represents the summation of 12 scans from two such adsorptions. The bands observed for this system are the same as the strong bands seen in the spectrum at Ag. Chambers and Buck observed SERS at Cu with 595 nm excitation,³ and saw the splitting of the 1555 cm^{-1} vibration into two bands at 1547 cm^{-1} and 1557 cm^{-1} . In Figure 3.7 the spectrum is too weak to say definitively whether this occurs, but there is a distinct possibility that bands other than the 1556 cm^{-1} maximum are present.

Studies on the Os(II/III) Couple at Gold

Once more, the spectra obtained in these studies are far weaker than those obtained at roughened gold electrodes. Compared with copper, the excitation at 647.0 nm is not in resonance with any UV-visible absorbance band, but does support surface-enhancement at the roughened gold electrode: the scattering process is SERS. The comparison between data from Figure 3.10 and literature results, given in Table 3.4, show reasonable agreement between the two data sets; however, because of the weakness of the bands at *ca.* 1555 cm^{-1} and 1610 cm^{-1} , especially at +0.6 V, there is some degree of error. The clearest indication of the potential dependent oxidation is the shift in the most intense band from 1482 cm^{-1} to 1492 cm^{-1} on oxidation. Note that there is some intensity at around 1492 cm^{-1} even at 0 V. This is because some of the spectra used in Figure 3.10(b) were acquired after excursions to +0.6 V and the reduction back to Os(II) may be incomplete.

3.5 Conclusions

The surface Raman data from 4 vinyl-pyridine, PVP and [PVP-M(bpy)₂Cl]Cl (M = Ru and Os) have been considered. 4VP and PVP spectra show considerable potential dependence, and at negative potentials, any free double bonds present are susceptible to electropolymerization. Significant bands appear as a result of this due to the production of peroxide type species from dissolved oxygen. These are not observed when commercial PVP (which has a relatively high molecular weight and, therefore, a low concentration of double bonds) is used. The bipyridine assigned bands of the metallopolymer are qualitatively unaffected by potential and excitation

wavelength, and are very similar to those recorded for tris(bipyridyls). Small changes in the position of bands are observed on substituting Os for Ru and on change of oxidation state between Os^{II} and Os^{III}, however.

3.6 References

- 1 J. A. Chambers and R. P. Buck, *J. Electroanal. Chem.*, 1982, **140**, 173.
- 2 J. A. Chambers and R. P. Buck, *J. Electroanal. Chem.*, 1984, **163**, 297.
- 3 J. A. Chambers and R. P. Buck, *J. Raman Spec.*, 1984, **15**, 160.
- 4 A. Juris, V. Balzani, F. Barigelleti, S. Campagna, P. Belser and A. von Zelewsky, *Coord. Chem. Revs.*, 1988, **84**, 85.
- 5 E. Krausz and J. Ferguson, *Prog. Inorg. Chem.*, 1989, **37**, 293.
- 6 L. A. Worl, G. F. Strouse, J. N. Younathan, S. M. Baxter and T. J. Meyer, *J. Am. Chem. Soc.*, 1990, **112**, 7571.
- 7 P. G. Bradley, N. Kress, B. A. Hornberger, R. F. Dallinger and W. H. Woodruff, *J. Am. Chem. Soc.*, 1981, **103**, 7441.
- 8 H. R. Virdee and R. E. Hester, *J. Phys. Chem.*, 1984, **88**, 451.
- 9 D. P. Strommen, P. K. Mallick, G. D. Danzer, R. S. Lumpkin and J. R. Kincaid, *J. Phys. Chem.*, 1990, **94**, 1357.
- 10 G. D. Danzer and J. R. Kincaid, *J. Phys. Chem.*, 1990, **94**, 3976.
- 11 J. G. Gaudiello, P. G. Bradley, K. A. Norton, W. H. Woodruff and A. J. Bard, *Inorg. Chem.*, 1984, **23**, 3.
- 12 T. J. Dines and R. D. Peacock, *J. Chem. Soc., Faraday Trans. I*, 1988, **84**, 3445.
- 13 J. M. Clear, J. M. Kelly, C. M. O'Connell and J. G. Vos, *J. Chem. Res. (M)*, 1981, 3039.
- 14 A. I. Vogel, *Textbook of Practical Organic Chemistry*, Longman, London, 1978.
- 15 G. Spritschnick, H. W. Spritschnick, P. P. Kirsch and D. G. Whitten, *J. Am. Chem. Soc.*, 1977, **99**, 4947.

- 16 D. A. Buckingham, F. P. Dwyer, H. A. Goodwin and A. M. Sargeson, *Aust. J. Chem.*, 1964, **17**, 325.
- 17 R. J. Forster and J. G. Vos, *Macromolecules*, 1990, **23**, 4372.
- 18 A. Katchalsky, K. Rosenheck and B. Altmann, *J. Polym. Sci.*, 1957, **23**, 795.
- 19 J. M. Calvert and T. J. Meyer, *Inorg. Chem.*, 1981, **20**, 27.
- 20 D. Ghesquiere, B. Ban and C. Chachaty, *Macromolecules*, 1979, **10**, 743.
- 21 D. Leech, R. J. Forster, M. R. Smyth and J. G. Vos, *J. Mater. Chem.*, 1991, **1**, 629.
- 22 B. Chase and B. Parkinson, *J. Phys. Chem.*, 1991, **95**, 7810.
- 23 K. Tashiro, K. Matsushima and M. Kobayashi, *J. Phys. Chem.*, 1990, **94**, 3197.
- 24 B. Pettinger, *Chem. Phys. Lett.*, 1981, **78**, 404.
- 25 C. M. Lindall, J. A. Crayston, D. J. Cole-Hamilton, A. Glidle and R. D. Peacock, in preparation.
- 26 J. V. Caspar, T. D. Westmoreland, G. H. Allen, P. G. Bradley, T. J. Meyer and W. H. Woodruff, *J. Am. Chem. Soc.*, 1984, **106**, 3492.
- 27 P. G. Roth and F. J. Boerio, *J. Polym. Sci. B: Polym. Phys.*, 1987, **25**, 1923.
- 28 R. L. Garrell and K. D. Beer, *Langmuir*, 1989, **5**, 452.
- 29 S. Ahmad, J. D. McCallum, A. K. Shiemke, E. H. Appelman, T. M. Loehr and J. Sanders-Loehr, *Inorg. Chem.*, 1988, **27**, 2230.
- 30 A. Pal, D. L. Stokes, J. P. Alarie and T. Vo-Dinh, *Anal. Chem.*, 1995, **67**, 3154.
- 31 R. Hiatt, in *Organic Peroxides Vol. 3*, D. Swern ed., John Wiley & Sons, New York, 1972.
- 32 S. M. Oh and L. R. Faulkner, *J. Electroanal. Chem.*, 1989, **269**, 77.
- 33 G. Xue, *Polym. Bull.*, 1994, **33**, 229.
- 34 A. M. Stacy and R. P. van Duyne, *Chem. Phys. Lett.*, 1983, **102**, 365.

Chapter 4

Quantitative Studies of the SE(R)RS Intensities at PMEs

4.1 Introduction

In this section SE(R)RS studies in which attempts have been made to quantify the response of band intensity as a function of other parameters will be briefly reviewed. The two most commonly considered parameters are excitation wavelength (the resultant plot from which is called an excitation profile), and concentration of adsorbate, expressed either in terms of solution concentration or of surface concentration. At electrodes, determination of the intensity of a band as a function of potential can be done over the timescale of a slow cyclic voltammogram. On a scanning instrument the spectrometer is held at one potential and operated in time-drive mode, as demonstrated for pyridine by Marinyuk.¹ Alternatively, an optical multichannel analyzer (OMA) can be used to monitor the development of a whole region of the Raman spectrum as a function of time, as was done² for adsorbed water modes during roughening in 1 mol dm⁻³ KBr(aq) and for pyridine and other amines.³

Of course, the time-dependence of SERS spectra can be an informative tool even if electrochemical control is not used. Instances of its use in the pyridine system include monitoring of photodegradation of surface species and enhancement sites⁴ and the slow equilibration of adsorbates onto surface sites after *ex-situ* roughening cycles,⁵ both of which have provided evidence for the assignment of the pyridine 1025 cm⁻¹ band to the ν_{12} mode of an anion-assisted chemisorbed species. Time-dependent methods are relatively straightforward, since all the data can be acquired in a single acquisition and, as a result, there is no need to change either the sample or the experimental set-up and little chance of optical misalignment. Also, for the electrochemical experiments the potential is a parameter defined by the potentiostat and is therefore easily measured. Experiments to determine excitation or concentration profiles, on the other hand, are not so simple, since several acquisitions need to be done, either at different wavelengths or with different samples, and so care needs to be taken to ensure Raman

intensities are directly comparable. Moreover, X-axis parameters such as surface concentration may need the use of independent techniques in order that they can be determined. The next section will consider some of the approaches that have been used to obtain parameters for various Raman intensity plots, before the results of such studies are considered.

4.1.1 Determination of Parameters in Quantitative Raman Studies

Excitation Profiles

A detailed example of one method by which RR and SERRS excitation profiles can be obtained from solutions and Langmuir-Blodgett monolayers, respectively, of S-120 dye is given by Kim *et al.*⁶ Corrections are made for differences in laser power and slitwidth, and the effect on instrument throughput of changing the laser line was gauged for the RR profile by referencing the spectra to a Raman band assigned to the methanol solvent used. The study also describes experiments to determine the absolute values of surface-enhancement factors (SEFs) from comparison of the SERRS and RR intensities, as given by:

$$\text{SEF} = \frac{I_{\text{SERRS}} / N_{\text{Ag}}}{I_{\text{RR}} / N_{\text{soln}}}$$

Equation 4.1

In the above, I represents Raman intensity and N the number of molecules sampled in each case. N, in the resonance Raman case, is determined by estimating the penetration of the laser beam through a given solution of the dye, and is controlled during SERRS of the Langmuir-Blodgett film by mixing the dye with an inert matrix molecule in appropriate proportions.

Concentration-Intensity Relationships

The earliest studies of the effect of adsorption on the Raman signal were done in an attempt to determine the mechanisms involved. These were *ex-situ* studies under UHV conditions that allowed separation of the effect of monolayer and multilayer adsorption in the pyridine system,

thus allowing estimates to be made for the range of the classical EM enhancement mechanism.⁷⁻¹⁰ UHV allows for accurate determination of surface coverage by, for example, Auger electron spectroscopy or quartz-crystal microbalance methods.

The main *in-situ* studies of pyridine have been carried out by Lipkowski, Irish and co-workers at Au electrodes.^{11,12} They compared the results of adsorption studies from chronocoulometry and radiochemistry,¹² and found that, whilst the former gives better accuracy, the radiochemical response of ¹⁴C-pyridine is less affected by the non-ideality (i.e. roughening) of electrode surfaces. A chronocoulometric method was also used in the study of 2-amino 5-nitro pyridine adsorption.¹³

Studies have also been done on resonance-enhanced adsorbates. Kim *et al.*,⁶ as mentioned above, used Langmuir-Blodgett films specifically in order to control surface concentration. Hildebrandt and Stockberger¹⁴ were able to estimate the adsorption of Rhodamine-6G at Ag sols by measuring their fluorescence, given that one of the consequences of adsorption at an enhancing surface is fluorescence quenching.

In the SERRS spectroscopy of solution species at electrodes, the contribution of solution RR scattering is significant. A number of studies have been done on separating the contributions of surface and solution scattering for methyl viologen radical cation, as detailed in Feng *et al.*¹⁵ These workers attributed the Raman response in a linear region of their plot of solution concentration of MV²⁺ vs intensity (Figure 4.2), which occurred at high concentration, to RR scattering, and so estimated the RR contribution as proportional to the solution concentration with gradient equal to that of the linear region.

4.1.2 Results from SERS Quantification Studies

Excitation profiles of RR and SE(R)RS experiments are closely related to UV-visible absorption spectra, as described by Equation 4.1. Surface-enhancement, however, does complicate the relationship to an extent. For SERS without resonance, the enhancement-factors are related to the surface plasmon resonance of the metal involved and charge-transfer interactions, which in turn do bear some relation to the UV-visible absorption of metal colloid

particles. When both surface and resonance-enhancement occur together in SERRS, then the surface plasmon and adsorbate absorptions can interact to give a different UV-visible spectrum and, therefore, a different excitation profile from either of the components when considered separately.

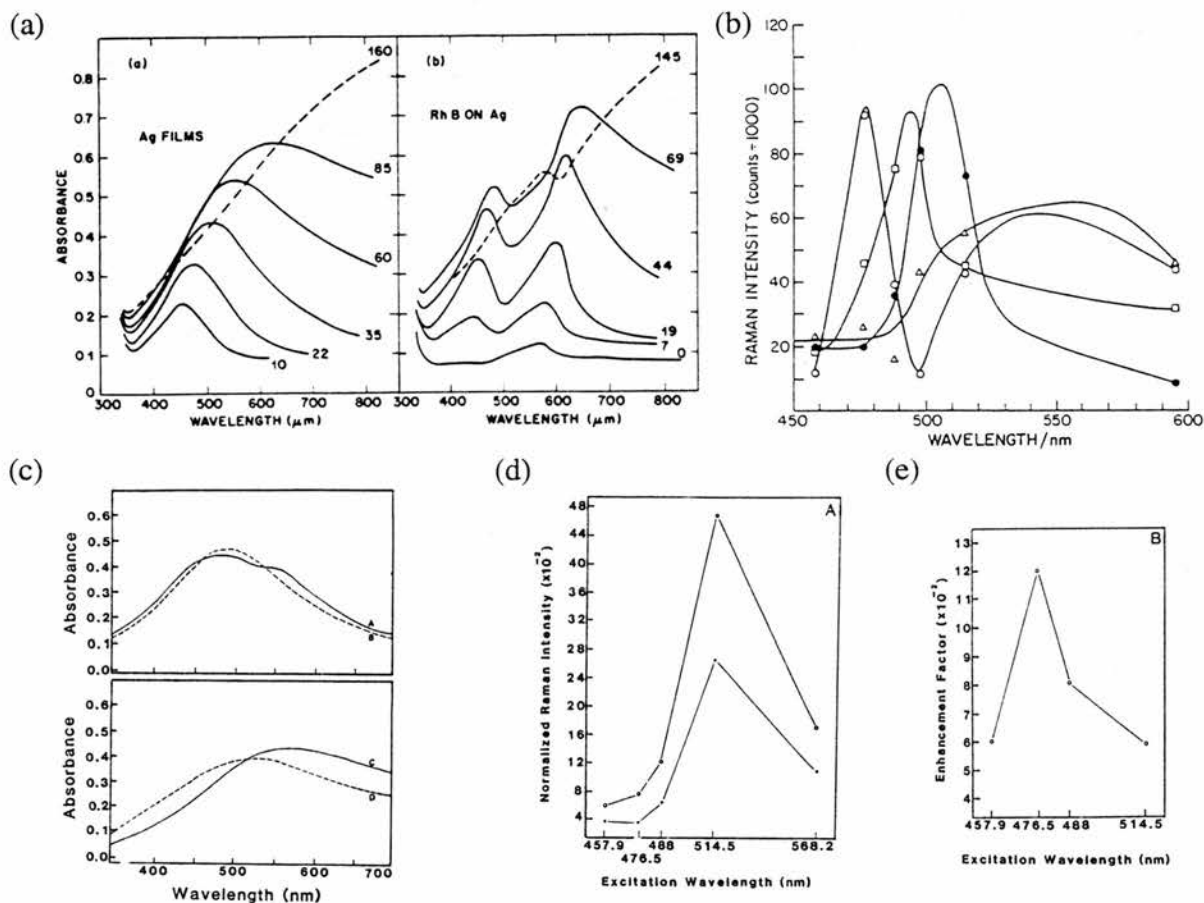


Figure 4.1: Examples of excitation profiles from RR, SERS and SERRS systems: (a) (from ref. 16) Visible absorbance spectra of Ag films alone (left) and with a constant thickness overlayer of Rhodamine B (right). Numbers denote thickness in Å of Ag; (b) (from ref. 17) Surface excitation profiles for bands of (from top to bottom at 590 nm) 2,2'-bipyridine, $Ru(py)_6^{2+}$, $Ru(bpy)(py)_4^{2+}$ and " $[(PVP)_4-Ru(bpy)]^{2+}$ "; (c)-(e) from ref. 6 for L-B films of S120 dye on thin Ag films; (c) Visible absorbance spectra of two preparations of Ag alone (dotted) and Ag-dye monolayer (solid); (d) Excitation profile and; (e) Surface enhancement factor vs wavelength.

Figure 4.1 shows a number of literature excitation profiles and UV-visible spectra that demonstrate some of the points made above. Figure 1(a) shows the visible absorption of Rhodamine-B on silver-island films^{16,18} demonstrating a splitting of bands that occurs when dye and plasmon resonances closely coincide. Theoretical studies also predict that the excitation profiles should show splitting in similar cases;¹⁹ however, because the wavelength resolution of these profiles is limited by the number of laser lines available, such behaviour has not been demonstrated.

Figure 4.1(b) shows a SERRS excitation profile from a study by Chambers and Buck¹⁷ on a number of adsorbates including their version of a PVP-Ru(bpy) metallopolymer. The excitation maximum at around 506 nm shows a substantial shift from the solution UV-visible maximum of the metallopolymer at 468 nm.

Figures 4.1(c-e) allow a comparison between various different plots for the Langmuir-Blodgett system of Kim *et al.*⁶ None of the three maxima (for UV-visible absorption, excitation profile, and SEFs of the Ag-dye layer) coincide with one another. Aggregation of the dye is cited as a reason for the difference between the UV-visible spectra and excitation profiles, but here the main point is that though the results of these two plots are related, they can differ from one another. The substantial fall in surface-enhancement factor at 514.5 nm can be contrasted with the UV-visible spectra of the bare Ag layer which maximizes close to this wavelength. Here the effect of the adsorbate on surface-enhancement is clearly seen, the absorbance of the dye layer interfering with the surface plasmon resonance. The effect is that the theoretical enhancement given by SERRS is rather lower than the value given by multiplying the separate theoretical SERS and theoretical RR enhancements. At very low concentrations (1 pmol dm⁻³ of adsorbate in Ag sols) it has been claimed that this damping of the surface plasmon is not observed,²⁰ and an experimental and theoretical study for cobalt phthalocyanine has confirmed this, concluding that damping at higher concentrations is consistent with the effect of either surface-adsorbate or adsorbate-adsorbate interactions.¹⁹

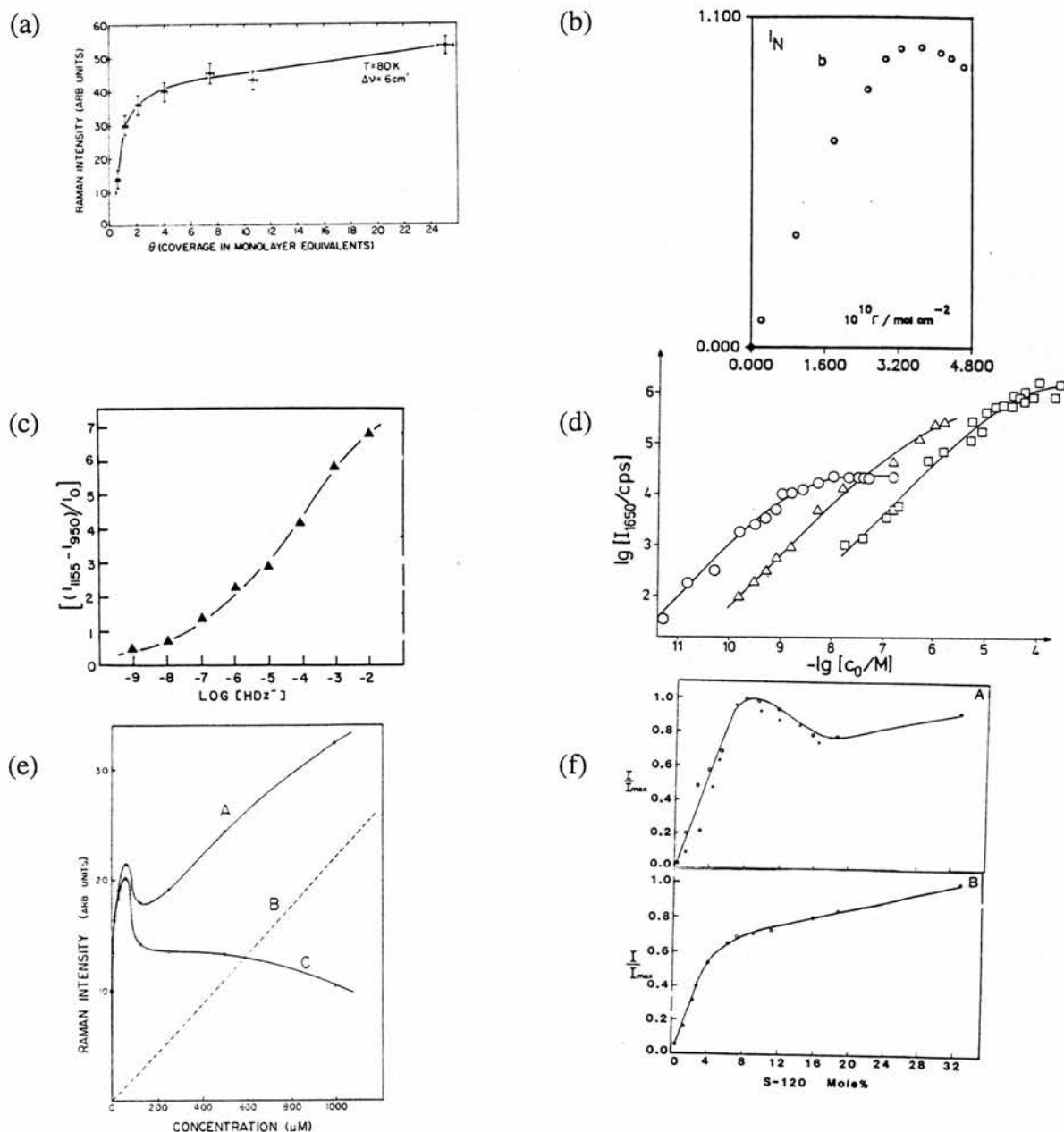


Figure 4.2: Concentration-Intensity plots from literature studies. (a) (ref. 7) I vs surface coverage for UHV study of pyridine at Ag film; (b) (ref. 11) I vs chronocoulometric surface coverage obtained by varying potential of pyridine in-situ at Au electrode; (c) (ref. 21) Normalized I vs log solution concentration for diphenylthiocarbazone at Ag electrode; (d) (ref. 14) $\text{Log } I$ vs log solution concentration of R6G at Ag sol. Different plots represent different anions, squares = no anion; (e) (ref. 15) SERRS intensity of MV^+ vs solution concentration of MV^{2+} . A, B and C denote measured intensity, estimated RR contribution, and estimated SERRS contribution (A - B) respectively; (f) (ref. 6) I vs surface coverage of dye (mole% in L-B film). Top = 1 scan, bottom = 30 scans and takes into account effect of photodecomposition.

In Figure 4.2 various examples of concentration vs intensity plots are given. These can be divided into two main categories: those where the signal is observed to maximize at sub-monolayer coverage (b, e, f) and those where intensity increases with increasing concentration over the whole range studied (a, c, d). Figure 4.2 (a) and (b) show two different responses for pyridine, (a) showing a monotonic increase for the first monolayer and then smaller increases for subsequent layers that demonstrate the long range EM enhancement and (b) showing a maximum signal for a coverage of around two-thirds of an monolayer which is more or less independent of solution concentration.

Figures 4.2 (c) and (d) show two more examples of plots where Raman intensity increases to quite high solution concentrations, where as (e) and (f) demonstrate maxima at low concentrations, although in (f) decomposition of the sample when the SERRS enhancement is greatest means that no maximum is observed unless spectra are acquired immediately upon illumination. A number of factors have been used to explain non-linearity including the saturation of surface active sites at sub-monolayer coverage, increasing dipole-dipole interactions as a function of surface concentration, differing aspect ratios and coupling interactions between films and sols, and the proximity of the excitation to resonance and the effect of resonance enhanced molecules to damp the surface plasmon (as discussed above) in SERRS studies. Many of these are covered in more detail by Kim *et al.*⁶ The effect of different experimental designs and methods of estimation on the apparant response is also crucially important, as evidenced by Figure 4.2 (a) and (b). However, no unifying theory has yet been developed to embrace the effects observed in all these different studies.

4.1.4 Chapter Precis

In the rest of the chapter, various quantification studies on [PVP-Ru(bpy)₂Cl]Cl are described. The SERRS intensity of this polymer is considered as a function of excitation wavelength, PVP:Ru ratio (loading), and the mass of polymer deposited on the electrode for a given loading (coverage). Since a scanning instrument is used, the time-dependence of the SERRS signal is important and so is considered. The possible influence of a number of other experimental

factors is also discussed. Attempts are made to match the results with a mathematical treatment based on a Freundlich isotherm. The experimental procedures used are critically appraised and improvements suggested. The potential advantages and inherent limitations of the SE(R)RS technique in the determination of PME structure are discussed, and a possible extension of this work to the determination of parameters for the diffusion of SERRS active ions into PMEs is considered.

4.2 Experimental and Theory

4.2.1 Quantification of [PVP-Ru(bpy)₂Cl]Cl Signal

The Raman spectrometer, potentiostats and instrumentation are as described in chapter 2. The synthesis of the metallopolymers and the basic methods of roughening and polymer deposition are as described in chapter 3. The sections below describe the efforts that have been made to maximize the reproducibility of the data detailed in this chapter.

Roughening

The response of home-made reference electrodes was monitored carefully as they had a tendency to drift by a few mV, as evidenced by the potential of onset of the Ag → AgCl roughening reaction. Cycles were rejected if the charge passed on each was less than 3.5 mC or greater than 4 mC (*i.e.* 28 - 32 mC cm⁻²) and the polishing and roughening procedure recommenced.

Polymer Deposition

A minimum of 5 minutes was allowed for the solvent to dry in quantification experiments.

Time Dependent Scans

Laser focussing was optimized on the bare electrode before roughening in the dark, and commencing with the procedure. The polymer depositions used were: "3:1" polymer; mass =

$5.95 \mu\text{g cm}^{-2}$, $\Gamma_{\text{Ru}} = 6.97 \text{ nmol cm}^{-2}$ and “100:1” polymer, mass = $5.82 \mu\text{g cm}^{-2}$, $\Gamma_{\text{Ru}} = 0.47 \text{ nmol cm}^{-2}$. After polymer deposition and drying the working electrode was screwed into the SERS cell containing electrolyte solution, the potentiostat connected, the laser block removed and the scan commenced. All this could be achieved within 20 seconds of initial immersion, and so $t = 0 \text{ s}$ on the time-dependent scans corresponds to $t < 20 \text{ s}$ in real terms. The errors expressed in Table 4.2 are twice the standard deviation divided by the root of the number of determinations.

Excitation Profile Scans

The excitation profile scans were carried out using a deposition of $2 \mu\text{l}$ of 0.320 g dm^{-3} solutions of the “10:1” metallopolymer, equivalent to a ruthenium loading (Γ_{Ru}) of $2.75 \text{ nmol cm}^{-2}$. After deposition and drying the polymer layer was immersed for 5 minutes under scan conditions, including illumination, before the spectrum was acquired. Scans were acquired from $100 - 1700 \text{ cm}^{-1}$ at $2 \text{ cm}^{-1} \text{ s}^{-1}$ and at $-0.6 \text{ V vs Ag / AgCl}$ with the following laser powers: 457.9 nm , 50 mW ; 488.0 nm , 80 mW ; 496.5 nm and 501.7 nm , 100 mW ; 514.5 nm , 130 mW . The optical alignment was checked between each change of laser wavelength by visual comparison of the scattered spot. Time scans were carried out to compare the deterioration of the 1485 cm^{-1} signal at each wavelength. The results quoted are corrected for differences in laser power and self-absorption, but not for the ν^4 wavelength dependence of normal Raman scattering. The latter exclusion is in line with the studies of Chambers and Buck,¹⁷ who note that this dependence has not been established for SERRS experiments.

Surface Coverage - Intensity Plots

Preparation and pre-immersion of each sample was carried out as for the excitation profile scans. Scans were typically performed between $1400 - 1700 \text{ cm}^{-1}$ at $2 \text{ cm}^{-1} \text{ s}^{-1}$. On most occasions, but not always, quoted values are the average of two or three concordant acquisitions for each sample, and the normalizing data point was always obtained in this way. A small number of experiments disagreed considerably from the values obtained, as detailed further in the discussion section, and such data were discarded.

The dependence on loading was carried out by depositing the same volume of solutions containing the same w/v concentrations of each metallopolymer. To access a broader range solutions were made up containing “10:1” metallopolymer and commercial PVP in varying proportions, but with the same w/v concentration of 0.416 g dm^{-3} . The “10:1” metallopolymer was chosen to enable comparison of results from samples diluted with the appropriate proportion of PVP with those from the “20:1” and “100:1” metallopolymer samples. The “3:1” sample was not used because it was considered that the substantially different solubility properties of this from pure PVP and other metallopolymer samples might cause partition of the PVP and metallopolymer components on deposition, leading to a highly inhomogeneous film.

The dependence on coverage was carried out by using the same metallopolymer sample to make up all the solutions, either by using different volumes of a single standard solution or by depositing a set volume of each of a set of serial dilutions.

The methods chosen mean that it is convenient for both loading and coverage dependence studies to obtain plots of SERRS intensity vs Γ_{Ru} .

Studies on the Effect of Electrolyte in [PVP-M(bpy)₂Cl]Cl

The procedure for these studies followed as closely as possible those of Clarke *et al.*,²² who estimated the polymer swelling of a 10:1 osmium metallopolymer by quartz-crystal microbalance studies for concentrations of HClO_4 between $1 \times 10^{-5} \text{ mol dm}^{-3}$ and 1 mol dm^{-3} . ORCs were carried out as normal in 0.1 mol dm^{-3} KCl electrolyte, before a solution of [PVP-M(bpy)₂Cl]Cl was deposited on the electrode. In the results section, spectra that are compared used deposition of equivalent amounts of the same metallopolymer sample. Two series of experiments were done, the first to gauge the effect of concentration over several decades of HClO_4 concentration, as in the Clarke study, the second to compare the signals given by 0.1 mol dm^{-3} aqueous solutions of KCl, LiClO_4 and NaNO_3 . KCl was also compared with HCl in this study to assess the effect of pH. All of the above experiments used standard ORC and deposition procedures.

CV Study on Photosubstitution of [PVP-Ru(bpy)₂Cl]Cl under Laser Illumination

These imitated conditions for the Raman quantification experiments as far as was possible, given the consideration that the Ru(II/III) couple of the metallopolymer, quoted at +0.64 V vs SCE²³ is out of the potential range of a silver working electrode. A standard electrochemical cell set-up of glassy carbon working, SCE reference and Pt wire counter electrode were used. Deposition, drying and transfer of the polymer to the Raman chamber were done under minimal lighting. The deposition was of 10 μl of a 0.356 g dm^{-3} solution of "3:1" metallopolymer, equivalent to $\Gamma_{\text{Ru}} = 59.0 \text{ nmol cm}^{-2}$ given the electrode area of 0.07 cm^2 . Illumination used 457.9 nm, 488.0 nm, and 514.5 nm laser lines, as discussed in the results section. Cycles were carried out between 0 V and +1.2 V vs SCE at 100 mV s^{-1} .

4.2.2 Mathematical Treatment of Data

Expression of Results

Except where stated, for SERS intensity versus Γ_{Ru} plots, the intensity is estimated as the summation of peak heights of the bands at *ca.* 1485 cm^{-1} , 1555 cm^{-1} and 1603 cm^{-1} , the background signal being subtracted out by taking an average of the value for the signal minima on each side of the peak. Corrections are made, where appropriate, for self-absorption, as discussed in the next section. The intensities are normalized relative to a determination for a reference sample, which was run on each occasion that quantitative studies were done. The references used were depositions of 2 μl of 0.36 - 0.37 g dm^{-3} of "20:1" metallopolymer solutions, equivalent to $\Gamma_{\text{Ru}} = 2.00 - 2.10 \text{ nmol cm}^{-2}$.

In the time dependence study, variation of the background signal was not monitored, and therefore the surface intensity vs time plots shown in Figure 4.3 just demonstrate the deterioration of the peak signal with no background correction.

Self-Absorption Estimates

Assuming that a large majority of scattered photons originate from the SERRS effect, a numerical value can be obtained for the transmission of the exciting wavelength radiation to the

surface and of the Raman scattered photon from the surface. In algebraic terms the transmission can be given by the usual rearrangement of Beer's law, given in equation 4.2:

$$I_{tr} / I_{inc} = \exp^{-\epsilon c l}$$

Equation 4.2.

In Equation 4.2 I_{tr} is the intensity of transmitted light and I_{inc} the intensity of the incident beam. The term I_{tr} / I_{inc} is a constant, as given by Beer's law. Other terms can be substituted into this equation to make it more readily usable for the purpose of this analysis. The pathlength, l , can be related to the thickness of the film, t , by considering the angles at which the incident and Raman scattered beams make with the electrode surface, which are 30° and 60° respectively. This means:

$$l_{inc} = 2t \text{ and } l_{Ram} = 2/\sqrt{3}t$$

Now, the surface concentration as expressed in nmol cm^{-2} is also related to the 3-D concentration, c , and the film thickness, as follows:

$$\Gamma_{Ru} = c (\text{nmol cm}^{-3}) t (\text{cm})$$

$$\rightarrow \Gamma_{Ru} = 10^6 c (\text{mol dm}^{-3})^{1/2} l_{inc} (\text{cm}) \text{ or } 10^6 c (\text{mol dm}^{-3})^{1/2} l_{Ram} (\text{cm})$$

These are now expressed in appropriate units for direct substitution into Eqn 4.2, to give:

$$I_{tr} / I_{inc} = \exp[-2 \times 10^{-6} \Gamma_{Ru} \epsilon_{inc}] \exp[-1.15 \times 10^{-6} \Gamma_{Ru} \epsilon_{Ram}]$$

$$T = \exp[-2 \times 10^{-6} \Gamma_{Ru} (\epsilon_{inc} + 0.58 \epsilon_{Ram})]$$

Equation 4.3.

Estimates of the two extinction coefficients are made assuming $\epsilon_{496} = 8500$ for the maximum of the band at this position,²⁴ and then reading off values from the appropriate UV-visible

spectrum. A UV-visible spectrum of the “20:1” polymer is shown in Figure 4.3. Because the calculation of surface coverages is based on the UV-visible determination of the py:Ru ratios (chapter 3), which themselves assume that $\epsilon_{496} = 8500$, then the determination of self-absorption through Equation 4.3 is self-consistent. The only factor that is not allowed for in the estimate is any change in absorption that results from interaction between ruthenium centres and the surface plasmon.

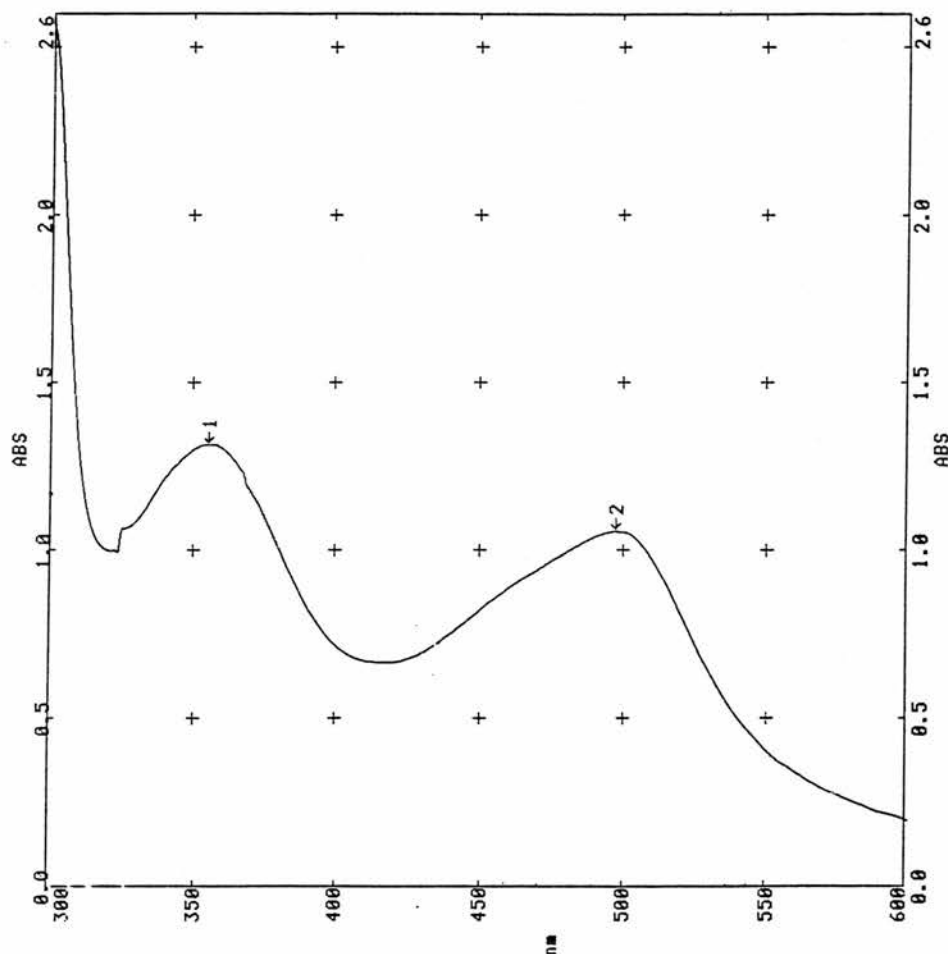


Figure 4.3: UV-visible spectrum of “20:1” [PVP-Ru(bpy)₂Cl]Cl.

The most commonly used values are $\lambda_{\text{inc}} = 514.5$ nm, for which $\epsilon_{514.5}$ is found to be 7400, and for the mean Raman shift of the scattered lines at 1485 cm^{-1} , 1555 cm^{-1} and 1603 cm^{-1} , which is at 1547 cm^{-1} , $\lambda_{\text{Ram}} = 559.0$ nm, for which ϵ_{559} is found to be 2900. Substituting these into Equation 4.3 gives $I_{\text{tr}} / I_{\text{inc}} = \exp(-0.018 \Gamma_{\text{Ru}})$. This leads to % transmissions of around 96% for $\Gamma_{\text{Ru}} = 1$ nmol cm^{-2} and 66% for $\Gamma_{\text{Ru}} = 10$ nmol cm^{-2} .

Analysis of Errors

All the data used in this determination come from the surface coverage vs intensity experiments, and include the results of 5 triplicate determinations and 22 duplicate determinations. The mean intensities obtained for each instance have been normalized to 1.00 for the purpose of this analysis, and the results for each individual determination adjusted accordingly, in order that different average values do not bias the standard deviation and error calculations. Highly discordant data points that are believed to arise from anomalous time dependence, as detailed in section 4.3.2, are discarded and play no part in the analysis (duplicate etc. also refer to the number of determinations used in analysis, and not those made and subsequently discarded). Overall, the standard deviation and error have been calculated from 59 data points, and a further 7 data points were rejected for anomalous behaviour. An example for a determination in triplicate, made for $\Gamma_{Ru} = 10.77 \text{ nmol cm}^{-2}$ of the “20:1” metallopolymer, is given below:

(i) Raw Data (summation of peak heights - backgrounds of 1485 cm^{-1} , 1555 cm^{-1} and 1603 cm^{-1} bands) – determination 1 = 4546 cts, determination 2 = 3725 cts, determination 3 = 4343 cts. Mean = 4205 cts.

(ii) Normalize mean to 1.00 by dividing each determination by 4205 – determination 1 = 1.081, determination 2 = 0.886, determination 3 = 1.033.

(iii) Values 1.081, 0.886, 1.033 used to calculate standard deviation and error, along with similarly obtained values for other duplicate and triplicate scans.

The analysis is done in this manner to give a rough estimate of the % error involved for all data points. Because similar influences affect the accuracy of each determination (discussed below), this method of error analysis was considered acceptable and the error for each individual data point was not calculated.

Modelling of Intensity Response of [PVP-Ru(bpy)₂Cl]Cl

Attempts have been made to fit the SERS intensity vs Γ_{Ru} response to the Freundlich isotherm,²⁵ given in Equation 4.4:

$$I = Kc^n$$

Equation 4.4.

In the above, K and n are constants, with $0 < n < 1$, and I and c are SERRS intensity and 3-D concentration, respectively. A double log plot, of log I vs log c, can be used to yield the two constant values, since:

$$\log I = \log K + n (\log c)$$

Equation 4.5

Two further points need be made about the application of such an analysis to this particular study. Firstly, the Raman intensity has already been shown to be dependent on self-absorption of the sample, a parameter which Equation 4.4 does not include. Thus the equation becomes:

$$I = Kc^n \cdot (I_{tr}/I_{inc})$$

$$I = Kc^n \exp[2 \times 10^{-6} \Gamma_{Ru} (\epsilon_{inc} + 0.58 \epsilon_{Ram})]$$

Equation 4.6

Since the double log plot analysis would be complicated by the inclusion of the self-absorption in the equation, the intensity values are corrected for self-absorption, in the manner described above, so that Equations 4.4 and 4.5 can be used directly.

The second point regards the estimation of the traditional 3-dimensional concentration of ruthenium centres ([Ru]) in the polymer film. In contrast to the analysis for self-absorption, [Ru] cannot be substituted out of Equation 4.4. The estimate used is based on a study by Leech *et al*,²⁴ who used flotation experiments in mixtures of carbon tetrachloride and hexane, to

determine the dry density of PVP-co-styrene metallopolymers with $[\text{Ru}(\text{bpy})_2\text{Cl}]^+$ (10 monomer units: 1 Ru) as a function of styrene content. From this they estimated $[\text{Ru}]$ to be 0.82 mol dm^{-3} for the pure PVP metallopolymer. Assuming the same overall density of 1.259 g cm^{-3} for the metallopolymer, independent of loading, Table 4.1 gives estimates for $[\text{Ru}]$ and film thicknesses for $\Gamma_{\text{Ru}} = 1 \text{ nmol cm}^{-2}$ in the polymers used for this study. The film thicknesses, t , are estimated using the following equation:

$$t (\mu\text{m}) = \frac{0.01 \Gamma_{\text{Ru}} (\text{nmol cm}^{-2})}{[\text{Ru}] (\text{mol dm}^{-3})}$$

Equation 4.7

Polymer Sample	Molecular Mass per Ru	$[\text{Ru}] / \text{mol dm}^{-3}$	Thickness / μm , for $\Gamma_{\text{Ru}} = 1 \text{ nmol cm}^{-2}$
Leech <i>et al</i> ²⁵	1535.75	0.82	0.012
“3:1”	853.39	1.48	0.0068
“10:1”	1860.63	0.68	0.015
“20:1”	2853.15	0.44	0.023
“100:1”	12505.00	0.15	0.066

Table 4.1: Values of in-situ 3-dimensional ruthenium concentrations of metallopolymer films used to model SERRS response.

4.3 Results

4.3.1 Error Calibration for SERS Spectra

Time Dependence

The deterioration of the SERS signal at 1485 cm^{-1} over 800 s is approximately 35 - 40 % for 150 mW power of the 514.5 nm laser. This value shows slight dependence on potential and on

loading, with a greater deterioration of the signal in the “3:1” polymer and for a potential of -0.6 V. A more detailed summary of these values and the errors associated with them is given in Table 4.2, which also breaks the signal deterioration down into values for the first 300 s (the soaking time used in other determinations) and for the next 150 s (the time taken to execute the scan described in the experimental for surface coverage vs intensity plots).

A small number of determinations ($3/23$) gave anomalous behaviour, in which the signal actually increases slightly over 800 s. Figure 4.4 compares a typical signal-time plot with one of these anomalous plots.

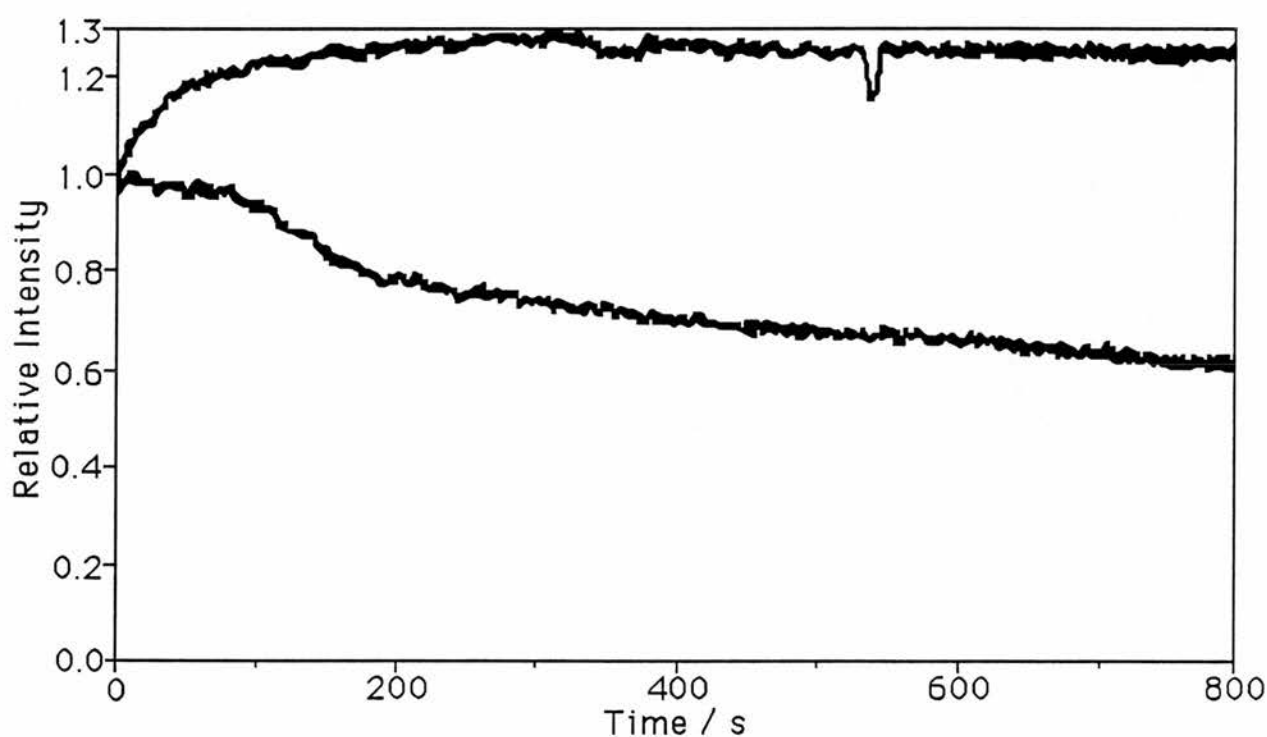


Figure 4.4: Change of normalized ($I = 1$ at $t = 0$) SERS Intensity of $[PVP-Ru(bpy)_2Cl]Cl$ at 1485 cm^{-1} as a function of time. Conditions: power = 150 mW, 514.5 nm excitation, “100:1” polymer, $\Gamma_{Ru} = 0.45\text{ nmol cm}^{-2}$, 0 V vs Ag / AgCl. (upper trace) Typical anomalous scan showing intensity increase. (lower trace) Typical scan showing intensity decrease.

Sample	Potential /V	No. runs	I_0/I_8	I_0/I_3	$I_3/I_{4.5}$
"3:1"	-0.6	3	0.53 ± 0.09	0.63 ± 0.06	0.93 ± 0.04
	0	3	0.60 ± 0.05	0.70 ± 0.06	0.93 ± 0.009
"100:1"	-0.6	3	0.64 ± 0.06	0.73 ± 0.05	0.96 ± 0.016
	0	5	0.65 ± 0.05	0.77 ± 0.06	0.94 ± 0.01

Table 4.2: Deterioration of signal with time for various experimental conditions. Laser line = 514.5 nm, Power = 150 mW. I_x/I_y expresses the intensity at $t = 100y$ s normalized to $I = 1$ at $t = 100x$ s. The errors expressed are the standard deviation divided by the root of the no. of determinations.

Reproducibility of Signal

The analysis of errors detailed in the experimental section yields a sample standard deviation of 0.142, and therefore an error of $\pm 28.3\%$ on each data point when considered separately, of $\pm 20.0\%$ on a duplicate determination, and of $\pm 16.3\%$ on a triplicate determination. Of a total of 66 data points considered, 7 were rejected as anomalous, about the same rate of anomalous behaviour as seen in the time-dependent experiments. Because these errors are also present in reference samples, the errors in relative values are larger still, and so the results obtained using different references (i.e. for different curves) can only be compared with some caution. However, this is still some improvement on the situation where a reference sample is not used and no comparison can be made between data acquired on different occasions.

4.3.2 Wavelength Dependence

Before considering the wavelength dependence, it should be noted that all the spectra acquired during the course of the various quantitative studies detailed below are very similar in appearance, and a typical spectrum of the 1450 cm^{-1} - 1650 cm^{-1} region is given in Figure 4.5.

Figure 4.6 shows a plot of the SERS peak heights of the 666 cm^{-1} and 1485 cm^{-1}

bands relative to those at 457.9 nm excitation, and allowing for the different powers of the samples. The % transmission of the samples, calculated using Equation 4.3, is between 88% - 92% at all the laser and Raman scattering wavelengths. Both bands show similar dependence on wavelength, although the variations in the 1485 cm^{-1} band are slightly smaller in relative intensity terms. The maximum relative intensity in each case is for 501.7 nm excitation, very close to the UV-visible maximum of the complex at 497 nm. This is in contrast with the findings of Chambers and Buck¹⁷ who observed differences of *ca.* 40 nm between excitation profile and UV-visible maxima for their polymer.

The time dependence of the signal at different wavelengths, under the same conditions as used for the excitation profiles, was also studied. For single determinations of I_0/I_{300} , as defined in Table 4.1, the 457.9 nm, 488.0 nm and 501.7 nm bands gave a value of around 0.8 and 496.5 nm and 514.5 nm gave values of around 0.70 - 0.75. Corrections have not been made for these differences in the excitation profiles.

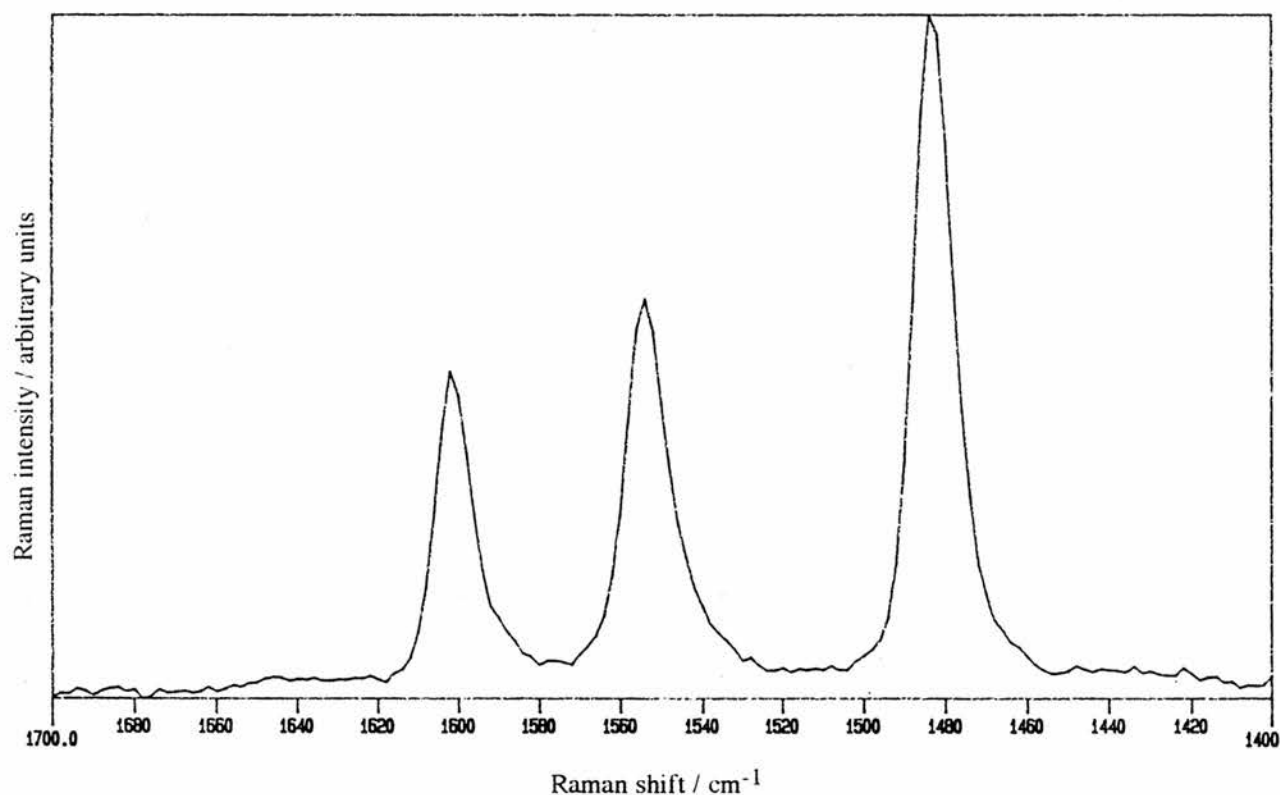


Figure 4.5: Typical SERRS spectrum from quantitative studies. Conditions in this case are laser line = 514.5 nm, power = 140 mW, potential = -0.6 V vs Ag / AgCl, "3:1" ruthenium metallopolymer, $\Gamma_{Ru} = 0.80 \text{ nmol cm}^{-2}$.

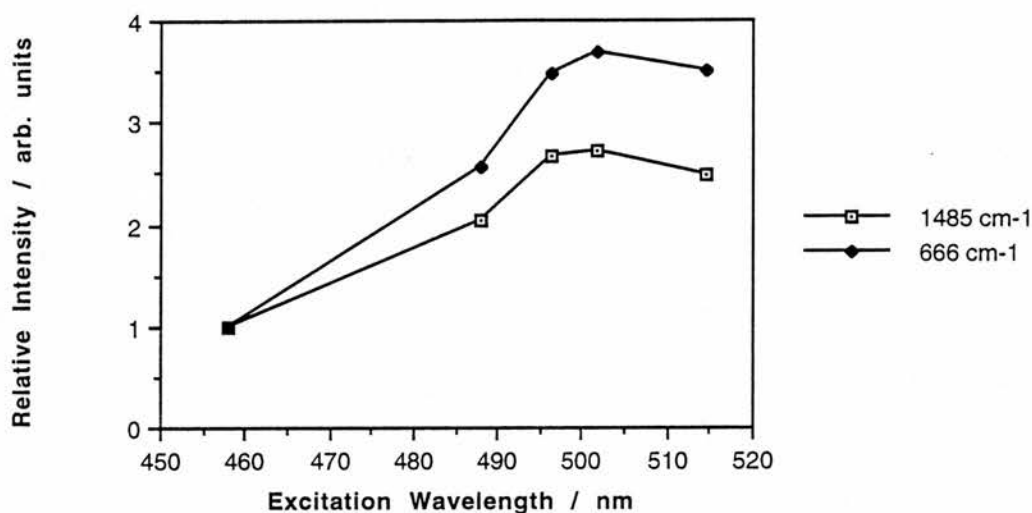


Figure 4.6: Excitation profiles for the 666 cm^{-1} and 1485 cm^{-1} Raman bands of "20:1" [PVP-Ru(bpy)₂Cl]Cl. Corrected for self-absorption and laser power.

4.3.3 Dependence on Loading (Pyridine:Ru ratio)

Figure 4.7 shows intensity vs Γ_{Ru} plots for various mass coverages of the polymers synthesized. Each line, therefore, represents the SERRS intensities for depositions of the same mass of polymer per unit area (and, in the approximations made here, the same thickness of polymer) in each case, but with a varying Ru content. The values determined from Table 4.1 for thickness are 15.8 nm, 31.7 nm and 63.4 nm for the $3\text{ }\mu\text{g cm}^{-2}$, $6\text{ }\mu\text{g cm}^{-2}$, and $12\text{ }\mu\text{g cm}^{-2}$ samples, respectively. The lines drawn are primarily for clarity and do not represent any sort of mathematical fit of the data; however, in the line for the $12\text{ }\mu\text{g cm}^{-2}$ data set, the maximum is exaggerated to emphasize the resemblance between this particular curve and the one found by Feng *et al*¹⁵ for methyl viologen. The curves for the lower thicknesses of polymer show less obvious maxima, the $6\text{ }\mu\text{g cm}^{-2}$ data set showing a slight peak, and the $3\text{ }\mu\text{g cm}^{-2}$ data set none. A possible trend given by the data is that for lower thickness films the maximum occurs at higher Γ_{Ru} , though this cannot be definitely stated.

Figure 4.8 shows the same treatment for a data set obtained from polymer blends of the

“10:1” metallopolymer with PVP, the deposition in this case being $3 \mu\text{g cm}^{-2}$, corresponding once more to a film thickness of 15.8 nm. No line is drawn in this case since the plot of $\log I$ versus $\log [\text{Ru}]$ (Figure 4.9) uses the four best data points from Figure 4.8 to calculate an intercept and gradient for Equation 4.5. This gives $\log K = 0.15$ and $n = 0.38$. The constants in Equation 4.5 have also been determined using all the data points from Figures 4.6 and 4.7 and give $\log K = 0.21$ and $n = 0.37$, though with a larger spread of data points from this line. The former set of values, when substituted into Equation 4.4 give Equation 4.8:

$$I = 1.41c^{0.38}$$

Equation 4.8

Figure 4.10 shows the theoretical curve that would result from the experiments done in Figure 4.6 obeying the Equation above. This curve does not give a value of 1.00 for the reference sample used in every experiment, i.e the $6 \mu\text{g cm}^{-2}$ deposition of the “20:1” metallopolymer, and so a small adjustment is made to bring the curve back through 1.00 at this point. The effect of this is to change the value of K from 1.41 to 1.35. The theoretical curve is obviously quite different from the data shown in Figure 4.7, in that the SERRS intensity increases with loading at all loadings. The reasons for this dissimilarity are considered further in the discussion session.

4.3.4 Dependence on Coverage (Mass of polymer deposited)

Figure 4.11 shows the data for different thickness depositions of polymers of the same loading. These use the same data set as in Figure 4.7, but the general trends seen, of curves with minima at low and high loadings and of straighter lines at intermediate loadings have been observed in other experiments within this study. Results from the theoretical model can be visualized from Figure 4.10: connecting the data points in the same manner as for Figure 4.11 would give four horizontal lines, showing that the absorption adjusted SERRS intensity should be independent of Γ_{Ru} . It is expected that, with very low mass depositions, as the thickness of

the film becomes less than the range of classical SERS enhancement, there will eventually be some loss of signal, such that the SERRS intensity decreases to zero at zero surface coverage. The onset of this is expected to occur slowly at film thicknesses of less than 10 nm,¹⁰ and since all the films used in quantitative studies here have minimum thicknesses of about 15 nm, this consideration is not expected to have a major influence on the observed results.

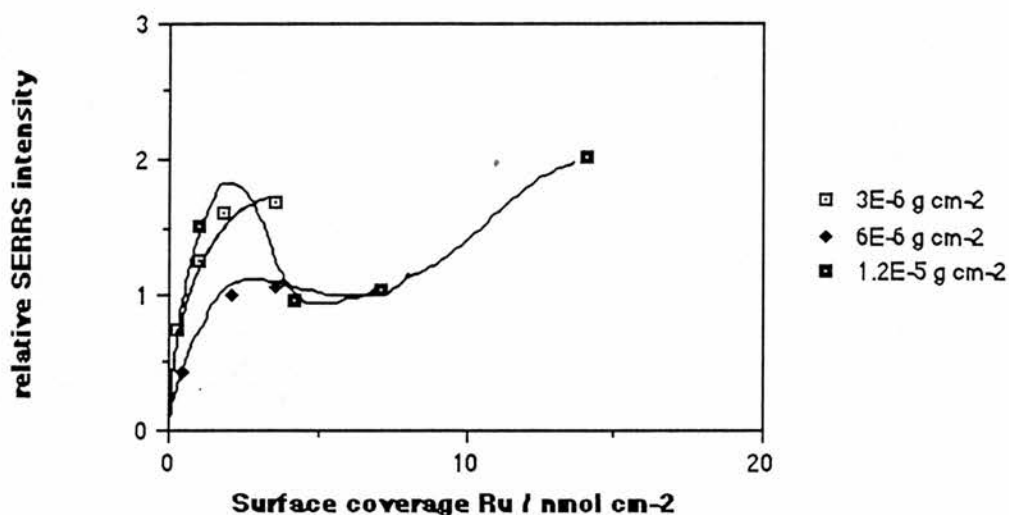


Figure 4.7: Intensity vs surface coverage plot. Each line represents a set of different polymer loadings at a constant mass of polymer (given on right hand side of the figure).

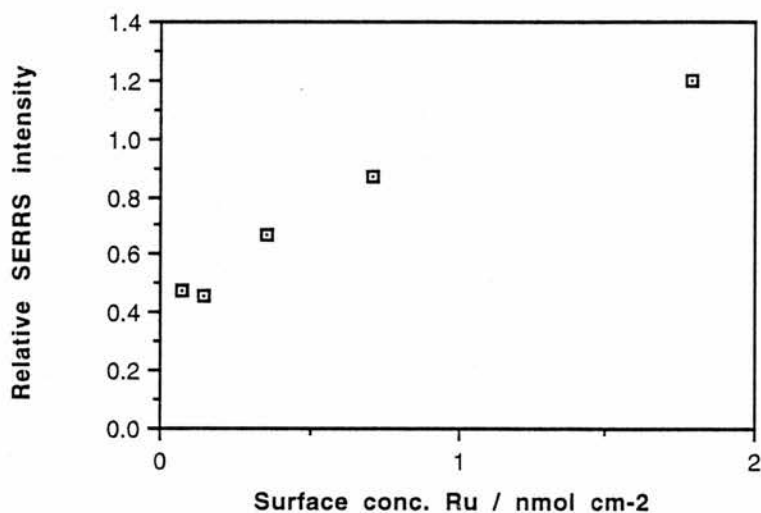


Figure 4.8: Plot of intensity vs Γ_{Ru} for polymer blends of the "10:1" metallopolymer with PVP. Total mass of polymer on electrode surface = $3.33 \mu\text{g cm}^{-2}$.

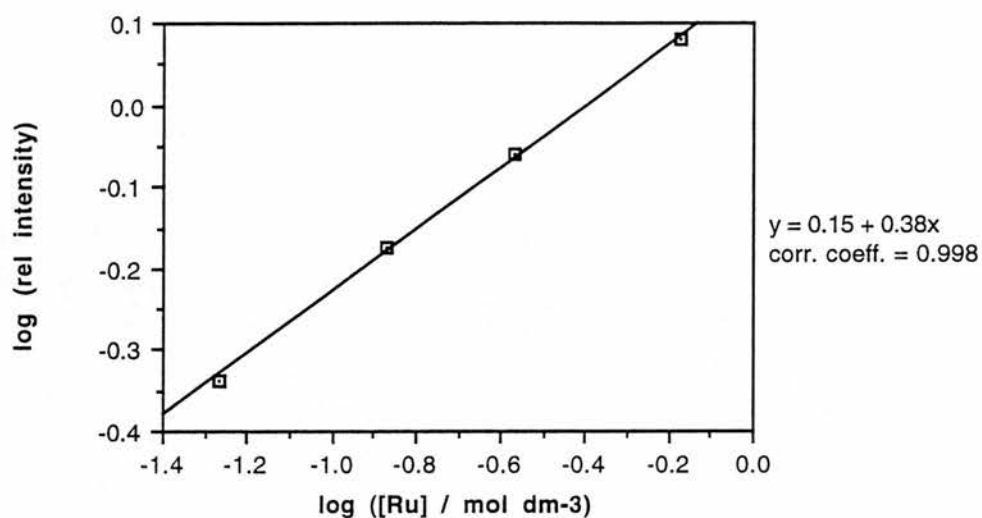


Figure 4.9: Double log plot of the data in Figure 4.7 with best fit straight line shown, and its equation given on the right hand side.

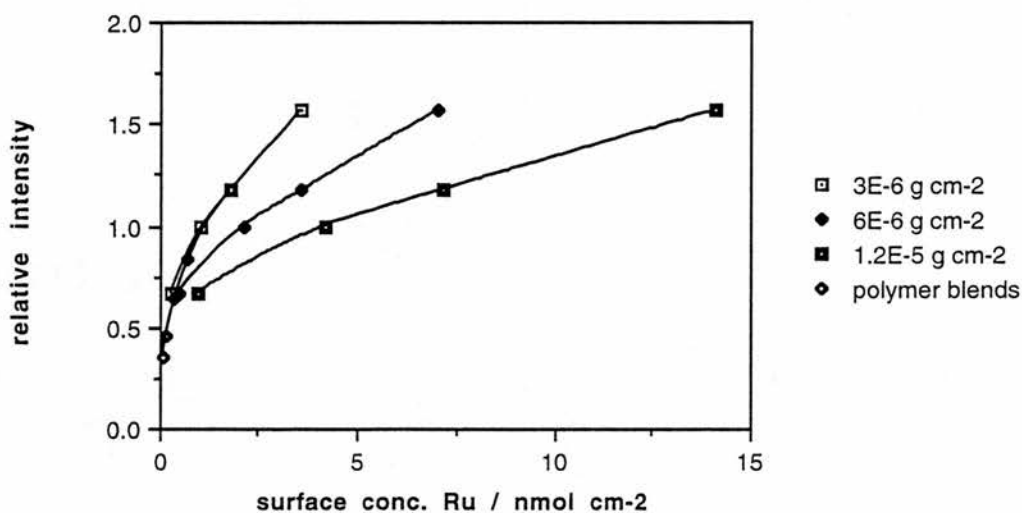


Figure 4.10: Theoretical curves based on Equation 4.4 for the absorption corrected SERS intensity vs loading for the curves in Figures 4.6 - 4.8

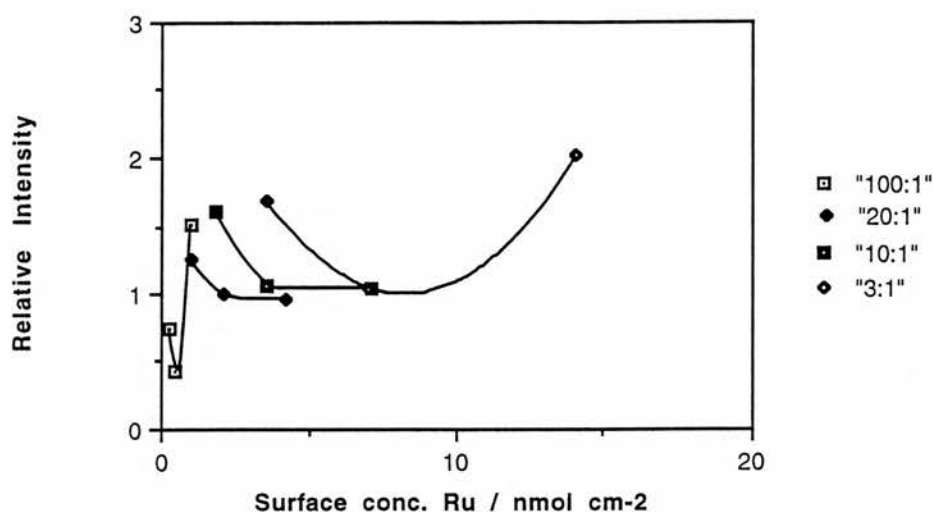


Figure 4.11: Intensity vs surface coverage plot. Each line represents a set of different polymer film thicknesses for a constant loading (given on right hand side of the figure).

4.3.5 Other Experiments on [PVP-M(bpy)₂Cl]Cl

Signal as a Function of Electrolyte

A few experiments have been done to gauge the effect of electrolyte anion and pH on the SERRS signal of [PVP-M(bpy)₂Cl]Cl, but will be reported here in less depth than the studies detailed above, since the experiments done were designed to assess trends in the intensity data, rather than as a full quantitative study.

The first set of experiments, to compare the results of Clarke *et al*²² from QCM studies, with SERRS intensities. The HClO₄ solutions of all concentrations give lower signals than 0.1 mol dm⁻³ KCl electrolyte. The 1 x 10⁻⁴ mol dm⁻³ HClO₄ solution gives a slightly lower intensity than the chloride, and the intensity continues to decrease with increasing HClO₄ concentration, all the way up to molar solution. The effect of acidity is determined by comparing the signals given in 0.1 mol dm⁻³ solutions of KCl and HCl. The acidic solution in this case gives slightly stronger SERRS.

The second experiment was done to assess the effect on signal of the electrolyte ions

Cl^- , ClO_4^- and NO_3^- . These have differing effects on polymer swelling in acidic and neutral solutions,²⁶ and so give films with differing concentrations and thicknesses for the same Γ_{Ru} . The least swelling occurs in ClO_4^- electrolyte, giving the highest $[\text{Ru}]$ (mol dm^{-3}) and the lowest thickness, and the most in NO_3^- , giving the lowest $[\text{Ru}]$ (mol dm^{-3}) and the greatest thickness. For a single determination of each, it was found that Cl^- gave the greatest SERS intensity (relative intensity = 1.00), followed by ClO_4^- (rel. I. = 0.84) and finally NO_3^- (rel. I. = 0.66). Time dependence studies of the signal at 1485 cm^{-1} were done in order to determine whether signal deterioration contributed to the intensity differences, but the results were similar for each case.

CV Studies on Photosubstitution Reactions

Figures 4.12 and 4.13 show two CVs, one taken before irradiation of the sample and one taken after 5 minutes of irradiation at 457.9 nm and 80 mW power and still under illumination. The former shows just one couple, centred at +0.75 V vs SCE, but in the latter an additional weak couple is observed at +0.43 V vs SCE. The redox potential found for the dominant peak is about half-way between the +0.64 V and +0.84 V couples found for $[\text{PVP-Ru}(\text{bpy})_2\text{Cl}]^+$ and $[\text{PVP-Ru}(\text{bpy})_2(\text{H}_2\text{O})]^{2+}$ by Haas *et al.*²³ in aqueous perchlorate electrolyte. To confirm whether this was due to electrolyte or loading dependent alterations in the half-wave potential, or due to photosubstitution within the standard solutions, UV-visible spectra were acquired immediately after these experiments. The absorption maximum was found at 495 nm, typical of the chloro- complex, confirming that measures to prevent photosubstitution before laser irradiation of the samples was adequate. The complex in which MeOH is substituted has $\lambda_{\text{max}} = 475 \text{ nm}$ ²⁷ and the EtOH complex is expected to give a very similar result.

Once under laser irradiation in 0.1 mol dm^{-3} KCl (aq), the appearance of the aqua-complex is still not observed and instead the wave at +0.43 V appears, although only at excitation wavelengths of 496.5 nm or less. This photoreaction does not go to completion, and the +0.75 V wave continues to dominate the voltammogram.

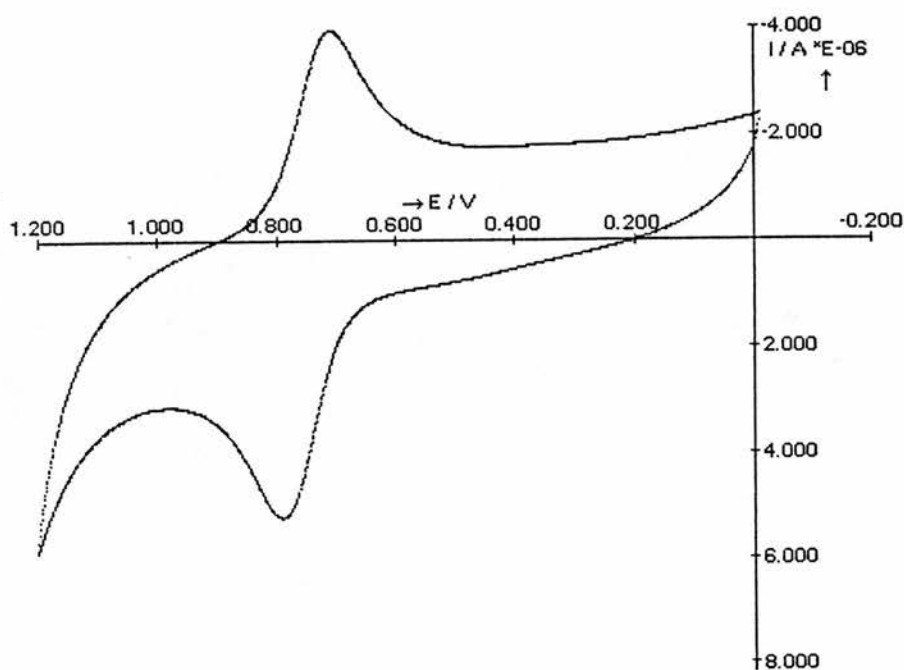


Figure 4.12: CV of "3:1" [PVP-Ru(bpy)₂Cl]Cl modified glassy carbon electrode in the dark.

Scan rate = 100 mV s^{-1} , electrolyte = $0.1 \text{ mol dm}^{-3} \text{ KCl(aq)}$ and reference = SCE.

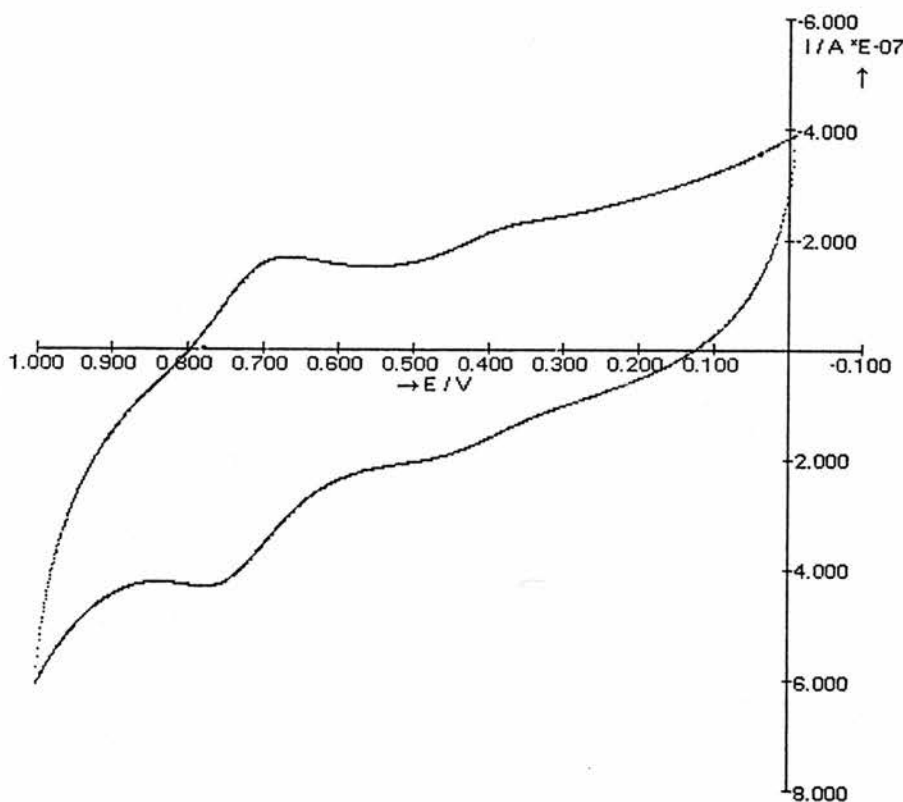


Figure 4.13: CV under conditions as in Figure 4.12 except that the working electrode was illuminated with 80 mW power of a 457.9 nm laser for 5 minutes prior to and then during the sweep.

4.4 Discussion

4.4.1 Initial Assumptions

The model for SERRS intensity, based on the Freundlich adsorption isotherm, views the polymer layer as a homogeneous solution with ruthenium centres in a dynamic equilibrium between adsorbed (i.e. SERRS active) and desorbed (i.e. SERRS inactive) states. The similarity between the SERRS and RR spectra show that Ru does not adsorb specifically at the surface and so the concentration of Ru sites in the vicinity of the surface can be represented by solution concentration. The fact that SERRS intensity does not increase linearly with this concentration can be attributed to there being a limited number of surface-active sites, which can therefore saturate at higher ruthenium concentrations.

Other assumptions for the modelling studies are: (a) all SERRS scattering takes place in the immediate vicinity of the electrode, in other words, that the distance over which surface-enhancement takes place is insignificant compared with the thickness of the polymer film, (b) that metal bipyridyl centres further from the surface act only to attenuate the beam, (c) that the polymer film is of even thickness and is homogeneous, (d) that the density of the swollen metallopolymer film is independent of loading. To find reasons for the deviation of Raman intensity vs surface coverage plots from theoretical curves, one must carefully scrutinize all these assumptions for possible sources of deviation from the idealized model. In this section, several such possibilities will be considered to explain the observed behaviour.

4.4.2 Time Dependence Studies

The values obtained for signal deterioration with time were done to give an indication of any major differences between samples and potentials, and to determine the effect of the five minutes solution equilibration step on the signal. The slight potential and loading dependences shown by these data may be due to either different degrees of solvent swelling in the samples or, in the case of the "3:1" polymer, to greater decomposition of the metal centres upon

heating, due to this metallopolymer absorbing more photons. Swelling differences may be one cause of deviation of the observed intensity vs surface coverage plots, for which the concentration of Ru centres is calculated using a single swelling estimate for the "10:1" polymer. This will be considered further below. The errors involved in the signal deterioration will also contribute to the errors determined for intensity vs surface coverage plots.

The cause of so-called anomalous behaviour is of interest since it is another source of irreproducibility in the quantification technique. The reason for this behaviour is not known, since no consistent pattern of occurrence (e.g. at particular loadings, deposition volumes etc.) is observed. Possible causes could come from slight inconsistencies in the pre-treatment procedure, such as the deposition of the polymer layer before the electrode surface is completely dry, or immersion before complete evaporation of the solvent. The next consideration in this case is to determine whether the signal increase occurs because the initial signal is unusually low and the polymer layer then equilibrates on immersion to give SERRS intensities typical of those given by similar films, or whether an anomalously high SERRS intensity results. On study of the data it seems that the latter is the case: anomalous behaviour in the time dependence leads to anomalously large signals in quantitative studies. From this it can be concluded that a different final state is reached upon immersion of an anomalous film. If water were incompletely removed from the electrode surface before deposition of the film, it is possible that this would increase the concentration of ionic ruthenium bipyridyl groups at the aqueous/polymer interface and, therefore, once the water diffuses away into the film, a greater concentration of these SERRS active groups is present at the electrode/polymer interface. However, it is possible that the effect of increasing the concentration of Ru at the surface could be to increase surface plasmon damping, meaning that a re-arrangement of the Ru centres would not necessarily lead to an increase in SERRS intensity.

4.4.3 Factors Affecting SERS Intensity vs Surface Concentration Plots

Interaction between the Surface Plasmon and Adsorbates

In the absence of UV-visible experiments on the surface-adsorbate system, comparison of the SERRS excitation profile with the adsorbate UV-visible spectrum is the best gauge of the interaction of the surface plasmon and adsorbate electronic transitions. The proximity of the excitation profile maximum at 501.7 nm to the UV-visible maximum at 497 nm seems to suggest that surface plasmon damping is rather weak in this instance. However, the intensity maximum for 501.7 nm excitation is rather shallow and it must be borne in mind that the slightly greater deterioration seen for the 514.5 nm line is not corrected for in the excitation profile. Because full-range scans from 100 cm^{-1} - 1700 cm^{-1} were done, the time between immersion and scanning over the two bands is large, estimated at $t \approx 600\text{ s}$ and 1000 s for the 666 cm^{-1} and 1485 cm^{-1} bands, respectively. The above facts, when combined, lead to the possibility that the true excitation profile maximum may be at longer wavelength than the value that is actually observed, which in turn would suggest greater interaction between the surface plasmon and adsorbate transitions.

The effect of surface plasmon damping on SERRS intensity would be to reduce it at higher values of Γ_{Ru} and also possibly for higher loading samples of metallopolymer at similar Γ_{Ru} values. As the distance between the ruthenium bipyridyl centre and the surface is increased, however, the damping of the plasmon will become weaker and above a certain distance will become insignificant. If greater Γ_{Ru} is achieved by increasing the thickness, as in the coverage dependent plots (Figure 4.11), then a point will be reached when the surface concentration increases occur far enough away from the electrode surface so that they no longer contribute to the surface plasmon damping. The work of Glass *et al.*,¹⁶ in which a 30 Å layer of PMMA was spun onto a silver film to study the distance dependence of surface plasmon damping in rhodamine 6G, suggests that plasmon damping does operate over this range, in a similar manner to EM type surface enhancement. The decreases in the self-absorption adjusted SERRS intensities seen for all polymer loadings between 15 nm and 30 nm thicknesses in Figure 4.11, in deviation from the Freundlich model, suggest that this surface plasmon

damping has a more significant contribution than the surface-enhancement of Ru centres at this range.

Resonance Raman Scattering

This type of scattering is assumed to be insignificant in the modelling of SERRS intensities, but, as has been observed by Feng *et al.*,¹⁵ resonance scattering can contribute significantly to observed surface coverage vs intensity plots (Figure 4.2e), especially where plasmon damping reduces the surface-enhancement factor. RR will be the major contribution to the Raman signal for metal centres further than about 10 nm from the Ag electrode and should increase linearly with the number of scattering centres, Γ_{Ru} .

The contribution of any RR scattering will be exaggerated by one element of the data treatment used here: the attenuation adjustment. Because SERRS scattering is assumed to be localized at the surface, the pathlength used to calculate attenuation values is calculated from the total thickness of the film, and all contributions to the Raman intensity, be they RRS or SERRS, are adjusted accordingly. For the resonance case, however, this adjustment is incorrect, since the resonant scatterer can be located at any any point in the film and thus the pathlength can have any value between zero and that for SERRS. This leads to higher transmission for the average RR scatterer, meaning in turn that the adjusted value overestimates the number of Raman scattering events taking place. For the maximum surface coverage used in Figures 4.7 and 4.11, which is $14.10 \text{ nmol cm}^{-2}$, the transmission through the film is estimated as 0.557. The inaccuracy of this transmission value for any RR scattering contribution is significant, but will not be large enough to reverse the observed trend that the Raman intensity is increasing in this region. Thus, the net effect of the resonance Raman contribution is to increase the signal between 30 nm and 60 nm thicknesses. One can also surmise that surface plasmon damping does not have a major contribution to the observed trends at these thicknesses.

Together, surface plasmon damping and resonance Raman considerations can, therefore, fully explain the appearance of curvature in the SERS intensity vs Γ_{Ru} plots shown in Figure 4.11. However, the reason for differences in the broadnesses of minima between

curves in Figure 4.11 is not known. In particular, the very sharp minimum found for the “100:1” polymer is at variance with the trend for the other polymers and also with the expectation that, as the polymer with fewest Ru centres contributing to long-range plasmon damping and resonance Raman scattering, this should vary the least with Γ_{Ru} .

SERRS Intensity as a Function of Loading

The two major contributions that cause deviation from the Freundlich isotherm have been shown above to be most conveniently discussed in terms of the dependence of the SERRS intensity on the thickness of the film at constant loading (Figure 4.11). Figure 4.7 presents the same data in a different way, and thus the explanations given above provide all the discussion needed for an understanding of the shape of the observed SERRS intensity-loading curves. The resultant curves are very similar to those observed by Feng *et al*¹⁵ for methyl viologen, with the SERRS contribution maximizing at low Γ_{Ru} and then levelling off at a lower intensity, and the RR contribution increasing with Γ_{Ru} over the whole range.

Polymer Blend Studies

The data given by the polymer blends in Figure 4.8 provide the best fit to Equation 4.8 not simply because this data set is the one used to calculate values of K and n for the Freundlich isotherm (note that very similar values are obtained if all data points are considered), but also because long-range surface plasmon damping and resonance Raman scattering are expected to interfere less with the SERRS signal in this case due to the low concentration of Ru bipyridyl centres. The film thickness in these studies is 30 nm. The value of 0.38 obtained for n , the more important of the two parameters, shows that at these concentrations (15-600 mmol dm⁻³), the relationship does not approach linearity. This is in agreement with other studies, since such linearity has only been observed for sub-millimolar concentrations.¹⁴

Photosubstitution Reactions

The possibility, for the ruthenium metallopolymers, that the chloride ligand was photosubstituted by water under laser irradiation was investigated by cyclic voltammetry in a

study similar to that of Haas *et al.*,²³ except that they used aqueous perchlorate rather than chloride. The consequences of any photosubstitution are important for interpretation of the data for several reasons. The UV-visible spectrum of $[\text{PVP-Ru}(\text{bpy})_2(\text{H}_2\text{O})]^{2+}$ is different from that of the chloride, having a maximum at 474 nm.²⁸ Thus the excitation wavelength dependence would be expected to be quite different from the chloride, and estimates of film absorbance in the SERRS study would be in error. Also, the replacement of a monopositive cation with a dipositive cation would alter the swelling properties of the film, leading to errors in the thickness estimates.

Fortunately, no CV wave appears at around +0.9 V vs SCE, the expected potential for the Ru(II/III) oxidation of the aqua complex, showing that this reaction is not important for the polymer films. On illumination at wavelengths below 496.5 nm a reaction is observed, producing a small wave at +0.43 V. However, the +0.75 V wave remains the largest in the voltammogram over illumination timescales comparable to those used in SERRS experiments, and hence it is felt that no adjustments to the model calculations are needed on the basis of this evidence.

Two important differences between this study and that of Haas *et al.*²³ may be cited to explain why the photoaquation does not occur. Firstly, the presence of Cl^- in the electrolyte may alter the photochemical equilibrium such that photoaquation is disfavoured. This is supported by the study of van Houten and Watts,²⁹ who saw no evidence for photoaquation of chloride containing photolysis products of $\text{Ru}(\text{bpy})_3^{2+}$ in HCl or NaCl containing aqueous solutions. Secondly, illumination using Ar^+ laser wavelengths may not give the correct excited state to enable the reaction to proceed. Haas, who used a polychromatic 500 W projector lamp, suggested a reaction scheme to explain the photoaquation phenomenon, which started with an MLCT excitation that eventually led to occupation of an antibonding σ^* -orbital, weakening the Ru-Cl bond.

4.4.3 Other Considerations

Other Factors of Possible Significance in all Experiments

The different coverages and loadings for the quantitative experiments are achieved by varying other parameters during the deposition procedure. The changes in loading are simply achieved by using standard solutions of similar w/v concentrations for each of the different metallopolymers synthesized. Although there will be errors due to estimating the film thicknesses based entirely on results for a 10:1 polymer sample, especially for the "3:1" polymer where ion-ion repulsions are expected to be significant, the deposition procedure itself is not a cause for concern.

The changes in coverage are achieved either by using the same deposition volume for different concentrations or different deposition volumes of a single solution, which is the case in Figure 4.11. Both of these may introduce errors. Roark and Rowlen³⁰ have demonstrated by SEM and UV-visible absorption for acetone, that some of the effects usually attributed to plasmon damping may be due to solvent-induced morphological changes. It follows that a higher deposition volume, for which the solvent resides on the surface for a longer period of time, may lead to a subtly different surface from one which has been exposed to less solvent. The alternative procedure, to use different concentrations, may introduce errors by allowing the polymer chains more flexibility to adsorb at the electrode in the most stable orientation. The effect of such coil-shrinkage has been investigated for PVP itself by Xue.³¹

One final and potentially important source of errors in the above determination would come from unevenness in the polymer layer. The deposition of metallopolymer was achieved by droplet evaporation rather than spin-coating, and so in this respect the experimental set-up was not idealized. However, the incident laser beams were slightly de-focussed and so microscopic thickness differences in the film are expected to approximately cancel one another out. If any larger scale unevenness was present, this could affect the results, leading to higher sample errors.

Electrolyte and pH

Other than photosubstitution, discussed above, there are two possible causes of variation of SERRS intensities with different electrolytic solutions: the differences in film swelling and the effect that the solution has on the stability of the roughened electrode. It is the film swelling effect that is of interest, as this is a measure of the variation of signal as a function of film thickness (and therefore $[M]$) at constant Γ_M , and therefore the effects of the other two processes need to be separated from those due to this film swelling. The photosubstitution can be prevented by using Os rather than Ru metallopolymers³² and these were used in some of the electrolyte studies. The effect of SERS site stability, however, is more difficult to resolve, since both this and film swelling will influence the results of time-dependence experiments.

Good quality SERS spectra have been obtained in many electrolyte systems, and Saito has even demonstrated that non-halide electrolytes can be used in roughening cycles to give intense SERS, provided that the charge passed is adequate.³³ These suggest that SERS sites are relatively insensitive to changes in the electrolyte. However, the differences in SERRS intensities as a function of thickness, predicted by the Freundlich isotherm to follow $[M]^{0.38}$, may also be quite small, such that even small differences in SERS site stability could be significant. The thickness differences for each electrolyte have not been quantitatively estimated for the polymers studied, and so, although a general trend towards more swollen, thicker layers is established on going from $\text{ClO}_4^- \rightarrow \text{Cl}^- \rightarrow \text{NO}_3^-$,²⁶ the extent of the thickness and concentration changes is not known.

Acidifying a PVP film to pH 2 - 3 causes swelling because the pyridine N-atoms become protonated, and the film then admits counterions and solvent.³⁴ In $[\text{PVP-M}(\text{bpy})_2\text{Cl}]\text{Cl}$ the film is ionic throughout the pH range, and so acidification makes less difference to the swelling. Again quantification of these changes by SERRS is made difficult by the intractability of film stability and swelling difference effects. In conclusion, the observed changes in SERRS intensity between different electrolytes and different pHs are of limited use in assessing changes in metallopolymer swelling.

4.5 Conclusions and Suggestions for Further Study

In this chapter excitation profiles for [PVP-M(bpy)₂Cl]Cl have been acquired along with plots of the SERRS signal vs surface coverage for both polymers with different Ru concentrations and polymer layers of different thicknesses. The results were adjusted for self-absorption of samples and then modelled using a Freundlich isotherm. The SERRS intensity was found to increase as $[M]^{0.37}$. For low surface coverages the isotherm is a good model of the observed behaviour, but at higher coverages and for thicker films deviations are seen due to surface plasmon damping, which lowers the signal, particularly at intermediate polymer thicknesses (15 - 30 nm), and resonance Raman scattering, which increases the signal at higher thicknesses (>30 nm). The errors inherent in these experiments have been considered and several possible sources of such errors have been discussed. Photoaquation of [PVP-Ru(bpy)₂Cl]Cl is not found to be a problem in this particular system but errors due to deposition volume, deposition solution concentration and uneven film formation cannot be discounted. The possible effect of active site decomposition makes conclusions difficult to draw in a study of the variation of SERRS intensity in different electrolytes.

Preliminary experiments that are not detailed above have been done in an attempt to monitor the ingress of SE(R)RS active anions and cations into ion-exchange polymer films.³⁵ Providing that calibration curves of these anions as a function of concentration at bare electrodes are done, then the time dependent growth of the ion signal might be used to yield two parameters of use to electrochemists. The partition coefficient, κ , will be given by the equilibrium concentration of ion in the film for a given solution concentration. Since values of κ often exceed one hundred,³⁶ calibration of anion concentrations at bare electrodes will be needed for far greater concentrations than the solution concentration in the anion study. A second parameter that is of interest is the ion diffusion coefficient, D_{ion} , through the film to the electrode surface. This could be found through time-dependence studies. A slightly more involved mathematical treatment is needed for this determination since the diffusion coefficient is difficult to separate from the diffusion of the ion across the polymer / solution interface.

For experiments of this type to be successful, spin-coated polymer layers, OMA

detection (to increase the time-resolution of the analysis) and the production of roughened surfaces with good stability over time will be required. Also, many ions may only be amenable to study under certain conditions, for instance $[\text{Mo}(\text{CN})_8]^{4-}$ has given poor results in preliminary experiments because it is photoactive in aqueous solution, or redox activity may complicate the data analysis. Two previous studies give some encouragement as to the possibility of achieving this aim, one by Hutchinson *et al.*,³⁷ in which they determine that the reduction and oxidation between leucothionine and thionine adsorbed at electrodes takes place from the film / solution interface in to the electrode, and the other by Pal *et al.*,³⁸ who use poly(vinylpyrrolidinine) films on vacuum evaporated Ag surfaces for the separation of organics. Another very recent visible spectroscopic technique, variable angle of incidence evanescent wave spectroscopy (VIEWS) on which only two papers have yet been published,^{39,40} is also considered to have potential for similar ion diffusion studies

4.6 References

- 1 V. V. Marinyuk, *Sov. Electrochem.*, 1986, **22**, 260.
- 2 T. T. Chen, J. F. Owen, R. K. Chang and B. L. Laube, *Chem. Phys. Lett.*, 1982, **89**, 356.
- 3 R. Dornhaus, M. B. Long, R. E. Benner and R. K. Chang, *Surface Sci.*, 1980, **93**, 240.
- 4 M. Fleischmann and I. R. Hill, *J. Electroanal. Chem.*, 1983, **146**, 353.
- 5 H. Saito, *J. Raman Spec.*, 1993, **24**, 191.
- 6 J.-H. Kim, T. M. Cotton, R. A. Uphaus and D. Möbius, *J. Phys. Chem.*, 1989, **93**, 7313.
- 7 P. N. Sanda, J. M. Warlaumont, J. E. Demuth, K. Christmann and J. A. Bradley, *Phys. Rev. Lett.*, 1980, **45**, 1519.
- 8 D. A. Zwemer, C. V. Shank and J. E. Rowe, *Chem. Phys. Lett.*, 1980, **73**, 201.
- 9 I. Pockrand, *Chem. Phys. Lett.*, 1982, **92**, 509.

- 10 A. Otto, I. Mrozek, H. Grabhorn and W. Akemann, *J. Phys.: Condens. Matter*, 1992, **4**, 1143.
- 11 L. Stolberg, J. Lipkowski and D. E. Irish, *J. Electroanal. Chem.*, 1991, **300**, 563.
- 12 J. Lipkowski, L. Stolberg, S. Morin, D. E. Irish, P. Zelaney, M. Gamboa and A. Wieckowski, *J. Electroanal. Chem.*, 1993, **355**, 147.
- 13 M. Foresti, A. M. Funtikov, R. Guidelli and M. Muniz-Miranda, *J. Electroanal. Chem.*, 1994, **367**, 223.
- 14 P. Hildebrandt and M. Stockberger, *J. Phys. Chem.*, 1984, **88**, 5935.
- 15 Q. Feng, W. Yue and T. M. Cotton, *J. Phys. Chem.*, 1990, **94**, 2082, and references therein.
- 16 A. M. Glass, P. F. Liao, J. G. Bergman and D. H. Olson, *Opt. Lett.*, 1980, **5**, 368.
- 17 J. A. Chambers and R. P. Buck, *J. Electroanal. Chem.*, 1984, **163**, 297.
- 18 S. Garoff, D. A. Weitz, T. J. Gramila and C. D. Hanson, *Opt. Lett.*, 1981, **6**, 245.
- 19 E. J. Zeman, K. T. Carron, G. C. Schaltz and R. P. Van Duyne, *J. Chem. Phys.*, 1987, **87**, 4189.
- 20 T. J. Dines and R. D. Peacock, *J. Chem. Soc., Faraday Trans. 1*, 1988, **84**, 3445.
- 21 J. E. Pemberton and R. P. Buck, *Anal. Chem.*, 1981, **53**, 2263.
- 22 A. P. Clarke, J. G. Vos, A. Glidle and A. R. Hillman, *J. Chem. Soc., Faraday Trans.*, 1993, **89**, 1695.
- 23 O. Haas, M. Kriens and J. G. Vos, *J. Am. Chem. Soc.*, 1981, **103**, 1318.
- 24 D. Leech, R. J. Forster, M. R. Smyth and J. G. Vos, *J. Mater. Chem.*, 1991, **1**, 629.
- 25 H. G. Cassidy, in *Techniques of Organic Chemistry*, ed. A. Weissberger, Interscience, New York, 1951, **5**, *Adsorption and Chromatography*.
- 26 A. Aoki and A. Heller, *J. Phys. Chem.*, 1993, **97**, 11014.
- 27 J. M. Clear, J. M. Kelly, D. C. Pepper and J. G. Vos, *Inorg. Chim. Acta*, 1979, **33**, L139.
- 28 J. M. Calvert and T. J. Meyer, *Inorg. Chem.*, 1982, **21**, 3978.
- 29 J. van Houten and W. J. Watts, *Inorg. Chem.*, 1978, **17**, 3381.
- 30 S. E. Roark and K. L. Rowlen, *Anal. Chem.*, 1994, **66**, 261.

- 31 G. Xue, *Polym. Bull.*, 1994, **39**, 229.
- 32 R. J. Forster and J. G. Vos, *Macromolecules*, 1990, **23**, 4372.
- 33 H. Saito, *Bull. Chem. Soc. Jpn.*, 1993, **66**, 963.
- 34 S. M. Oh and L. R. Faulkner, *J. Electroanal. Chem.*, 1989, **269**, 77.
- 35 A. P. Taylor, J. A. Crayston and T. J. Dines, unpublished results.
- 36 A. R. Hillman, in *Electrochemical Science and Technology of Polymers*, ed. R. G. Linford, Elsevier, 1987, p. 103.
- 37 K. Hutchinson, R. E. Hester, W. J. Albery and A. R. Hillman, *J. Chem. Soc., Faraday Trans. 1*, 1984, **80**, 2053.
- 38 A. Pal, D. L. Stokes, J. P. Alarie and T. Vo-Dinh, *Anal. Chem.*, 1995, **67**, 3154.
- 39 M. Trau, F. Grieser, T. W. Healy and L. R. White, *J. Chem. Soc., Faraday Trans.*, 1994, **90**, 1251.
- 40 D. J. Neivandt and M. L. Gee, *Langmuir*, 1995, **11**, 1291.

Chapter 5

Electrochemistry and SERS of Chromium Bipyridyl Complexes

5.1 Introduction

When compared to ruthenium and osmium (II) bipyridyls, the chromium (III) complexes have quite weak electronic absorptions in the visible region and significant resonance enhancement is not expected with the 514.5 nm line of an argon-ion laser. The original aim of this study was to synthesize a non-resonant analogue of $[\text{PVP-Ru}(\text{bpy})_2\text{Cl}]^{2+}$ in order to gauge the effect of resonance on the studies in chapter 4. The ideal target compound would be the equivalent Cr(II)-PVP metallopolymer, but this has not been reported in the literature. Indeed, there are no well documented examples of bis(bipyridyl) complexes containing other pyridine-like ligands for any transition metals other than ruthenium and osmium.¹ Features in the electronic spectrum of an aqueous mixture of $[\text{Cr}(\text{bpy})_3]^{2+}$ and 4,4'-bipyridine have been assigned to $[\text{Cr}(\text{bpy})_2(4,4'\text{-bpy-H}^+)(\text{H}_2\text{O})]^{4+}$ by Ulstrup, but the complex was never isolated.²

Because of their fairly long excited state lifetimes (60 μs for the ${}^2\text{E}$ state in the $[\text{Cr}(\text{bpy})_3]^{3+}$ complex), the Cr(III) polypyridyls, like their Ru(II) equivalents, have been considered as potential photocatalysts for water photolysis.³ SERS studies on $[\text{Cr}(\text{bpy})_3]^{3+}$ have concentrated on trying to determine the nature of this excited-state by combining use of pulsed and continuous-wave lasers.⁴⁻⁶

Cr(III) complexes are almost exclusively octahedral, and with their d^3 configuration are quite substitutionally inert. Because of this, synthesis of the $[\text{Cr}(\text{bpy})_3]^{3+}$ cation is best achieved *via* oxidation of the Cr(II) complex,⁷ although $[\text{Cr}(\text{bpy})_2\text{L}_2]^{3+}$ complexes may also be produced in side reactions.⁸⁻¹⁰

The direct reaction of Cr(III) salts with 2,2' bipyridine usually results in bis(bipyridyl) complexes. A few examples of such reactions are contained in the experimental section, and a large number more are detailed by the papers cited therein. Complexes with aqua and hydroxo ligands in the two remaining coordination positions tend to form binuclear complexes.^{11,12} The

crystal structure of the red complex (Fig. 5.1),¹³ $[(bpy)_2Cr(OH)_2Cr(bpy)_2](ClO_4)_4 \cdot 2 H_2O$, showed that two hydroxyls are attached directly to each metal centre, and that two protons are shared equally between the four ligands, such that the bridges between the Cr centres should be formulated in the solid as two $H_3O_2^-$ ligands.

Several previously reported Cr(III) bis(bipyridyl) complexes have been studied by cyclic voltammetry and SERS in this chapter as is the coupling of poly(acrylic acid) (PAA) to $[Cr(bpy)_2Cl_2]^+$.¹⁴ Although a synthesis of $[PVP-Cr(en)_2]$ ($en = 1,2$ ethylene diamine) has been reported previously,¹⁵ the work below includes the first example of PVP being coupled to $[Cr(bpy)_2Cl_2]^+$, which is also a rare example of an electrosynthetic route to mixed Cr(III) complexes.

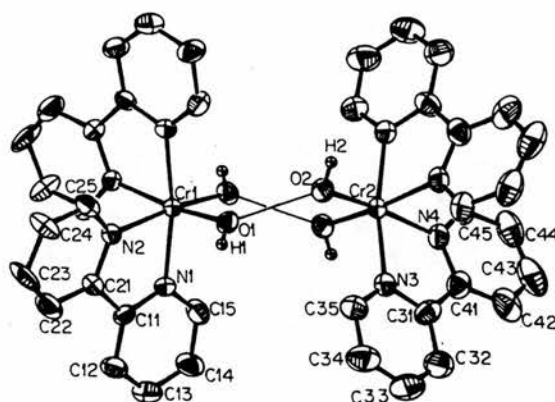


Figure 5.1: Crystal structure of $[(bpy)_2Cr(OH)_2Cr(bpy)_2](ClO_4)_4 \cdot 2 H_2O$. (from ref. 13). The thin lines indicate O-H-O bonds.

5.2 Experimental

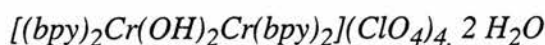
5.2.1 Syntheses

Materials

All materials were reagent grade and were used as received. Poly(acrylic acid) (Aldrich) had a weight-average molecular weight of 5000 AMU and was supplied as a 50 wt. % solution.

Characterization

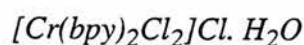
The instrumentation for UV-visible spectroscopy and CHN microanalysis are as detailed in chapter 3.



This followed the method of Josephsen and Schäffer.¹¹ $Cr^{III}(NO_3)_3 \cdot 9H_2O$ (10.09 g, 25.2 mmols) and 2,2' bipyridine (8.75 g, 56.0 mmols) were refluxed in aqueous $HClO_4$ (78.5 mmols, 100 cm^3 , $\approx 1\text{ mol dm}^{-3}$) for 8 hrs with periodic addition of NaOH (99.25 mmols total, $\approx 2\text{ mol dm}^{-3}$). The solution was cooled to room temperature, and the precipitated product was filtered off and washed with ethanol. The red product was dissolved on the sinter with dilute $HClO_4$ at $90\text{ }^\circ\text{C}$ and the solution was cooled slowly. This recrystallisation procedure was repeated once more. Yield = 3.9 g, 22.5 % (as % Cr). (Found: C, 39.11; H, 2.65; N, 9.12. Calc. for $C_{40}H_{38}N_8O_{20}Cl_4Cr_2$: C, 40.15; H, 3.20; N, 9.36). UV-vis (0.1 mol dm^{-3} $HClO_4(aq)$) (λ_{max} , nm (ϵ , $\text{dm}^3\text{ mol}^{-1}\text{ cm}^{-1}$; rel. ϵ given $\epsilon_{536} = 1$): found; 536 (-; 1.00); literature (1 mmol dm^{-3} HCl);⁶ 447 (79; 1.49), 537 (53; 1.00); (λ_{sh} (ϵ ; rel. ϵ)): found; 392 (-; 3.76), 420 (-; 2.59), 446 (-; 1.25).



This preparation followed the method of Hancock, Josephsen and Schäffer.¹⁶ $[(bpy)_2Cr(OH)_2Cr(bpy)_2](ClO_4)_4$ (0.75 g, 0.64 mmols) was heated at $55\text{ }^\circ\text{C}$ for 24 hrs in 72 w / w perchloric acid (17 g, 122 mmols). The reaction mixture was allowed to cool and was neutralized first with $Na_2CO_3 \cdot 10 H_2O$ (14.17 g, 50 mmols = 100 mmols OH^-) in hot water (10 ml) then with 1 mol dm^{-3} NaOH (22 cm^3 , 22 mmols). At this stage the solution became orange and product precipitated. The product was filtered and washed with cold water then ethanol. Yield = 0.15 g, 20 %.



The synthesis follows the method of Burstall and Nyholm,¹⁷ except that an alternative purification scheme suggested by Hancock *et al* is used.¹⁶ Anhydrous $CrCl_3$ (1.56 g, 9.85

mmols) and 2, 2'-bipyridine (4.72 g, 30.2 mmols) were refluxed in dry ethanol (50 ml) containing a catalytic quantity of zinc dust for 20 minutes. The solution was allowed to cool and a brown powder was filtered off. This product was washed repeatedly with ethanol until its colour became olive-green. The powder thus obtained was dried *in vacuo* at 60 °C. Yield = 2.44 g, 49%. (Found: C, 48.80; H, 3.44; N, 11.12. Calc. for $C_{20}H_{18}N_4CrCl_3O$: C, 49.12; H, 3.68; N, 11.46). UV-vis (H_2O) (λ_{max} , nm (ϵ , $dm^3 mol^{-1} cm^{-1}$)): found; 311 (5000), 394 (350), 556 (50); literature;¹⁷ 553 (43.7); (λ_{sh} (ϵ)): found; 416 (270), 445 (100), literature; 445 (90).

[PAA-Cr(bpy)₂]Cl

The procedure followed that of Anbalagan and Natarajan.¹⁴ 50% w/w poly(acrylic acid) (PAA, 2.16 g, 15.0 mmols of monomer unit) was made up to 20 ml with distilled water and the solution was neutralised to pH 7.2 with aqueous KOH. The solution was made up to 75 ml and was heated at 75 - 85 °C for 1 hr before the addition to the stirred solution, over 1 hr and in the dark, of $[Cr(bpy)_2Cl_2]Cl \cdot H_2O$ (0.65 g, 1.28 mmols) in water (30 cm^3). The solution was allowed to cool to ambient temperature and stirred for a further day. The total volume was made up to 150 ml, and the solution was dialysed in Visking tubing (BDH) placed in 1500 cm^3 of water, which was changed after 3 hours and then every day for the next three days. After this most of the water was removed *in vacuo* and the solution poured into a beaker containing 300 ml of acetone and 100 ml of 1,4 dioxane. The precipitated polymer was filtered, and redissolved in minimum water. The solution was reprecipitated, filtered, and redissolved twice further and was stored as the aqueous solution in the dark at 5 °C. Estimated yield = 31% as % Cr (given volume of solution obtained and UV-visible absorbance, and using the literature extinction coefficient for the 515 nm band). UV-visible (H_2O) (λ_{max} , nm (ϵ , $dm^3 mol^{-1} cm^{-1}$; rel. ϵ given $\epsilon_{513} = 1$)): found; 309 (-; -), 513 (-; 1.00); literature;¹⁴ 307 (16650; 277), 515 (60; 1.00); (λ_{sh} (ϵ ; rel. ϵ)): found; 393 (-; 3.05), 416 (-; 2.25), 445 (-; 1.31); literature; 390 (226; 3.77), 415 (165; 2.75), 445 (72; 1.20).

5.2.2 Electrochemistry

Instrumentation was as described in chapter 3. Investigations used a glassy carbon working, an SCE reference, and a Pt wire counter electrode. Electrochemical scans were generally performed between 0 and -1.2 to -1.5 V vs SCE in either 0.1 mol dm⁻³ KCl (aq) or 0.2 mol dm⁻³ CF₃COONa (aq) adjusted to pH 3.1 with CF₃COOH. The electrolytes were made up to approximately 1 mmol dm⁻³ in the complex of interest.

Electrochemical incorporation of [Cr(bpy)₂Cl₂]Cl into PVP

A glassy carbon working electrode was polished with three grades of diamond-paste, the finest of which was 1 μm, before it was sonicated in distilled water and rinsed with acetone. It was then dip coated in 70 μmol dm⁻³ PVP in DMF and dried in an oven. It was then placed in an electrochemical cell with a SCE reference electrode and a Pt wire counter electrode. The electrolyte was [Cr(bpy)₂Cl₂]Cl·H₂O (35 mg, 5 mmol dm⁻³) in 0.1 mol dm⁻³ KCl (15 cm³). The cell was held in the dark at -1.05 V for 12 hrs with a constant stream of argon through the solution. At the end of the reduction period the solution was emptied and the cell washed through three times with argon degassed 0.1 mol dm⁻³ KCl. The electrolytic solution was saved and kept under argon and in the dark before re-introduction into the electrochemical cell.

5.2.3 Raman Spectroscopy

The spectrometer, potentiostats, instrumentation, *ex-situ* roughening cycles, and data analysis method are as described in chapter 2. Scan conditions were: laser line, 514.5 nm; laser power, 150 mW; scan range, 100 - 1700 cm⁻¹. Once more, the concentration of the complex of interest was *ca.* 1 mmol dm⁻³.

5.3 Results

5.3.1 Electrochemistry

Chromium(III) bis(bipyridyl) complexes

Table 5.1 shows the positions of the cyclic voltammetric peaks for the various $[\text{LCr}(\text{bpy})_2]^{n+}$ complexes synthesized. Some of the scans from which the results were collated are given in Figures 5.2 -5.6. One general feature of all the CVs is that the cathodic peaks are much more poorly defined than the anodic peaks. This complicates any assignment of redox couples, and in Table 5.1, therefore, only the individual peak positions are given. The subject is considered further in the discussion section.

In addition to the potentials indicated on the Table and Figures, the solutions of the complexes were also swept between 0 V and +1 V. No faradaic processes were observed in this region.

The scan rate dependence of the CVs of each complex in KCl electrolyte has been investigated at 10, 20 and 100 mV s^{-1} and, in general, at slower scan rates additional peaks appear on the anodic scan. These peaks can also be reproduced at faster scan rates if the potential is held for any more than two seconds at the cathodic limit. An exception to this behaviour is given by solutions of PAA metallopolymer, which have very similar CVs at all scan rates, except that at 100 mV s^{-1} there is a weak shoulder at -1.04 V on the -0.98 V anodic peak.

In pH 3 CF_3COONa electrolyte all the chromium complexes except the PAA metallopolymer quickly turn red and give very similar voltammetric traces to that given for $[(\text{bpy})_2\text{Cr}(\text{OH})_2\text{Cr}(\text{bpy})_2]^{4+}$ in Figure 5.6, suggesting that this species is formed. The PAA polymer was not studied since it is insoluble at this pH. The results for the 5 day old $[\text{Cr}(\text{bpy})_2\text{Cl}_2]^+$ in KCl also resemble those in $\text{CF}_3\text{COONa} / \text{H}$ solution, except that the peaks at -0.68 and -0.44 V are much stronger. The latter peak tends to shift to higher potentials on subsequent scans and has been observed as high as -0.31 V in the dinuclear Cr complex.

Cr(bpy) ₂ Complex	Electro- lyte	Scan rate / mV s ⁻¹	Cathodic limit / V	Cathodic peaks / V	Anodic peaks / V
Dimer	Cl ⁻	100	-1.2	-	-0.96
	Cl ⁻	20	-1.2	-1.06	-0.98, -0.81
	CF ₃ CO ₂ ⁻	20	-1.5	-0.77, -1.03, -1.22	-0.98, -0.77, -0.68, -0.43
Monomer	Cl ⁻	100	-1.5	-	-1.14, -1.06 (sh)
	Cl ⁻	10	-1.5	-	-1.14, -1.09(sh), -1.01, -0.98
ML ₂ Cl ₂ ⁺	Cl ⁻	100	-1.5	-1.14	-1.07, -0.94 (sh), -0.90
	Cl ⁻	10	-1.5	-1.11	-1.18, -0.95, -0.91
	Cl ⁻ §	20	-1.5	-0.79, -0.98	-1.11, -1.01, -0.78, -0.65, -0.44
PAA- complex	Cl ⁻	20	-1.5	-1.28	-1.21, -0.98

Table 5.1: Electrochemistry of Cr bis(bipyridyl) complexes in aqueous solution, where dimer = $[(bpy)_2Cr(OH)_2Cr(bpy)_2](ClO_4)_4 \cdot 2 H_2O$, monomer = $[Cr(bpy)_2(OH_2)(OH)](ClO_4)_2$, and § designates a 5 day old solution.

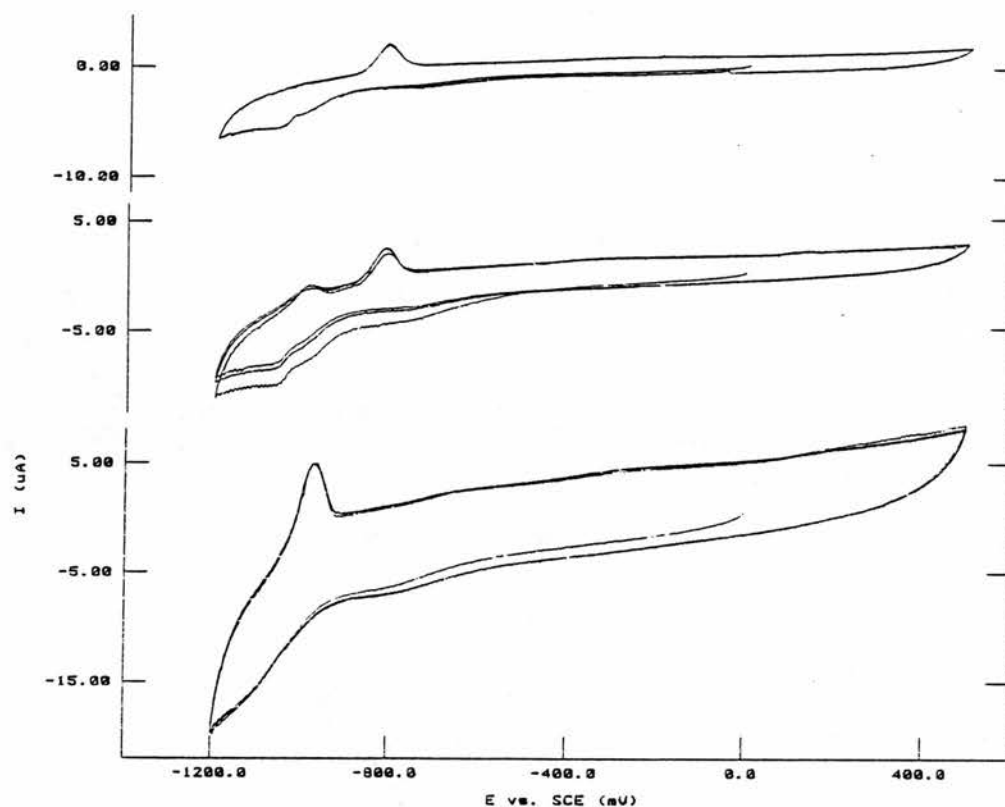


Figure 5.2: CVs of $0.5 \text{ mmol dm}^{-3} [(bpy)_2Cr(OH)_2Cr(bpy)_2](ClO_4)_4 \cdot 2 H_2O$ in $0.1 \text{ mol dm}^{-3} KCl (aq)$ at 10 (top), 20 (middle), and 100 (bottom) mV s^{-1} . Glassy carbon working electrode.

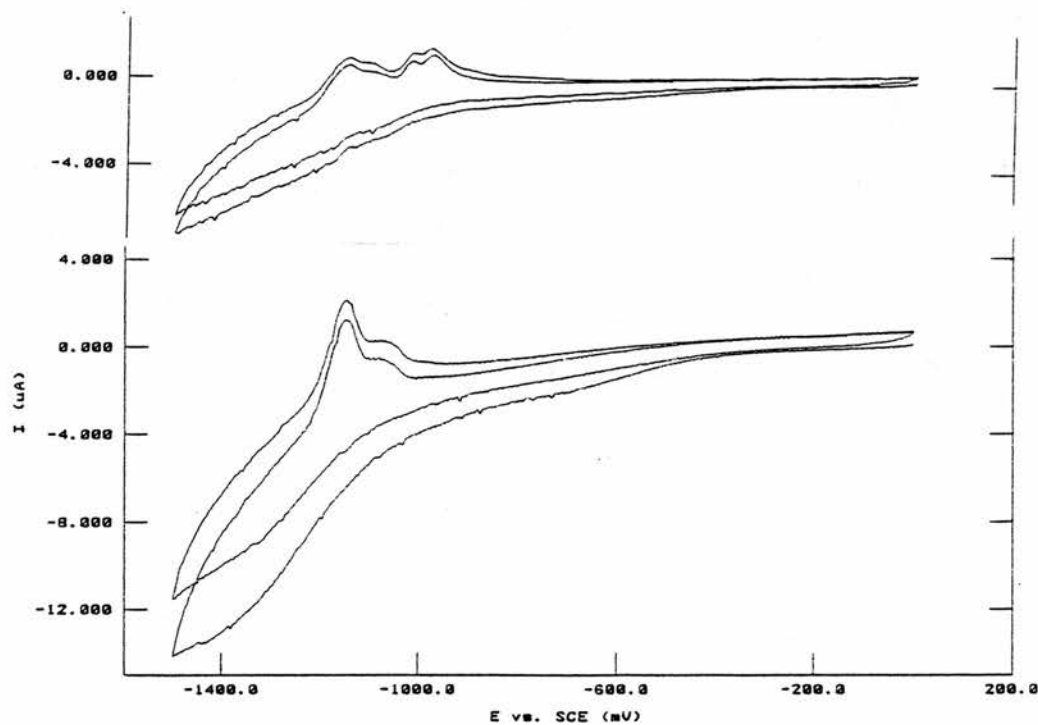


Figure 5.3: CVs of $1 \text{ mmol dm}^{-3} [Cr(bpy)_2(OH)_2(OH)](ClO_4)_2$ in $0.1 \text{ mol dm}^{-3} KCl (aq)$ at 10 (top) at 20 (bottom) mV s^{-1} scan rates. Glassy carbon working electrode,

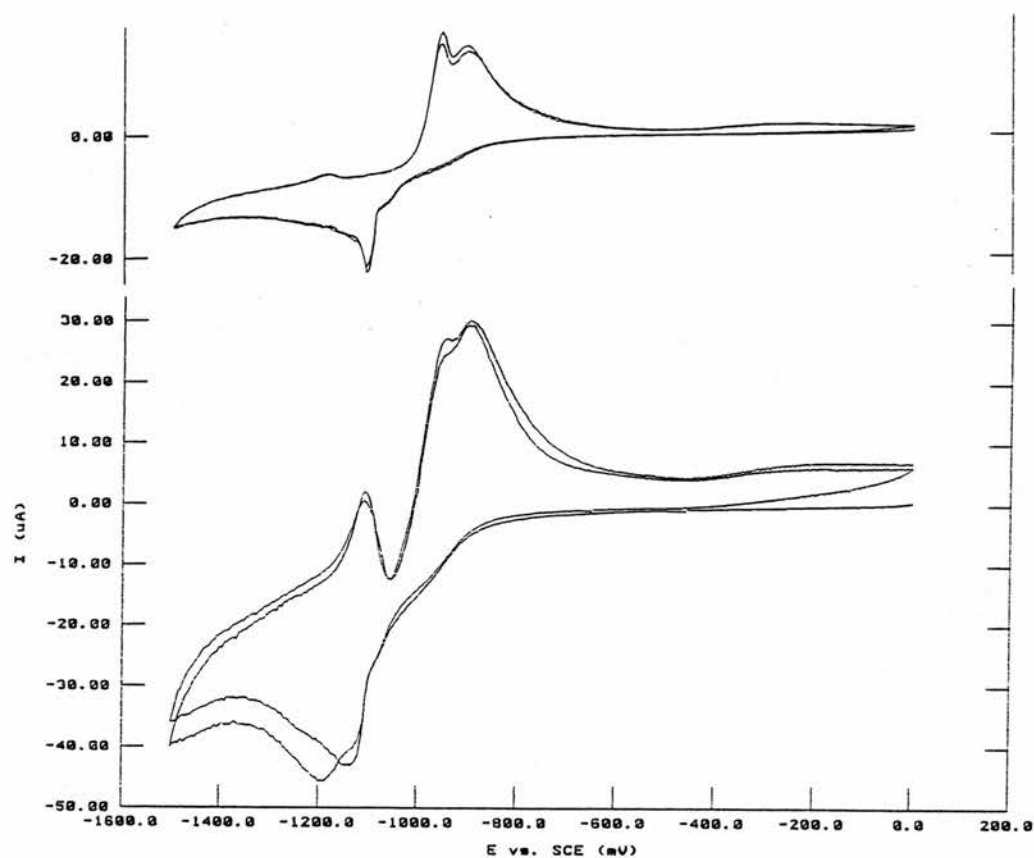


Figure 5.4: CVs of $1 \text{ mmol dm}^{-3} [\text{Cr}(\text{bpy})_2\text{Cl}_2]\text{Cl} \cdot 1 \text{ H}_2\text{O}$ in $0.1 \text{ mol dm}^{-3} \text{ KCl (aq)}$ at 10 (top) and 100 (bottom) mV s^{-1} scan rates. Glassy carbon working electrode.

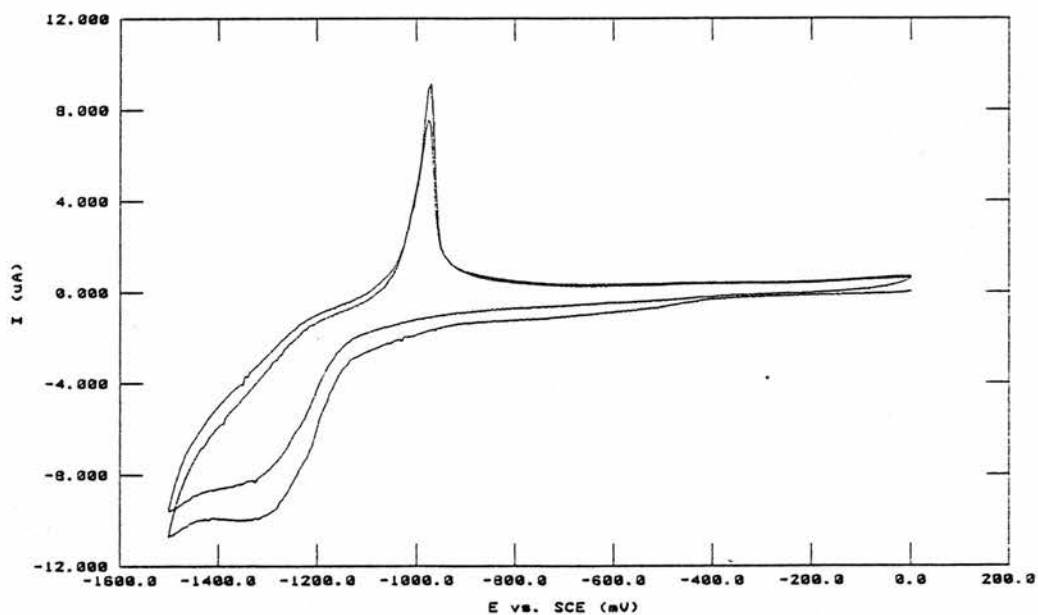


Figure 5.5: CV of $[\text{PAA-Cr}(\text{bpy})_2]\text{Cl}$ in $0.1 \text{ mol dm}^{-3} \text{ KCl (aq)}$ at 20 mV s^{-1} scan rate. Glassy carbon working electrode. Estimated concentration of $\text{Cr} = 8 \text{ mmol dm}^{-3}$.

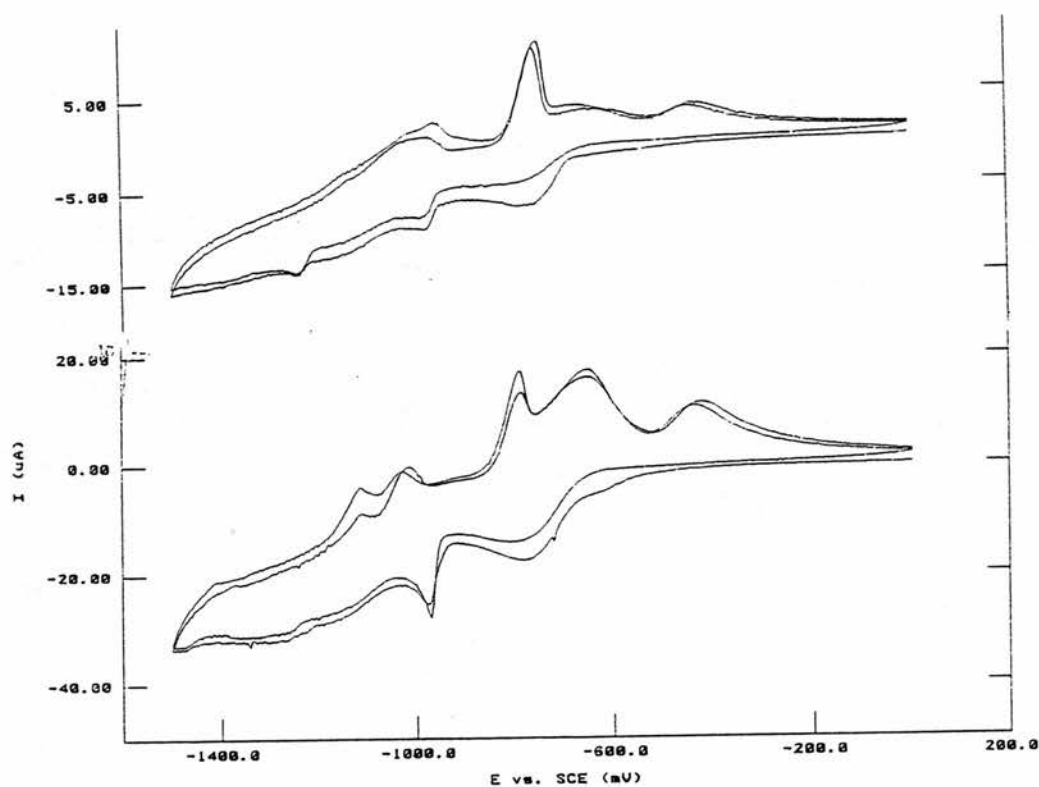


Figure 5.6: CVs of 1 mmol dm^{-3} $[(\text{bpy})_2\text{Cr}(\text{OH})_2\text{Cr}(\text{bpy})_2](\text{ClO}_4)_4 \cdot 2\text{H}_2\text{O}$ in 0.2 mol dm^{-3} $\text{pH}3 \text{ CF}_3\text{COONa}(\text{aq})$ electrolyte (top) and 5 day old solution of 1 mmol dm^{-3} $[\text{Cr}(\text{bpy})_2\text{Cl}_2]\text{Cl} \cdot \text{H}_2\text{O}$ in 0.1 mol dm^{-3} $\text{KCl}(\text{aq})$ electrolyte (bottom), both at 20 mV s^{-1} scan rate and a glassy carbon working electrode.

Incorporation into PVP

Figure 5.7 gives a typical trace of the PVP film in fresh 0.1 mol dm^{-3} KCl after 12 h exposure to a $[\text{Cr}(\text{bpy})_2\text{Cl}_2]\text{Cl}$ solution according to the procedure described in the experimental section. One redox couple is seen on cycling from -1 V to 0 V and back, with a half-wave potential of -0.32 V , and the anodic current significantly greater than the cathodic current. No other bands are observed, even with cathodic limits of up to -1.5 V . The scan rate dependence of the anodic peak current is linear, as shown by Figure 5.8.

Figure 5.9 shows the CV of the solution at a clean glassy carbon electrode after the incorporation procedure. This has a cathodic peak at -1.12 V and anodic peaks at -0.93 , -0.73 and -0.41 V .

Other attempts were made to incorporate chromium complexes into PVP by cycling a

coated electrode between 0 V and -1.5 V both in CF_3COO^- and chloride electrolytes. When CVs were taken in fresh solution no peaks were observed, indicating that the procedure had not been successful.

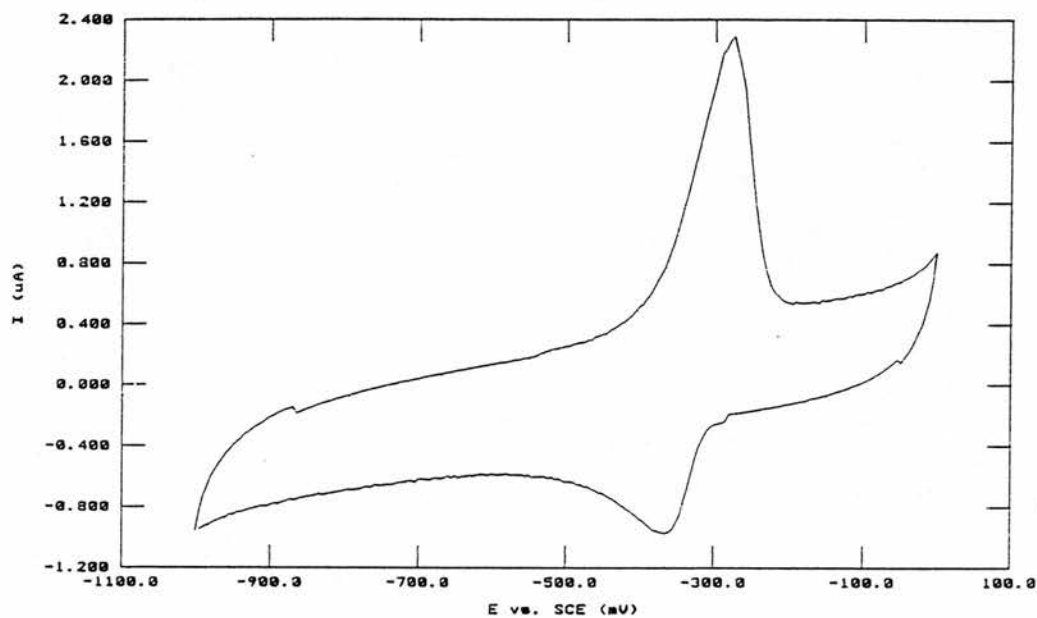


Figure 5.7: CV in $0.1 \text{ mol dm}^{-3} \text{ KCl (aq)}$ of dip coated PVP film on GC after incorporation of $[\text{Cr}(\text{bpy})_2\text{Cl}_2]^+$. Scan rate = 50 mV s^{-1} .

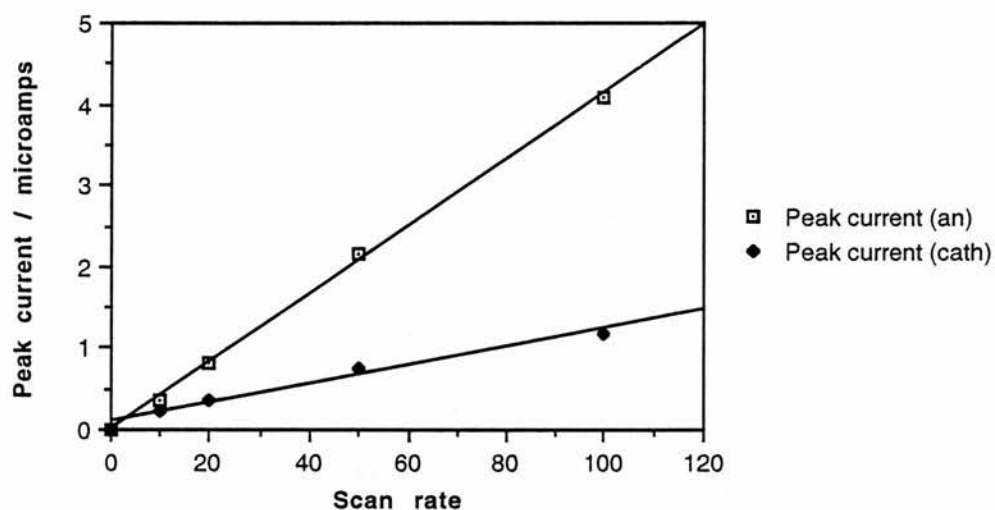


Figure 5.8: Current vs scan rate for anodic and cathodic peaks of PVP film after incorporation of $[\text{Cr}(\text{bpy})_2\text{Cl}_2]^+$.

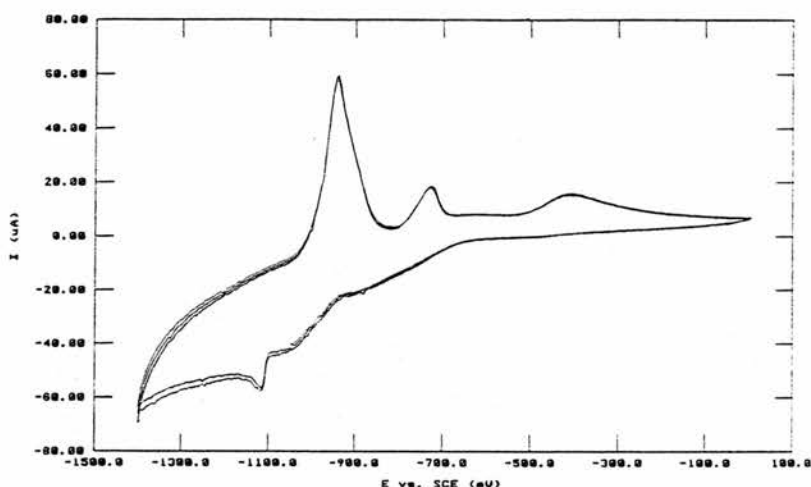


Figure 5.9: CV of electrolyte solution from the incorporation into PVP experiment after 12 hrs at -1.05 V. Scan rate = 20 mV s^{-1} .

5.3.2 SER Spectroscopy

The SERS bands and assignments for the chromium complexes studied are given in Tables 5.2 and 5.3. The corresponding spectra are displayed in Figures 5.10 - 5.13. The main features common to all of the spectra are the large changes in peak positions and intensities on adjusting the potential from -0.4 V to -1.1 V vs Ag / AgCl. For the dinuclear complex spectra were acquired at various potentials and the main change in spectral features was observed between -0.7 and -0.9 V. For the dichloride too, the -0.7 V spectrum more closely resembles the -0.4 V spectrum than that at the more cathodic potential. Both the dinuclear complex and the dichloride, however, do display some significant band shifts on changing the potential from -0.4 to -0.7 V, notably in the 1604, 1568, 1488, 1279, 1176 and 1040 cm^{-1} bands. The bands generally shift 5 - 10 cm^{-1} to lower wavenumbers at -0.7 V, and a further 5 - 10 cm^{-1} at -1.1 V. This potential dependence very closely mimics that of $\text{Co}(\text{bpy})_3^{2+}$ reported recently by Rubim *et al.*¹⁸

Bipyridine assigned bands dominate the spectrum, in accordance with the results of Kniepp *et al.*⁴ for $\text{Cr}(\text{bpy})_3^{3+}$ and studies on the Ru complex.¹⁹ The bipyridine appears both as a neutral ligand and, at more negative potentials, the radical anion, as evidenced by comparison with $\text{Li}^+\text{bpy}^{\cdot-}$.^{20,21} There is not much evidence to suggest that symmetry lowering affects the

spectrum of the Cr complexes, though the 1486 cm^{-1} band of Kniepp splits into two components, at around 1500 cm^{-1} and 1486 cm^{-1} in all the spectra acquired at -0.4 V. The relative intensities of the two bands vary from complex to complex; the 1500 cm^{-1} band is strongest in $[\text{Cr}(\text{bpy})_2(\text{OH})(\text{OH}_2)]^{2+}$, followed by $[\text{Cr}(\text{bpy})_2(\text{OH})(\text{OH}_2)]_2^{4+}$, $[\text{Cr}(\text{bpy})_2\text{Cl}_2]^+$ and finally $[\text{PAA-Cr}(\text{bpy})_2]^+$, where the 1486 cm^{-1} band dominates.

The spectra of the mononuclear and dinuclear aquahydroxo complexes at -1.1 V are as intense as those at -0.4 V, despite the expectation that this potential excursion would remove atomic scale roughness features. For the dinuclear complex, on returning to -0.4 V after such an excursion the Raman intensity was only slightly less than it was beforehand. The SERS spectrum after the excursion was essentially unchanged, except that the intensity of the 1486 cm^{-1} band increases at the expense of the 1500 cm^{-1} band and the broad band at 568 cm^{-1} becomes less intense.

In contrast to this behaviour are the potential dependences of the dichloride and PAA-complexes, for which the intensities at -1.1 V are much weaker than those at -0.4 V. The potential dependent shifts in band positions and relative band intensities, however, are very similar for all four complexes, once allowances are made for the fact that some weak bands are not detectable in all cases.

Spectra were also taken for the dinuclear complex in pH3 CF_3COONa electrolyte, after the electrode was roughened, as normal, in chloride. No significant differences between these and the KCl spectra were seen either at -0.4 or -1.1 V, although there was loss of intensity during acquisition of the spectrum at -1.1 V.

Raman shift / cm^{-1}								Assign- ment
Ru $(\text{bpy})_3^{2+}$ (ref. 19)	Cr $(\text{bpy})_3^{3+}$ (ref. 4)	Li ⁺ bpy• (20, 21)	$[(\text{bpy})_2\text{Cr}(\text{OH})_2\text{Cr}(\text{bpy})_2]^{4+}$			$[\text{Cr}(\text{bpy})_2(\text{OH}_2)\text{OH}].(\text{ClO}_4)_2$		
			-0.4 V	-0.7 V	-1.1 V	-0.4 V	-1.1 V	
1602	1601	1598	1604	1595	1584	1604	1582	v _{8a}
1558	1563	1558	1568	1562		1566		

Table 5.2: (continued on next page)

(continued from previous page)

Raman shift / cm ⁻¹								Assignment
Ru (bpy) ₃ ²⁺	Cr (bpy) ₃ ³⁺	Li ⁺ bpy•	Dimer			Monomer		
			-0.4 V	-0.7 V	-1.1 V	-0.4 V	-1.1 V	
					1525		1522	
		1497	1500			1499		ν _{19a}
1486	1486	1478	1488	1483	1464	1485	1466	
		1429			1415		1418	
1320	1325	1357	1324	1319	1326	1323	1339	C ₂ -C ₂ '
1276	1275	1273	1279	1273		1283	1279	ν _{9a}
1264					1260		1258	
		1205			1236		1236	
1176	1174	1151	1176	1173	1168	1177	1164	ν _{9a}
1109		1090			1102	1112	1101	ν _{18a}
1065	1062		1062	1062		1063		
1042	1036	1033	1040	1031	1025	1038	1027	ν ₁₂
1027	1012		1018	1015				ν ₁
		982			985		969	
820	808					809		CH _{op}
766	768		772	766	762	770	760	δ(ring _{ip})
732			732	735	733	737	738	2 x 371
667	663		664	669	658	667	656	δ(ring _{ip})
	625	<900		635	625		621	
			568 (br)	567 (br)		581 (br)	576 (br)	Cr-O _{str}
554				546				δ(ring _{ip})
491					478		469	
454			452	454	443		445	δ(rin _{op})
438								
424					431		425	
371	373		372	363	374	371	373	M-N _{str.}
286					283		273	-
236			232			226		δ(rin _{op})

Table 5.2: SERS bands and assignments for Cr(bpy)₂ complexes containing aqua and hydroxo ligands. Fuller descriptions of the assignments and abbreviations used are given in Table 3.3.

Raman shift / cm ⁻¹						Assignment
Cr(bpy) ₃ ³⁺ (ref. 4)	[Cr(bpy) ₂ Cl ₂] ⁺			[PAA-Cr(bpy) ₂] ⁺		
	-0.4	-0.7	-1.1	-0.4	-1.1	
1601	1604	1596	1580	1600	1584	ν _{8a}
1563	1566	1562		1566		
			1528			
	1500	1492		1500		ν _{19a}
1486	1484	1478	1474	1484	1466	
	1432	1440	1420			
1325	1324	1322		1312		C ₂ -C ₂ '
1275	1280	1274	1260	1280	1280	ν _{9a}
1174	1178	1168	1158	1176	1178	
	1110	1108	1100	1108	1100	ν _{18a}
1062	1062	1060	1058	1062	1056	
1036	1038	1032	1026	1040	1022	ν ₁₂
1012	1016	1014		1018		ν ₁
	902	888				
808	808	806				CH _{op}
768	768	766	762	768	762	δ(ring _{ip})
	736	736	736	738	736	2 x 371
663	666	664		664		δ(ring _{ip})
	652	652	654	656	656	
625		626	622	628	624	
	548	550				δ(ring _{ip})
	480	472	476		482	
	448	454	454			δ(ring _{op})
	424	422	422			
373	360	372	374	366	374	M-N _{str.}
	272	274	280			-
	226	208		226		δ(ring _{op})

Table 5.3: SERS bands and assignments for [Cr(bpy)₂Cl₂]⁺ and [PAA-Cr(bpy)₂]⁺ complexes.

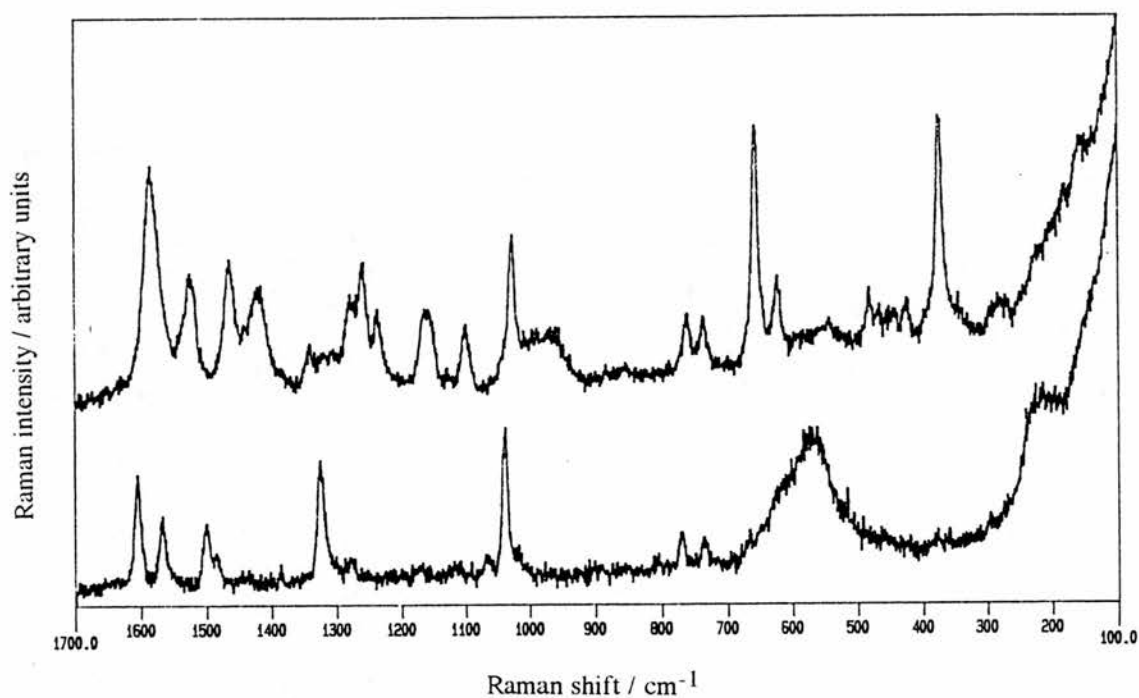


Figure 5.10: SERS spectra of $[(bpy)_2Cr(OH)_2Cr(bpy)_2](ClO_4)_4$ on Ag at -0.4 V (bottom) and -1.1 V (top), 514.5 nm excitation, 150 mW power, $100 - 1700$ cm^{-1} at 1 $cm^{-1}s^{-1}$.

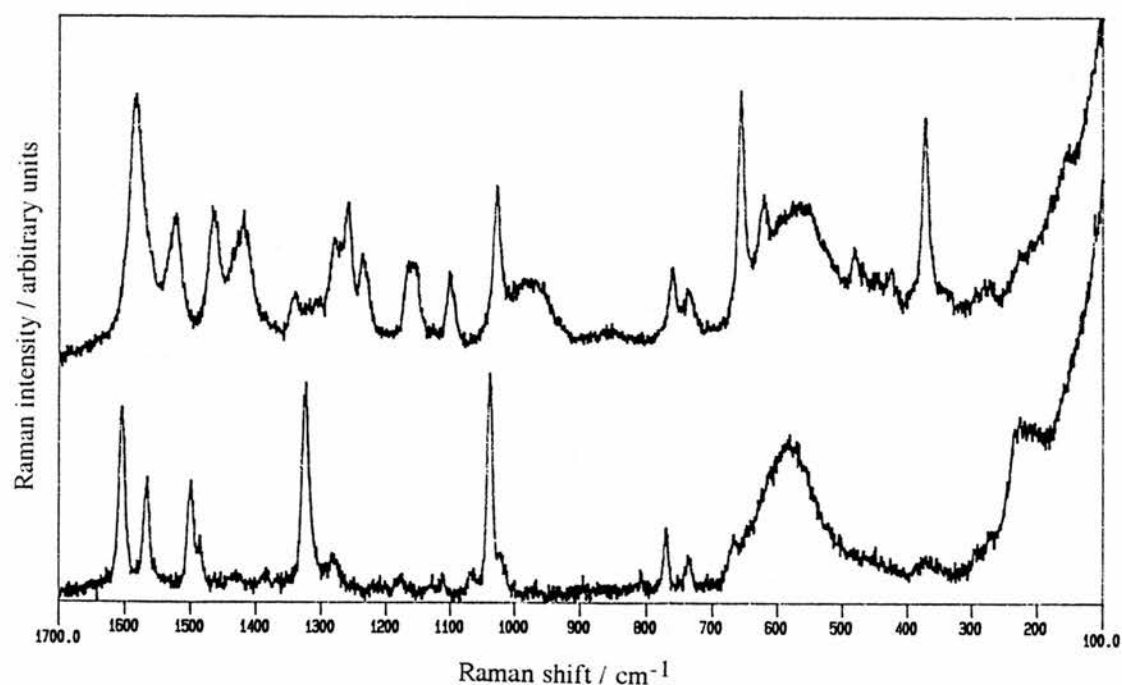


Figure 5.11: SERS spectra of $[Cr(bpy)_2(OH_2)(OH)](ClO_4)_2$ on Ag at -0.4 V (bottom) and -1.1 V (top), 514.5 nm excitation, 150 mW power, $100 - 1700$ cm^{-1} at 1 $cm^{-1}s^{-1}$.

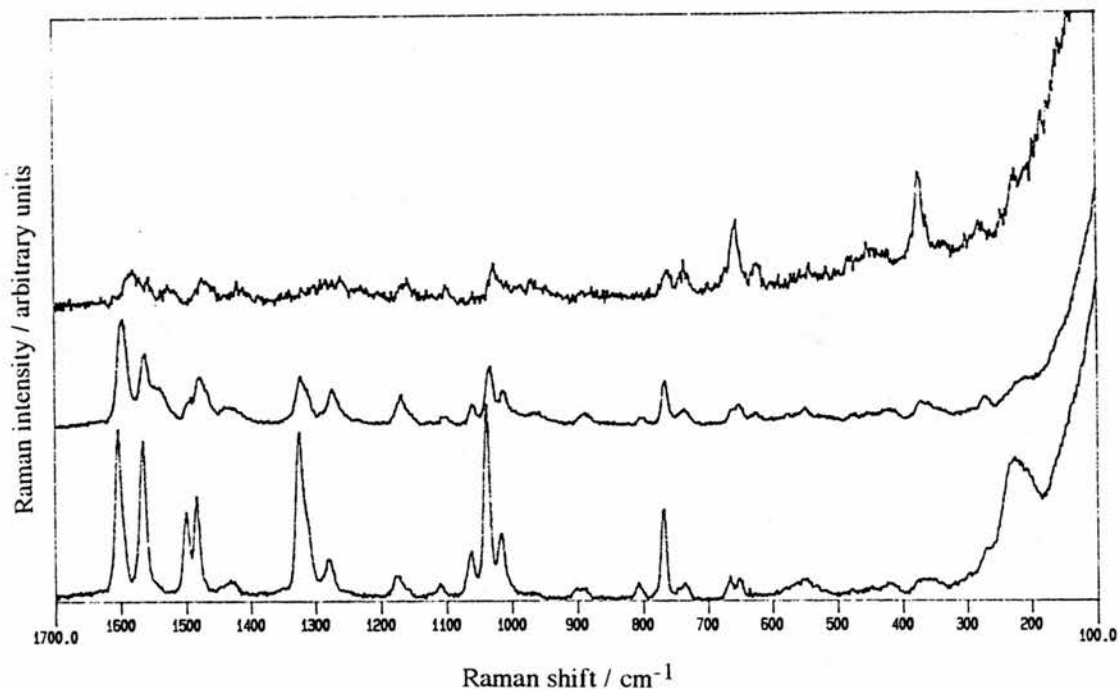


Figure 5.12: SERS spectra of $[\text{Cr}(\text{bpy})_2\text{Cl}_2]\text{Cl}$ on Ag at -0.4 V (bottom), -0.7 V (middle) and -1.1 V (top, 10x scale), 514.5 nm excitation, 150 mW power, $100 - 1700$ cm^{-1} at 2 $\text{cm}^{-1}\text{s}^{-1}$.

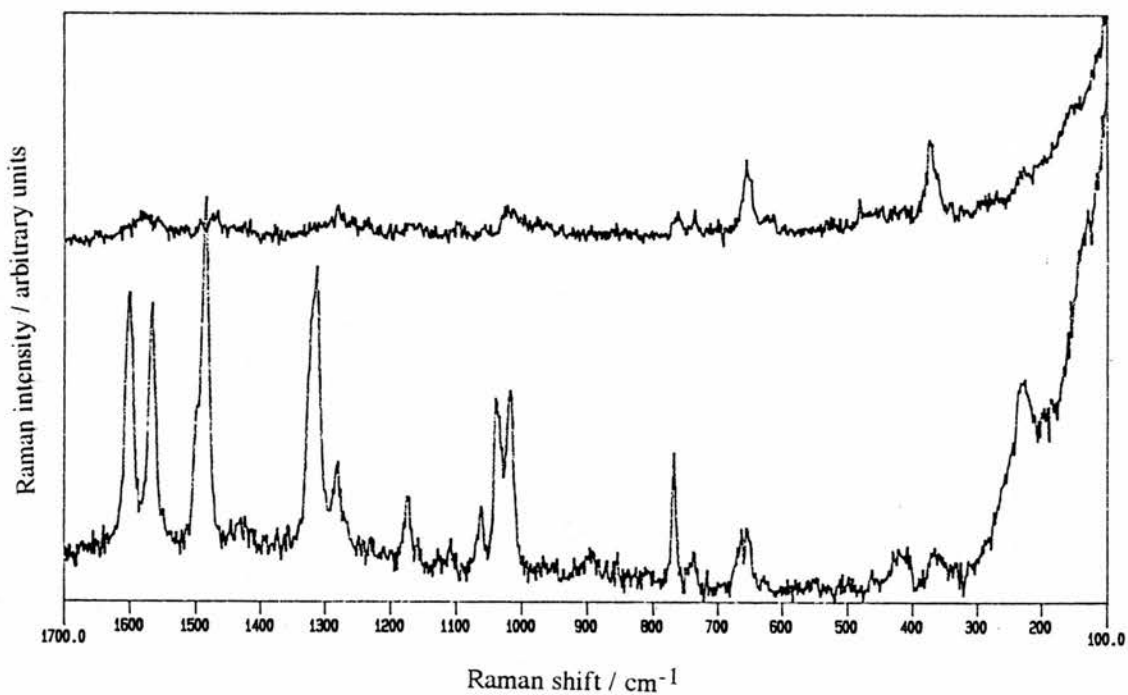


Figure 5.13: SERS spectra of $[\text{PAA-Cr}(\text{bpy})_2]\text{Cl}$ on Ag at -0.4 V (bottom) and -1.1 V (top), 514.5 nm excitation, 150 mW power, $100 - 1700$ cm^{-1} at 2 $\text{cm}^{-1}\text{s}^{-1}$.

5.4 Discussion

5.4.1 Syntheses

Although all of the chemical syntheses detailed in this chapter follow literature procedures, a number of new observations are worthy of brief consideration. Firstly, the red dinuclear and orange mononuclear hydroxo- complexes synthesized have the same empirical formula: $[\text{Cr}(\text{bpy})_2(\text{OH})(\text{OH}_2)]_n$, $n = 1, 2$. The orange complex is synthesized *via* cleavage of the red dinuclear complex in concentrated perchloric acid. In the method of Hancock *et al.*,¹⁶ after washing with ethanol the complex is dried at 60 °C for 2 hrs and dissolved from the filter by cold 1 mol dm⁻³ HClO₄ before the recrystallization step. Bearing in mind the explosive nature of perchlorate salts, it was attempted to perform this recrystallization without such a drying step. If the drying is not performed at all, or if the crude product is dried *in vacuo* for several hours, then the red dinuclear complex is re-formed instantaneously on contact with the 1 mol dm⁻³ HClO₄, and does not dissolve from the filter. Dissolving the re-formed complex in concentrated HClO₄ and re-neutralizing with carbonate followed by hydroxide precipitates the orange mononuclear species once more. Therefore, no improvement could be found on the published procedure. One other observation is that the neutralization and precipitation steps need to be carried out within 24 hrs of the heating otherwise no significant yield is obtained.

Unsuccessful attempts were made to recrystallize the olive-green $[\text{Cr}(\text{bpy})_2\text{Cl}_2]\text{Cl}\cdot\text{H}_2\text{O}$ from ethanol and 0.1 mol dm⁻³ HCl. Although crystals formed, these were brown, a colour indicative of the impure product obtained by Burstall and Nyholm,^{16,17} and probably due to traces of aqua complexes.

$[\text{Cr}(\text{bpy})_2\text{Cl}_2]\text{Cl}\cdot\text{H}_2\text{O}$ was also used in attempts to substitute pyridine onto the metal centre chemically (as a model study for PVP) by refluxing in 5:1 pyridine : water solution. No product was isolated and UV-visible spectral changes could be accounted for by slow discoloration of the solvent mixture. Addition of excess AgNO₃ to try and precipitate ligated Cl⁻ also failed: AgCl is soluble in pyridine, and the only precipitation that occurred over time was of lilac silver complexes. Clearly, this Cr(III) complex is inert to thermal substitution

under these conditions. A recent publication has used silver complexes of bidentate ligands, including bipyridine, phenanthroline, and 2-substituted pyridines to prepare mixed ligand complexes of Cr(III).²² Such an approach may be worthy of investigation for pyridine substitution.

In the synthesis of [PAA-Cr(bpy)₂]Cl described in the experimental section not all the experimental parameters have been optimized. In particular the polymer used was of a rather low average molecular weight (5000) due to reasons of immediate availability. If the Cr complex is estimated to attach to the polymer in the same stoichiometry as the reaction mixture contains, i.e. 11.71 acrylic acid units : 1 Cr, then the average molecular weight of the metallopolymer would be around 8000. Usually, only high molecular weight polymers (Mwt > 50000) give good quality films on evaporation.²³ Also, given that molecular separation using Visking tubing is efficient only for moieties of molecular weight above *ca.* 13000, it can be seen that this step is not ideal. The result is a low estimated yield of polymer, and although the product obtained has been adequate for the solution studies described herein, it is expected that a higher molecular weight polymer (commercially available) will be required to produce a polymer with satisfactory film-casting properties.

5.4.2 Electrochemical Experiments

Previous Studies

There have been numerous studies on the electrochemistry of chromium complexes with bipyridine and phenanthroline. In acetonitrile electrolytes the tris complexes, [Cr(bpy)₃]³⁺ and [Cr(phen)₃]³⁺ can be reduced by as many as four electrons without ligand substitution taking place.²⁴ The first three reductions, at -0.20 V, -0.71 V and -1.28 V vs SCE for [Cr(bpy)₃]³⁺, are considered to be metal centred, such that the formal oxidation state below -1.28 V is Cr⁰. The reduction to the monoanion at -1.91 V, on the other hand, is ligand centred (i.e. bpy → bpy^{-•}).

In aqueous solution, reduction of [Cr(bpy)₃]³⁺ by even one electron results in substitution of one or more of the bipyridine ligands by coordinated water via an EC

mechanism (where E = electrochemical [reduction] step, C = chemical [ligand substitution] step).¹⁰ A reaction scheme of the processes that take place during a CV sweep is given in Figure 5.14. The kinetics of this electrochemistry has also been investigated.²⁵

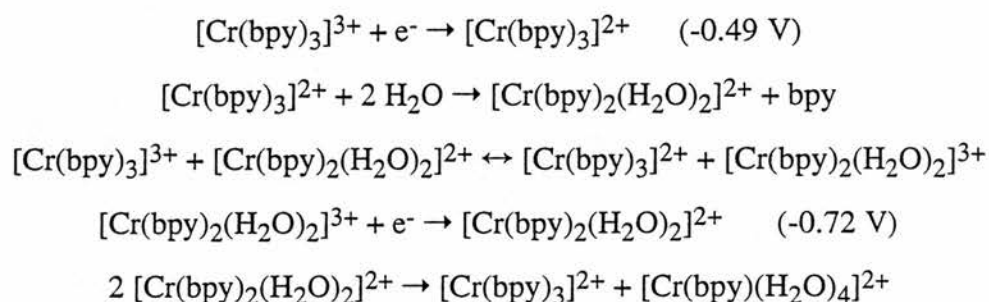


Figure 5.14: Reaction scheme for the electrochemical reduction of $\text{Cr}(\text{bpy})_3^{3+}$ by one electron in $0.1 \text{ mol dm}^{-3} \text{ KCl}(\text{aq})$ and subsequent ligand substitution steps. From ref. 10

The studies mentioned above use the hanging mercury drop electrode (HMDE), which has a high overpotential for hydrogen evolution in water. The aqueous electrochemistry of the complexes $[\text{Cr}(\text{bpy})_2(\text{H}_2\text{O})_2]^{3+}$ ^{10,26} and $[\text{Cr}(\text{bpy})_2\text{Cl}_2]^+$ ²⁶⁻²⁸ have also been studied at this electrode, the former to confirm the role of the diaqua species in the mechanism shown in Figure 5.14. The mechanism also operates in solutions of the dichloride, which undergoes initial aquation according to the equation:

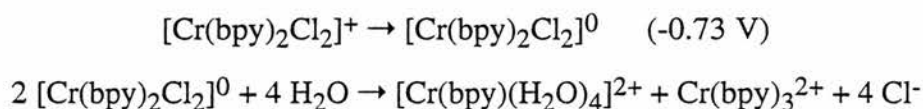


Figure 5.15: Scheme of reaction for $[\text{Cr}(\text{bpy})_2\text{Cl}_2]^+$ reduction by one electron in $0.1 \text{ mol dm}^{-3} \text{ KCl}(\text{aq})$. (From ref. 20)

The electrochemistry of these complexes has also been studied at solid electrodes. Sugden *et al*²⁹ used a mercury coated Pt electrode to study the redox activity of $[\text{Cr}(\text{bpy})_3]^{3+}$ and $[\text{Cr}(\text{bpy})_2\text{Cl}_2]^+$ in an attempt to relate the results to the mutagenicity of the complexes. Fitch *et*

al³⁰ studied the tris complex and $[\text{Cr}(\text{bpy})_2(\text{H}_2\text{O})_2]^{3+}$ at platinum and trapped within the pores of clay modified electrodes.

In this study, the electrochemical responses of PAA and PVP metallopolymer are reported for the first time, the properties of the dimeric and monomeric aquahydroxo complexes are compared and attempts are made in a later section to correlate the electrochemical results with those from SERS spectroscopy.

Common Features of Cyclic Voltammograms

Before considering each complex in turn, one feature common to many of the CVs displayed in Figures 5.2 - 5.7, especially of the aquahydroxo complexes, is worthy of note. This is the fact that the cathodic peaks are much more poorly defined than the anodic peaks. In other words, if one was able to measure the full-width at half-maximum (FWHM) of the cathodic peaks, then they would give larger values than those for the corresponding anodic peaks. Two factors could contribute to the observed voltammograms, these being slow electron transfer between glassy carbon and the Cr complexes and a greater number of products being present on the cathodic scan, each with smaller reduction currents. The latter of these can be discounted since the cathodic sweep is carried out first, and substitution reactions to form a range of products are only expected once the initial reduction to Cr^{2+} commences. Thus, slow electron transfer is invoked as the main cause of the broadening, and the role of the GC electrode is important, since a similar phenomenon is not seen for any of the complexes at HMDE^{10,24-26} or bare platinum³⁰ electrodes. The phenomenon is seen for $[\text{Cr}(\text{bpy})_2\text{Cl}_2]^+$ at mercury-coated platinum,²⁹ but is not evident for the same complex in this study.

If the slow electron transfer is general, then better defined peaks may arise from the reduction or oxidation of adsorbed species. If the electron transfer rate, however, is specifically a property of Cr^{III} reduction at the glassy carbon electrode then the nature of the electron transfer may have a role in determining its rate. During reduction to the $[\text{Cr}^{\text{II}}(\text{bpy})_2\text{X}_2]$ complexes, which are low-spin, the electron is transferred into a bonding orbital to give a t_{2g}^4 configuration. However, substitution of a second bipyridine ligand, by water for example (see Figure 5.14), will lead to spin-crossover,³¹ and if any such species persists and is

subsequently re-reduced from Cr^{III} to Cr^{II}, an e_g antibonding orbital will be filled, and the electron transfer will be accompanied by distortion of the octahedral geometry.

Comparison of $[\text{Cr}(\text{bpy})_2(\text{OH}_2)(\text{OH})^{2+}]_n$ ($n = 1,2$) and $[\text{Cr}(\text{bpy})_2\text{Cl}_2]^+$

In the CVs of the complexes, the anodic limit is kept the same for each scan rate, and so the length of time any species spends in the Cr^{II} state, and therefore the length of time during which it is susceptible to substitution, is scan rate dependent. The appearance of a larger number of peaks at slower scan rates is therefore indicative of EC mechanisms.

In the mononuclear and dinuclear aquahydroxo complexes, the reduction peaks are very weak, although the reduction of the parent dimer is seen at around -1.06 V, and forms a redox couple with the oxidation at around -0.97 V. For both dimer and monomer, oxidation bands appear at slow scan rates at around 120 - 170 mV more positive than the Cr(II/III) oxidation of the parent complex. For the monomer, both the parent oxidation and an oxidation band that appears at slow scan rates have two current maxima. This is probably due to the presence of two slightly different species in solution at the measured pH of 5.7, these being the $[\text{Cr}(\text{bpy})_2(\text{OH}_2)(\text{OH})]^{2+}$ and $[\text{Cr}(\text{bpy})_2(\text{OH})_2]^+$ ions (the pK_a of the former is 6.1)²⁹. By analogy with the scheme in Figure 5.14, further reaction to give a species with a total of four aqua and hydroxo ligands could occur, with the concomitant production of $[\text{Cr}(\text{bpy})_3]^{2+}$. However, no Cr(II/III) oxidation at around -0.49 V is seen for the tris(bipyridyl) complex and it may be that surface adsorption, for example via hydrogen bonding of aqua and hydroxo ligands with surface carboxylate groups, stabilizes the complex against this particular reaction pathway. The two new peaks that appear for the monomer are centred at about -1.00 V, very close to the value for the dimer. One of the peaks can be assigned, therefore, to the dimerization product. The second oxidation peak is suggested to be a related species in a slightly different protonation state. One possibility is a species containing a single H_3O_2^- bridge, as shown in Figure 5.16, which could result from the reaction between aquahydroxo and dihydroxo monomers. The study of Sugden *et al*²⁹ on the dihydroxo complex at pH7 corresponds well with this result in the anodic sweep. Because of the higher pH the aquahydroxo monomer is present in much lower concentration and it is this species rather than

the dihydroxo that gives a shoulder on the oxidation curve. No dimerization is seen in Sugden's study, partly due to the lower concentration of $[\text{Cr}(\text{bpy})_2(\text{OH}_2)(\text{OH})]^{2+}$ present and also because of the higher scan rates used. The mechanism suggested for the dimerization is given below in Figure 5.16:

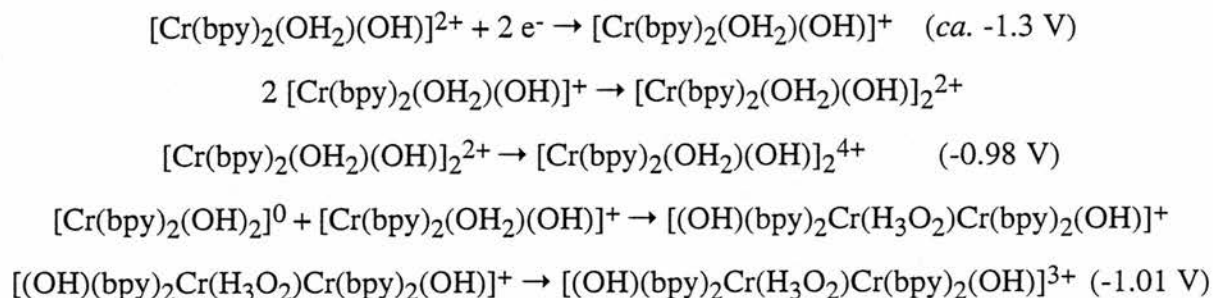


Figure 5.16: Reaction scheme for the reduction and dimerization of $[\text{Cr}(\text{bpy})_2(\text{OH}_2)(\text{OH})]^{2+}$

The dimer itself undergoes an EC reaction at slow scan rates, as evidenced by an anodic peak at -0.81 V (Figure 5.2), although this reaction is not seen for the dimer produced from monomer reduction, as shown in Figure 5.16. At 10 mV s^{-1} scan rate, the oxidation peak for the parent complex disappears and is replaced completely by the new peak. The nature of the reaction is not immediately obvious. The possibility of substitution of one bipyridine ligand with water is again rejected because of the absence of an anodic peak for $[\text{Cr}(\text{bpy})_3]^{2+}$ at -0.50 V , and also because the driving force for the substitution in Figure 5.14 is the production of $[\text{Cr}(\text{bpy})_3]^{3+}$. The conversion of the dimer to some mononuclear compound is a prerequisite for formation of the tris(bipyridyl) complex, but, as evidenced by the conditions needed for its hydrolysis,¹⁶ the bridging ligands are quite robust. The product of the chemical step may be monomeric, but its oxidation potential does not match that of $[\text{Cr}(\text{bpy})_2(\text{OH}_2)(\text{OH})]^+$.

There is a difference of *ca.* 150 mV between the oxidation potentials of monomeric and dimeric analogues of the same metal complex in this study. The work of Holwerda *et al*³², who predicted that linear oxo- and bent μ -hydroxo bridged dimers should have similar redox potentials to the equivalent monomers, is thus shown not to be correct for the case of the H_3O_2^- bridges present here.

$[\text{Cr}(\text{bpy})_2\text{Cl}_2]$ CVs have usually been rationalized in terms of immediate conversion to the diaqua complex upon reduction, as shown in Figure 5.15. The CVs in this study show that after reduction of the chloride, which has been assigned in previous studies at around -0.75 V, adsorption of the neutral $[\text{Cr}(\text{bpy})_2\text{Cl}_2]^0$ accompanies aquation. The main product of this is probably the aquahydroxo complex, $[\text{Cr}(\text{bpy})_2(\text{OH}_2)(\text{OH})]^+$, as a redox couple corresponding to this is seen at -1.10 V. The reduced complex, of course, will not generate a cathodic peak at this potential, but if the complex is re-oxidized to $[\text{Cr}(\text{bpy})_2(\text{OH}_2)(\text{OH})]^{2+}$ by unreduced dichloride, and after this remains adsorbed at the surface, then the sharp cathodic peak at -1.14 V would be expected. The anodic portions of the voltammograms are therefore similar to those given by $[\text{Cr}(\text{bpy})_2(\text{OH}_2)(\text{OH})]^{+/2+}$, except that the dimerization reaction is further advanced at each scan rate than at the same scan rate when $[\text{Cr}(\text{bpy})_2(\text{OH}_2)(\text{OH})]^{2+}$ is the initial solution species, and is essentially complete at 10 mV s^{-1} . This is because the adsorption and reduction of the complex takes place earlier in the cycle and the chemical reaction of the reduced complex has more time to proceed to completion. The reactions involved in this reduction are summarized in Figure 5.17:

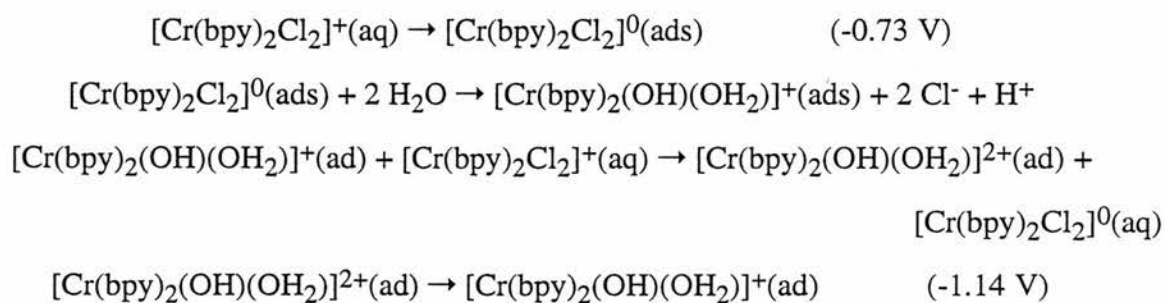


Figure 5.17: Reaction scheme for reduction and substitution of $[\text{Cr}(\text{bpy})_2\text{Cl}_2]^+$ at the glassy carbon electrode.

The voltammograms in Figures 5.6 and 5.9 represent mixtures of products from various reactions detailed in the preceding schemes. Over the course of 5 days (Fig 5.6, top), there is significant aquation of $[\text{Cr}(\text{bpy})_2\text{Cl}_2]$, even though this is in its oxidized state. This can be distinguished from the situation above, where little aquation has taken place before reduction

commences, because of the nature of the predominant aquated complex, which has a half-wave potential of -0.88 V (reduction at -0.98 V, oxidation at -0.78 V), and is the same as the product given in slow scans of the dimer. A couple for the dichloride is also seen at $E_0^{1/2} = -0.73$ V as is an oxidation peak for $[\text{Cr}(\text{bpy})_3]^{2+}$ at -0.44 V. The other peaks that appear only on the anodic scan could be due to the presence of any of a number of products including mono (bipyridyl) species. The fact that reduction waves for the dichloride and dimer are readily observable is also worthy of note, since it shows that both oxidized species adsorb onto the electrode over a period of time.

Slightly different mixtures of complexes are given by the pH3 solution of dimer and the exhaustively electrolysed solution used to prepare the PVP metallopolymer. In the former (Figure 5.6, bottom) the couple centred at -0.73 V is attributed to the diaqua complex, $[\text{Cr}(\text{bpy})_2(\text{H}_2\text{O})_2]^{2+/3+}$, in accordance with Soignet and Hargis.¹⁰ This complex has a pK_a of 3.5²⁹ and so the reduction of some adsorbed aquahydroxo complex is also seen at -1.22 V.

Electrochemistry of Metallopolymer

The CV of the PAA complex at 20 mV s^{-1} is shown in Figure 5.5, and the response seen is relatively unaffected by changing the scan rate. The initial reduction potential of the polymer can be roughly estimated by comparison with the mixed ligand complex $[\text{Cr}(\text{bpy})_2(\text{ox})]^+$, which undergoes an initial reduction only 60 mV negative of the value seen for $[\text{Cr}(\text{bpy})_3]^{3+}$.³³ An adsorption enhanced peak is seen for the oxalate at -1.17 V, close to the potential of the single cathodic peak observed, at -1.21 V, in this study. Lawrance and Sangster³³ do not speculate on the nature of the species involved in this reduction, but do note that ligand dissociation of the mono(oxalate) Cr^{III} mixed ligand complexes is $10^4 - 10^5$ times more rapid in aqueous solution than for the tris(bipyridyl) complex. The dissociation of the Cr^{II} complex should be even faster. The dissociation in this study is evidenced by the strong anodic peak due to the aquahydroxo-dimer, and it seems likely that the couple centred at around -1.25 V is due to some intermediate aquation product.

The appearance of the CV in Figure 5.7 suggests that the electrolytic reduction of $[\text{Cr}(\text{bpy})_2\text{Cl}_2]^+$ to give a metallopolymer complex is successful. The half-wave potential of

-0.32 V is even more positive than that of $[\text{Cr}(\text{bpy})_3]^{2+/3+}$. When it is considered that hexacoordination of pyridine to Cr stabilizes the Cr^{II} state in air,³⁴ a $[\text{Cr}(\text{bpy})_2(\text{py})_2]$ core is the probable product of this reaction. The core is much more stable on reduction to Cr^{II} than the other complexes studied herein. A very recent report of in which 2-vinylpyridine is polymerized by $\text{Cr}(0)$ under cryogenic conditions is worthy of note here, since this also yield a $\text{Cr}(\text{II})$ metallopolymer with N_6 coordination.³⁵

One can speculate that during the initial stage of the reaction between the metal complex and PVP, the choice of the $[\text{Cr}(\text{bpy})_2\text{Cl}_2]^+$ complex is important. The polymer will have a slight positive charge in pH 5-6 solution, and will not be highly permeable to cations. However, neutral Cr^{II} dichloride will be able to permeate slowly into the film, where it may react initially either with pyridine or water, generating a cationic metal complex, free Cl^- anions and possibly H^+ . As the reaction proceeds, therefore, the ionic strength of the polymer layer will increase, and the layer is expected to swell, facilitating access of more Cr centres.

5.4.3 SERS Experiments

Correlation of SERS Intensity and Adsorption

Since the SERS spectral features of the four complexes studied are all quite similar, they will be considered together. The main difference between the spectra, that of signal intensity upon reduction to -1.1 V, splits the complexes into two groups, with the aquahydroxo monomer and dimer in one group, and $[\text{Cr}(\text{bpy})_2\text{Cl}_2]^+$ and $[\text{PAA-Cr}(\text{bpy})_2]^+$ in the other. The fact that there is little intensity difference in spectra taken at -0.4 V before and after a lengthy (long enough to scan from 100 - 1700 cm^{-1}) excursion to -1.1 V in the former pair of complexes suggests that stabilization of the atomic-scale SERS active surface rather than any resonance enhancement is responsible for the good spectra obtained at negative potentials. At -1.1 V the aquahydroxo species are expected to be present in all four solutions, as discussed in the previous section; however, these species will only be present in low concentrations in the dichloro and PAA complexes before reduction. The crucial factor seems to be the charge of the complex immediately after reduction. In the absence of any stabilization atomic-scale roughness sites,

associated with Cl^- desorption, are lost below about -0.6 V (chapter 2). At this potential the aquahydroxo complexes are still in the Cr^{III} oxidation state and carry a $2+$ charge per Cr centre. These may adsorb on the Cl^- layer and therefore stabilize it at -0.6 V , and indeed even to -1.1 V in the case of the monomer. The dimer is expected to be reduced at a slightly less cathodic potential of -0.95 V vs Ag / AgCl (N.B. different reference electrode from CV studies), assuming the same redox potential as at glassy carbon, and although some stabilization may be lost, the adsorbed complex will still be cationic and strong SERS spectra are therefore still seen at -1.1 V .

The case with the dichloro- and PAA- complexes is different. These are monocations in the Cr^{III} state, and are reduced to Cr^{II} neutral complexes prior to any large scale substitution by H_2O . As a consequence at around -0.6 V to -0.7 V , where both complexes are expected to have their reductions, neutral species will be generated. These are not expected to stabilize Cl^- at the surface and a majority of SERS sites will therefore be lost before substitution reactions to give the aquahydroxo species regenerate cationic metal complexes.

Potential Dependent Band Shifts

The spectra of all the complexes at -0.4 V share some similarities to those of Kniepp *et al*⁶ for both “normal” Raman spectra of $[\text{Cr}(\text{bpy})_3]^{3+}$ and the SER spectra of $[\text{Cr}(\text{bpy})_3]^{2+}$. In addition to the bands seen in their SERS, additional bands are consistently observed in this study at 1500 cm^{-1} , 1110 cm^{-1} , 732 cm^{-1} , and at around 570 cm^{-1} , along with several below 500 cm^{-1} . Most of these may be assigned to weak bipyridine modes by comparison with SERS of $[\text{Ru}(\text{bpy})_3]^{2+}$,¹⁸ and the broad band at around 570 cm^{-1} , seen most strongly in the aquahydroxo monomer and dimer, is assigned to a Cr-O stretch. The fact that this band is reasonably intense suggests that it is probably the O-donor ligands that are involved in anchoring the complexes to the SERS active electrode.

The band at 1503 cm^{-1} in the Kniepp study is seen for solution Raman spectra at both 514.5 nm and 457.9 nm , and this shifts to 1486 cm^{-1} on reduction in the SERS spectrum. These SERS data were obtained on a silver sol, and from calibration using 1,1'-diethyl-2,2'-cyanine it was determined that the surface was equivalent to an electrode held at *ca.* -0.85 V vs

Ag / AgCl. At -0.4 V, in this study, all the complexes are expected to be in the Cr^{III} oxidation state, so the presence of both the 1500 cm⁻¹ and 1486 cm⁻¹ bands for all the complexes cannot indicate the presence of both oxidation states for each. However, all three other bands whose Raman shifts change between oxidation states in the Kniepp study are observed at intermediate wavenumber shifts here, as shown in Table 5.4 for the aquahydroxo dimer. Similar results are obtained for the other complexes (see main assignment Tables: 5.2 and 5.3). Separate bands for the two different states are not observed in this study except for the 1503 cm⁻¹ band, which has a wavenumber shift of 17 cm⁻¹ on change of state, rather than the more typical shift of 7 cm⁻¹ for other bands.⁶

Raman shift / cm ⁻¹		
Soln. Raman ⁶ - [Cr(bpy) ₃] ³⁺	SERS ⁶ - “[Cr(bpy) ₃] ²⁺ ”	SERS - [(bpy) ₂ Cr(OH)] ₂ ⁴⁺
1608	1601	1604
1571	1563	1568
1503		1500
	1486	1488
1325	1325	1324
1043	1036	1040

Table 5.4: Comparison of SERS band positions in this study with normal Raman and SERS bands observed by Kniepp et al⁶.

From the relative intensities of the 1500 cm⁻¹ and 1488 cm⁻¹ bands in each complex one might expect to be able to predict the shifts of bands occurring at values intermediate between those of Kniepp for normal Raman and SERS. Such analysis proves inconclusive; however, when both the 1500 cm⁻¹ and 1488 cm⁻¹ bands are present the relative intensities of other bands are intermediate between those observed in Kniepp's spectra, and do change as expected with differing values of I_{1500}/I_{1488} .

That two different species are involved is, therefore, undeniable, though at this potential these are not consistent with different redox states. They could represent different adsorption states of the Cr^{III} complexes, in which case the bands that resemble Kniepp's Cr^{II} spectra would be expected from adsorbed species. However, it is the 1500 cm⁻¹ band, found in solution studies by Kniepp, that seems to correlate with stronger adsorption at the surface at -0.4 V. It was checked to see if the intensity of this band could be correlated with the intensity of the Cr-O stretching frequency, itself thought to be indicative of adsorption, and although some correspondence is found in initial spectra at -0.4 V, the relationship breaks down for spectra acquired after a cathodic excursion, which have very strong Cr-O stretches despite the 1500 cm⁻¹ band being absent.

At -0.55 V and -0.70 V, the dinuclear complex gives spectra that increasingly resemble the SER spectra assigned by Kniepp to [Cr(bpy)₃]²⁺, suggesting, given the new interpretation described above, that the adsorption state changes on going to more negative potentials. After a potential excursion to -1.1 V in this complex, the 1500 cm⁻¹ band does not re-appear, suggesting an irreversible loss of this adsorption state.

Spectra taken at more negative potentials show significant changes in both the intensities and positions of bands. A strong resemblance is evident between the results of this study and those of Corio and Rubim¹⁸ for the reduction of [Co(bpy)₃]²⁺ monitored by 647.1 nm excitation. However, under 514.5 nm excitation, the wavelength used here, the Co complex gives a quite different spectrum, with only a weak contribution from the reduction products. The researchers attribute this wavelength dependence to a resonance with a bpy^{•-} $\pi_7 \rightarrow \pi_{10}^*$ transition at the longer wavelength, claiming that this absorbance shifts from 550 nm in free radical anion to 630 nm in the metal complex. This means that the absorption maximum of the bpy^{•-} containing species in this study must be significantly lower than 630 nm, although with the broadness of the bpy^{•-} $\pi_7 \rightarrow \pi_{10}^*$ band, the maximum need not be very close to 514.5 nm itself to promote resonance at this wavelength.

The reason for the similarity between [Co(bpy)₃]⁺, which has high-spin character,³⁶ and Cr^{II}, which is d⁴ low-spin, is not immediately apparent, especially considering the reduction of [Cr(bpy)₃]^{3+→2+} is generally considered to be metal based. However, ¹H NMR

studies do show spin delocalization between the metal and ligand for both $[\text{Co}(\text{bpy})_3]^+$ ³⁷ and $[\text{Cr}(\text{bpy})_3]^{2+}$.³⁸ These are different from the MLCT and reduced states of ruthenium bipyridyls, because the spin spends significant time at the metal centre, and thus the complex cannot formally be denoted as $[\text{M}(\text{bpy})_2(\text{bpy}^{\bullet})]^{n+}$. However, resonance with the $\pi_7 \rightarrow \pi_{10}^*$ transition under laser excitation has the effect of localizing the spin onto bipyridine during the Raman scattering event, and thus the SERS spectra indicate this localized structure.

There is another possibility that must be considered when assigning the spectrum. The reduction of the complexes may lead to the formation of $[\text{Cr}(\text{bpy})(\text{H}_2\text{O})_4]^{n+}$ as in Figure 5.14, giving free 2,2'-bipyridine, which could subsequently coordinate to the silver surface. No evidence for adsorption of the neutral ligand to the surface is seen when comparing the data from Tables 5.2 and 5.3 with the spectra obtained by Chambers and Buck³⁹ at -0.4 V and by Kim and Itoh at potentials down to -1 V.⁴⁰

5.5 Conclusions

The electrochemistry and SERS spectroscopy of a series of chromium bis(bipyridyl) complexes have been studied. Slow electron transfer at glassy carbon means that only adsorbed species give observable redox currents in cyclic voltammograms. The Cr^{II} species adsorb better than Cr^{III} species in general, meaning that anodic peaks are more prevalent. The reduced species are also more substitutionally labile, and a reaction pathway from dichloride to aquahydroxo monomer and then to dimer is observed at pH 5-6. A final product resulting from reaction of the dimer could not be unambiguously identified. Side reactions including disproportionation to Cr mono and tris(bipyridyls) occur slowly in Cr^{III} solution, but are accelerated in acid solution and under extensive reductive electrolysis. $[(\text{PVP})_2\text{-Cr}(\text{bpy})_2]^{3+}$ can be electrosynthesized by reduction of $[\text{Cr}(\text{bpy})\text{Cl}_2]^+$ at a PVP modified GC electrode and shows reversible electrode kinetics at -0.32 V.

Potential dependent SERS spectroscopy shows similar responses for each of the complexes studied. At -0.4 V spectra showing features of both the normal Raman spectrum of $[\text{Cr}(\text{bpy})_3]^{3+}$ and colloidal SERS of $[\text{Cr}(\text{bpy})_3]^{2+}$ are seen and can be explained in terms of

two types of adsorption of $[\text{Cr}^{\text{III}}(\text{bpy})_2(\text{X})(\text{Y})]^{n+}$ complexes, although the exact nature of these has not been determined in these experiments. When $n = 2$ stronger adsorption stabilizes SERS sites such that high quality spectra can be obtained down to -1.1 V for the Cr^{II} species. The spectra of these reduced species seem to show that the electron is localized onto a bpy, in disagreement with NMR studies that show delocalization of the spin between metal and ligands. However, the 514.5 nm line is probably in resonance with a ligand $\pi_7 \rightarrow \pi_{10}^*$ transition, and so the ground state resonance structure that has the highest Raman cross-section is that where the spin resides on the bipyridine. These results could be confirmed by UV-visible spectroelectrochemistry of the SERS active surfaces, as was carried out by Corio and Rubim¹⁸ for their system. The electrochemistry of the complexes at an Ag electrode and at intermediate potentials (*ca.* -0.5 V) is also worthy of further consideration to determine the nature of the two species with bands at 1486 cm^{-1} and 1500 cm^{-1} .

5.6 References

- 1 *Dictionary of Inorganic Compounds*, ed. J. E. Macintyre, Chapman & Hall, London, 1992.
- 2 J. Ulstrup, *Acta Chem. Scand.*, 1971, **25**, 3397.
- 3 M. A. Jamieson, N. Serpone and M. Z. Hoffman, *Coord. Chem. Rev.*, 1981, **39**, 121.
- 4 M. Asano, D. Mongeau, D. Nicollin, R. Sasseville and J. A. Koningstein, *Chem. Phys. Lett.*, 1979, **65**, 293.
- 5 M. Asano, J. A. Koningstein and D. Nicollin, *J. Chem. Phys.*, 1980, **73**, 688.
- 6 K. Kniepp, H. Kniepp and E. Dinjus, *Chem. Phys. Lett.*, 1986, **126**, 69.
- 7 F. H. Burstall and R. S. Nyholm, *J. Chem. Soc.*, 1952, 3570.
- 8 W. A. Wickramasinghe, P. H. Bird, M. A. Jamieson, N. Serpone and M. Maestri, *Inorg. Chim. Acta*, 1982, **64**, L85.
- 9 M. Maestri, F. Bolletta, N. Serpone, L. Moggi and V. Balzani, *Inorg. Chem.*, 1976, **15**, 2048.

- 10 D. M. Soignet and L. G. Hargis, *Inorg. Chem.*, 1972, **11**, 2349.
- 11 J. Josephsen and C. E. Schäffer, *Acta Chem. Scand.*, 1970, **24**, 2929.
- 12 P. Andersen, *Coord. Chem. Rev.*, 1989, **94**, 47.
- 13 M. Ardon and A. Bino, *Inorg. Chem.*, 1985, **23**, 1343.
- 14 K. Anbalagan and P. Natarajan, *J. Polym. Sci. A, Polym. Chem.*, 1991, **29**, 1739.
- 15 H. Nishide, S. Hata and E. Tsuchida, *Makromol. Chem.*, 1978, **179**, 1445.
- 16 M. P. Hancock, J. Josephsen and C. E. Schäffer, *Acta Chem. Scand.*, 1976, **A30**, 79.
- 17 F. H. Burstall and R. S. Nyholm, *J. Chem. Soc.*, 1952, 3570.
- 18 P. Corio and J. C. Rubim, *J. Phys. Chem.*, 1995, **99**, 13217.
- 19 T. J. Dines and R. D. Peacock, *J. Chem. Soc., Faraday Trans. 1*, 1988, **84**, 3445.
- 20 P. G. Bradley, N. Kress, B. A. Hornberger, R. F. Dallinger and W. H. Woodruff, *J. Am. Chem. Soc.*, 1981, **103**, 7441
- 21 M. Forster and R. E. Hester, *Chem. Phys. Lett.*, 1981, **81**, 42.
- 22 W. Khamawphlang, S. Choudhury, A. K. Deb and S. Goswami, *Inorg. Chem.*, 1995, **34**, 3825.
- 23 R. S. Lawton and A. M. Yacynych, *Anal. Chim. Acta*, 1984, **160**, 149.
- 24 M. C. Hughes and D. J. Macero, *Inorg. Chem.*, 1976, **15**, 2040.
- 25 S. D. Nadler, J. G. Dick and C. H. Langford, *Can. J. Chem.*, 1985, **63**, 2732.
- 26 C. K. Ryu and J. F. Endicott, *Inorg. Chem.*, 1988, **27**, 2203.
- 27 B. V. Tucker, J. M. Fitzgerald, L. G. Hargis and L. B. Rogers, *J. Electroanal. Chem.*, 1967, **13**, 400.
- 28 D. M. Soignet and L. G. Hargis, *Inorg. Chem.*, 1973, **12**, 877.
- 29 K. D. Sugden, R. D. Geer and S. J. Rogers, *Biochemistry*, 1992, **31**, 11626.
- 30 A. Fitch, A. Lavy-Feder, S. A. Lee and M. T. Kirsh, *J. Phys. Chem.*, 1988, **92**, 6665.
- 31 J. M. Crabtree, D. W. Marsh, J. C. Tonkinson, R. J. P. Williams and W. C. Fernelius, *Proc. Chem. Soc.*, 1961, 336.

- 32 R. A. Holwerda, T. F. Tekut, B. G. Gafford, J. H. Zhang and C. J. O'Connor, *J. Chem. Soc., Dalton Trans.*, 1991, 1051.
- 33 G. A. Lawrance and D. F. Sangster, *J. Chem. Soc., Dalton Trans.*, 1987, 1425.
- 34 D. G. Holah and J. P. Fackler, *Inorg. Chem.*, 1965, **4**, 1112.
- 35 L. Deakin, C. DenAuwer, J.-F. Revol and M. P. Andrews, *J. Am. Chem. Soc.*, 1995, **117**, 9915.
- 36 Y. Kaizu, Y. Torii and H. Kobayashi, *Bull. Chem. Soc. Jpn.*, 1970, **43**, 3296.
- 37 R. J. Fitzgerald, B. B. Hutchinson and K. Nakamoto, *Inorg. Chem.*, 1970, **9**, 2618.
- 38 G. N. La Mar and G. R. Van Hecke, *Inorg. Chem.*, 1973, **12**, 1767.
- 39 J. A. Chambers and R. P. Buck, *J. Electroanal. Chem.*, 1984, **163**, 297.
- 40 M. Kim and K. Itoh, *J. Electroanal. Chem.*, 1985, **188**, 137.